



KIT SCIENTIFIC REPORTS 7576

Results of Severe Fuel Damage Experiment QUENCH-15 with ZIRLO™ cladding tubes

J. Stuckert, M. Große, U. Stegmaier, M. Steinbrück

J. Stuckert, M. Große, U. Stegmaier, M. Steinbrück

**Results of Severe Fuel Damage Experiment
QUENCH-15 with ZIRLO™ cladding tubes**

Karlsruhe Institute of Technology
KIT SCIENTIFIC REPORTS 7576

Results of Severe Fuel Damage Experiment QUENCH-15 with ZIRLO™ cladding tubes

by

J. Stuckert,

M. Große,

U. Stegmaier,

M. Steinbrück

Report-Nr. KIT-SR 7576

Impressum

Karlsruher Institut für Technologie (KIT)
KIT Scientific Publishing
Straße am Forum 2
D-76131 Karlsruhe
www.ksp.kit.edu

KIT – Universität des Landes Baden-Württemberg und nationales
Forschungszentrum in der Helmholtz-Gemeinschaft



Diese Veröffentlichung ist im Internet unter folgender Creative Commons-Lizenz
publiziert: <http://creativecommons.org/licenses/by-nc-nd/3.0/de/>

KIT Scientific Publishing 2011
Print on Demand

ISSN 1869-9669
ISBN 978-3-86644-670-0

Zusammenfassung

Ergebnisse des Schwere-Störfall-Experiments QUENCH-15 mit ZIRLO™ Hüllrohren

Das experimentelle Programm QUENCH am Karlsruher Institut für Technologie (das frühere Forschungszentrum Karlsruhe) ermittelt den Wasserstoffquellterm, der aus der Wassereinspeisung in einen trockengefallenen Leichtwasserreaktorkern nach einem Kühlmittelverlust resultiert, untersucht das Verhalten überhitzter Brennelemente unter verschiedenen Flutungsbedingungen und schafft eine Datenbasis für die Modelentwicklung und Verbesserung der Schwere-Störfall-Rechencodes. Die Großversuche werden in der QUENCH-Testanlage mit Bündeln von etwa 2,5 m Gesamtlänge durchgeführt.

Im QUENCH-15 Experiment wurden speziell die Auswirkungen des ZIRLO™ Hüllrohrmaterials auf die Bündeloxidation und das Flutverhalten untersucht, und zwar im Vergleich zu den früheren Tests QUENCH-06 (ISP-45, mit Standardmaterial Zircaloy-4), QUENCH-12 (VVER, E110) und QUENCH-14 (M5®). Die DWR-Bündelanordnung von QUENCH-15 bestand aus 24 beheizten Rohren (ZIRLO™-Hüllrohre), acht Eckstäben aus Zircaloy-4 und E110 und einem Dampfleitungsrohr aus Zr-702. Der Test wurde nach demselben Ablauf wie QUENCH-06, -12 und -14 gefahren, so dass die Auswirkungen des unterschiedlichen Hüllrohrmaterials direkt bestimmt werden können.

Das QUENCH-15 Experiment wurde am 27. Mai 2009 am Karlsruher Institut für Technologie erfolgreich durchgeführt. Das Paul Scherrer Institut (PSI, Schweiz) hat hierzu mit auf SCDAP basierenden und mit MELCOR Codes Vorausrechnungen durchgeführt. Der Testverlauf sah eine Voroxidationsphase in 3,45 g/s Argon und 3,5 g/s überhitzten Dampfs bei ~1470 K für ~2800 s vor, gefolgt von einer transienten Phase, die das Bündel auf maximale Temperatur von 2150 K führte. Zum Ende der Voroxidationsphase wurde ein erster Eckstab (Stab B) aus dem Bündel gezogen. Die maximale Oxidschichtdicke von 143 µm wurde bei 950 mm erreicht. Ein zweiter Eckstab (Stab F) wurde zum Ende der Transiente, etwa 30 s vor dem Einleiten des Flutens, gezogen. Seine maximale Oxidschichtdicke betrug 378 µm. Das Bündel wurde mit 48 g/s Wasser bei Raumtemperatur geflutet, die elektrische Heizleistung wurde dabei reduziert.

Die gesamte Wasserstoffproduktion beläuft sich auf 48 g. Hierzu im Vergleich stehen 36 g bei QUENCH-06, 58 g bei QUENCH-12 und 40 g bei QUENCH-14. Von der Gesamtmenge der 48 g wurden 41 g während der Voroxidation und der transienten Phase produziert und 7g während des Flutens.

Nach dem Einleiten des Flutvorgangs wurde keine Temperaturerhöhung beobachtet. Somit wurde die maximale Temperatur am Ende der Transienten mit 2150 K auf 950 mm Bündelhöhe gemessen. Die metallographische Untersuchung des Bündels nach dem Test zeigte weder auffällige Breakawayoxidation an den Hüllrohren noch Schmelzefreisetzung in die Zwischenräume der Stäbe. Die durchschnittliche äußere Oxidschichtdicke auf der heißesten Ebene bei 950 mm betrug 620 µm (QUENCH-06: 630 µm). Das geschmolzene metallische Hüllrohrmaterial verblieb zwischen äußeren und inneren Oxidschichten. Die Dicke der inneren Oxidschicht erreichte 20% der äußeren Oxidschicht.

Zusammenfassend lassen die Auswertungen des Tests QUENCH-15 auf ein ähnliches globales Verhalten des Bündels wie in den Tests QUENCH-14 (M5®) und QUENCH-06 (Zircaloy-4) schließen.

Abstract

The QUENCH experimental program at the Karlsruhe Institute of Technology (formerly Forschungszentrum Karlsruhe) is to investigate the hydrogen source term resulting from water injection into an uncovered core of a Light-Water Reactor (LWR), to examine the behavior of overheated fuel elements under different flooding conditions, and to create a data base for model development and improvement of Severe Fuel Damage code packages. The large-scale experiments are being performed in the QUENCH test facility with test bundles with a total length of approximately 2.5 m.

The QUENCH-15 experiment investigated the effect of ZIRLO™ cladding material on bundle oxidation and core reflood, in comparison with the tests QUENCH-06 (ISP-45, standard Zircaloy-4), QUENCH-12 (VVER, E110), and QUENCH-14 (M5®). The PWR-type bundle QUENCH-15 consisted of 24 heated rods (ZIRLO claddings), eight corner rods made of Zircaloy-4 and E110, and a Zr-702 shroud. The test was conducted according to the same test procedure as QUENCH-06, -12 and -14, so that the effects of the change of cladding material could be more easily observed.

The QUENCH-15 experiment was successfully conducted at the Karlsruhe Institute of Technology on May 27, 2009 supported by pretest calculations performed by the Paul Scherrer Institute (PSI) using SCDAP-based and MELCOR codes. The test involved pre-oxidation in a flow of 3.45 g/s argon and 3.5 g/s superheated steam at ~1470 K and ~2800 s followed by the transient phase leading to maximum bundle temperatures of 2150 K. At the end of preoxidation a first corner rod (rod B) was withdrawn from the bundle; the maximal oxide layer thickness of 143 µm was reached at 950 mm. A second corner rod (rod F) was pulled out of the test bundle at the end of the transient, i.e. approximately 30 s prior to quenching; the maximal oxide thickness reached 378 µm. The quenching of the test bundle was done with 48 g/s of water at room temperature and reduction of electrical power.

The total hydrogen production amounts to 48 g, compared to QUENCH-06, -12, -14 with 36, 58 and 40 g, respectively. Of 48 g of the total H₂, 41 g were produced during the preoxidation and transient phases and 7 g during quenching in test QUENCH-15.

After the reflood initiation no temperature excursion was observed so that the maximum temperature of 2150 K was measured at the end of the transient phase (at the 950 mm bundle elevation). The post-test metallography of the bundle showed neither noticeable breakaway oxidation of the cladding nor melt release into space between rods. The average outer oxide layer thickness at the hottest elevation of 950 mm was 620 µm (QUENCH-06: 630 µm). The molten cladding metal at the hottest elevation was localized between outer and inner oxide layers. The thickness of the inner oxide layer reaches 20% of that of the outer oxide layer.

In summary, the analyses of the QUENCH-15 test data indicate a similar global bundle behavior as of experiments QUENCH-14 (M5® cladding) and QUENCH-06 (Zircaloy-4 cladding).

Contents

- Introduction..... 1
- 1 Test facility 2
- 2 Instrumentation and data acquisition..... 3
- 3 Conduct and pertinent results of the QUENCH-15 experiment..... 5
- 4 Posttest appearance, final state of the test bundle 7
- 5 Metallographic examination..... 8
 - 5.1 Layer thicknesses 10
- 6 Axial distribution of absorbed hydrogen 11
- 7 Conclusions..... 13
- Acknowledgements 13
- References 15

List of Tables

- Table 1: QUENCH test matrix
- Table 2: Design characteristics of the QUENCH-15 test bundle
- Table 3: QUENCH-15; Electrical resistances of rods [mΩ]
- Table 4: Main characteristics of the ZrO₂ pellet material, yttria-stabilized (type FZY)
- Table 5: Properties of zirconia fiber insulating boards
- Table 6: Diameters of the materials used for the QUENCH high-temperature thermocouples
- Table 7: Main characteristics of the HfO₂ thermocouple insulator
- Table 8: List of instrumentation for the QUENCH-15 test
- Table 9: QUENCH-15; Bundle thermocouples positions
- Table 10: QUENCH-15; Sequence of events
- Table 11: QUENCH-15; Failure of thermocouples
- Table 12: QUENCH-15; Water/steam balance
- Table 13: QUENCH-15; Cross sections of the test bundle (which contains rods 4, 7, 10, 16, 19 over the entire length), for metallographic examination
- Table 14: QUENCH-15; Cross sections of the individual fuel rod simulators 1, 2, 3, 5, 6, 8, 9, 11, 12, 13, 14, 15, 17, 18, 20, 21, 22, 23, for metallographic examination
- Table 15: QUENCH-15; Average oxide layer thicknesses measured for rods #1 - #17
- Table 16: QUENCH-15; Average oxide layer thicknesses measured for rods #18 - #24, shroud and corner rods

List of Figures

- Fig. 1: Flow diagram of the QUENCH test facility.
- Fig. 2: QUENCH facility - main components.
- Fig. 3: QUENCH facility - containment and test section.
- Fig. 4: QUENCH-15; Test section with flow lines.
- Fig. 5: QUENCH-15; Fuel rod simulator bundle (cross section) including rod type indications.
- Fig. 6: Comparison of two different test bundles.
- Fig. 7: QUENCH-15; Heated fuel rod simulator.
- Fig. 8: QUENCH-15; Designation of the various thermocouples.
- Fig. 9: Axial temperature measurement locations in the QUENCH test section.
- Fig. 10: QUENCH-15; High-temperature thermocouple.
- Fig. 11: QUENCH-15; Concept for TC fastening at the test rod.
- Fig. 12: QUENCH-15; Arrangement of the thermocouples inside the corner rods.
- Fig. 13: QUENCH Facility; H₂ measurement with the GAM 300 Mass spectrometer.
- Fig. 14: Mass spectrometer sampling position at the off-gas pipe of the QUENCH test facility.
- Fig. 15: Hydrogen measurement with the CALDOS analyzer connected to the exhaust gas pipe of the QUENCH facility.
- Fig. 16: QUENCH-15 pre-test to adjusting of calculation parameters.
- Fig. 17: QUENCH-15 test conduct (schematics of histories of bundle temperature, power, argon and steam flow rate and hydrogen production rate).
- Fig. 18: QUENCH-15 test performance with reproduction of QUENCH-06 (Zry-4) temperature history.
- Fig. 19: Performance of tests QUENCH-06 (Zry-4), QUENCH-12 (E110), QUENCH-14 (M5) and QUENCH-15 (ZIRLO) under identical scenario.
- Fig. 20: QUENCH-15; Total electric bundle power vs. time, top, and heating rates of the transient phase, bottom.
- Fig. 21: QUENCH-15; Readings of cladding surface thermocouples.
- Fig. 22: QUENCH-15; Readings of cladding surface thermocouples (excluding failed TC) on the transient end and during reflood.

- Fig. 23: QUENCH-15; shroud temperatures during test.
- Fig. 24: QUENCH-15; shroud temperatures during second part of transient and flooding.
- Fig. 25: QUENCH-15; Readings of thermocouples installed inside corner rods. Top: during the test; bottom: during transient and flooding.
- Fig. 26: Comparison of temperature radial scattering at hottest elevation of 950 mm for bundles QUENCH-06 (Zry-4) and QUENCH-15 (ZIRLO) at the beginning of the transient phase (~6000 s).
- Fig. 27: Comparison of axial bundle temperature profiles (averaged cladding surface TC readings) for QUENCH-06 (Zry-4), -15 (ZIRLO).
- Fig. 28: Comparison of axial shroud temperature profiles (averaged shroud TC readings) for QUENCH-06 (Zry-4) and QUENCH-15 (ZIRLO).
- Fig. 29: QUENCH-15; Quench water mass flow rate (F 104), top, measurement of collapsed water level (L 501), center, off-gas flow rate (F 601), bottom.
- Fig. 30: QUENCH-15; cooling in 2-phase fluid above collapsed water surface during reflow phase.
- Fig. 31: QUENCH-15; indication of rod simulator failures on the basis of Kr release.
- Fig. 32: QUENCH-15; Argon and system pressure.
- Fig. 33: Comparison of bundle peak temperature evolution for QUENCH-06 (Zry-4), QUENCH-12 (E110), QUENCH-14 (M5) and QUENCH-15 (ZIRLO).
- Fig. 34: QUENCH-15; Post-test view of the shroud.
- Fig. 35: QUENCH-15; Appearance of withdrawn corner rods B, D, F, H – solid rods; A, C, E, G – tube at lower part (up to TIT position) and solid rod at upper part.
- Fig. 36: QUENCH-15; Segments of Zircaloy-4 corner rods B (withdrawn before transient) and A, C, D (withdrawn after test).
- Fig. 37: QUENCH-15; Segments of corner rods F (Zry-4, withdrawn before transient), E and H (E110, withdrawn after test), G (Zry-4, withdrawn after test).
- Fig. 38: QUENCH-15; position of molten metal segments of originally solid corner rod H: optical view (left), neutron radiography (right) and metallography (top right).
- Fig. 39: QUENCH-15; Upper part of corner rod A: transition between molten and solid β -Zr.
- Fig. 40: QUENCH-15; Upper part of corner rod D.
- Fig. 41: QUENCH-15; Elevation 950 mm: cross-sections of the Zircaloy-4 solid corner rods B, F and D withdrawn at different test stages.
- Fig. 42: QUENCH-15; Elevation 950 mm: cross-sections of the Zircaloy-4 instrumented corner rods A, C and G withdrawn after the test.

- Fig. 43: QUENCH-15; Elevation 950 mm: cross-sections of the E110 corner rods E and H withdrawn after the test. Influence of bundle circumferential temperature difference.
- Fig. 44: QUENCH-15; Elevations lower (850 mm) and upper (1050 mm) of hottest elevation: cross-sections of the Zircaloy-4 corner rods A and G withdrawn after the test.
- Fig. 45: QUENCH-15; Videoscope photos at the (partly empty) location of corner rod A, view from bottom, camera was moved along heated rod 6 and between rods 7 and 18.
- Fig. 46: QUENCH-15; Videoscope photos taken at empty positions of the corner rods, exhibiting the status of different high-temperature W/Re thermocouples.
- Fig. 47: QUENCH-15; bundle remnant after dismounting.
- Fig. 48: QUENCH-15; Posttest view of 18 withdrawn fuel rod simulators at elevation 520-1300 mm.
- Fig. 49: QUENCH-15; Detailed photographs of the test rods 2, 3, 11, and 22.
- Fig. 50: QUENCH-15; Detailed photographs of the test rods 1, 2, 3, 6, 15, 17, and 18.
- Fig. 51: QUENCH-15; Detailed photographs of the test rod No. 24.
- Fig. 52: QUENCH-15; Detailed photographs of the test rod No. 24.
- Fig. 53: QUENCH-15; Bundle cross sections at 534 mm, 550 mm, 634 mm and 650 mm.
- Fig. 54: QUENCH-15; Bundle cross sections at 734 mm and 750 mm.
- Fig. 55: QUENCH-15; Bundle cross sections at 834 mm and 850 mm.
- Fig. 56: QUENCH-15; Bundle cross sections at 934 mm and 950 mm.
- Fig. 57: QUENCH-15; Bundle cross sections at 1000 mm and 1050 mm.
- Fig. 58: QUENCH-15; Bundle cross sections at 1134 mm and 1150 mm.
- Fig. 59: QUENCH-15; Bundle cross sections at 1234 mm and 1250 mm.
- Fig. 60: QUENCH-15; Cladding structure of rod #12 at 550 mm, 0°.
- Fig. 61: QUENCH-15; QUENCH-15; Cross section at elevation 650 mm depicting individual test rods 4, 10..
- Fig. 62: QUENCH-15; Cladding structure of rods #4 and #10 at 650 mm, 0°: different oxidation degree for inner and outer rod groups.
- Fig. 63: QUENCH-15; Cross section at elevation 750 mm depicting individual test rods 1-6.
- Fig. 64: QUENCH-15; Cross section at elevation 750 mm depicting individual test rods 7-12.

- Fig. 65: QUENCH-15; Cross section at elevation 750 mm depicting individual test rods 13-18.
- Fig. 66: QUENCH-15; Cross section at elevation 750 mm depicting individual test rods 19-23.
- Fig. 67: QUENCH-15; Cladding structure of rods #4, #12 and #18 at 750 mm, 0°: different oxidation degree for inner and outer rod groups.
- Fig. 68: QUENCH-15; Cross section at elevation 850 mm depicting individual test rods 1-11.
- Fig. 69: QUENCH-15; Cross section at elevation 850 mm depicting individual test rods 16-21.
- Fig. 70: QUENCH-15; Cladding structure of rods #4, #7 and #10 at 850 mm: different oxidation degree depending on radial position of cladding segment in bundle.
- Fig. 71: QUENCH-15; Cross section at elevation 950 mm depicting individual test rods 7-15.
- Fig. 72: QUENCH-15; Cross section at elevation 950 mm depicting individual test rods 16-22.
- Fig. 73: QUENCH-15; Cladding structure of rods #16 at 950 mm: absence of metallic layer due to melt relocation inside the pellet-cladding gap; inner oxide layer formation.
- Fig. 74: QUENCH-15; Cladding structure of rods #19 at 950 mm: melt relocation inside gap between oxide and α -Zr(O).
- Fig. 75: QUENCH-15; Cladding structure of rods #7, #11 and #19 at 950 mm: oxide precipitates inside α -Zr(O) layer.
- Fig. 76: QUENCH-15; Cross section at elevation 1000 mm depicting individual test rods 3-9.
- Fig. 77: QUENCH-15; Cross section at elevation 1000 mm depicting individual test rods 10-19.
- Fig. 78: QUENCH-15; Cross section at elevation 1000 mm depicting individual test rods 20-23.
- Fig. 79: QUENCH-15; Cladding structure of adjacent rods #9 and #20 at 1000 mm.
- Fig. 80: QUENCH-15; Cladding structure of adjacent rods #17 and #18 at 1000 mm: molten metallic layer; inner oxide layer; void formation due to melt relocated under outer oxide layer.
- Fig. 81: QUENCH-15; Cladding structure of rod #17: oxidation of molten layer with ceramic precipitate formation at elevation of 1000 mm.
- Fig. 82: QUENCH-15; Cross section at elevation 1050 mm depicting individual test rods 1-6.
- Fig. 83: QUENCH-15; Cross section at elevation 1050 mm depicting individual test rods 7-12.
- Fig. 84: QUENCH-15; Cross section at elevation 1050 mm depicting individual test rods 13-18.
- Fig. 85: QUENCH-15; Cross section at elevation 1050 mm depicting individual test rods 19-23.

- Fig. 86: QUENCH-15; Structure of rods #3, #6 and #16 at 1050 mm: partially molten α -Zr(O) layer.
- Fig. 87: QUENCH-15; Cross section at elevation 1050 mm depicting different oxidation degree for internal rod #6 and external rod #19.
- Fig. 88: QUENCH-15; Cladding structure of rod #3: oxidation of molten layer with inner oxide formation at elevation of 1050 mm.
- Fig. 89: QUENCH-15; Cross section at elevation 1150 mm depicting individual test rods 1-6.
- Fig. 90: QUENCH-15; Cross section at elevation 1150 mm depicting individual test rods 7-12.
- Fig. 91: QUENCH-15; Cross section at elevation 1150 mm depicting individual test rods 13-18.
- Fig. 92: QUENCH-15; Cross section at elevation 1150 mm depicting individual test rods 19-23.
- Fig. 93: QUENCH-15; Cross section at elevation 1150 mm depicting morphology of cladding layers for internal rod #4 and external rod #19. Two difference ZrO_2 sub-layers due to tensile and compressive stress.
- Fig. 94: QUENCH-15; Cross section at elevation 1250 mm depicting individual test rods 4, 19.
- Fig. 95: QUENCH-15; Cross section at elevation 1250 mm depicting morphology of cladding layers for internal rod #4 and external rod #19. Waved boundary between ZrO_2 and α -Zr(O) layers.
- Fig. 96: QUENCH-15; axial distribution of ZrO_2 for corner rods. Eddy current measurement.
- Fig. 97: QUENCH-15; axial distribution of ZrO_2 for Zry-4 corner rods. Metallographic results.
- Fig. 98: QUENCH-15; Oxide layer thickness at bundle elevation 550 mm (Cross section QUE-15-550).
- Fig. 99: QUENCH-15; Oxide layer thickness at bundle elevation 650 mm (Cross section QUE-15-650).
- Fig. 100: QUENCH-15; Oxide layer thickness at bundle elevation 750 mm (Cross section QUE-15-750).
- Fig. 101: QUENCH-15; Oxide layer thickness at bundle elevation 850 mm (Cross section QUE-15-850).
- Fig. 102: QUENCH-15; Oxide layer thickness at bundle elevation 950 mm (Cross section QUE-15-950).
- Fig. 103: QUENCH-15; Oxide layer thickness at bundle elevation 1000 mm (Cross section QUE-15-1000).
- Fig. 104: QUENCH-15; Oxide layer thickness at bundle elevation 1050 mm (Cross section QUE-15-1050).
- Fig. 105: QUENCH-15; Oxide layer thickness at bundle elevation 1150 mm (Cross section QUE-15-1150).

- Fig. 106: QUENCH-15; Oxide layer thickness at bundle elevation 1250 mm (Cross section QUE-15-1250).
- Fig. 107: Axial distribution of cladding outer oxide thicknesses for the bundles QUENCH-06 (Zry4), QUENCH-12 (E110), QUENCH-14 (M5) and QUENCH-15 (ZIRLO).
- Fig. 108: Axial distribution of cladding metal converted to oxide for the bundles QUENCH-06 (Zry4), QUENCH-12 (E110), QUENCH-14 (M5) and QUENCH-15 (ZIRLO).
- Fig. 109: QUENCH-15; Measurement of hydrogen production with mass spectrometer and CALDOS analyzer during whole test (left) and during transient and reflood phases (right).
- Fig. 110: Hydrogen production for three bundle tests according to mass-spectrometer measurements.
- Fig. 111: Hydrogen uptake by ZIRLO cladding and different corner rods of QUENCH-15 bundle in comparison to M5 cladding of QUENCH-14.

Introduction

The most important accident management measure to terminate a severe accident transient in a Light Water Reactor (LWR) is the injection of water to cool the uncovered degraded core. The QUENCH experiments are set up to investigate the hydrogen source term that results from the water or steam injection into an uncovered LWR core.

In 12 out of 15 QUENCH experiments Zircaloy-4 was used as standard rod cladding material. QUENCH-12 was performed with Nb-bearing E110 cladding material in a VVER geometry and QUENCH-14 with M5[®] (product of AREVA) in the frame of the Advanced Cladding Materials (ACM) test series in the standard PWR-type bundle arrangement (see [Table 1](#)). QUENCH-15 as the second ACM experiment was to investigate the effect of ZIRLO[™] cladding material (provided by Westinghouse Electric Sweden) on bundle oxidation and core reflood, in comparison with tests QUENCH-06 [1, 2] (ISP-45, standard Zircaloy-4), QUENCH-12 [3] (VVER, E110), and QUENCH-14 [4] (M5[®]). The arrangement of the PWR-type bundle QUENCH-15 was different due to rod outer diameter and pitch and consisted of 24 heated rods with ZIRLO[™] claddings, eight corner rods made of Zircaloy-4 and E110, and a Zr-702 shroud. The test was conducted in principle with the same protocol as QUENCH 06, -12 and -14, so that the effects of the change of cladding material could be more easily observed.

To support and improve the pretest calculations two pretests were run on May 7 and 8, 2009 up to a maximum bundle temperature of 920 K (950 mm elevation). After these pretests corner rod B was pulled out of the bundle, and the oxide layer was measured to a thickness of ~2 μm . The main experiment was successfully conducted at the Karlsruhe Institute of Technology (KIT) on May 27, 2009 with help of the final pretest calculations performed by the Paul Scherrer Institute (PSI) using SCDAPSIM, SCDAP/RELAP5 and MELCOR, modified locally as necessary for ZIRLO[™] oxidation kinetics based on separate-effects data from the QUENCH program [5, 6].

Pretest calculations showed that the mass flow rates of argon and superheated steam should be increased by 15%, i.e. to 3.45 and 3.5 g/s, respectively, to achieve the same flow velocity with the increased flow area of the QUENCH-15 bundle geometry.

No ZIRLO[™] material was available for the corner rod design (solid rod of 6 mm diameter) so that the evolution of the oxide layer growth during the test was determined with help of two Zircaloy-4 corner rods withdrawn successively from the test bundle, i.e. at the end of preoxidation and at the end of the transient. The remaining six corner rods installed in the QUENCH-15 bundle, including one that was made of E110 (VVER material Zr1%Nb), were removed from the bundle after the experiment.

It should be noted in general that the oxidation behavior of the ZIRLO[™] cladding material has been checked thoroughly by industry for normal operational temperature (maximum of ~350 °C for outer surface and ~450 °C for inner surface). In this temperature range the oxide layer thickness of ZIRLO[™] cladding is smaller when compared to Zircaloy-4.

1 Test facility

The main component of the QUENCH test facility is the test section with the test bundle (Figs. 1-4). The facility can be operated in two modes: a forced-convection mode depicted and a boil-off mode. In the forced-convection mode (relevant for QUENCH-15) superheated steam from the steam generator and superheater enters the test bundle at the bottom together with argon as a carrier gas for off-gas measurements. The argon, the steam not consumed, and the hydrogen produced in the zirconium-steam reaction flow from the bundle outlet at the top through a water-cooled off-gas pipe to the condenser where the steam is separated from the non-condensable gases. The water cooling circuits for bundle head and off-gas pipe are temperature-controlled to guarantee that the steam/gas temperature is high enough so that condensation at test section outlet and inside the off-gas pipe can be avoided. So, the temperature at the bundle head is kept at 348 K, and the water inlet temperature of the off-gas pipe is controlled at 393 K.

The system pressure in the test section is 0.2 MPa.

The design characteristics of the test bundle are listed in Table 2. The test bundle is approximately 2.5 m long and is made up of 24 fuel rod simulators (Fig. 5). A comparison with usual bundle configuration is pictured in Fig. 6. Heating is electric by 5 mm diameter tungsten heaters installed in the rod center (Fig. 7). Electrodes of molybdenum/copper are connected to the tungsten heaters at one end and to the cable leading to the DC electrical power supply at the other end. The measured electric resistance of a single heater (W+Mo+Cu sections) is $4.4 \pm 0.5 \text{ m}\Omega$ at room temperature (Table 3). This value increases significantly with temperature. The additional resistance of the external electric circuit between the axial end of the single heater and the connection to the generator (sliding contacts, cables, and bolts) is $0.4 \text{ m}\Omega + 0.22 \text{ m}\Omega = 0.62 \text{ m}\Omega$. This value can be taken as independent of temperature because the external electric circuit remains at room temperature throughout the experiment.

The fuel rod simulators are held in position by five grid spacers all made of Zircaloy-4. The tungsten heaters are surrounded by annular ZrO_2 pellets. Main properties of the ZrO_2 pellets are given in Table 4. The rod cladding of the fuel rod simulator is ZIRLO™, a Westinghouse product, and identical to that used in LWRs: 9.5 mm outside diameter, inner diameter 8.357 mm; see also Table 2. All test rods were filled with Kr at a pressure of approx. 0.22 MPa. The rods were connected to a controlled feeding system that compensated minor gas losses and allowed observation of a first cladding failure as well as a failure progression.

There are eight corner rods installed in the bundle. Four of them, i.e. rods “A”, “C”, “E”, and “G” are made of a solid rod at the top and a tube at the bottom and are used for thermocouple instrumentation. Three of them are made of Zircaloy-4 whereas rod “E” is made of E110 (VVER material $\text{Zr}1\%\text{Nb}$). The other four rods, i.e. rods “B”, “D”, “F”, and “H” (solid rods of 6 mm diameter) are designed to be withdrawn from the bundle to check the amount of ZrO_2 oxidation at specific times. Again, three of them are made of Zircaloy-4 whereas rod “H” is made of E110.

The test bundle is surrounded by a shroud of Zirconium 702 with a 37 mm thick ZrO_2 fiber insulation (see properties in Table 5) extending from the bottom to the upper end of the heated zone and a double-walled cooling jacket of Inconel 600 (inner)/stainless steel (outer)

over the entire length. The annulus between shroud and cooling jacket with the fiber insulation is purged (after several cycles of evacuation) and then filled with stagnant argon of 0.22 MPa. The annulus is connected to a flow- and pressure-controlled argon feeding system in order to keep the pressure constant at the target of 0.22 MPa (beyond this pressure gas is released) and to prevent an access of steam to the annulus after shroud failure (argon feeding below the target value). The 6.7 mm annulus of the cooling jacket is cooled by argon from the upper end of the heated zone to the bottom of the bundle and by water in the upper electrode zone. Both the absence of a ZrO₂ insulation above the heated region and the water cooling are to avoid too high temperatures of the bundle in that region.

2 Instrumentation and data acquisition

For **temperature** measurements the test bundle, shroud, and cooling jackets are equipped with thermocouples at orientations and elevations as illustrated in [Fig. 8](#) and [Fig. 9](#) correspondingly, and listed in [Table 8](#). An overview of the positions of the bundle thermocouples is given in [Table 9](#).

The dimensions of the thermocouple components are provided in [Table 6](#), some properties of the thermocouple insulator in [Table 7](#). The thermocouples attached to the outer surface of the rod cladding at elevations between -250 and 1350 mm are designated “TFS” for all heated rods.

In the lower bundle region, i.e. up to 550 mm elevation, NiCr/Ni thermocouples with stainless steel sheath/MgO insulation and an outside diameter of 1.0 mm are used for measurements of the rod cladding and shroud temperatures. The thermocouples in the hot zone and above are high-temperature thermocouples with W5Re/W26Re wires, HfO₂ insulation, and a duplex sheath of tantalum (inside) and Zircaloy (outside) with an outside diameter of about 2.2-2.3 mm ([Fig. 10](#)).

The thermocouple attachment technique for the surface-mounted high-temperature TCs is shown in [Fig. 11](#). The TC tip is held in place by two clamps of zirconium (0.2 mm thick). As these clamps are prone to oxidation and embrittlement in a steam environment an Ir-Rh wire of 0.25 mm diameter is additionally used in test QUENCH-15. The leads of the thermocouples from the -250 mm to the 850 mm level leave the test section at the bottom whereas the TCs above 850 mm are routed to the top avoiding to route TC cables through the hot zone (see [Fig. 9](#)). Additionally, the cables of shroud thermocouples (designated TSH xx/x “I”) were routed toward outside the shroud insulation to avoid heat transfer from the shroud into the TC cable, apart from the TC junction.

The shroud thermocouples (designation “TSH”) are mounted at the outer surface between -250 mm and 1250 mm. The thermocouples that are installed inside the Zircaloy instrumentation rods at the two corner positions of the bundle (positions A, C, E and G) are designated “TIT” (see [Fig. 12](#)). All “TIT” thermocouples are of the high-temperature type. The thermocouples of the cooling jacket (TCI and TCO) are 1 mm NiCr/Ni thermocouples with stainless steel sheath for all levels. The thermocouples of the cooling jacket are installed inside the wall of the inner cooling tube (from -250 mm to 1150 mm, designation “TCI”) and at the outer surface of the outer cooling tube (from -250 mm to 950 mm, designation “TCO”) as illustrated in [Fig. 8](#).

The thermocouples which failed during the experiment are listed in [Table 11](#).

The **hydrogen** released in the test section is analyzed by two different measurement systems: (1) a state-of-the-art mass spectrometer (MS) Balzers "GAM300" located at the off-gas pipe ~2.66 m downstream the test section ([Figs. 13 and 14](#)), (2) a commercial-type hydrogen detection system "Caldos 7 G" by Hartmann&Braun ([Fig. 15](#)) located behind the condenser, at the end of the off-gas line. Due to the different locations in the facility the mass spectrometer "GAM 300" responds almost immediately to changes in the gas composition whereas the Caldos device has a delay time of about 40 s. With the mass spectrometer all off-gas species including steam can be analyzed whereas the Caldos system works only for binary Ar/H₂ mixtures.

The mass spectrometer "BALZERS GAM 300" is a completely computer-controlled quadrupole MS with an 8 mm rod system which allows certain quantitative measurement of gas concentrations down to about 10 ppm. For the MS measurement a sampling tube is inserted in the off-gas pipe located approx. 2.7 m downstream from the test section outlet (see [Fig. 2 and 4](#)). It has several holes at different elevations to guarantee that the sampling of the gas to be analyzed is representative (see [Fig. 14](#)). To avoid steam condensation in the gas pipes between the sampling position and the MS the temperature of the gas at the MS inlet is controlled by heating tapes to be between 110 and 150 °C (the upper operating temperature of the MS inlet valves). This allows the MS to analyze the steam production rate. Besides, the concentrations of the following species were continuously measured by the mass spectrometer during all test phases: argon, hydrogen, steam, nitrogen, oxygen, and krypton. The fuel rod simulators are filled with krypton which can be used as an indicator for a cladding failure. Additionally, the MS is used to control the atmosphere in the facility, e.g., to monitor the gas composition at the beginning of the test.

The temperature and pressure of the analyzed gas are measured near the inlet valve of the MS. The MS is calibrated for hydrogen, oxygen and nitrogen with well-defined argon/gas mixtures and for steam with mixtures of argon and steam supplied by a Bronkhorst controlled evaporator mixing (CEM) device. The MS off-gas is released into the atmosphere because the amount of hydrogen taken out of the system is negligible. A heated measuring gas pump was used to ensure a continuous flow of the steam-gas mixture from the off-gas pipe to the mass spectrometer.

The principle of measurement of the Caldos system is based on the different heat conductivities of different gases. The Caldos device is calibrated for the hydrogen-argon gas mixture. To avoid any moisture in the analyzed gas a gas cooler, which is controlled at 276 K, is connected to the gas analyzer (see also [Fig. 15](#)). The response time of the gas analyzer is documented by the manufacturer to be 2 s, i.e. a time in which 90 % of the final value should be reached. In contrast to the mass spectrometer the Caldos device only measures the hydrogen content. Gases other than H₂ cannot be analyzed by this system.

For the MS device as well as for the Caldos the hydrogen mass flow rate is calculated by referring the measured H₂ concentration to the known argon mass flow rate according to equation (1):

$$\dot{m}_{H_2} = \frac{M_{H_2}}{M_{Ar}} \cdot \frac{C_{H_2}}{C_{Ar}} \cdot \dot{m}_{Ar} \quad (1)$$

with M representing the molecular masses, C the concentrations in vol-% and \dot{m} the mass flow rates of the corresponding gases.

With an argon-hydrogen (two-component) mixture that in fact exists at the location of the Caldos analyzer equation (1) can be written as follows

$$\dot{m}_{H_2} = \frac{M_{H_2}}{M_{Ar}} \cdot \frac{C_{H_2}}{100 - C_{H_2}} \cdot \dot{m}_{Ar} \quad (2)$$

The data of the main **data acquisition** system and of the mass spectrometer were stored on different computers. All computers were synchronized against each other. The data of the main acquisition system as well as those of the mass spectrometer data were stored at a frequency of 1 Hz, the ones with the MS with approximately 1.1 Hz. The latter were interpolated to 1 Hz for further data processing.

3 Conduct and pertinent results of the QUENCH-15 experiment

To support and improve the pretest calculations two pretests were run on up to a maximum bundle temperature of 920 K at 950 mm elevation ([Fig. 16](#)). After these pretests corner rod B was pulled out of the bundle, and the oxide layer was measured to a mere thickness of ~2 μm .

A listing of the major events during the QUENCH-15 experiment is given in [Table 10](#). The main test phases of the QUENCH-15 experiment are shown in [Fig. 17](#) and summarized below:

- Phase I Heatup to ~860 K and **stabilization**. Facility checks.
- Phase II Heatup to ~1470 K.
- Phase III **Preoxidation** of the test bundle in a flow of 3.45 g/s argon and 3.5 g/s superheated steam at ~1470 K for ~2800 s. Withdrawal of corner rod B at the end of preoxidation.
- Phase IV **Transient** heatup from ~1470 to ~2150 K in a flow of 3.45 g/s argon and 3.5 g/s superheated steam. Withdrawal of corner rod F ~30 s before quench initiation.
- Phase V **Quenching** of the bundle by a flow of ~48 g/s of water.

The test was conducted in principle with the same protocol as the reference test QUENCH-06 ([Fig. 18](#)) as well as tests QUENCH-12 and QUENCH-14 ([Fig. 19](#)). The experiment started with an application of electrical bundle power of ca. 4.0 kW, which was

ramped step-wise to 11.5 kW over nearly 3000 s to achieve the desired pre-oxidation temperature at bundle peak position of ca. 1470 K (based on TIT G/13, whose reading values corresponds to peak bundle temperatures), in a flow of 3.45 g/s argon and 3.5 g/s steam. Pre-oxidation was continued to 6000 s; at about this time a first corner rod (rod B) was withdrawn to check the oxidation level. The power was then ramped at a rate of 5.9 W/s to cause a temperature increase until the desired maximum bundle temperature of 2150 K (based on TIT G/13) which was reached after about 1120 s. The temperature increase rate during the transient changed from 0.24 K/s to 2.8 K/s (Fig. 20). Figs. 21, 23 and 25 show temperature histories for cladding outer surfaces, shroud outer surface and inside corner rods, correspondingly. The radial temperature scattering at the hottest elevation of 950 mm is illustrated in Fig. 26. Axial temperature distributions at the beginning and end of transient are presented in Fig. 27 (averaged readings of cladding surface thermocouples) and Fig. 28 (averaged readings of shroud thermocouples). Approximately 30 s before the maximum bundle temperature was reached the corner rod F was withdrawn from the bundle, again to check the oxidation level.

The quench criterion and reflood rate were identical to those in QUENCH-06, -12 and -14. The reflood with 48 g/s water at room temperature was initiated (Fig. 29), following fast water injection (4 liter water injected with rate of ~ 1 kg/s from special pressure vessel with $p = 6.5$ bar) to fill the lower plenum. The cladding surface thermocouples at all bundle elevations immediately showed temperature decrease, which indicates a prompt distribution of cool fluid along the whole bundle (Fig. 22). The cladding surface temperature increased again after evaporation of the injected water. The shroud thermocouples, protected from direct contact with fluid, showed no sharp reaction on the fast water injection (Fig. 24). Due to the formation of a 2-phase region above the collapsed water level, the wetting of thermocouples for certain elevations was observed earlier than the water front reached this bundle elevation (Fig. 30). The amounts of injected and collected water are in good agreement which indicates the good functionality of the measuring devices (Table 12). Shortly after fast water injection first rod failure was observed, indicated by decrease of rod internal pressure P411 and Kr measurement with MS (Fig. 31). Shroud failure was not observed during the test (Fig. 32). The electrical power was reduced to 4.4 kW during the reflood phase, approximating effective decay heat levels.

After reflood initiation no temperature excursion was observed (Fig. 33). The maximum temperature, i.e. 2150 K, was measured at the 950-mm bundle elevation, at the end of the transient phase.

The remaining six corner rods (Zircaloy-4 and E110) were withdrawn after the test, again to check oxide levels and hydrogen absorption.

The online measurement results for the hydrogen release rate are shown in Fig. 109. The rapid rate increase, measured with the mass spectrometer, corresponds exactly with the fast water injection ($t=7120$ s). The maximal hydrogen release rate of 1.83 g/s was reached at 7124 s. The hydrogen release rate decreased to the pre-reflood value (0.18 g/s) at 7127 s, i.e. the hydrogen release peak width is 7 s. The hydrogen peak, registered by Caldos, was delayed by 20 s because of the remote position of its sampling connection, and it is broader and lower than the MS peak due to slower response time of Caldos in comparison with the

mass spectrometer. The integral values of hydrogen release are very comparable between both systems. Based on the MS results, the total hydrogen release was 48 g, compared to QUENCH-06, -12, -14 with 36, 58 and 40 g, respectively ([Fig. 110](#)). 41 g hydrogen were released during the pre-quench phases and 7 g during quenching in test QUENCH-15.

4 Posttest appearance, final state of the test bundle

The visual inspection of the shroud revealed no crack development at the outer surface of the shroud ([Fig. 34](#)). Only local melting of the not oxidized surface of the shroud was observed between elevations 880 and 1020 mm. This indicates that the surface shroud temperatures reached the melting point of β -Zr (~ 2100 K) at these bundle elevations.

The observation of solid corner rod B, withdrawn before transient initiation, reveals the formation of a dark oxide layer along the whole rod, whereas the region between ~ 900 and ~ 1050 mm for rod F, withdrawn on the end of the transient, shows the formation of white oxide ([Figs. 35 – 37](#)). The other Zry-4 corner rods A, C, D and G, withdrawn after the test, reveal the formation of a white oxide layer without visible breakaway effect in the region between ~ 800 and ~ 1100 mm. Very strong breakaway oxidation was observed for the E110 corner rods between elevations ~ 600 and ~ 1300 mm. Neutron radiography of the corner rods shows formation of voids 1) due to downwards relocation of the β -Zr melt from elevations between ~ 910 and ~ 970 mm ([Fig. 38](#)), and 2) due to shrinkage of internal rod material during solidification of initially molten β -Zr ([Figs. 39, 40](#)). This molten region extended between ~ 850 and ~ 1035 mm according to metallographic observations at longitudinal cross-sections. A detailed metallographic investigation of corner rod cross-sections at the hottest elevations of 850 – 1050 mm shows a circumferential temperature gradient in the bundle. Indeed, corner rods C, D and E were not molten, whereas corner rods G, H and A reveal melt formation and relocation ([Figs. 41 – 44](#)).

Before the disassembly of the QUENCH-15 unit of shroud and test rod bundle, the empty channels of the corner rods were used for visual inspection by endoscope (with an OLYMPUS IPLEX videoscope inserted from the bottom at the eight empty positions of the corner rods). The post-test endoscopy ([Figs. 45 and 46](#)) did not show any noticeable melt formation in the test bundle but some cracks in the rod claddings and minor spalling of thin oxide layers.

After endoscopy the shroud was taken off of the test bundle to view the test rods in detail and document the appearance of the individual test rods by photography. However, during the separation of test bundle and shroud, nearly all test rods broke. In the end there were two “separate” bundle parts: (a) the upper parts of the individual rods No. 1, 2, 3, 5, 6, 8, 9, 11, 12, 13, 14, 15, 17, 18, 20, 21, 22, 23, and 24, (b) the remaining test bundle including the lower parts of the individual rods given above and the rods No. 4, 7, 10, 16, and 19 which “survived” the dismantling process in full length. After photography, in particular of the hot regions, test rod 24 was taken together with the corner rods for the examination for hydrogen uptake by neutron radiography. Overview photographs are given in [Figs. 47, 48](#) and detailed ones in [Figs. 49-52](#).

5 Metallographic examination

The two parts of the test bundle were encapsulated separately in epoxy resin (Bakelite EPR 0273 with the pertinent hardener Bakelite EPH 350) and cut (by a saw with a diamond blade ~3 mm thick) into slabs and slices at identical levels where it was possible (see sectioning list in [Tables 13](#) and [14](#)). The cross-section macrographs are presented as overview in [Figs. 53-59](#) and characteristic details of each section are described below. All micrographs, presented in this chapter, were taken from polished and etched cross-sections.

Bundle cross-section at elevation 550 mm. The oxidation state of cladding is illustrated in [Fig. 60](#). Homogeneous monoclinic oxide ($T_{550} < 1300$ K) is formed (bottom micrograph), underlayed by relatively wide hexagonal alpha-Zr stabilized by oxygen. By polarized light (middle micrograph, compare to top bright field micrograph) the contrast between the fine grained α -Zr(O) layer and the matrix of prior β -Zr phase is emphasized.

Bundle cross-section at elevation 650 mm. The macrographs of two typical rods from inner and outer bundle rod groups, as given in [Fig. 61](#), illustrate the absence of through-going cladding cracks. A comparison of cladding structures of these rods ([Fig. 62](#)) shows that the oxidation degree (thicknesses of ZrO_2 and α -Zr(O) layers) is noticeably higher for the inner rod, resulting from higher temperatures in the bundle center. The cracked outer part of the oxide layer for the inner rod #4 (diffuse white layer in polarized micrograph) was formed as monoclinic oxide during the preoxidation test phase, whereas the inner dense originally tetragonal part was developed during transient (max $T_{650} \sim 1500$ K) and reflood phases. The micro cracks inside the outer oxide scale were developed due to 1) conversion of monoclinic phase into tetragonal phase during transient, 2) tensile strength during the inner oxide growth. The homogeneous oxide and the uneven interface between oxide and α -Zr(O) at the surface of the colder rod #10 are a typical evidence for monoclinic oxide structure similar to elevation of 550 mm.

Bundle cross-section at elevation 750 mm. The macrographs of 23 embedded rod simulators, as given in [Figs. 63 – 66](#), show presence of relatively wide brittle α -Zr(O) layer, which were partially lost during preparation. Again, as depicted in [Fig. 67](#), the oxidation degree (thickness of ZrO_2 and α -Zr(O) layers) decreases from the bundle center (rod #4) to the bundle periphery (rod #18). Due to the very thin ductile β -Zr layer, the through-going cracks developed in claddings of center rods during the final phase of reflood (top micrograph in [Fig. 67](#)). The absence of the prior cubic oxide phase indicates that the temperature maximum at this elevation is $T_{750} < 1770$ K.

Bundle cross-section at elevation 850 mm. A relatively thick oxide layer can be seen already on the macrographs of the rod simulators ([Figs. 68, 69](#)). The tetragonal oxide layer was formed during the whole test at the surface of peripheral rods (1300 K $< T_{850p} < 1770$ K), whereas the microstructure of the inner oxide layer corresponds to a prior-cubic phase ([Fig. 70](#)). I. e. the temperatures in the bundle center reached values of more than 1770 K during the transient and reflood - which is in good agreement with the axial temperature distribution in [Fig. 27](#). Through going cracks developed in claddings of the center rod group: these claddings are very brittle at this elevation because they are composed of oxide and α -Zr(O) layers only.

Bundle cross-section at elevation 950 mm. Macrographs of the individual rods show very intensive cladding oxidation (Figs. 71 and 72). For some rods there is seen only oxide layer (e.g. rods #13 and #16). Nevertheless the corresponding claddings were not completely oxidized. Indeed, according to the Pilling-Bedworth ratio for Zr ($R_{PB} = 1.56$) the complete conversion of metallic cladding to oxide gives the oxide layer thickness of $572 \cdot 1.56 = 892 \mu\text{m}$. However, the maximal measured oxide layer thickness for rods #13 and #16 is $820 \mu\text{m}$ (Fig. 102). The remnant of the metallic layer melted and relocated downwards. Fig. 73 shows cladding position with boundary between the void at location of relocated metallic melt and the inner oxide layer. Two following mechanisms can be responsible for development of this inner oxide layer: 1) the melt oxidation by steam penetrated through cladding cracks (circumferential ruptures shown in Fig. 45); 2) growth of oxide layer on the free (non-oxidized) surface of melt owing to complicated oxygen transport from the outer oxide layer through the melt [8, 9]. Partial melting of the $\alpha\text{-Zr(O)}$ layer was observed for other rods. Sometimes the melt was relocated between oxide layer and solid part of $\alpha\text{-Zr(O)}$ (Fig. 74). The partially molten $\alpha\text{-Zr(O)}$ layer was mostly oversaturated with oxygen, which was the reason for the formation of ceramic precipitates during cooling (Fig. 75).

Bundle cross-section at elevation 1000 mm. This bundle elevation reveals similar oxidation degree and local melt relocations as elevation 950 mm (macrographs in Figs. 76 – 78). Significant parts of the cladding mainly consist of oxide. The typical structure of such oxide was observed for rod #9 (Fig. 79, top). The outer part ($\sim 140 \mu\text{m}$) of this oxide was formed during the pre-oxidation test period at temperatures between 1350 and 1450 K during $\sim 3300 \text{ s}$. This sub-layer has a characteristic fine columnar structure developed due to permanent conversion of monoclinic phase into tetragonal phase in this temperature interval. The middle oxide part was formed during the transient at temperatures between 1450 and 1750 K and has a coarse columnar structure of tetragonal phase. The inner oxide sub-layer was developed at temperatures above 1750 K as mixture of cubic and tetragonal phases and finally (after disappearance of the cladding metallic layer) completely transformed to tetragonal phase. The colder rod #20 has a relative thick $\alpha\text{-Zr(O)}$ layer as sink for oxygen from the upper oxide layer, therefore the inner oxide sub-layer was formed as predominantly cubic phase (Fig. 79, bottom). This unstable cubic oxide modification re-transforms to the tetragonal form under precipitation of $\alpha\text{-Zr(O)}$ phase, decorating the elongated zirconia crystallites.

Fig. 80 illustrates the presence of molten metallic layer localized between outer and inner oxide layers. Due to the absence of metallic precipitates in the ZrO_2 pellet, which would indicate the oxygen transport from the pellet to the cladding, it can be suggested that the inner oxide layer was developed either by interaction with steam which penetrated under the cladding through-going cracks (circumferential ruptures shown in Fig. 45), or by complicated transport mechanism of oxygen through the melt from the melt-ceramic boundary to free non-oxidized surface of melt [8, 9]. Fig. 81 shows three typical cladding layers for rod #17. The ceramic precipitate concentration in the melt is about 40% (area percent on the basis of image analysis). This allows estimation of the oxygen concentration in the prior melt to 14 wt% according to formula (4) in [10]. I. e. some ceramic precipitates were formed in the melt already at temperature (according to Zr-O phase diagram). At other cladding positions the concentration of ceramic precipitations is even higher with complete conversion of melt into oxide (Fig. 80, top).

Bundle cross-section at elevation 1050 mm. The ZrO₂-coated molybdenum electrodes are applied at this and higher elevations instead of the ZrO₂ pellets and tungsten heaters. The outer oxide layer with different thickness was formed at different claddings (Figs. 82 - 85). The oxidation degree of claddings decreases from bundle center to bundle periphery (Fig. 86). However, the temperatures at this elevation were high enough to melt the α -Zr(O) layer for most of the rod simulators. A relatively thick oxide layer was locally formed on claddings of the central rod group. No interaction between metallic melt and the ZrO₂ coating of the Mo electrodes was observed. No molten metal layer was developed for the peripheral rod group at angle positions between 270° and 90° (Fig. 87, right). Fig. 87 illustrates also the circumferential temperature gradient for each cladding: the same rod has different layer thicknesses at different angle positions. Nevertheless the temperatures have reached values over 1750 K, which is indicated by cubic oxide sub-layer for the coldest position (angle 0°; adjacent to shroud) of the outer rod #19. Fig. 88 shows the cladding structure of the inner rod #3 at high magnification. The content of ceramic precipitations in the frozen metal is low; it indicates low oxygen concentration in the prior melt. The melt was oxidized only at its free surface adjacent to the gap. Voids, observed in the oxide, were formed in the melt before its conversion to oxide.

Bundle cross-section at elevation 1150 mm. No through going cracks in the cladding can be observed at macrographs of individual rod simulators (Figs. 89 – 92). Fig. 93 shows a typical three-layer structure of oxidized cladding (ZrO₂, α -Zr(O), prior β -Zr). Two sub-layers can be distinguished for the oxide layer: outer porous sub-layer formed at temperatures between 1250 and 1450 K and internal dense sub-layer formed at temperatures above 1450 K. The outer sub-layer has a characteristic fine columnar structure developed due to permanent conversion of monoclinic phase into tetragonal phase in this temperature interval. Moreover micro cracks were developed in this sub-layer due to tension strength developed here during the growth of the internal oxide part, which was formed during the transient and has a coarse columnar structure of tetragonal phase.

Bundle cross-section at elevation 1250 mm. No peculiarities can be observed for claddings of central and peripheral rod groups on macrographs (Fig. 94) - the oxidation degree seems to be not significant. Indeed, corresponding micrographs (Fig. 95) reveal relatively thin oxide and α -Zr(O) layers. The boundary between oxide layer, developed at temperatures between 1200 and 1300 K, and α -Zr(O) layer has a waved form due to oxide phase transition at these transition temperatures.

5.1 Layer thicknesses

The evolution of the oxide layer growth during the test was determined by eddy-current measurements performed on the six Zircaloy-4 corner rods successively withdrawn from the bundle. The later metallography measurements delivered more precise results and corresponding values are: 145 μ m at the end of the pre-oxidation phase, 380 μ m at 30 s before reflow and about 380-560 μ m after the test. The posttest values of the two E110 corner rods were larger as stated above and in agreement with observed breakaway effect (chapter 4). The eddy-current measurements (Fig. 96) show for the E110 rods some overestimation of oxide layer thicknesses, which real values were determined by metallography (Fig. 97). Nevertheless, for the Zircaloy-4 corner rods with a dense oxide layer there is a good correspondence between both measurement methods. ZIRLO™ material

was not available for corner rods so that the layer thickness measured at the Zircaloy-4 corner rods B and F taken off the bundle during the experiment must be used qualitatively as QUENCH-15 test bundle data at the specific test times.

Measurements of layer thicknesses of outer oxide scales of the cladding are made at four points of each simulator rod with an azimuth interval of 90° and at each elevation according Tables 13 and 14. Results of these measurements, as well as measurement results for oxide thicknesses for shroud and corner rods, are summarized in [Table 15](#) and [Table 16](#). [Fig. 98](#) to [Fig. 106](#) illustrate the results of the oxide scale measurements for the respective bundle elevations. All these figures indicate scatter in the data due to radial temperature gradient from the center of bundle to its periphery. A comparison of axial oxide distribution for bundle tests QUENCH-06, -12, -14 and -15 ([Figs. 107, 108](#)) shows similar profiles for all four tests with a shift of the maximum oxidation for the QUENCH-15 bundle from elevation 950 mm to elevation 1000 mm. Similar maximum shifting was observed also for the Zircaloy-4 corner rods A, C and D ([Fig. 96](#)). These observations indicate some axial shifting of the temperature maximum to higher bundle elevations. The reason for this shifting can be connected with the different geometry of the QUENCH-15 bundle.

6 Axial distribution of absorbed hydrogen

The axial hydrogen distribution in six corner rods and in one cladding tube (No. 24) was determined by means of neutron radiography [7]. The neutron radiography was performed at the ICON facility at the Swiss neutron source SINQ (Paul Scherrer Institut Villigen) with a camera length L/d of 350. L is the aperture to sample distance and d the aperture opening size. The neutron radiographs were recorded by a camera system, specially developed for neutron micro-tomography applications. It consists of an ultra-thin Gadox scintillator (thickness 10 µm), a lens without any optical distortions (diameter: 155 mm, height: 620 mm mass: 30 kg) and the high resolution 1:1 magnification CCD camera ANDOR DV436 (Peltier cooled, pixel size 13.5 µm, field of view: 28 mm x 28 mm, 2048 x 2048 pixels, 16 bit). Due to the fact that the camera system has an active window with a size of 28 mm x 28 mm the rods were scanned with a step size of 20 mm.

The data were analyzed with the “ImageJ” software package. The measurements were normalized with an open beam frame and corrected for dark current. With an axial step size of 20 mm the intensity distribution of the position perpendicular to the rod axis was determined by integration over an axial width of 1 mm. In the region attenuated by the rods the intensity distribution can be described by the Eqs. (3) and (4). The transmission T of the neutron beam behind the specimen is given by:

$$T = \frac{I - I_B}{I_0 - I_B} = \exp(-\Sigma_{total} \cdot s) \quad (3)$$

where I is the intensity behind the specimen, I_0 the primary beam intensity, I_B the background intensity measured behind a Cd specimen with comparable dimension, Σ_{total} the macroscopic total neutron cross section of the material and s the path length through the specimen. As hydrogen is added to the Zircaloy-4, Σ_{total} can be given as:

$$N_H \sigma_{total,H} + \Sigma_{total,Zry-4} \quad (4)$$

where $\Sigma_{total,Zry-4}$ is the total macroscopic neutron cross section of the dehydrated Zircaloy-4 specimen, N_H is the hydrogen atom number density and $\sigma_{total,H}$ the total microscopic cross section of hydrogen. For an illumination in radial direction the path length s through a rod shaped specimen is given by the complex equation:

$$s = \Re\left(\sqrt{d^2 - (x - x_0)^2}\right) \quad (5)$$

$$s = \Re\left(\sqrt{r_o^2 - (x - x_0)^2} - \sqrt{r_i^2 - (x - x_0)^2}\right) \quad (6)$$

where \Re is the real part of the complex term, x the actual radial position, x_0 the radial middle position of the specimen, d the rod diameter, r_o and r_i the outer and inner radius, respectively. Due to the fact that the intensity fit at the sample edges is very sensitive for the sample alignment, only the middle positions were used for the analysis where $s \approx d = 6 \text{ mm}$ for the corner rods and $s \approx d_o - d_i = 1.5 \text{ mm}$ for the cladding tube.

Since the total cross section of hydrogen-free Zr-Nb-Sn alloy is very close to the cross section of hydrogen-free Zircaloy-4 (Zr-Sn), the hydrogen atomic concentration in at.% is given according to [7] by:

$$c_H^m = \frac{\frac{\Sigma_{total} - 0.21 \text{ cm}^{-1}}{2.90 \text{ cm}^{-1}}}{\frac{\Sigma_{total} - 0.21 \text{ cm}^{-1}}{2.90 \text{ cm}^{-1}} + 1} \quad (7)$$

The results for one Zircaloy-4 and two E110 corner rods withdrawn after the test as well as for one ZIRLO™ cladding tube withdrawn after quenching are compared in [Fig. 111](#). The data have qualitative nature, because they have to be corrected for the influence of the oxide layer on the total neutron cross section. The hydrogen concentrations determined for the two E110 corner rods are about one order of magnitude higher than the concentrations found in the Zircaloy-4 and ZIRLO™ specimens. They are in agreement with those obtained in the post-test examinations of the QUENCH-14 bundle. The hydrogen axial distributions for both E110 corner rods are comparable. No significant hydrogen uptake or release takes place during quenching. The distributions show two maxima in the hydrogen concentration. From former QUENCH tests it is known that such maxima are related to locations where a breakaway oxide has been formed. It can be expected that this is also the reason for the distributions determined for the QUENCH-15 corner rods. Maximal values of about 30 at% hydrogen for E110 were found at the elevation of around 1140 mm. The rapid decrease in the hydrogen concentration of rod C at elevations lower 780 mm is caused by a change in the rod geometry. At these bundle elevations the corner rod is made of a tube, whereas at axial positions above 780 mm rod C is a solid one. Rod H is a solid rod over the whole length. Obviously, the hydrogen release is much more effective in the tube region of the specimen than in the solid rod region.

The Zircaloy-4 and ZIRLO™ specimens as well as M5® cladding (withdrawn from the QUENCH-14 bundle) show similar axial distributions with measured maximal values of about

5 at.% for Zircaloy-4, 4 at.% for ZIRLO™ and about 3.5 at.% for M5® close to the hottest regions in the bundle. Unfortunately, no samples from the hottest region of QUENCH-15 could be prepared. Therefore, no certain information on the global maximal hydrogen concentration in these materials is available. It could be that the hydrogen concentrations in the axial regions which are lost are larger than the maximal measured values.

7 Conclusions

The QUENCH-15 experiment investigated the effect of tin-niobium-bearing ZIRLO™ cladding material on bundle oxidation and core reflood, in comparison with tests QUENCH-06 (Zircaloy-4), QUENCH-12 (E110) and QUENCH-14 (M5®). All four tests were conducted with similar electrical power histories.

The post-test examinations of the bundle showed neither noticeable breakaway cladding oxidation nor melt release into space between rods.

The part of the cladding converted to oxide at the hottest elevation of 950 - 1000 mm is 75% (QUENCH-06: 60%, QUENCH-12: 85%, QUENCH-14: 75%).

Post-test investigations of the QUENCH-15 bundle reveal (similar to QUENCH-06 and -14) significant cladding inner oxide layers with thickness up to 20% of outer oxide layers. Two mechanisms could be responsible for development of this layer: 1) oxidation by steam penetrating through cladding cracks; 2) oxygen transport from the outer oxide layer through the molten metal layer.

The measured hydrogen production during the QUENCH-15 test was 41 g in the pre-oxidation and transient phases and 7 g in the quench phase being similar to those in QUENCH-06 (32 g / 4 g) and QUENCH-14 (34 g / 6 g). The main reasons for a higher hydrogen production for QUENCH-15 were the increased bundle surface being in contact with steam and the presence of two non-prototypical corner rods.

Generally, it can be concluded that the type of cladding alloy has only a limited influence on the development of a severe accident and its termination by reflood.

Acknowledgements

The ZIRLO™ cladding and Zircaloy-4 spacer material was provided by Westinghouse Electric Sweden.

The determination of the test protocol was based on numerous calculations with SCDAP/RELAP5 and SCDAP-SIM performed by Dr. J. Birchley, Paul Scherrer Institute (PSI), Switzerland.

The broad support needed for preparation, execution, and evaluation of the QUENCH-15 experiment is gratefully acknowledged. In particular, the authors would like to thank Mr. J. Moch, assisted by Mrs. U. Peters, for the assembly including instrumentation as well as disassembly, encapsulation and sectioning of the test bundle, Mr. S. Horn (FZK/IK) for the

preparation and measurement of hydrogen with the “Caldos” analyzer and the various support, Mrs.J. Laier for processing the test data, Mrs. M. Heck for her detailed draft review.

The neutron radiography investigations were performed at the ICON facility at SINQ (PSI, Switzerland). The authors thank Mr. A. Kaestner for his support in these investigations.

References

1. L. Sepold, W. Hering, C. Homann, A. Miassoedov, G. Schanz, U. Stegmaier, M. Steinbrück, H. Steiner, J. Stuckert, "Experimental and Computational Results of the QUENCH-06 Test (OECD ISP-45)," FZKA-6664, Forschungszentrum Karlsruhe, February 2004.
2. W. Hering, C. Homann, J.S. Lamy, A. Miassoedov, G. Schanz, L. Sepold, M. Steinbrück, "Comparison and Interpretation Report of the OECD International Standard Problem No. 45 Exercise (QUENCH-06)," FZKA-6722, Forschungszentrum Karlsruhe, July 2002.
3. J. Stuckert, A. Goryachev, M. Große, M. Heck, I. Ivanova, G. Schanz, L. Sepold, U. Stegmaier, M. Steinbrück, "Results of the QUENCH-12 Test on Reflood of a VVER-type Bundle," FZKA-7307, Forschungszentrum Karlsruhe, September 2008.
4. J. Stuckert, M. Große, U. Stegmaier, M. Steinbrück, "Results of Severe Fuel Damage Experiment QUENCH-14 with Advanced Rod Cladding M5[®]," KIT Scientific Reports, KIT-SR 7549, Karlsruhe Institute of Technology, June 2010.
5. M. Steinbrück, "Oxidation of Zirconium Alloys in Oxygen at High Temperatures up to 1600 °C," Oxidation of Metals 70 (2008), 317-329.
6. M. Grosse, "Comparison of the high temperature steam oxidation kinetics of advanced cladding materials," Nuclear Technology, Vol. 170, Issue 1, April 2010, pp. 272-279.
7. M. Grosse, E. Lehmann, P. Vontobel, M. Steinbrueck, "Quantitative determination of absorbed hydrogen in oxidised Zircaloy by means of neutron radiography," Nucl. Instr. & Methods in Phys. Res. A 566 (2006), 739.
8. M. S. Veshchunov, J. Stuckert, A. V. Berdyshev. „Modelling of Zr-O and U-Zr-O melts oxidation and new crucible tests", FZKA-6792, Forschungszentrum Karlsruhe, December 2002.
9. M.S. Veshchunov, "Modelling of U-Zr-O Corium/ Vessel Steel Interactions. ISTC Project #3876 THOMAS," 15th International QUENCH Workshop, Karlsruhe Institute of Technology, 2009. Proceedings on CD.
10. P. Hofmann, J. Stuckert, A. Miassoedov, M.S. Veshchunov, A.V. Berdyshev, A.V. Boldyrev, "ZrO₂ dissolution by molten zircaloy and cladding oxide shell failure. New experimental results and modelling," FZKA-6383, Forschungszentrum Karlsruhe, December 1999.

Table 1: QUENCH Test Matrix

Test	Quench medium and injection rate	Temp. at onset of flooding ¹⁾	Max. ZrO ₂ before transient ²⁾	Max. ZrO ₂ (X s) before flooding ²⁾	Posttest average ZrO ₂ thickness ³⁾	H ₂ production before / during cooldown	Remarks, objectives
QUENCH-00 Oct. 9 - 16, 97	Water 80 g/s	≈ 1800 K			completely oxidized		Commissioning tests.
QUENCH-01 Febr 26, 98	Water 52 g/s	≈ 1830 K	312 μm		500 μm at 913 mm	36 / 3	COBE Project; partial fragmentation of pre-oxidized cladding.
QUENCH-02 July 7, 98	Water 47 g/s	≈ 2400 K			completely oxidized	20 / 140	COBE Project; no additional pre-oxidation; quenching from high temperatures.
QUENCH-03 January 20, 99	Water 40 g/s	≈ 2350 K			completely oxidized	18 / 120	No additional pre-oxidation, quenching from high temperatures.
QUENCH-04 June 30, 99	Steam 50 g/s	≈ 2160 K	82 μm		280 μm	10 / 2	Cool-down behavior of slightly pre-oxidized cladding by cold steam injection.
QUENCH-05 March 29, 2000	Steam 48 g/s	≈ 2020 K	160 μm		420 μm	25 / 2	Cool-down behavior of pre-oxidized cladding by cold steam injection.
QUENCH-06 Dec 13 2000	Water 42 g/s	≈ 2060 K	207 μm ⁵⁾	300 μm, (60 s), SVECHA modeling	630 μm ⁴⁾	32 / 4	OECD-ISP 45; prediction of H ₂ source term by different code systems.
QUENCH-07 July 25, 2001	Steam 15 g/s	≈ 2100 K	230 μm		completely oxidized	66 / 120	COLOSS Project; impact of B ₄ C absorber rod failure on H ₂ , CO, CO ₂ , and CH ₄ generation.

Test	Quench medium and injection rate	Temp. at onset of flooding ¹⁾	Max. ZrO ₂ before transient ²⁾	Max. ZrO ₂ (X s) before flooding ²⁾	Posttest average ZrO ₂ thickness ³⁾	H ₂ production before / during cooldown	Remarks, objectives
QUENCH-09 July 3, 2002	Steam 49 g/s	≈ 2100 K			completely oxidized	60 / 400	As QUENCH-07, steam-starved conditions prior to cooldown.
QUENCH-08 July 24, 2003	Steam 15 g/s	≈ 2090 K	274 μm		completely oxidized	46 / 38	As QUENCH-07, no absorber rod
QUENCH-10 July 21, 2004	Water 50 g/s	≈ 2200 K	514 μm	613 μm (at 850 mm)	completely oxidized	48 / 5	LACOMERA Project; Air ingress.
QUENCH-11 Dec 08, 2005	Water 18 g/s	≈ 2040 K		170 μm	completely oxidized	9 / 132	LACOMERA Project; Boil-off.
QUENCH-12 Sept 27, 2006	Water 48 g/s	≈ 2100 K	160 μm, breakaway	300 μm, (110 s), breakaway	completely oxidized	34 / 24	ISTC Project #1648.2; VVER bundle with E110 claddings
QUENCH-13 Nov 7, 2007	Water 52 g/s	≈ 1820 K		400 μm, after AgInCd rod failure	750 μm	42 / 1	SARNET; impact of AgInCd absorber rod failure on aerosol generation.
QUENCH-14 July 2, 2008	Water 41 g/s	≈ 2100 K	170 μm ⁶⁾	470 μm ⁶⁾ , (30 s)	900 μm	34 / 6	ACM series: M5 [®] cladding
QUENCH-15 May 27, 2009	Water 48 g/s	≈ 2100 K	145 μm ⁶⁾	380 μm ⁶⁾ , (30 s)	620 μm	41 / 7	ACM series: ZIRLO [™] cladding

¹⁾ Maximum measured bundle temperature at 950 mm elevation.

²⁾ Measured at the withdrawn corner rod at 950 mm elevation.

³⁾ Measured posttest at the bundle elevation of maximum temperature, i.e. 950 mm.

⁴⁾ Some claddings were completely oxidized at 950 mm elevation.

⁵⁾ Oxide thickness during transient phase.

⁶⁾ Zircaloy-4 corner rods (no M5[®] and ZIRLO[®] values available).

Table 2: Design characteristics of the QUENCH-15 test bundle

Bundle type		PWR
Bundle size (heated rods)		24 rods
Pitch		12.6 mm
Coolant channel area		34.57 cm ²
Hydraulic diameter		12.27 mm
Rod outside / inside diameter		9.5 ± 0.038 mm / 8.357± 0.038mm
Cladding material		Zirlo (Zr-1Sn-1Nb-0.1Fe-0.125O) *
Cladding length (levels)		2280 mm (-595 to 1685 mm)
Cladding thickness		0.572 mm
Heated rod length (levels)		2480 mm (-690 to 1790 mm)
Heater material		Tungsten (W)
Heater length		1024 mm
Heater diameter		5 mm
Annular pellet	material dimensions	ZrO ₂ ;Y ₂ O ₃ -stabilized ∅ 8.2/5.2 mm; L=11 mm
Pellet stack		0 mm to ~ 1020 mm
Internal rod pressure (gas)		0.22 MPa abs. (Kr)
Corner rod (8)	material instrumented (A, C, E, G) not instrumented (B, D, F, H)	Zircaloy-4 (A-D, F, G), E110 (E, H) tube ∅ 6x0.9 (bottom: -1140 mm) rod ∅ 6 mm (top: +1300 mm) rod ∅ 6 mm (-1350 to +1155 mm)
Grid spacer	material length location of lower edge	Zircaloy-4 48.7 -200; 50; 550; 1050, 1410 mm
Shroud	material wall thickness outside diameter length (extension)	Zirconium 702 (flange: Zry-4) 3.05 mm 88.9 mm 1600 mm (-300 mm to 1300 mm)
Shroud insulation	material insulation thickness elevation	ZrO ₂ fiber ~ 34 mm -300 mm to ~1000 mm
Molybdenum-copper electrodes	length of upper electrodes length of lower electrodes diameter of electrodes: - prior to coating - after coating with ZrO ₂	766 mm (576 Mo, 190 mm Cu) 690 mm (300 Mo, 390 mm Cu) 7.6 mm 8.0 mm
Cooling jacket	Material: inner/outer tube inner tube outer tube	Inconel 600 (2.4816) / SS (1.4571) ∅ 158.3 / 168.3 mm ∅ 181.7 / 193.7 mm

*) provided by Westinghouse Electric Sweden AB

11/2009

Table 3: QUENCH-15; Electrical resistances of rods [mΩ] at 20 °C

rod	1	2	3	4	5	6	7	8	9	10	11	12	13
pre-test	4.4	4.4	4.4	4.4	4.4	4.3	4.3	4.4	4.4	4.4	4.3	4.4	4.4
post-test	4.4	4.4	4.4	4.7	4.4	4.4	4.5	4.4	4.4	4.5	4.4	4.5	4.4

Note: 1, ... – connected to DC1 generator; 2,... – connected to DC2 generator

rod	14	15	16	17	18	19	20	21	22	23	24	ave- rage	24 rods parallel
pre-test	4.4	4.4	4.3	4.4	4.4	4.3	4.3	4.4	4.3	4.4	4.4	4.37	0.182
post-test	4.4	4.6	4.5	4.4	4.4	4.4	4.5	4.6	4.4	4.4	4.5	4.45	0.185

Note: Measurement device was connected between copper electrodes of each rod. Measured values include the resistance of slide contacts $R_s=0.4$ mΩ.

Each circuit (from two) connected to own DC generator with 4 parallel bonded cables. Resistance of each cable is $R_c=1.2$ mΩ. Therefore, the external (outside) resistance corresponding to each heated rod (indicated by SCDAP/RELAP as **fxwid**) is $R_e=R_s+12*R_c/4=4$ mΩ.

Table 4: Main characteristics of the ZrO₂ pellet material, yttria-stabilized (type ZYK3)

Property	Data
Y ₂ O ₃ content	5 %
Density	6.07 ± 0.03 g/cm ³
Open porosity	0
Average crystallite size	0.8 μm
Specific heat at 20 °C	400 J/kg K
Thermal conductivity at 100 °C	2.5 W/m K
Linear expansion, 20-1000 °C	11 x 10 ⁻⁶ /K
Vickers Hardness HV10	> 12000 N/mm ²
Bending strength	> 1150 MPa
Elastic modulus	> 200 GPa
Weibull modulus	20
Fracture toughness K _{1C}	12 MPa•m ^{1/2}

According to Barat Ceramics GmbH, 07955 Auma

Table 5: Properties of zirconia fiber insulating boards of type ZYFB3

Chemical composition

Oxide	ZrO ₂	Y ₂ O ₃	HfO ₂	TiO ₂	SiO ₂	CaO	MgO	Fe ₂ O ₃	Al ₂ O ₃	Na ₂ O
typical wt%	88	10	2	0.14	0.12	0.09	0.03	0.04	0.01	0.01

Physical properties

bulk density	porosity	shrinkage		thermal expansion coefficient @298-1453K	melting point	max service temperature	flexural strength	compressive strength @10% compression
		(1 hour @1925 K)	(24 hours @1925 K)					
g/cm ³	%	%		1/K	K	K	MPa	MPa
0.48	92	1.2	2.8	10.7*10 ⁻⁶	2866	2500	0.59	0.29

Thermal conductivity

temperature, K	673	1073	1373	1673	1923
conductivity, W/(m*K)	0.08	0.11	0.14	0.19	0.24

Specific heat capacity

temperature, K	366	2644
specific heat capacity, J/(kg*K)	544	754

According to specifications of manufacturer ZIRCAR PRODUCTS

Table 6: Diameters of the materials used for the QUENCH High-Temperature Thermocouples [mm]

Material	As-received	Final
W/Re wires	0.254	
HfO ₂ insulation OD (see drawing below)	1.1	
Ta tube OD / ID	2.15 / 1.65	1.4 / 0.94
Zr tube OD / ID	2.5 / 1.65 ± 0.05	2.2-2.3 / ~1.4

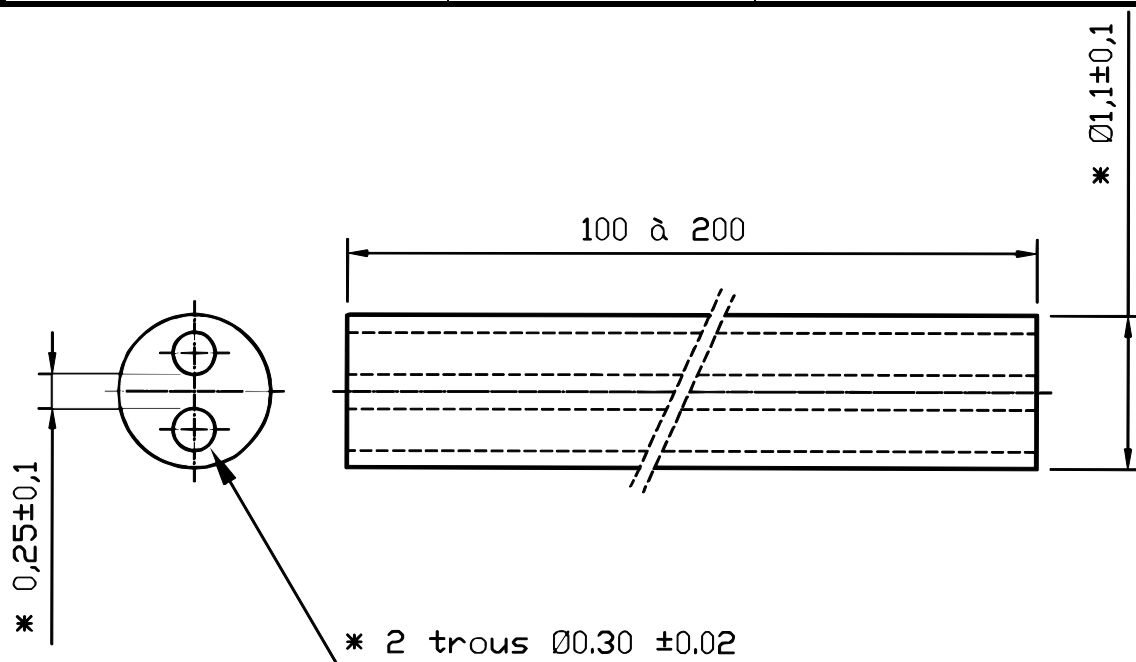


Table 7: Main characteristics of the HfO₂ thermocouple insulator

Property	Data
Composition of basic material	99 % HfO ₂
Melting temperature	2840 °C
Max. use temperature	2500 °C
Density	8.4 g/cm ³
Thermal conductivity at 20-1000 °C	1.14 W/m K
Linear expansion	5.8 x 10 ⁻⁶ /K

According to Saint-Gobain ceramics, 1997

Table 8: List of instrumentation for the QUENCH-15 test

Chan	Designation	Instrument, location	Unit
0	TFS 3/17	TC (W/Re), surface of fuel rod simulator 3, group 1, 1350 mm	K
1	TFS 6/17	TC (W/Re), surface of fuel rod simulator 6, group 2, 1350 mm	K
2	TFS 8/16	TC (W/Re), surface of fuel rod simulator 8, group 2, 1250 mm	K
3	TFS 13/16	TC (W/Re), surface of fuel rod simulator 13, group 3, 1250 mm	K
4	TFS 12/15	TC (W/Re), surface of fuel rod simulator 12, group 2, 1150 mm	K
5	TSH 16/180	TC (W/Re), shroud outer surface, 1250 mm, 291°, behind shroud insulation	K
6	TFS 22/12	TC (W/Re), surface of fuel rod simulator 22, group 4, 850 mm	K
7	TFS 19/14	TC (W/Re), surface of fuel rod simulator 19, group 4, 1050 mm	K
8	TFS 14/14	TC (W/Re), surface of fuel rod simulator 14, group 2, 1050 mm	K
9	TFS 5/14	TC (W/Re), surface of fuel rod simulator 5, group 2, 1050 mm	K
10	TFS 2/14	TC (W/Re), surface of fuel rod simulator 2, group 1, 1050 mm	K
11	TFS 21/13	TC (W/Re), surface of fuel rod simulator 21, group 4, 950 mm	K
12	TIT A/13	TC (W/Re), center line of corner rod A, 950 mm	K
13	TFS 17/13	TC (W/Re), surface of fuel rod simulator 17, group 4, 950 mm	K
14	TFS 15/13	TC (W/Re), surface of fuel rod simulator 15, group 2, 950 mm	K
15	TFS 9/13	TC (W/Re), surface of fuel rod simulator 9, group 2, 950 mm	K
16	TFS 9/15	TC (W/Re), surface of fuel rod simulator 9, group 2, 1150 mm	K
17	TSH 15/0	TC (W/Re), shroud outer surface, 1150 mm, 21°	K
18	TSH 15/180	TC (W/Re), shroud outer surface, 1150 mm, 201°	K
19	TSH 16/0	TC (W/Re), shroud outer surface, 1250 mm, 21°, behind shroud insulation	
20	TSH 14/270	TC (W/Re), shroud outer surface, 1050 mm, 289°, behind shroud insulation	K
21	TSH 14/90	TC (W/Re), shroud outer surface, 1050 mm, 11°, behind shroud insulation	K
22	TFS 22/9	TC (NiCr/Ni), surface of fuel rod simulator 22, group 4, 550 mm	K
23	TFS 17/9	TC (NiCr/Ni), surface of fuel rod simulator 17, group 4, 550 mm	K
24	F 902	Reserve	
25	Fm 401	Argon gas mass flow rate, (20 mA)	g/s
26..32		TC (W/Re), Reserve	K
32	TIT C/12	TC (W/Re), center line of corner rod C, 850 mm	

Chan	Designation	Instrument, location	Unit
33	TFS 3/10	TC (W/Re), surface of fuel rod simulator 3, group 1, 650 mm	K
34		Reserve	K
35	TSH 4/270	TC (NiCr/Ni), shroud outer surface, 50 mm, 291°	K
36	TSH 5/0	TC (NiCr/Ni), shroud outer surface, 150 mm, 21°	K
37	TFS 4/15	TC (W/Re), surface of fuel rod simulator 4, group 1, 1150 mm	K
38	TFS 14/9	TC (NiCr/Ni), surface of fuel rod simulator 14, group 2, 550 mm	K
39	TFS 8/9	TC (NiCr/Ni), surface of fuel rod simulator 8, group 2, 550 mm	K
40	TIT E/11	TC (W/Re), centerline of central rod, 750 mm	
41	TFS 6/10	TC (W/Re), surface of fuel rod simulator 6, group 2, 650 mm	K
42	TFS 4/9	TC (NiCr/Ni), surface of fuel rod simulator 4, group 1, 550 mm	K
43	TFS 2/9	TC (NiCr/Ni), surface of fuel rod simulator 2, group 1, 550 mm	K
44	TFS 9/8	TC (NiCr/Ni), surface of fuel rod simulator 9, group 2, 450 mm	K
45	TFS 6/8	TC (NiCr/Ni), surface of fuel rod simulator 6, group 2, 450 mm	K
46	TFS 3/8	TC (NiCr/Ni), surface of fuel rod simulator 3, group 1, 450 mm	K
47	TFS 3/13	TC (W/Re), surface of fuel rod simulator 3, group 1, 950 mm	K
48	TFS 1/13	TC (W/Re), centerline of central rod, 950 mm	K
49	TSH 11/180	TC (W/Re), shroud outer surface, 750 mm, behind shroud insulation	K
50		Reserve	
51	TIT G/13	TC (W/Re), center line of corner rod G, 950 mm	K
52	TSH 10/270	TC (W/Re), shroud outer surface, 650 mm, 289°	K
53	TSH 12/180	TC (W/Re), shroud outer surface, 850 mm, behind shroud insulation	K
54	TSH 11/0	TC (W/Re), shroud outer surface, 750 mm, 21°, behind shroud insulation	K
55	TSH 13/90	TC (W/Re), shroud outer surface, 950 mm, behind shroud insulation	K
56	TFS 14/11	TC (W/Re) surface of fuel rod simulator 14, group 2, 750 mm	K
57	TFS 1/11	TC (W/Re) surface of fuel rod simulator 1, group 1, 750 mm	K
58	TSH 6/270	TC (NiCr/Ni), shroud outer surface, 250 mm, 281°	K
59	TFS 16/12	TC (W/Re) surface of fuel rod simulator 16, group 3, 850 mm	K
60	TSH 10/90	TC (NiCr/Ni ; W/Re), shroud outer surface, 650 mm, 109°	K
61	T 206	Temperature upstream steam flow instrument location 1 g/s	K

Chan	Designation	Instrument, location	Unit
62	P 206	Reserve	
63	F 206	Reserve	
64	T 402 b	TC (NiCr/Ni), Ar super heater	K
65	TFS 8/12	TC (W/Re), surface of fuel rod simulator 8, group 2, 850 mm	K
66	TSH 13/270	TC (W/Re), shroud outer surface, 950 mm, behind shroud insulation	K
67	TSH 12/0	TC (W/Re) shroud outer surface, 850 mm, 11°, behind shroud insulation	K
68	T 512	TC (NiCr/Ni), gas temperature bundle outlet	K
69		W/Re reserve	K
70	TFS 2/12	TC (W/Re) surface of fuel rod simulator 2, group 1, 850 mm	K
71	Ref. T01	Temperature of measuring crate 1 (reference temperature)	K
72		Reserve (NiCr/Ni)	
73	TFS 1/7	TC (NiCr/Ni), surface of fuel rod simulator 1, group 1, 350 mm	K
74	TFS 11/6	TC (NiCr/Ni), surface of fuel rod simulator 11, group 2, 250 mm	K
75	TFS 4/1	TC (NiCr/Ni), surface of fuel rod simulator 4, fluid, -250 mm	K
76	TFS 17/5	TC (NiCr/Ni), surface of fuel rod simulator 17, group 4, 150 mm	K
77	TFS 2/5	TC (NiCr/Ni), surface of fuel rod simulator 2, group 1, 150 mm	K
78		Reserve (NiCr/Ni)	K
79	TSH 9/0	TC (NiCr/Ni), shroud outer surface, 550 mm, 11°	K
80		Reserve (NiCr/Ni)	K
81	TSH 9/180	TC (NiCr/Ni), shroud outer surface, 550 mm, 191°	K
82	TSH 8/90	TC (NiCr/Ni), shroud outer surface, 450 mm, 109°	K
83	TSH 8/270	TC (NiCr/Ni), shroud outer surface, 450 mm, 289°	K
84	TSH 7/0	TC (NiCr/Ni), shroud outer surface, 350 mm, 11°	K
85	TSH 7/180	TC (NiCr/Ni), shroud outer surface, 350 mm, 191°	K
86	TSH 6/90	TC (NiCr/Ni), shroud outer surface, 250 mm, 109°	K
87	TSH 5/180	TC (NiCr/Ni),	K
88	TSH 4/90	TC (NiCr/Ni), shroud outer surface, 50 mm, 109°	K
89	TSH 3/180	TC (NiCr/Ni), shroud outer surface, -50 mm, 191°	K
90	TSH 1/0	TC (NiCr/Ni), shroud outer surface, -250 mm, 11°	K
91	TCI 9/270	TC (NiCr/Ni), cooling jacket inner tube wall, 550 mm, 270°	K

Chan	Designation	Instrument, location	Unit
92	TCI 10/270	TC (NiCr/Ni), cooling jacket inner tube wall, 650 mm, 270°	K
93	TCI 11/270	TC (NiCr/Ni), cooling jacket inner tube wall, 750 mm, 270°	K
94	TCI 13/270	TC (NiCr/Ni), cooling jacket inner tube wall, 950 mm, 270°	K
95		Reserve (NiCr/Ni)	
96	TCI 1/180	TC (NiCr/Ni), cooling jacket inner tube wall, -250 mm, 180°	K
97	TCI 4/180	TC (NiCr/Ni), cooling jacket inner tube wall, 50 mm, 180°	K
98	TCI 7/180	TC (NiCr/Ni), cooling jacket inner tube wall, 350 mm, 180°	K
99	TCI 11/180	TC (NiCr/Ni), cooling jacket inner tube wall, 750 mm, 180°	K
100	TCI 12/180	TC (NiCr/Ni), cooling jacket inner tube wall, 850 mm, 180°	K
101	TCI 13/180	TC (NiCr/Ni), cooling jacket inner tube wall, 950 mm, 180°	K
102	TCI 15/180	TC (NiCr/Ni), cooling jacket inner tube wall, 1150 mm, 180°	K
103	T 002	TC (NiCr/Ni), cooling water, inlet of off-gas tube	K
104	TCI 9/90	TC (NiCr/Ni), cooling jacket inner tube wall, 550 mm, 90°	K
105	TCI 10/90	TC (NiCr/Ni), cooling jacket inner tube wall, 650 mm, 90°	K
106	TCI 11/90	TC (NiCr/Ni), cooling jacket inner tube wall, 750 mm, 90°	K
107	TCI 13/90	TC (NiCr/Ni), cooling jacket inner tube wall, 950 mm, 90°	K
108	TFS 8/4	TC (NiCr/Ni), surface of fuel rod simulator 8, group 2, 50 mm	K
109	TCI 1/0	TC (NiCr/Ni), cooling jacket inner tube wall, -250 mm, 0°	K
110	TCI 4/0	TC (NiCr/Ni), cooling jacket inner tube wall, 50 mm, 0°	K
111	TCI 7/0	TC (NiCr/Ni), cooling jacket inner tube wall, 350 mm, 0°	K
112	TCI 11/0	TC (NiCr/Ni), cooling jacket inner tube wall, 750 mm, 0°	K
113	TCI 12/0	TC (NiCr/Ni), cooling jacket inner tube wall, 850 mm, 0°	K
114	TCI 13/0	TC (NiCr/Ni), cooling jacket inner tube wall, 950 mm, 0°	K
115	TCI 15/0	TC (NiCr/Ni), cooling jacket inner tube wall, 1150 mm, 0°	K
116	T 003	TC (NiCr/Ni), cooling water, outlet of off-gas tube	K
117	T 309	TC (NiCr/Ni), Ar bundle top	K
118		Reserve (NiCr/Ni)	
119	TFS 3/3	TC (NiCr/Ni), surface of fuel rod simulator 3, group 1, -50 mm	K
120	TCO 1/0	TC (NiCr/Ni), cooling jacket outer tube surface, -250 mm, 0°	K
121	TCO 7/0	TC (NiCr/Ni), cooling jacket outer tube surface, 350 mm, 0°	K
122	TCO 13/0	TC (NiCr/Ni), cooling jacket outer tube surface, 950 mm, 0°	K

Chan	Designation	Instrument, location	Unit
123	T 601	Temperature off-gas, 2660 mm from test section outlet (flange)	K
124	T 513	Temperature bundle head top (wall)	K
125	T 514	Temperature bundle head, cooling water inlet	K
126	T 307	TC (NiCr/Ni), inner surface of inlet of off-gas pipe	K
127	TSH 2/90	TC (NiCr/Ni), shroud outer surface, -150 mm, 111°	K
128	T 104	Temperature quench water	K
129	T 201	Temperature steam generator heating pipe	K
130		Reserve	K
131	T 205	Temperature upstream steam flow instrument location 10 g/s	K
132	T 301A	Temperature downstream superheater	K
133	T 302	Temperature superheater heating pipe	K
134	T 303	Temperature upstream total flow instrument location	K
135	T 401	Temperature upstream Ar flow instrument (orifice) location	K
136	T 403	Temperature of Ar at inlet cooling jacket	K
137	T 404	Temperature of Ar at outlet cooling jacket	K
138	T 501	Temperature in containment (near from bundle head)	K
139	T 502	Temperature at outer surface of containment, 0°, 2.4 m	K
140	T 503	Temperature at outer surface of containment, 270°, 2.2 m	K
141	T 504	Temperature at outer surface of containment, 270°, 3.2 m	K
142	T 505	Temperature at outer surface of containment, 90°, 3.2 m	K
143	T 506	Temperature at outer surface of containment, 270°, 3.6 m	K
144	T 507	Temperature at outer surface of containment, 90°, 3.6 m	K
145	T 508	Temperature at outer surface of containment, 180°, 4.0 m	K
146	T 310	TC (NiCr/Ni), aerosol extraction tube in off-gas pipe	K
147	T 510	Temperature at outer surface of containment, 270°, 4.4 m	K
148	T 511	Gas temperature at bundle inlet	K
149	T 901	Temperature upstream off-gas flow instrument F 901	K
150	T 304	Temperature of pipe surface at valve V 302	K
151	<i>Ref. T02</i>	<i>Temperature of measuring crate 2 (reference temperature)</i>	K
152	P 201	Pressure steam generator	bar
153	P 204	Reserve	

Chan	Designation	Instrument, location	Unit
154	P 205	Pressure at steam flow instrument location 10 g/s	bar
155	P 303	Pressure upstream total flow instrument (orifice) location	bar
156	P 401	Pressure upstream gas flow instrument location	bar
157	P 511	Pressure at bundle inlet	bar
158	P 512	Pressure at bundle outlet	bar
159	P 601	Pressure upstream off-gas flow instrument (orifice) F 601	bar
160		Reserve	
161	L 201	Liquid level steam generator	mm
162	L 501	Liquid level quench water	mm
163	L 701	Liquid level condensation vessel	mm
164	Q 901	H ₂ concentration, off-gas (Caldos)	%H ₂
165	P 411	Pressure Kr supply for heated rods	bar
166	P 403	Pressure Ar cooling of cooling jacket	bar
167	P 406	Pressure insulation shroud/cooling jacket	bar
168	Fm 104	Flow rate quench water	g/s
169	F 204	Reserve	
170	Fm 205	Flow rate steam 10 g/s	g/s
171	F 303	Flow rate at bundle inlet (steam + argon), orifice	mbar
172	F 401	Reserve	
173	Fm 403	Flow rate cooling gas	g/s
174	F 601	Flow rate off-gas (orifice), 2000 mm from test section outlet (flange)	mbar
175	Fm 406	Flow rate argon into room between shroud and cooling jacket	g/s
176	E 201	Electric current steam generator	A
177	E 301	Electric current superheater	A
178	E 501	Electric current of left group of fuel rod simulators	A
179	E 502	Electric current of right group of fuel rod simulators	A
180	E 503	Electric voltage of left group of fuel rod simulators	V
181	E 504	Electric voltage of right group of fuel rod simulators	V
182	Hub_V302	Gas supply valve lift	%
183	<i>Ref. T03</i>	<i>Temperature of buffer amplifier (reference temperature)</i>	K

Chan	Designation	Instrument, location	Unit
184..... 199		Binary inputs	
200..... 215		Analog outputs	
250	E 505	Electric power inner ring of fuel rod simulators	W
251	E 506	Electric power outer ring of fuel rod simulators	W
252	EP	Gross electrical power	kW

Indications:


TFS – high-temperature TC at the rod surface,

TFS - low-temperature TC at the rod surface;

TCR – low-temperature TC at the rod surface;

TSH - high-temperature TC at outer surface of shroud;

TSH - low-temperature TC at outer surface of shroud;

 - gauge outside of containment.

Groups of the rods:

group 1: rods 1, 2, 3, 4;

group 2: rods 5, 6, 8, 9, 11, 12, 14, 15;

group 3: rods 7, 10, 13, 16;

group 4: rods 17, 18, 19, 20, 21, 22, 23, 24.

Table 9: QUENCH-15; Bundle thermocouple positions

Elevation, mm	-250	-150	-50	50	150	250	350	450	550	650	750	850	950	1050	1150	1250	1350
Rod/Elevation	1	2	3	4	5	6	7	8	9	10	11	12	13	14	15	16	17
1		N					N				W		W				
2					N				N			W		W			
3			N					N		W							W
4	N								N					W			
5						N											
6								N		W							W
7																	
8				N					N			W				W	
9								N							W		
10																	
11						N											
12															W		
13																W	
14				N					N		W			W			
15													W				
16												W					
17					N				N				W				
18																	
19														W			
20																	
21							N										
22									N			W					
23																	
24																	
Number per elevation	1	1	1	2	2	2	2	3	6	2	2	4	6	4	3	2	2

TCs to bundle bottom (8 W/Re+20 NiCr/Ni)

TCs to bundle top (17 W/Re on surface)

Heated rods (24)
NiCr/Ni (20 TCs)
W/Re (25 TCs)

Table 10: QUENCH-15; Sequence of events

Time [s]	Event
0 (11:29:29 h)	Start data recording, TIT G/13 = 864 K, el. power at 3.96 kW. L701 = 535 mm. L 501 = -394 mm.
3208	Temperature plateau reached (TIT G/13 = 1473 K); P_{el} = 11.46 kW.
5953	Corner rod B removed from bundle (reaction of TFS 8/16, TFS 19/14).
6018	Start of transient with electrical power rate of 5.880 W/s.
7050	Start of moderate temperature escalation at elevations from 850 mm to 1350 mm.
7089	Corner rod F removed from bundle (reaction of TFS 14/9, TFS 22/9).
7120	Initiation of fast water injection. First indication of cooling (T 511).
7121	Rod failure: P411 decrease. Small Kr indication by MS.
7122	Temperature maximum reached: TIT G/13 = 2155 K, TSH 13/90 = 2142 K.
7123	Start of quench water flow (F 104), water at -250 mm (TFSH 4/1).
7148	Electric power reduction from 18.12 kW.
7164	Electric power at 4.35 kW (simulation of decay heat).
7464	Quench pump shut off. Maximum water level reached: L 501 = 1300 mm; electric power shut off.
7517	End of quench water flow (Fm 104).
8259 (13:47:09)	End of data recording.
(14:07:015)	Bundle emptied from water: collected water 8 l, water level decreased from L 501 = 1263 mm to L 501 = -395 mm; L 701 = 609 mm.
(29.05.09)	Final water level data: L 701 = 785 mm (corresponded total condensed water column height of 2995 mm). L 501 = -412 mm.
(08.06.09)	Corner rods A, C, D, E, G, H removed from bundle.

Table 11: QUENCH-15; Failure of thermocouples

Thermocouple	Elevation [mm]	Time at failure [s]	Failure temperature [K]
TFS 2/14	1050	870	1145
TFS 3/13	950	4254	1535.9
TFS 1/13	950	4482	1494.5
TFS 2/12	850	6723	1605.3
TFS 8/16	1250	6767	1325
TFS 14/14	1050	6811	1545
TFS 15/13	950	6834	1529.4
TFS 21/13	950	6846	1601.3
TFS 17/13	950	6908	1676
TFS 13/13	950	6930	1636.4
TFS 9/13	950	7099	1857.3
TFS 5/14	1050	7105	1820.1
TFS 8/12	850	7138	476.9
TFS 7/16	1250	7146	554.6

Table 12: QUENCH-15; Water/steam balance

Accumulated mass of water g]	
Total steam injected (Fm 205)	23572
Total quench water injected (Fm 104)	15962
Quench water from fast injection system	4000
Total used water	43534
Condensed water collected (L 701)*: 2995 mm - 535 mm	35178
Water/steam consumed by Zr oxidation (40 g H ₂)	360
Water found posttest in the test bundle	8100
Water found posttest in the annulus of the upper plenum	150
Total water collected posttest as condensate	43788

*) water column of 1 mm corresponds to 14.3 g

Table 13: QUENCH-15; Cross sections of the test bundle (which contains rods 4, 7, 10, 16, 19 over the entire length), for metallographic examination

Sample	Sample length (mm)	Axial position (mm)		Remarks
		bottom	top	
			530	Remainder
Cut	4	530	534	
QUE-15-1	16	534	550	TC elevation 9, 550 mm polished
Cut	4	550	554	
QUE-15-a	76	554	630	
Cut	4	630	634	
QUE-15-2	16	634	650	TC elevation 10, 650 mm polished
Cut	4	650	654	
QUE-15-b	76	654	730	
Cut	4	730	734	
QUE-15-3	16	734	750	TC elevation 11, 750 mm polished
Cut	4	750	754	
QUE-15-c	76	754	830	
Cut	4	830	834	
QUE-15-4	16	834	850	TC elevation 12, 850 mm polished
Cut	4	850	854	
QUE-15-d	76	854	930	
Cut	4	930	934	
QUE-15-5	16	934	950	TC elevation 13, 950 mm polished
Cut	4	950	954	
QUE-15-e	76	954	996	
Cut	4	996	1000	
QUE-15-15	30	1000	1030	1000 mm polished
Cut	4	1030	1034	
QUE-15-6	16	1034	1050	TC elevation 14, 1050 mm polished
Cut	4	1050	1054	
QUE-15-f	76	1054	1130	
Cut	4	1130	1134	
QUE-15-7	16	1134	1150	TC elevation 15, 1150 mm polished
Cut	4	1150	1154	
QUE-15-g	76	1154	1230	
Cut	4	1230	1234	
QUE-15-8	16	1234	1250	TC elevation 16, 1250 mm polished
Cut	4	1250	1254	
		1254		Remainder

Table 14: QUENCH-15; Cross sections of the individual fuel rod simulators 1, 2, 3, 5, 6, 8, 9, 11, 12, 13, 14, 15, 17, 18, 20, 21, 22, 23, for metallographic examination

Sample	Sample length (mm)	Axial position (mm)		Remarks
		bottom	top	
			730	Remainder
Cut	4	730	734	
QUE-15-9	16	734	750	TC elevation 11, 750 mm polished; pertinent to QUE-15-3
Cut	4	750	754	
QUE-15-h	76	754	830	
Cut	4	830	834	
QUE-15-10	16	834	850	TC elevation 12, 850 mm polished; pertinent to QUE-15-4
Cut	4	850	854	
QUE-15-i	76	854	930	
Cut	4	930	934	
QUE-15-11	16	934	950	TC elevation 13, 950 mm polished; pertinent to QUE-15-5
Cut	4	950	954	
QUE-15-j	76	954	996	
Cut	4	996	1000	
QUE-15-16	30	1000	1030	1000 mm polished
Cut	4	1030	1034	
QUE-15-12	16	1034	1050	TC elevation 14, 1050 mm polished; pertinent to QUE-15-6
Cut	4	1050	1054	
QUE-15-k	76	1054	1130	
Cut	4	1130	1134	
QUE-15-13	16	1134	1150	TC elevation 15, 1150 mm polished; pertinent to QUE-15-7
Cut	4	1150	1154	
QUE-15-l	76	1154	1230	
Cut	4	1230	1234	
QUE-15-14	16	1234	1250	TC elevation 16, 1250 mm polished; pertinent to QUE-15-8
Cut	4	1250	1254	
		1254		Remainder

Table 15: QUENCH-15; Average oxide layer thicknesses measured for rods #1 - #17

rod # / elevation, mm	550	650	750	850	900	950	1000	1050	1100	1150	1250
1	26	78	199	580				688		172	57
	1	6	8	0				23		8	3
			192							179	53
2			5							2	8
3	27	82	209	588			850	800		179	61
	2	8	8	29			0	15		4	7
4	26	82	206	580				660		173	60
	1	5	11	50				20		6	5
5	21	47	148				700	528		139	40
	1	7	23				0	29		17	6
6	19	46	159				820	460		134	40
	0	11	12				20	50		13	6
7	17	32	112	250		585	678	270		85	32
	4	5	12	40		95	138	35		23	4
8	21	49	155			715	720	469		133	40
	2	6	15			63	80	81		13	3
9	20	51	152							140	44
	4	7	11							13	4
10	19	30	120	210		490	660	380		102	32
	3	5	21	0		0	65	60		30	5
11	24	46	162	253		673	767	543		143	44
	1	8	10	16		88	44	88		15	5
12	24	52	164					603		151	47
	1	10	12					78		8	4
13	18	31	125			773	765	445		120	32
	3	4	15			38	25	65		15	3
14	21	43	160					613		149	45
	1	9	12					43		16	4
15	23	49	172			415		595		145	34
	1	9	13			60		23		15	5
16	15	31	128	265		743		468		113	33
	2	5	17	15		63		58		18	4
17	14	27	109			615	780	329		76	30
	1	4	14			15	80	51		20	8

bold-face layer thickness in μm typeface radial scatter of thickness, $\pm \mu\text{m}$

Table 16: QUENCH-15; Average oxide layer thicknesses measured for rods #18 - #24, shroud and corner rods

rod # / elevation, mm	550	650	750	850	900	950	1000	1050	1100	1150	1250
18	13	27	98	240		705	820	280		71	25
	0	3	13	25		5	140	55		17	3
19	13	26	96	207		510	528	253		69	28
	2	0	12	11		60	76	43		14	2
20	14	27	93	213		470	545	249		61	28
	1	2	14	18		50	60	46		17	2
21	20	30	108	230				348		81	26
	3	3	9	0				48		17	1
22	18	30	112			725	775	380		90	29
	2	4	12			45	63	60		17	5
23	19	29	118					408		89	26
	4	4	15					58		20	5
24	16	31	130							80	25
	2	2	10							16	2
shroud		19	73	159	320	443	442	102	32		
		1	8	28	65	71	53	34	5		
corner rod A	7	20	62	143		391		303		59	23
	1	1	2	2		3	13			3	1
corner rod B	6	20	32	101		143		64		32	
	1	2	1	2		2		2		2	
corner rod C	10	26		301		561		142		112	23
	1	2		27		47		33		21	9
corner rod D	8	19	64	166		463		207		49	
	3	2	13	3		14		7		5	
corner rod E	7	22	62	147		411		166		30	20
	1	2	2	2		7		6		4	2
corner rod F	9	23	72	168		378		137		60	
	2	1	13	2		10		3		3	
corner rod G	8	21	94	265		564		108		47	19
	1	1	3	10		18		4		15	2
corner rod H	9	30	85	279		583		292		49	
	1	10	26	28		69		43		12	

bold-face layer thickness in μm typeface radial scatter of thickness, $\pm \mu\text{m}$

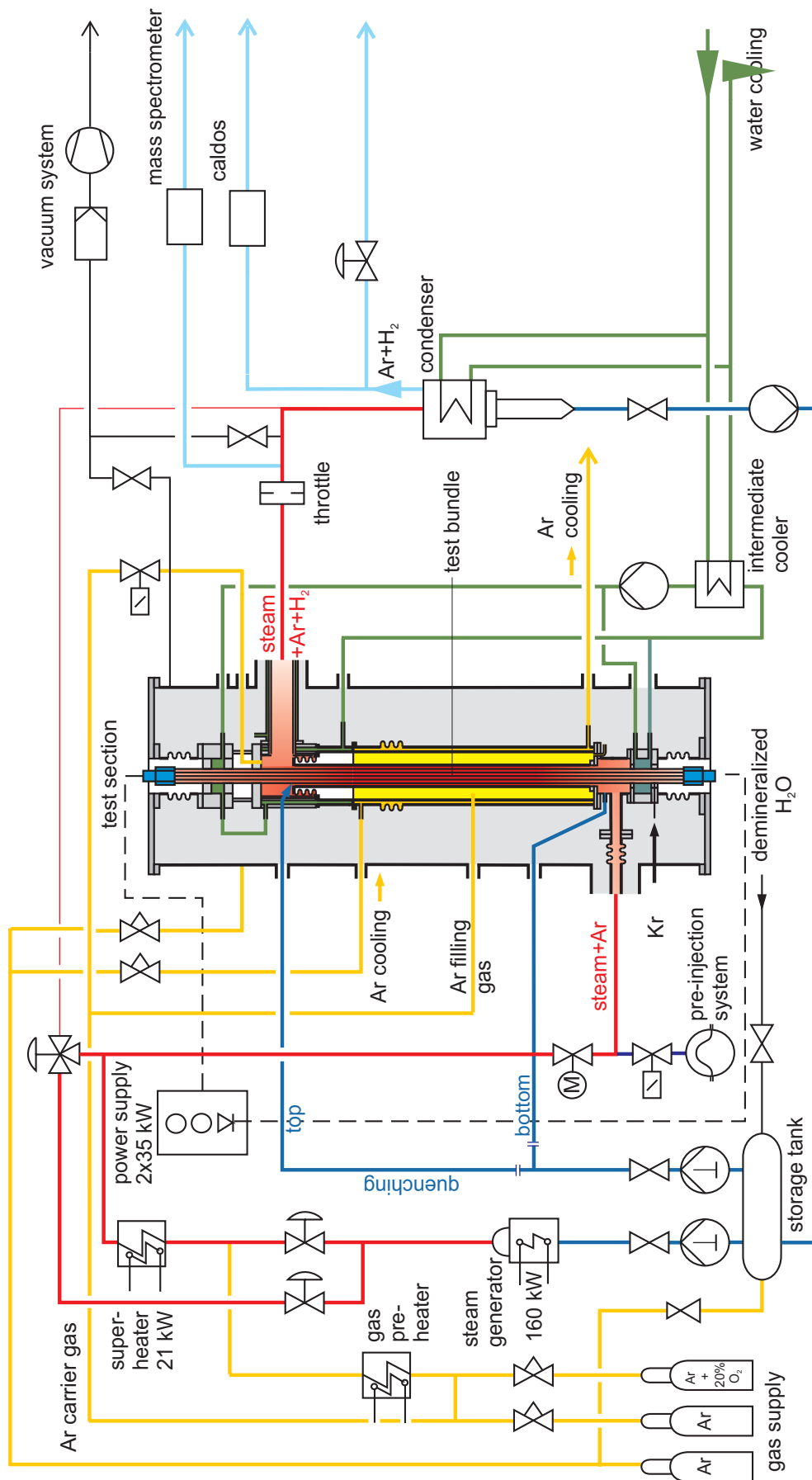


Fig.1-QUE15-Flow diagram.cdr
16.07.08 - IMF

Fig. 1: Flow diagram of the QUENCH test facility.

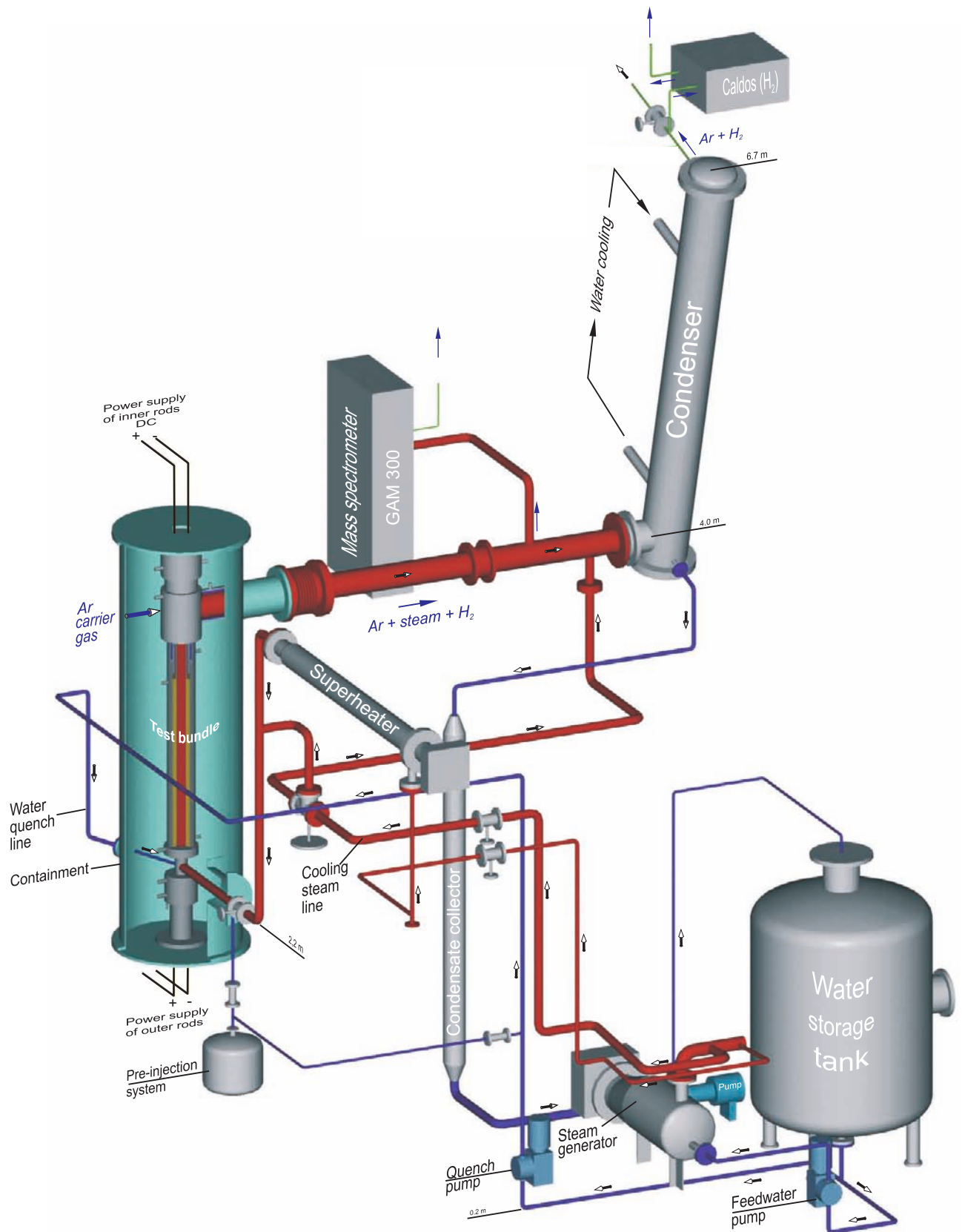


Fig.2-QUE15-Gesamtanlage.cdr
16.07.08 - IMF

Fig. 2: QUENCH facility - main components.

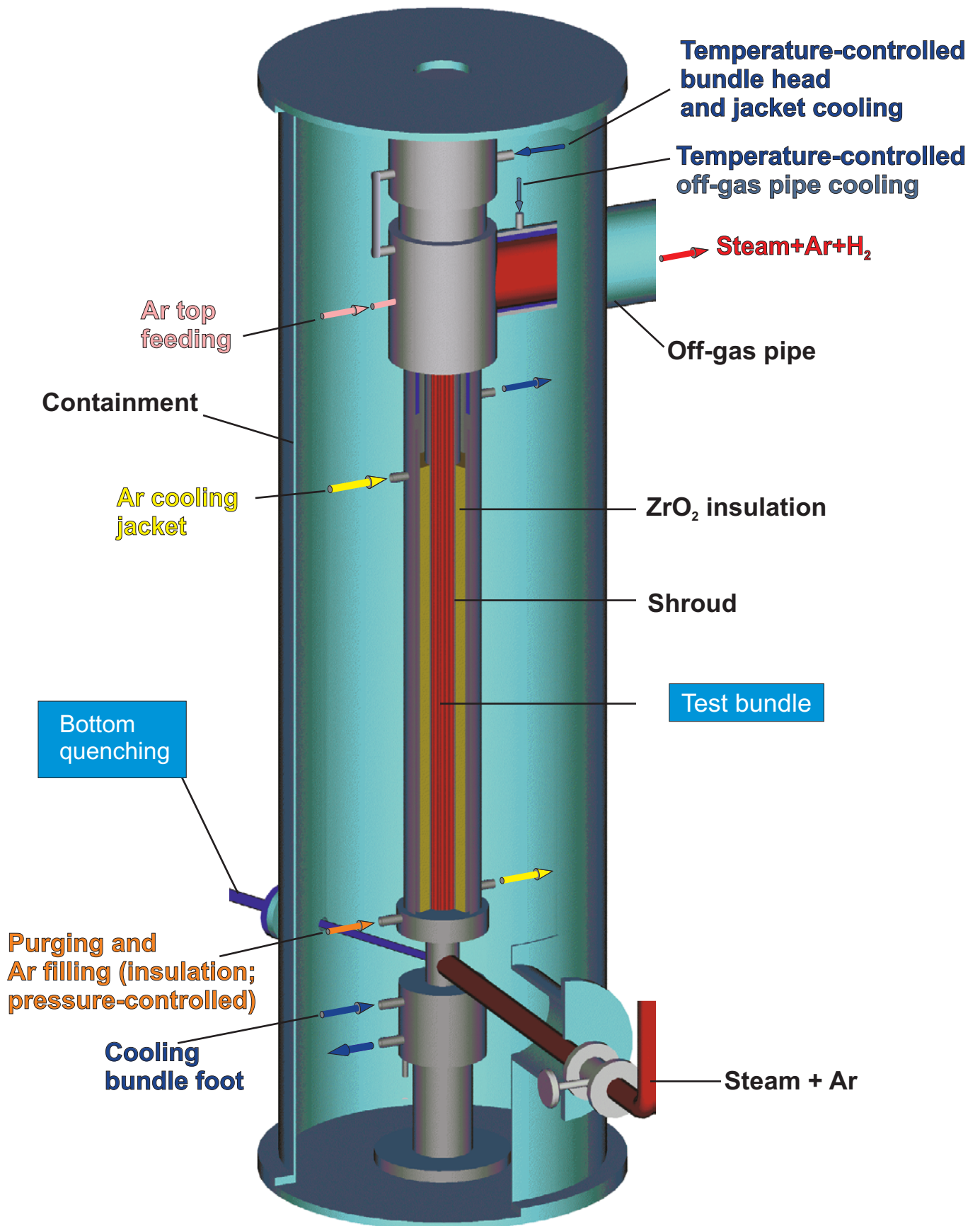


Fig.3-QUE15 Containment 3D.cdr
16.07.08 - IMF

Fig. 3: QUENCH facility - containment and test section.

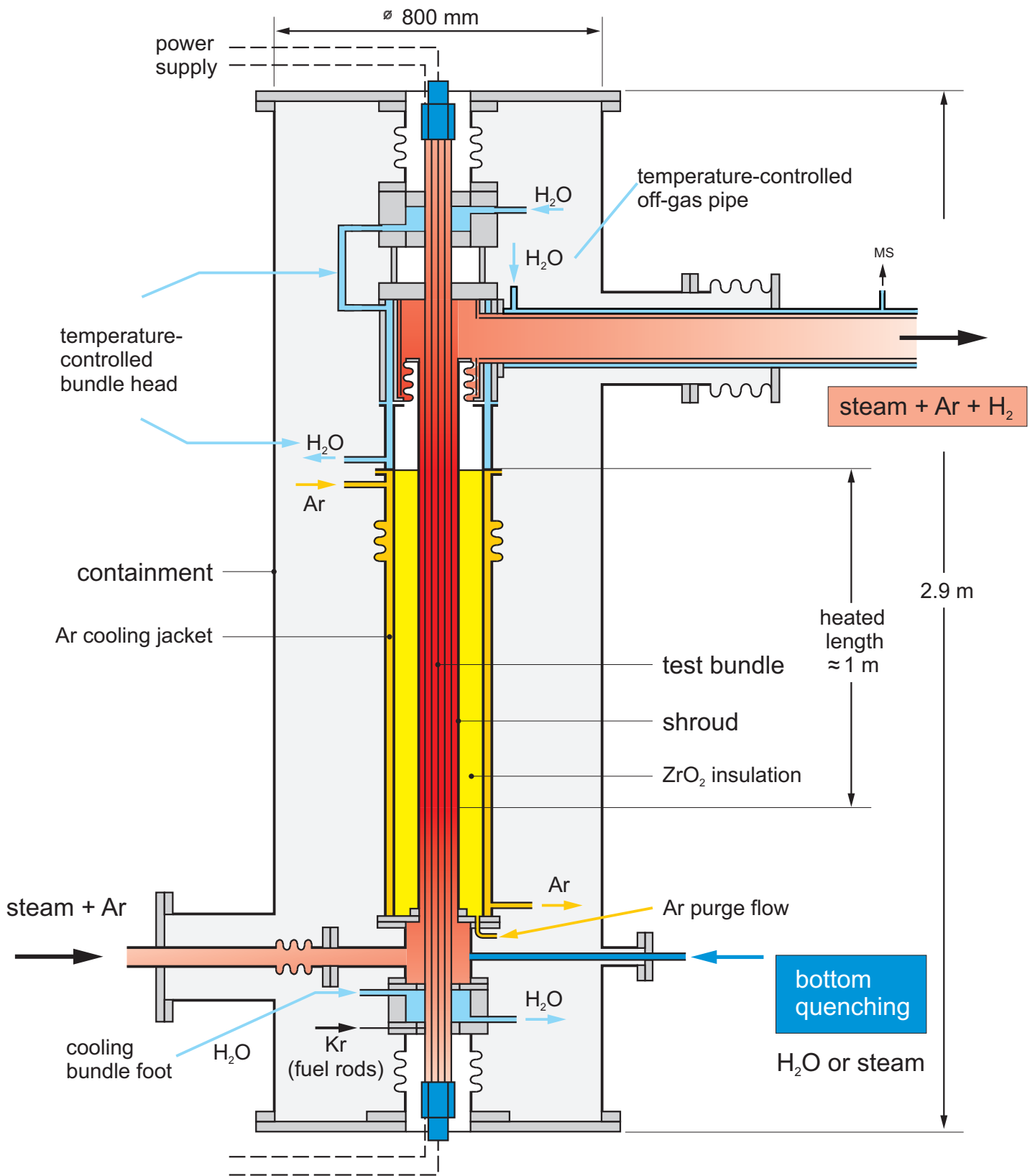


Fig 4-QUE15-Flow lines.cdr
05.08.09 - IMF

Fig. 4: QUENCH-15; Test section with flow lines.

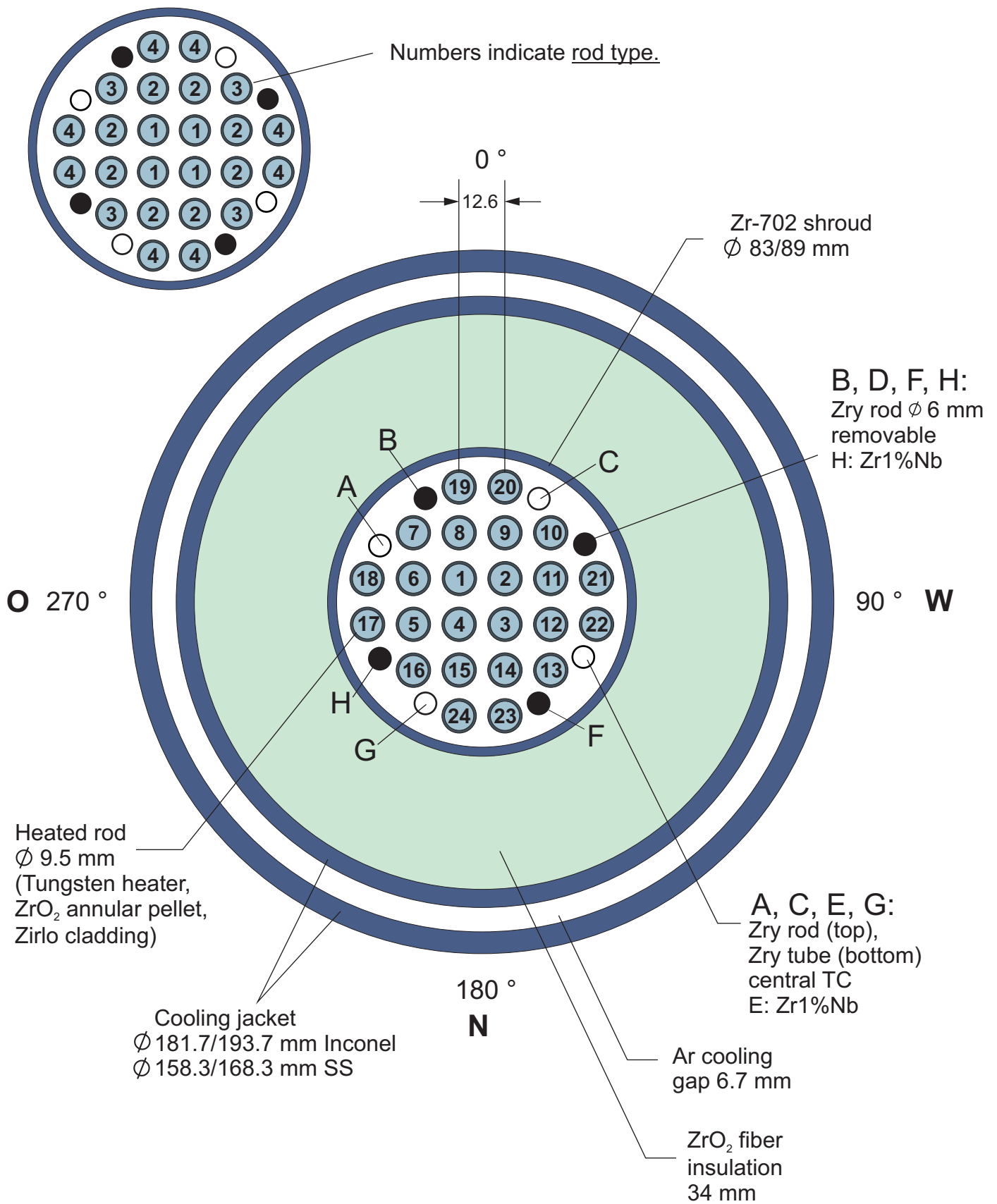


Fig.5-QUE15 Cross section.cdr
 17.08.09 - IMF

Fig. 5: QUENCH-15; Fuel rod simulator bundle (cross section, top view) including rod number and rod type indications.

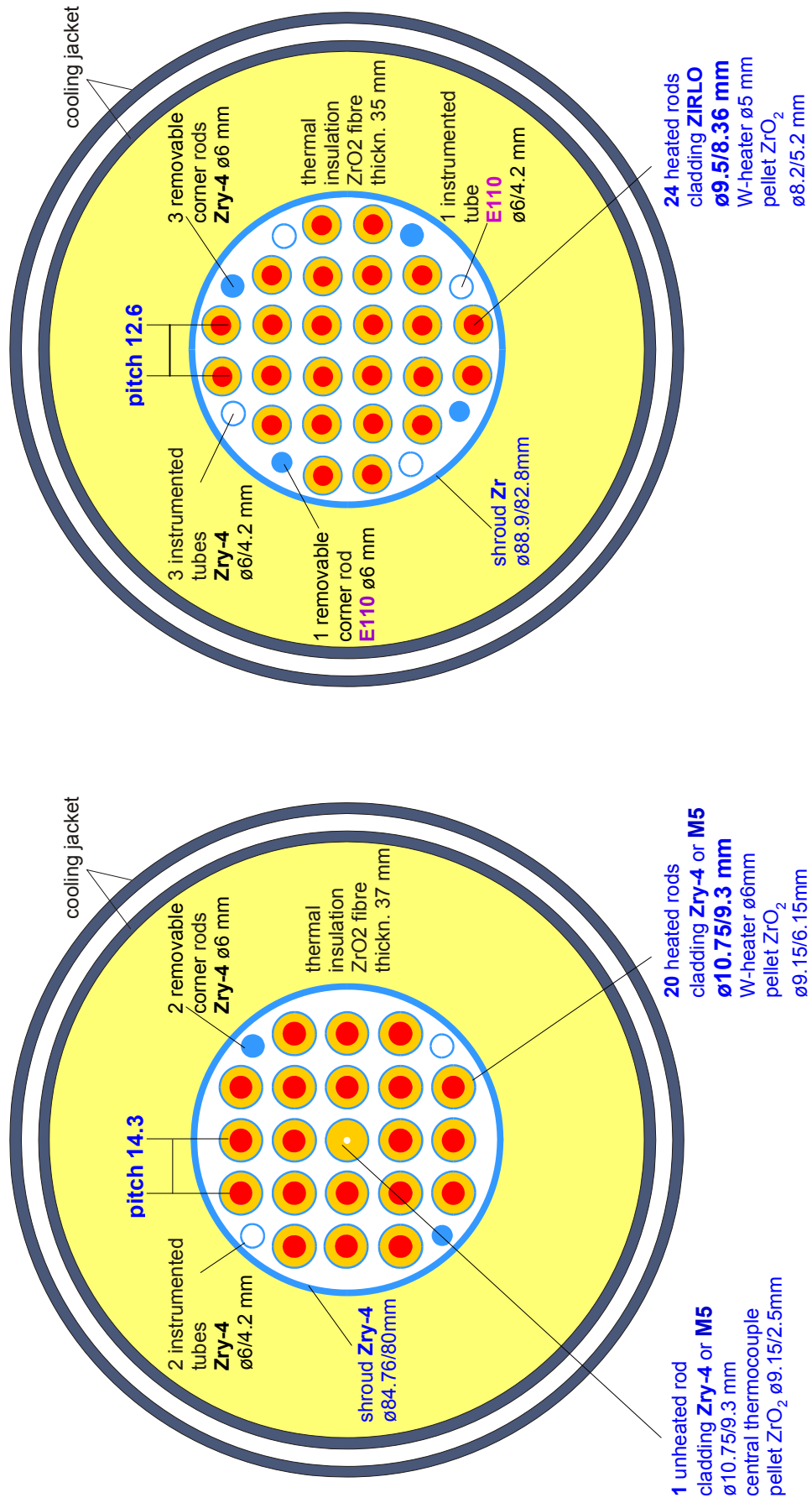


Fig. 6: Comparison of two different test bundles.

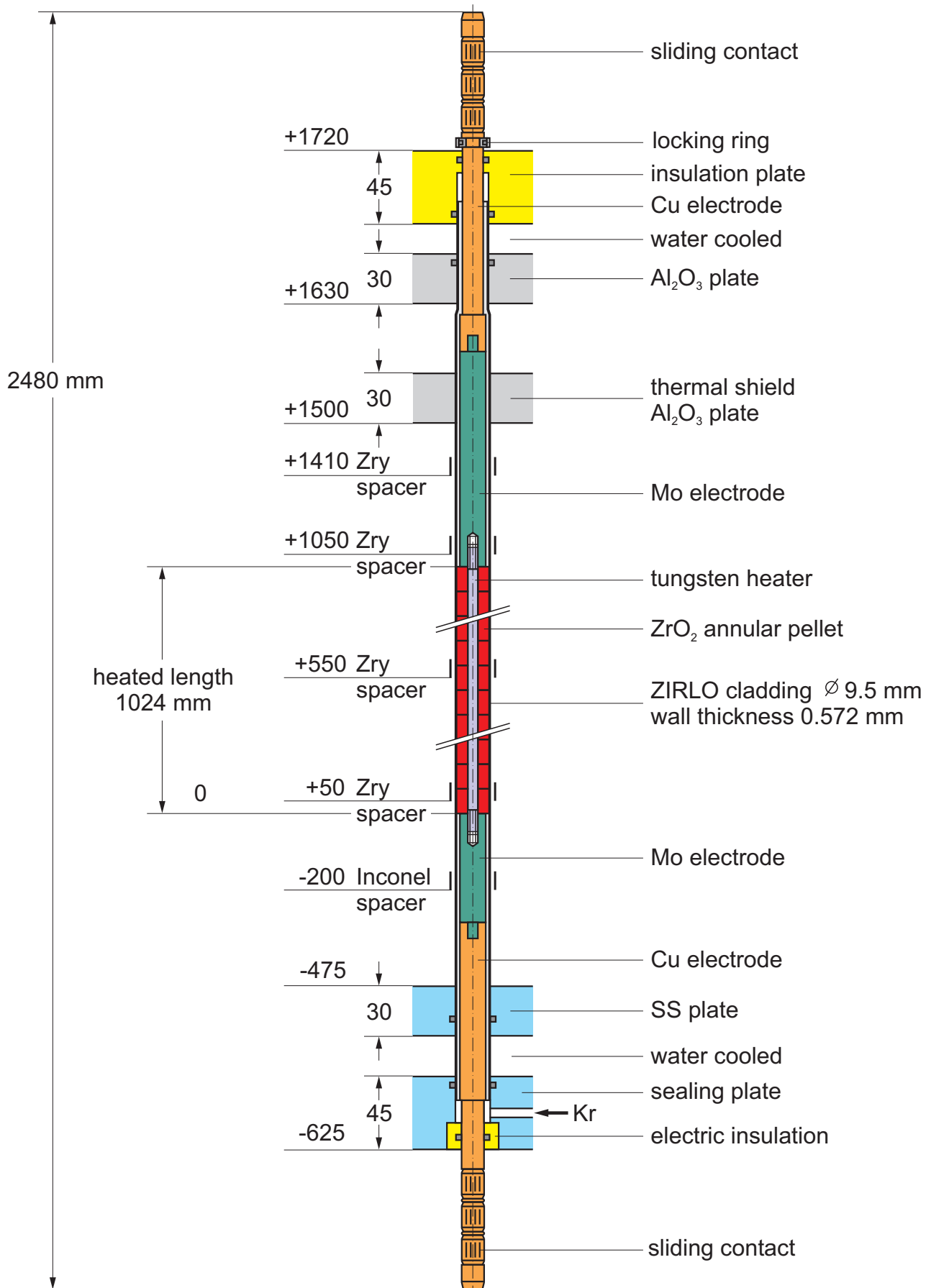


Fig.7-QUE15-Heated fuel rod sim.cdr
21.02.11 - IMF

Fig. 7: Heated fuel rod simulator.

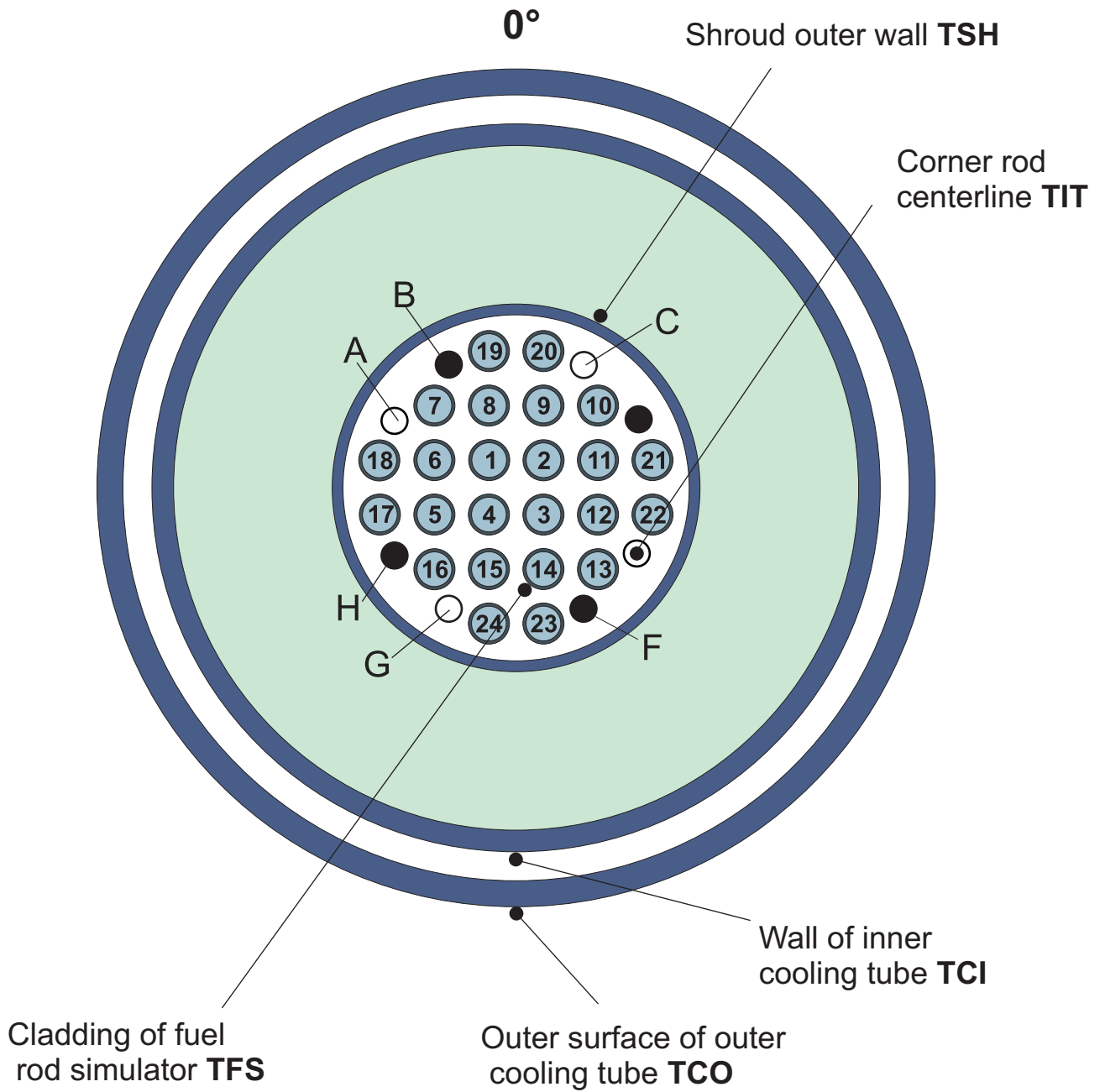


Fig.8-QUE15 TC instr.cdr
21.02.11 - IMF

Fig. 8: QUENCH-15; Designation of the various thermocouples.

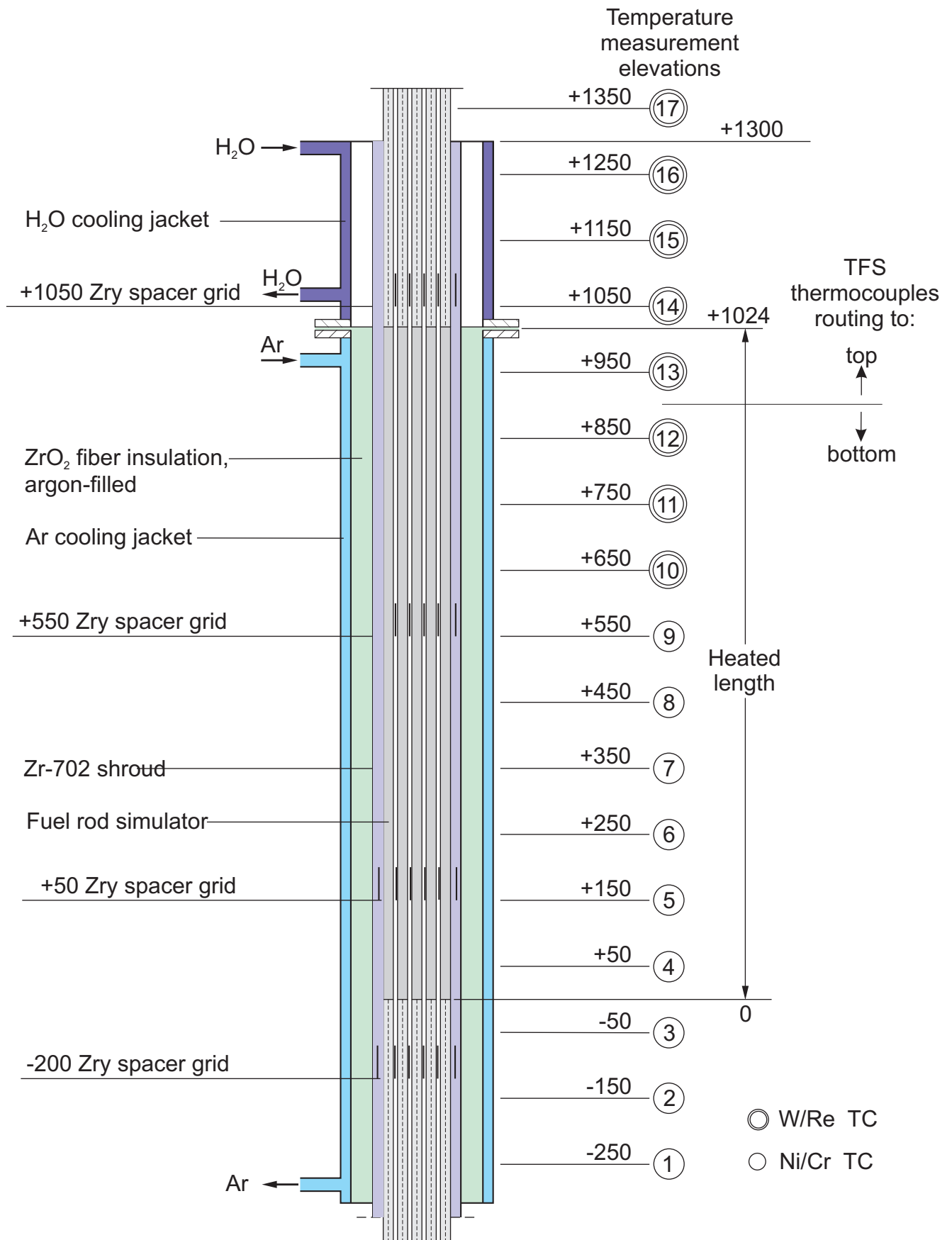
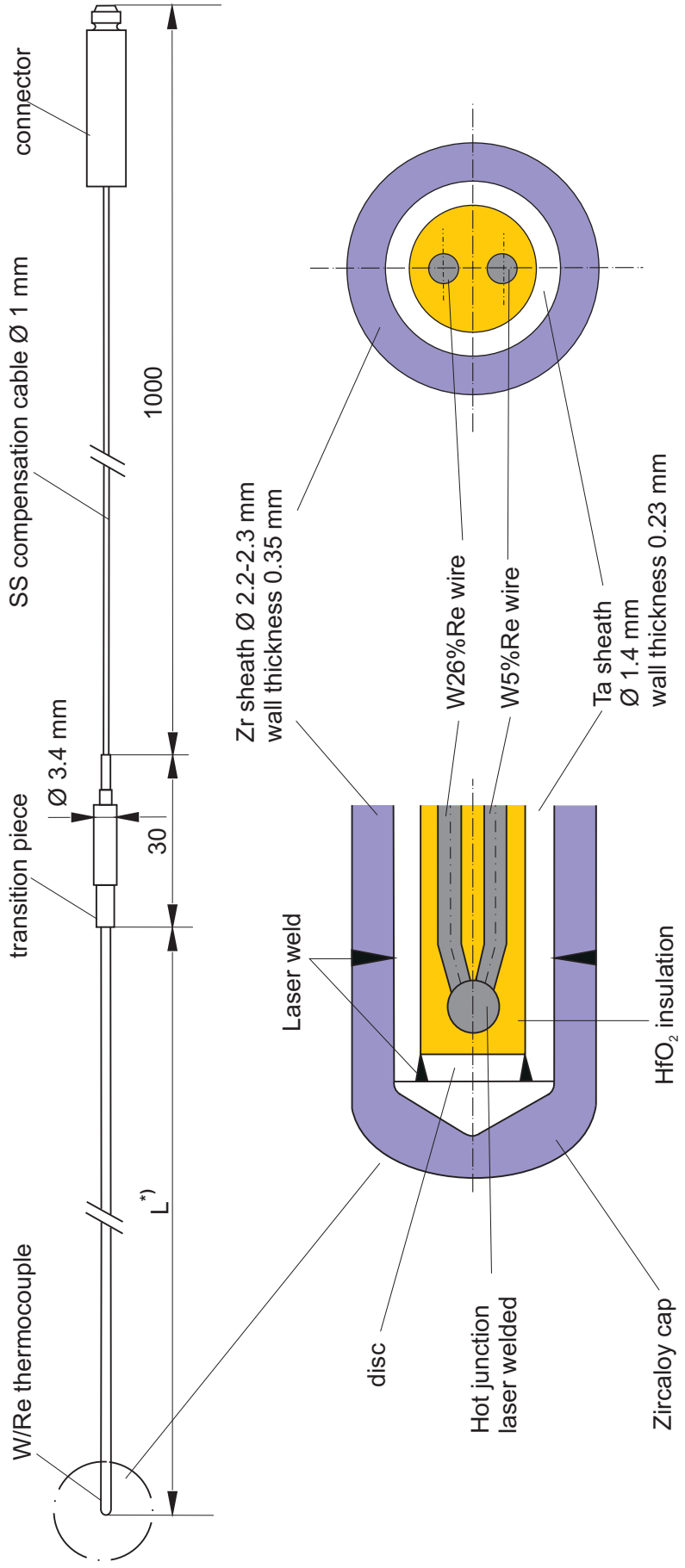


Fig.9-QUE15-TC elevations.cdr
21.02.11

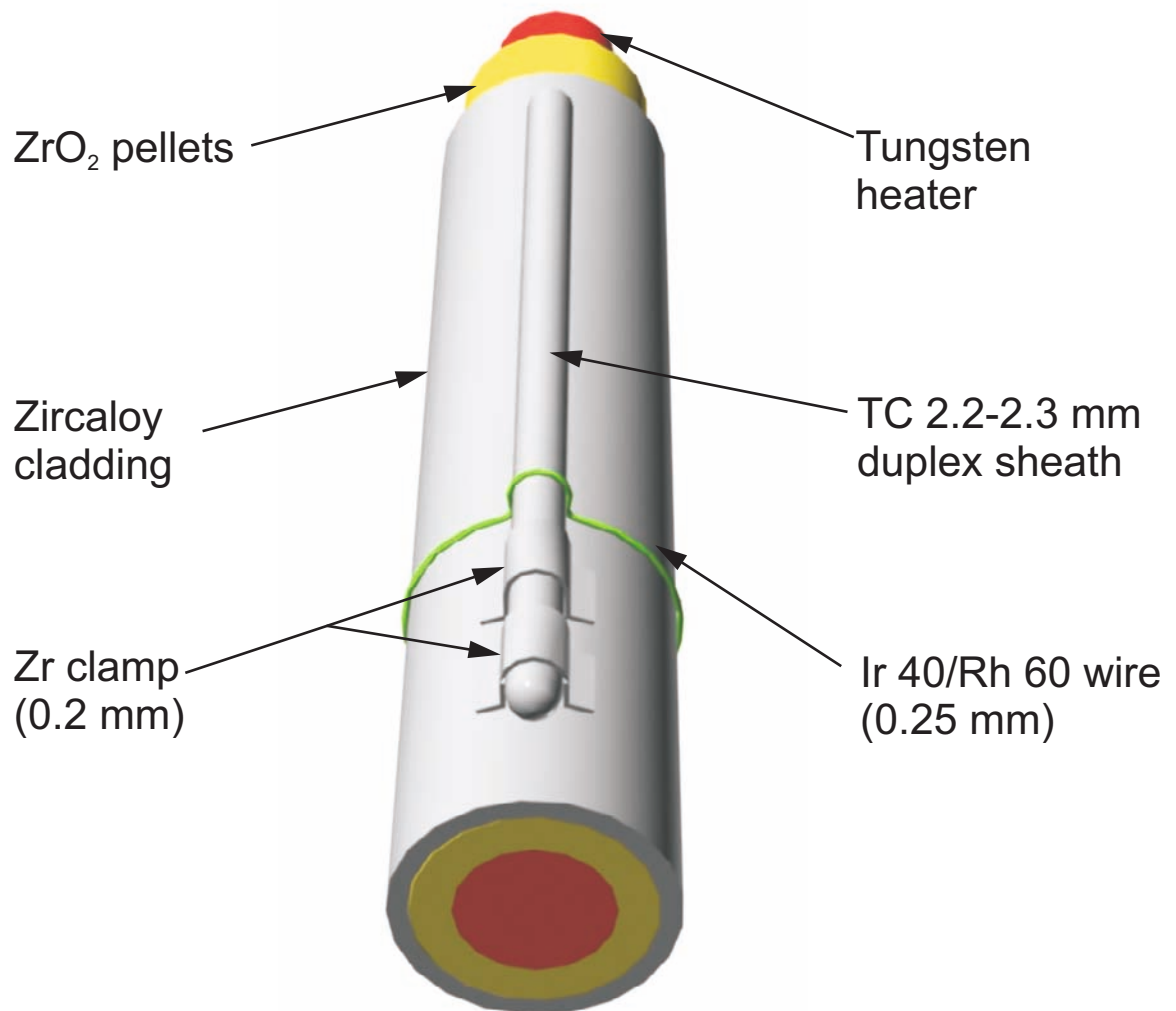
Fig. 9: Axial temperature measurement locations in the QUENCH-15 test section.



*) L : high-temperature section length dependent on the TC position in the test bundle: 500-1700 mm

Fig. 10-QUE15-High-temp thermocouple.cdr
21.02.11 - IMF

Fig. 10: QUENCH; High-temperature thermocouple.

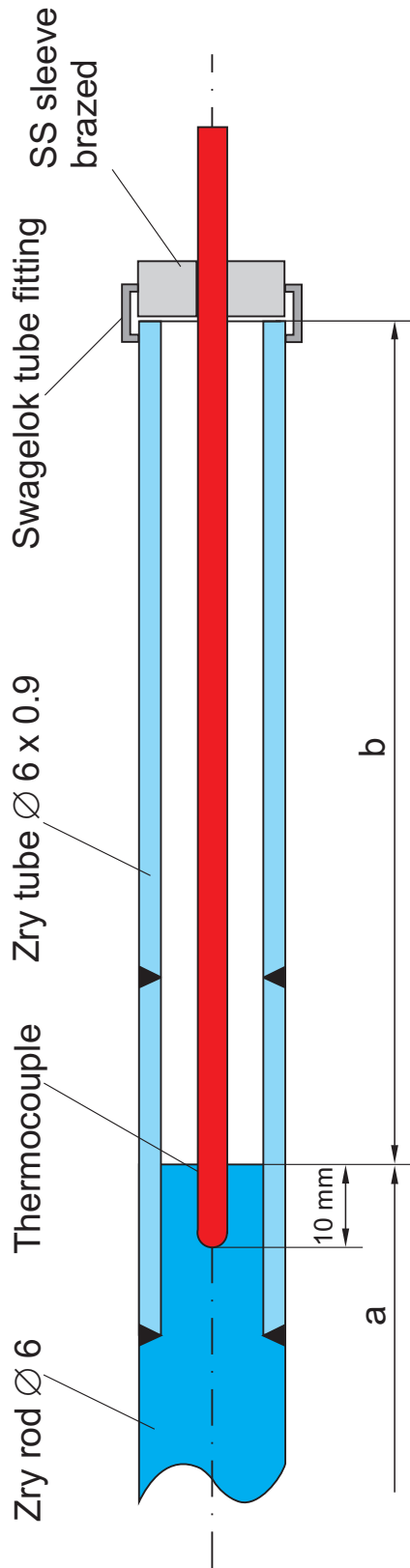


Tests with pre-oxidation: Zr clamp + wire

Tests without pre-oxidation: Zr clamp

Fig. 11: QUENCH-15; Concept for TC fastening at the test rod.

(TIT E/11, TIT C/12, TIT A/13, TIT G/13)



Rod A: TIT/A13 (950 mm), W/Re, $\varnothing 2.1$ mm, $a = 360$ mm, $b = 2080$ mm

Rod C: TIT/C12 (850 mm), W/Re, $\varnothing 2.1$ mm, $a = 460$ mm, $b = 1980$ mm

Rod E: TIT/E13 (950 mm), W/Re, $\varnothing 2.1$ mm, $a = 360$ mm, $b = 2080$ mm

Rod G: TIT/G/12 (850 mm), W/Re, $\varnothing 2.1$ mm, $a = 460$ mm, $b = 1980$ mm

(Rod B, D, F, H: $\varnothing 6$ mm, removable)

Fig 12-QUE15-TC in corner rod.cdr
21.02.11 - IMF

Fig. 12: QUENCH-15; Arrangement of the thermocouples inside the corner rods.

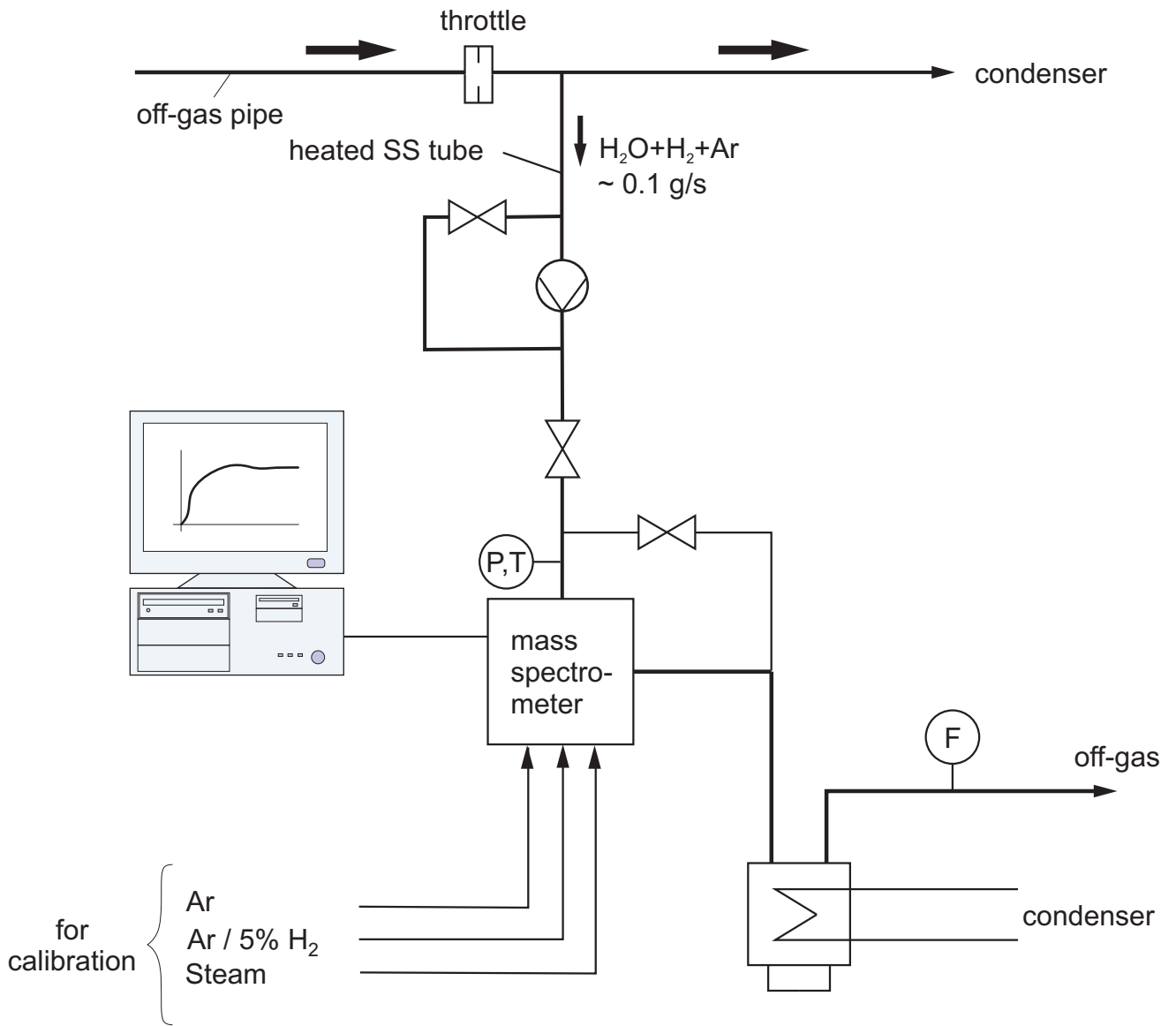


Fig.13-QUE15-MS Quench facility.cdr
21.02.11 - IMF

Fig. 13: QUENCH Facility; H_2 measurement with the GAM 300 mass spectrometer.

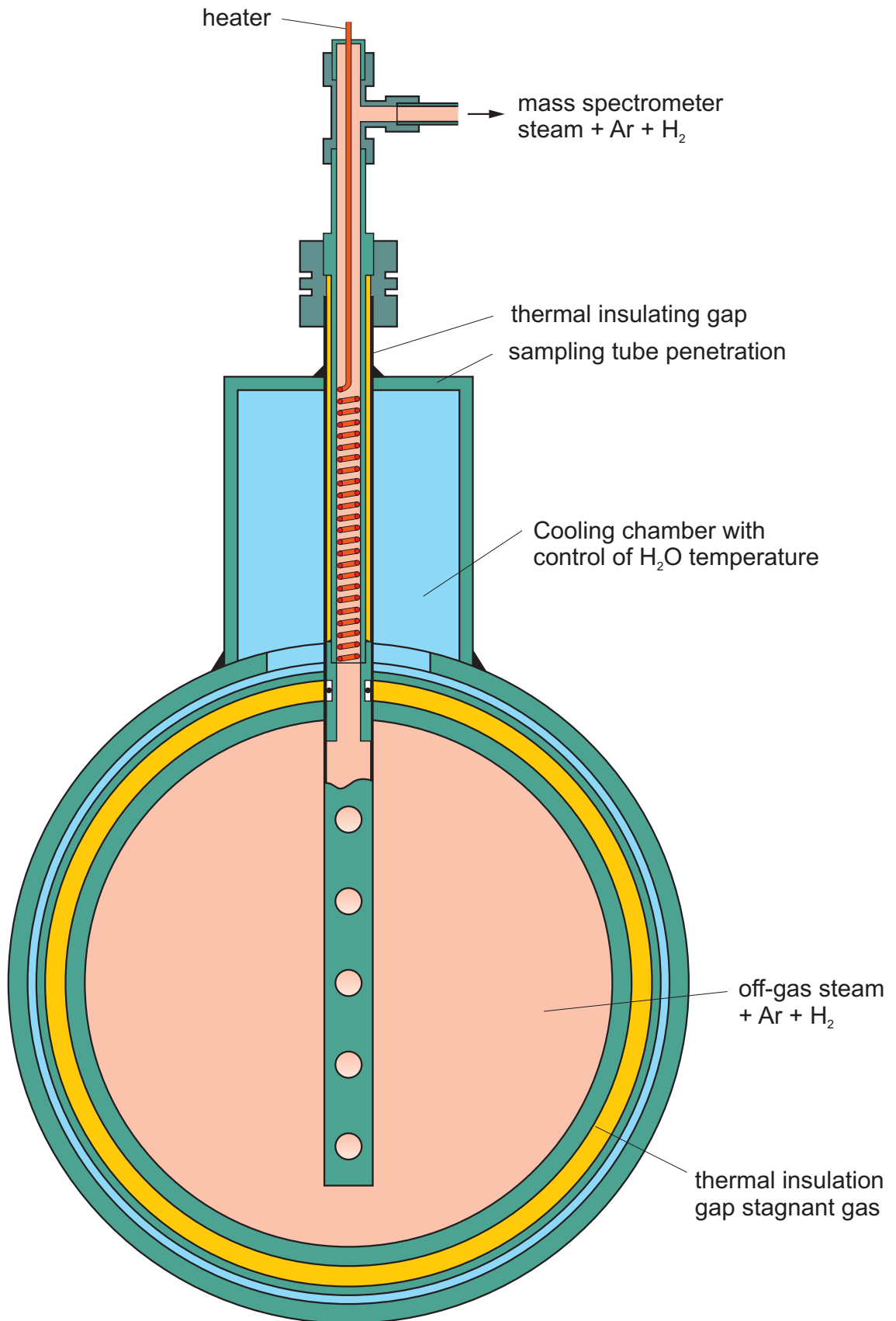


Fig 14-QUE15 MS sampling position new.cdr
21.02.11 - IMF

Fig.14: Mass spectrometer sampling position at the off-gas pipe of the QUENCH test facility.

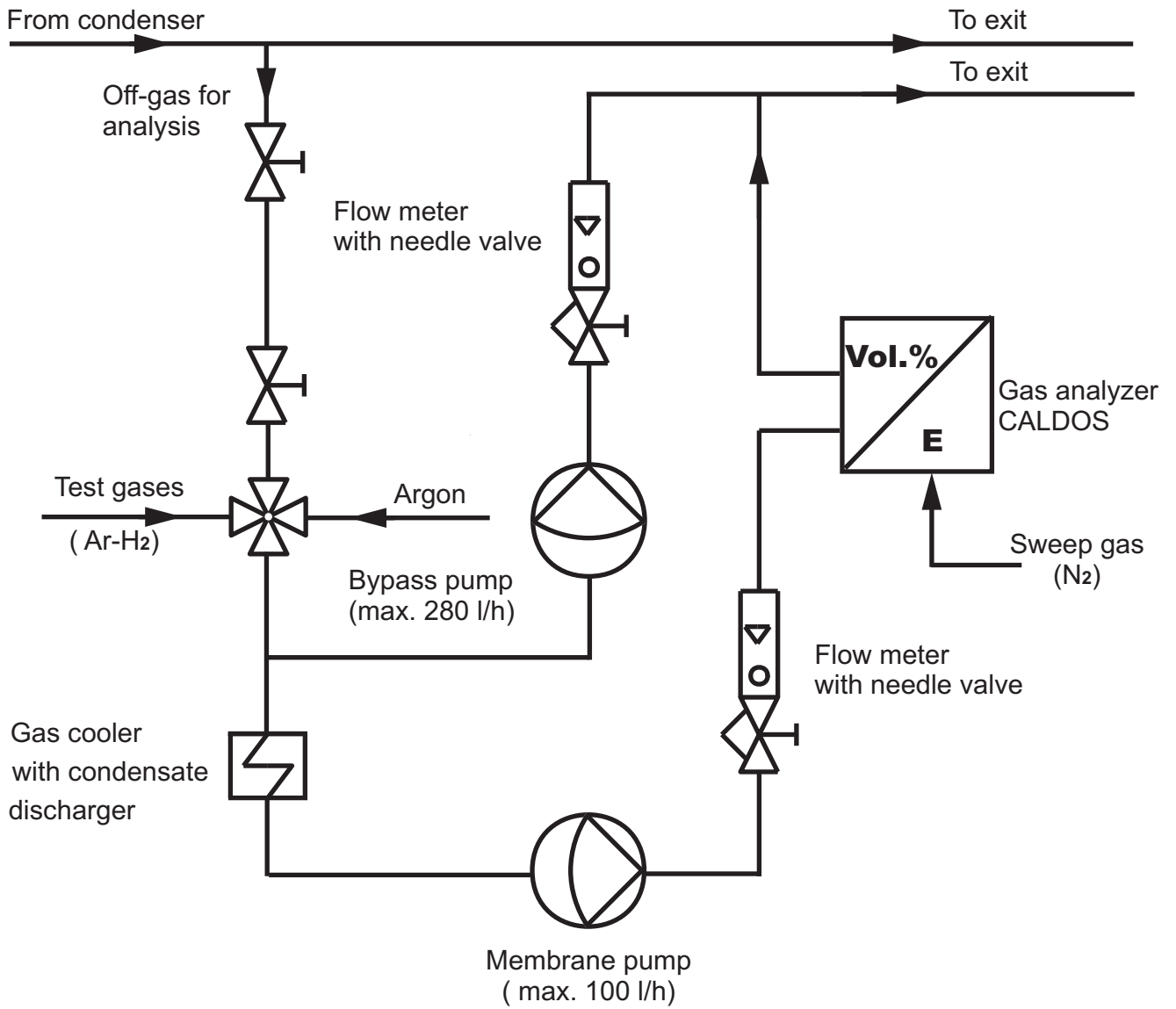
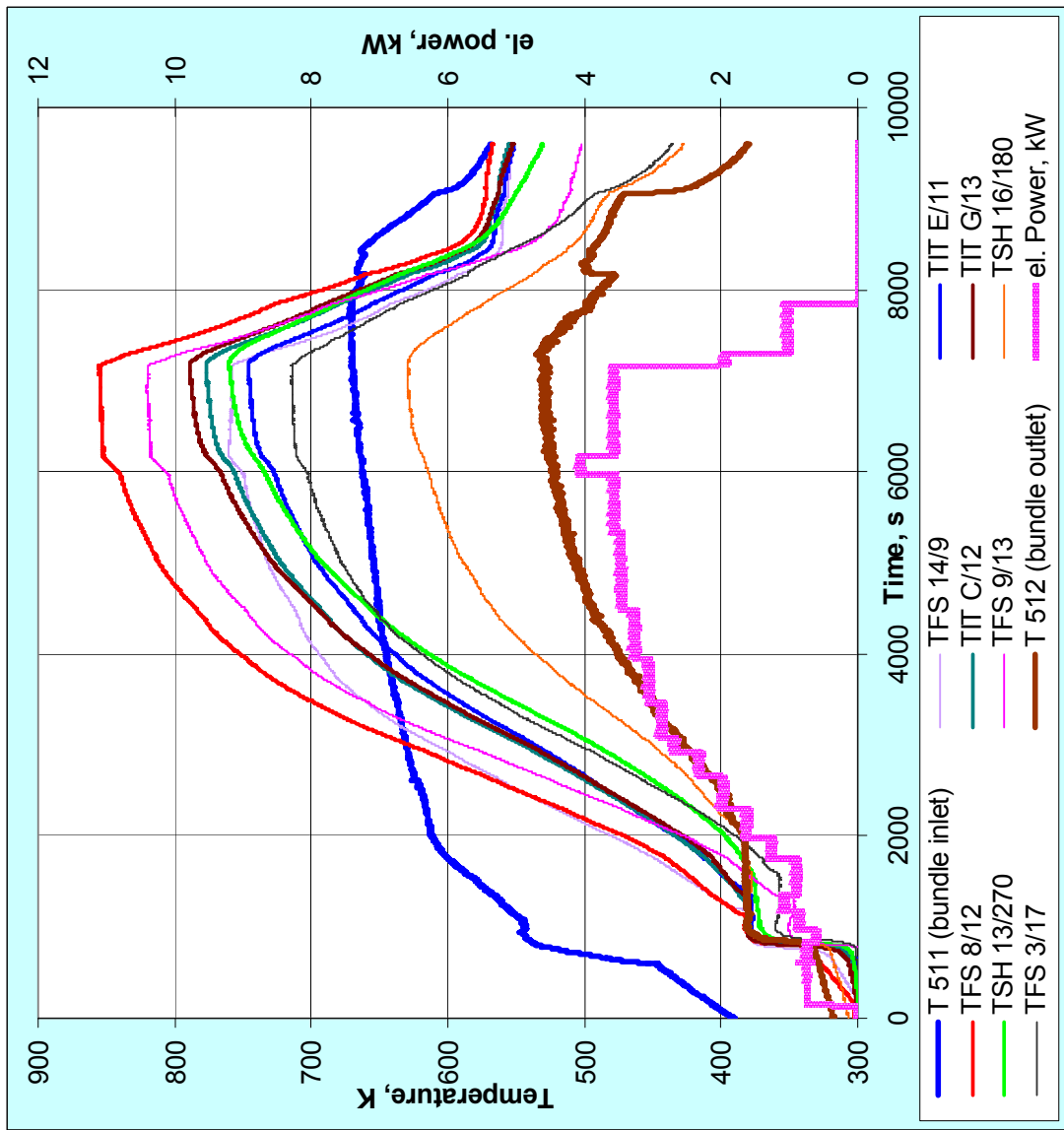


Fig 15 QUE15 Caldos Schema (ab QUE04).cdr
21.02.11 - IMF

Fig.15: Hydrogen measurement with the CALDOS analyzer connected to the exhaust gas pipe of the QUENCH facility.



post-pretest videoscope inspection: intact rods, spacer grids and thermocouples

ZrO₂ layer thickness after pre-test: 2 μm

Fig. 16: QUENCH-15 pre-test to adjusting of calculation parameters.

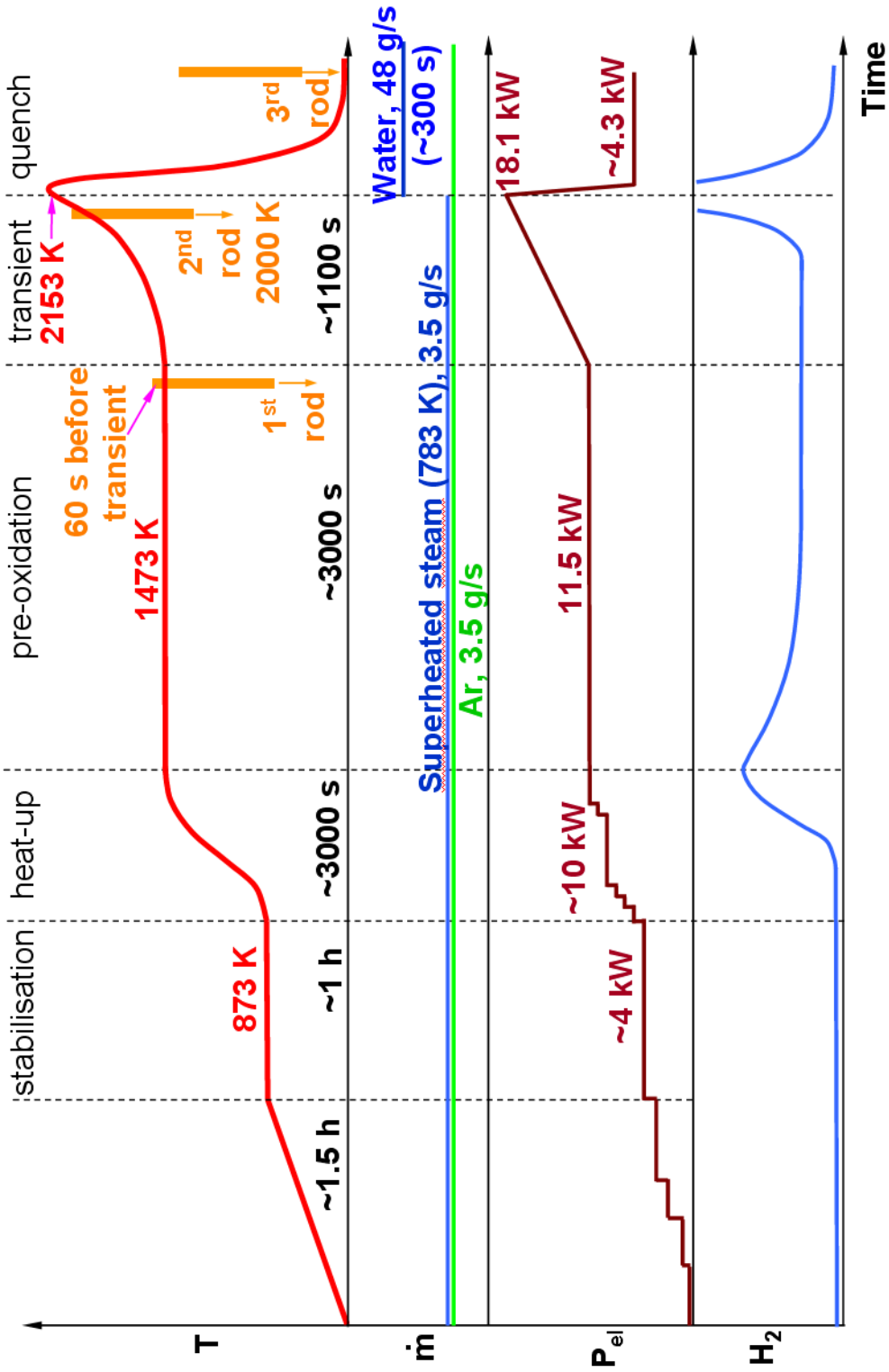


Fig. 17: QUENCH-15 test conduct (schematics of histories of bundle temperature, power, argon and steam flow rate and hydrogen production rate).

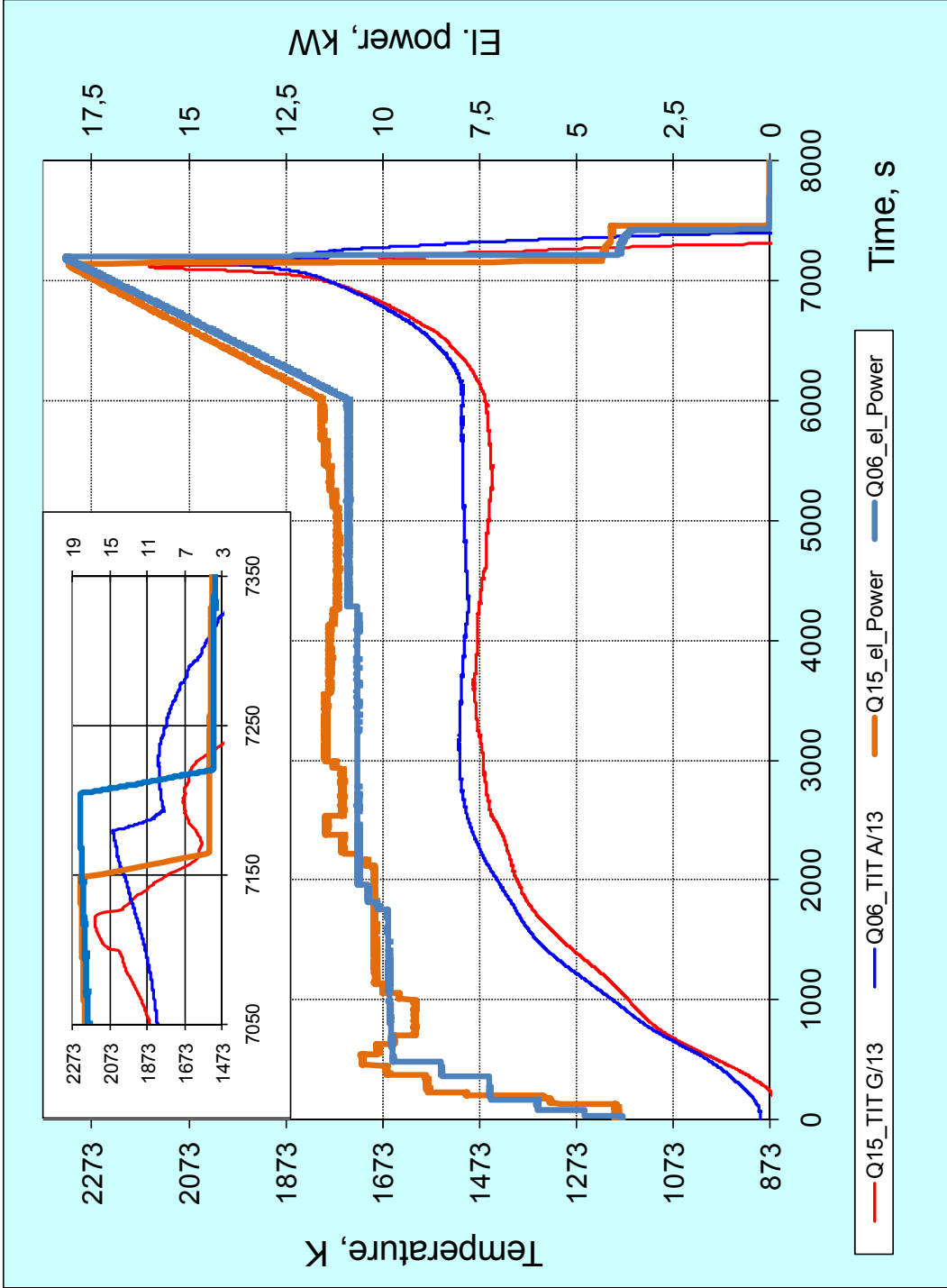


Fig. 18: QUENCH-15 test performance with reproduction of QUENCH-06 (Zry-4) temperature history.



Fig. 19: Performance of tests QUENCH-06 (Zry-4), QUENCH-12 (E110), QUENCH-14 (M5) and QUENCH-15 (ZIRLO) under identical scenario.

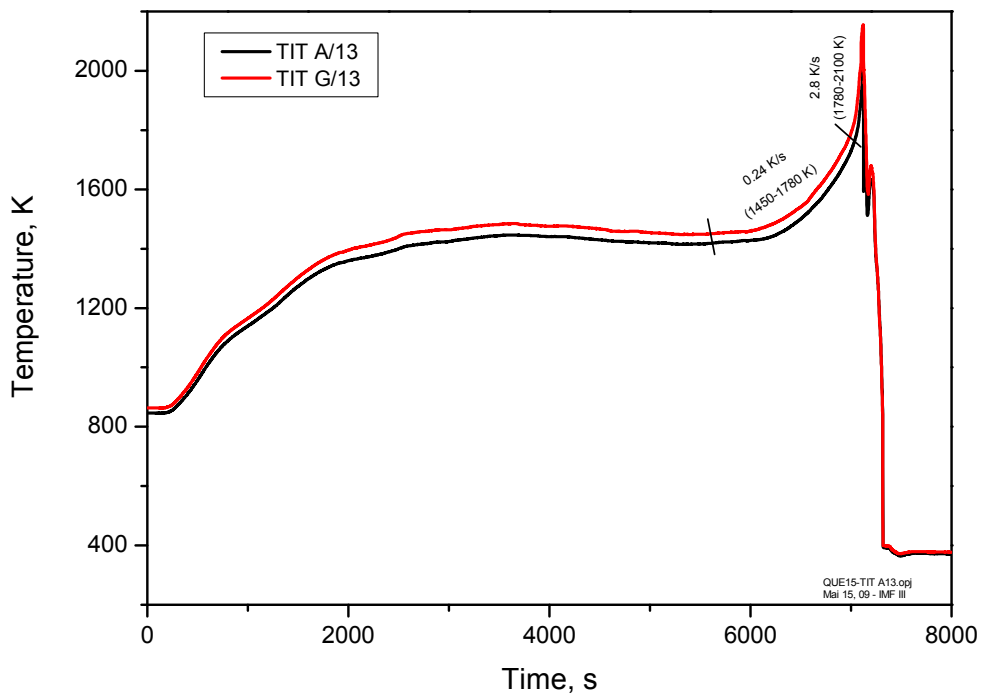
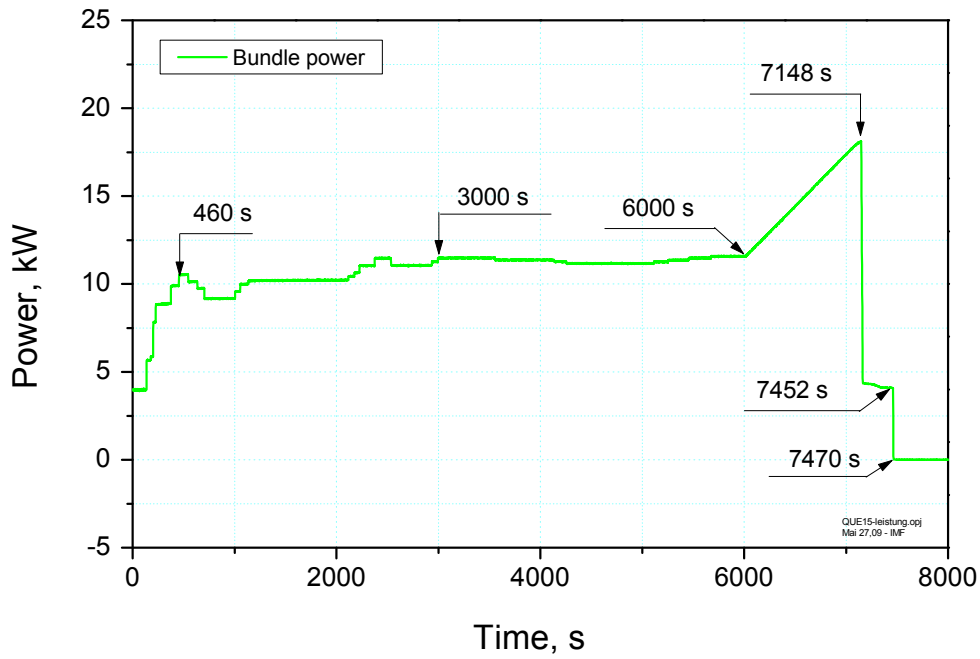


Fig. 20: QUENCH-15; Total electric bundle power vs. time, top, and heating rates of the transient phase, bottom.

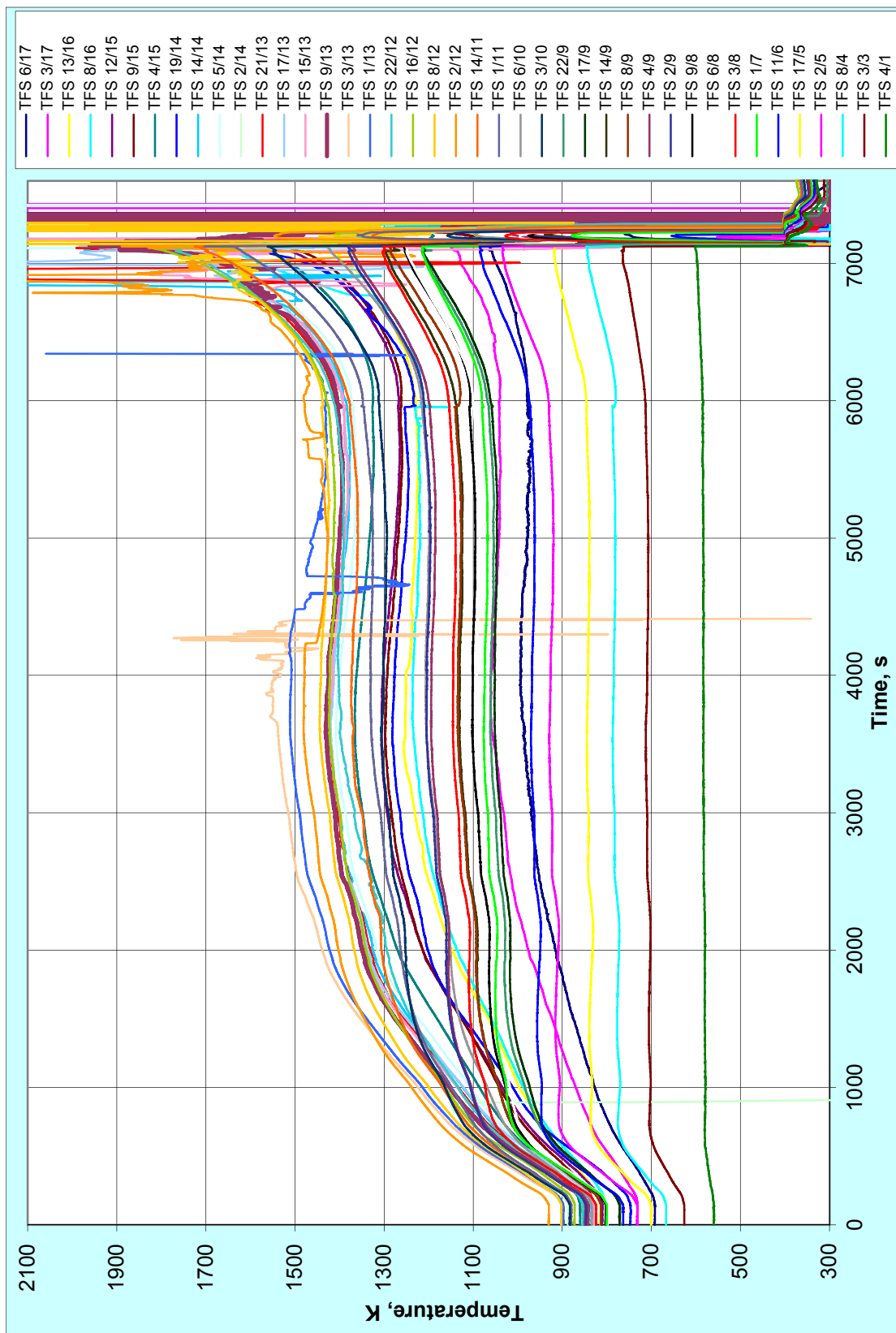


Fig. 21: QUENCH-15; Readings of cladding surface thermocouples.

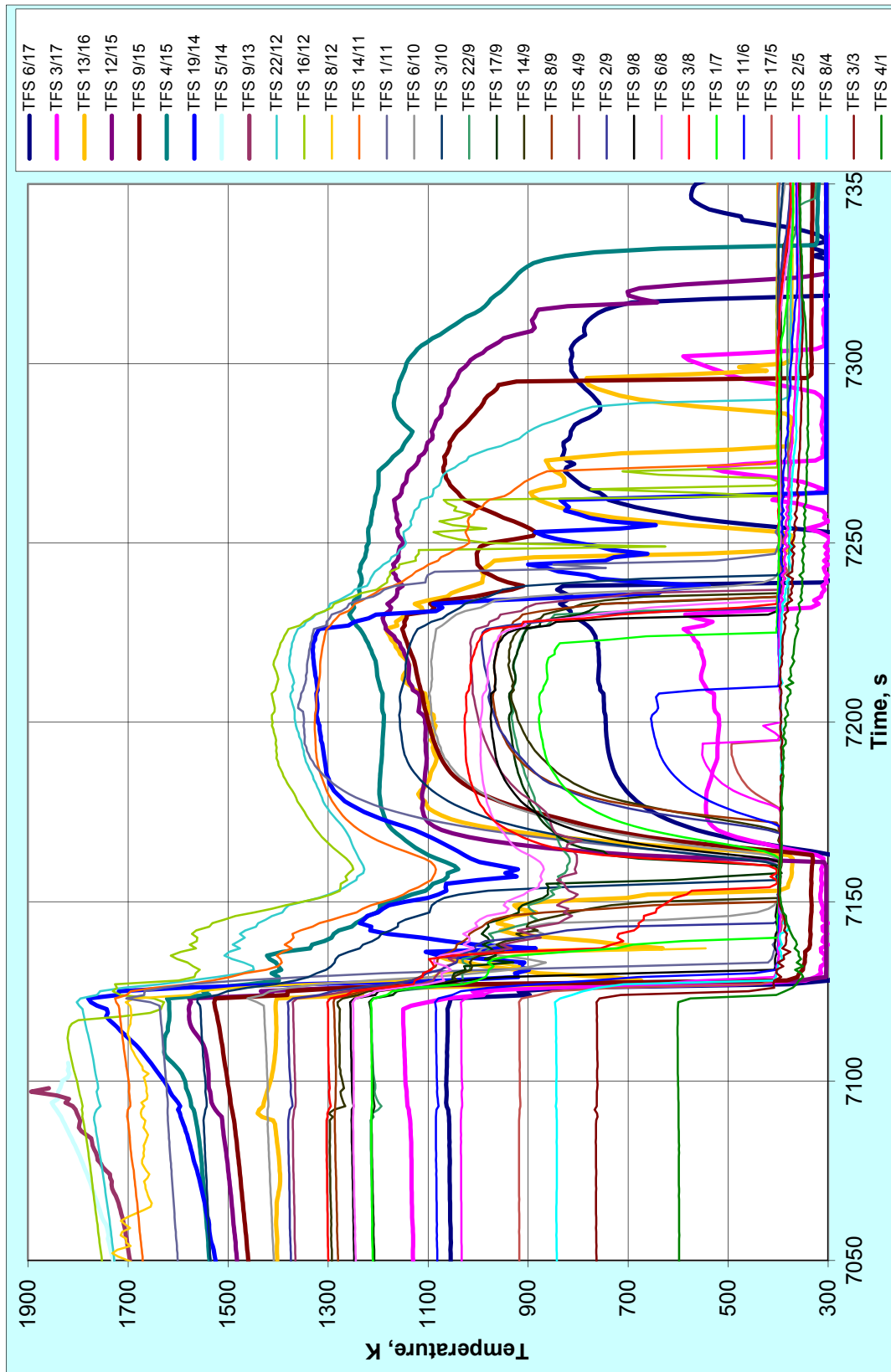


Fig. 22: QUENCH-15; Readings of cladding surface thermocouples (excluding failed TC) on the transient end and during reflow.

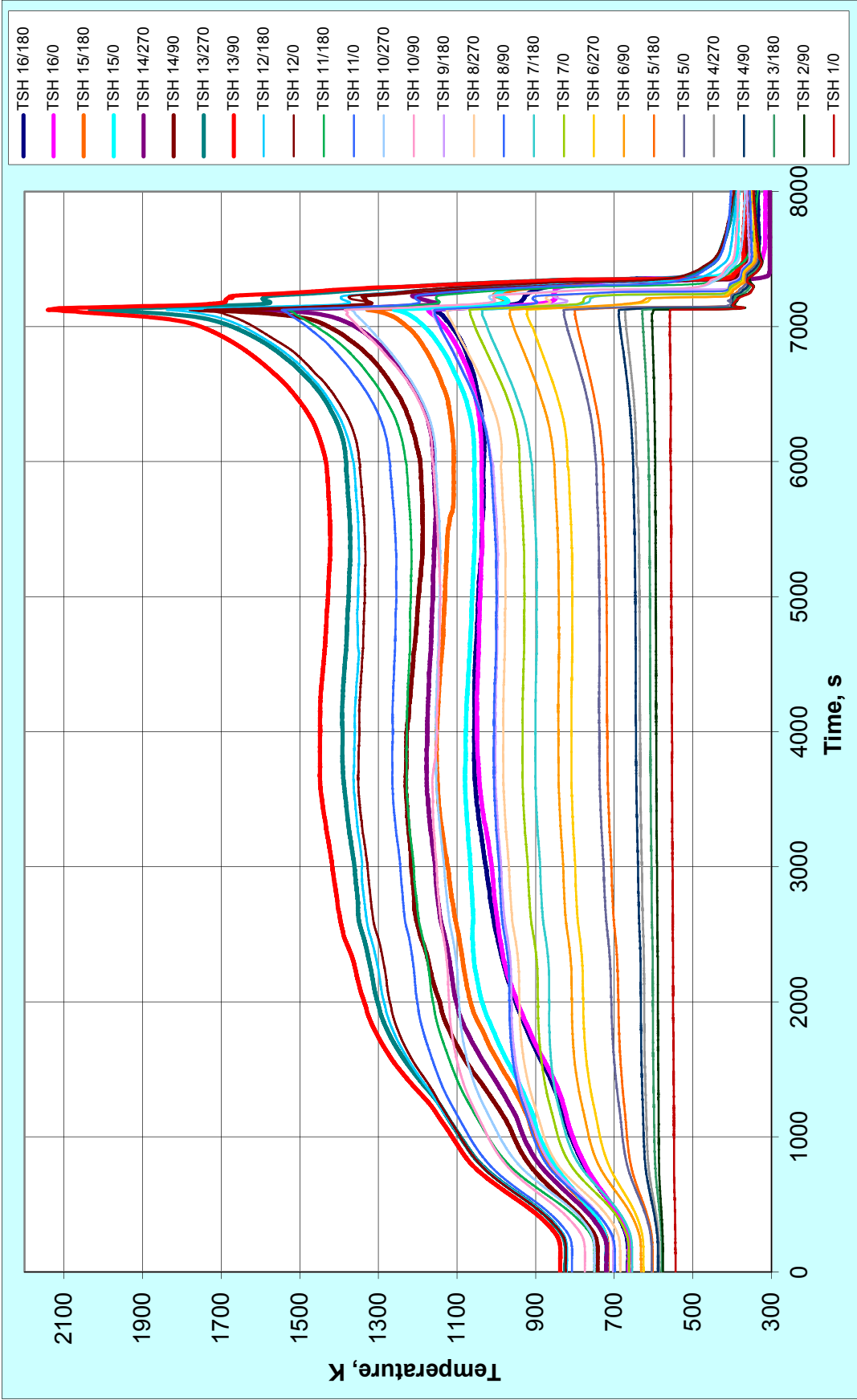


Fig. 23: QUENCH-15; shroud temperatures during test.

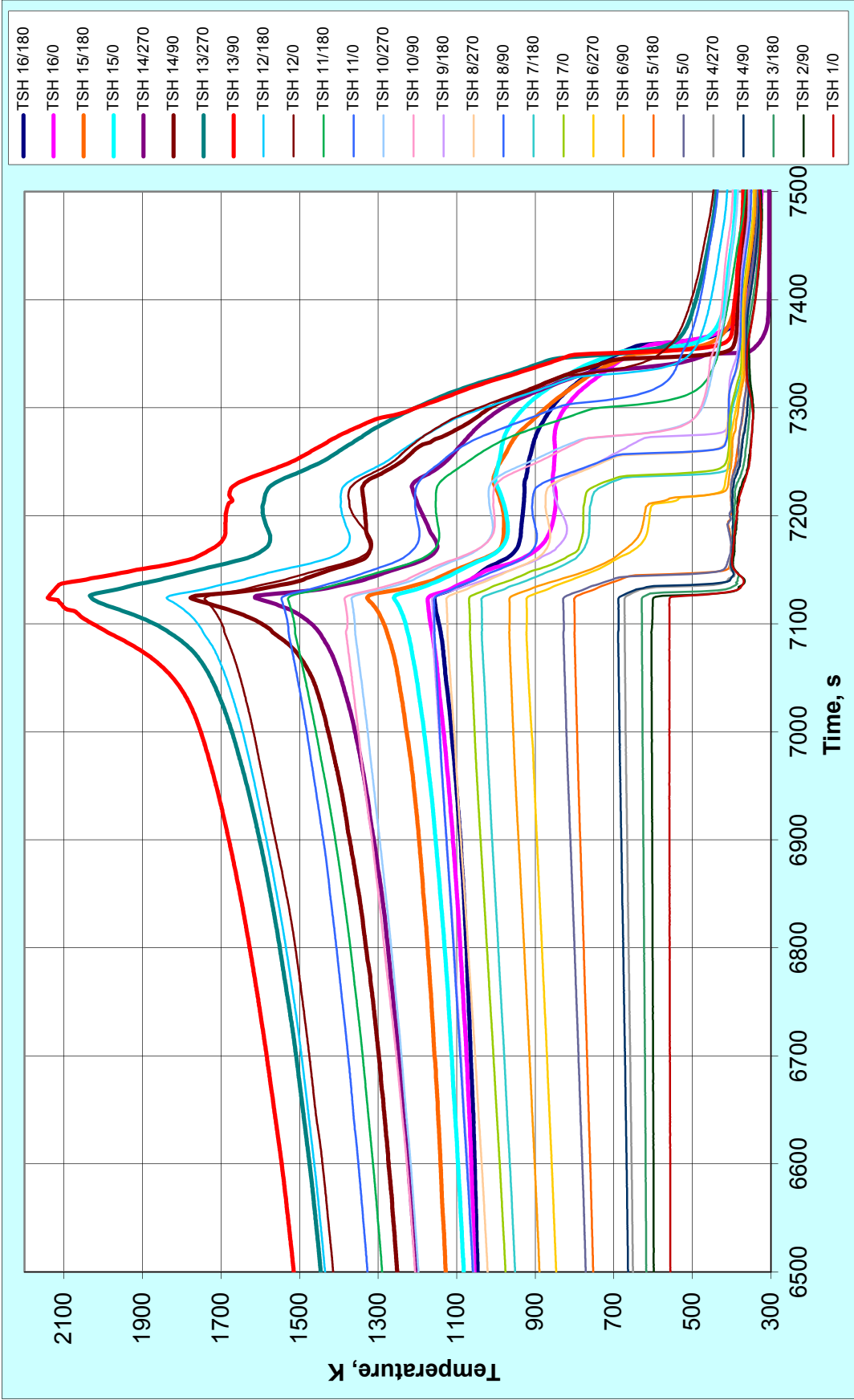


Fig. 24: QUENCH-15; shroud temperatures during second part of transient and flooding.

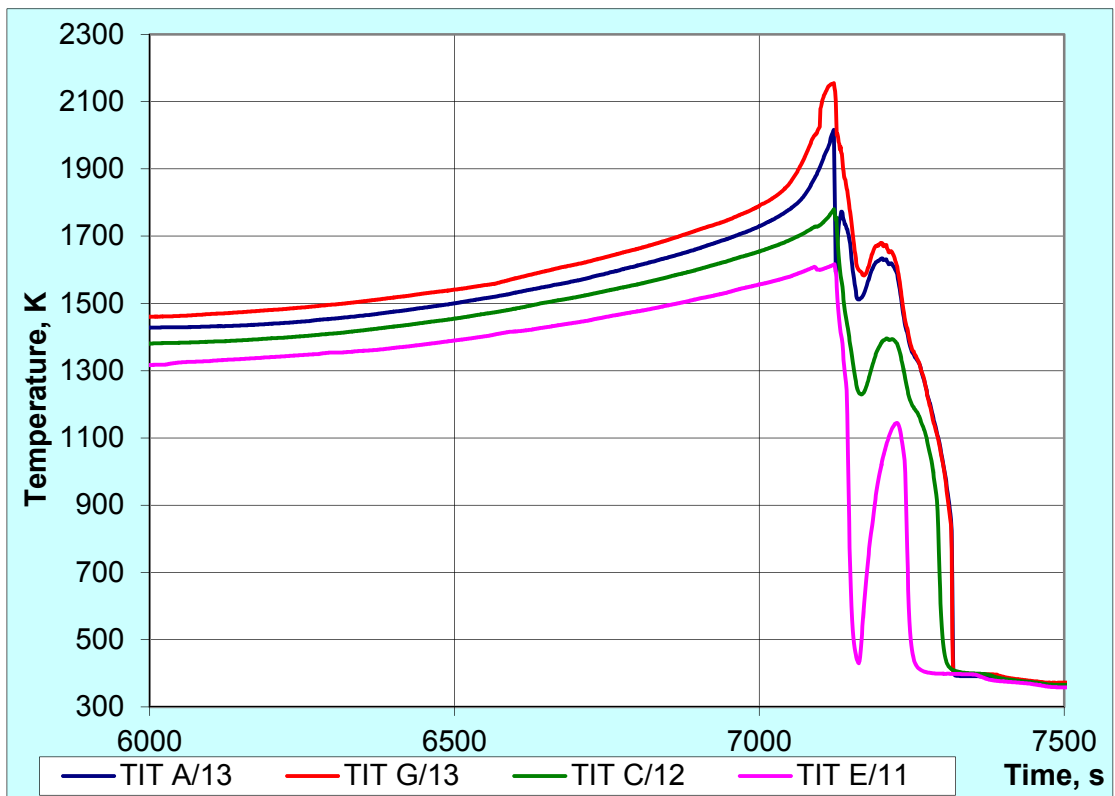
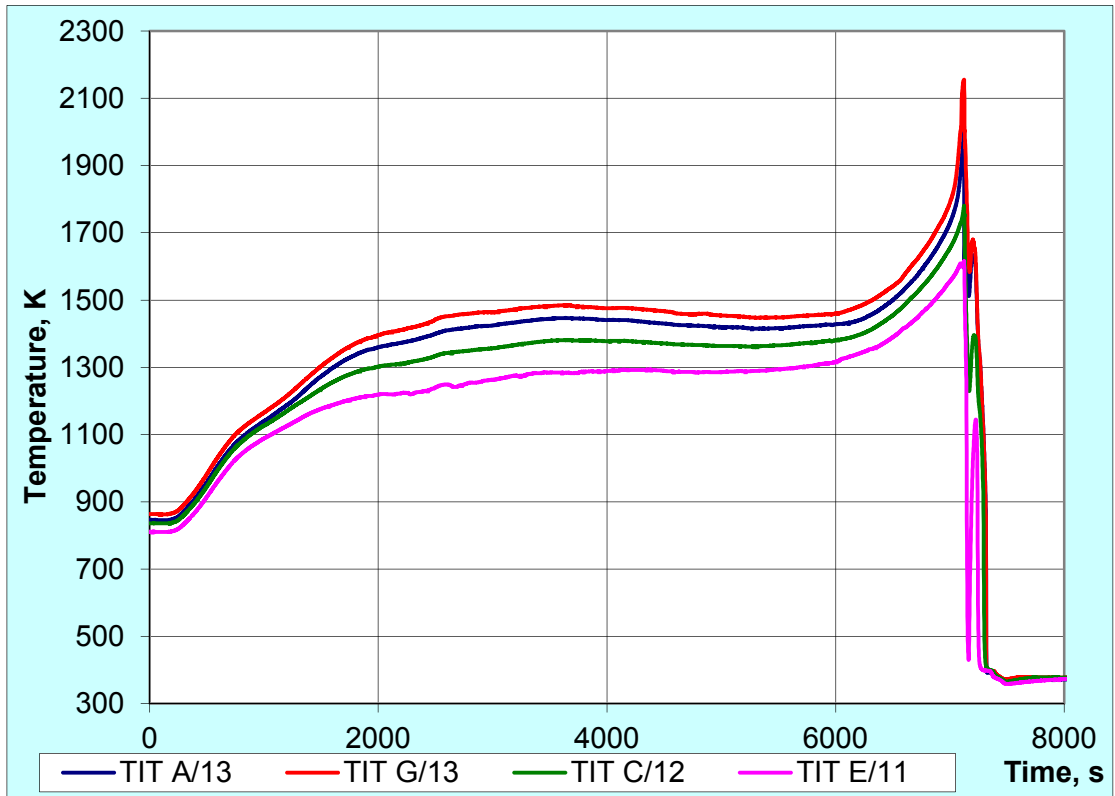


Fig. 25: QUENCH-15; Readings of thermocouples installed inside corner rods. Top: during the test; bottom: during transient and flooding.

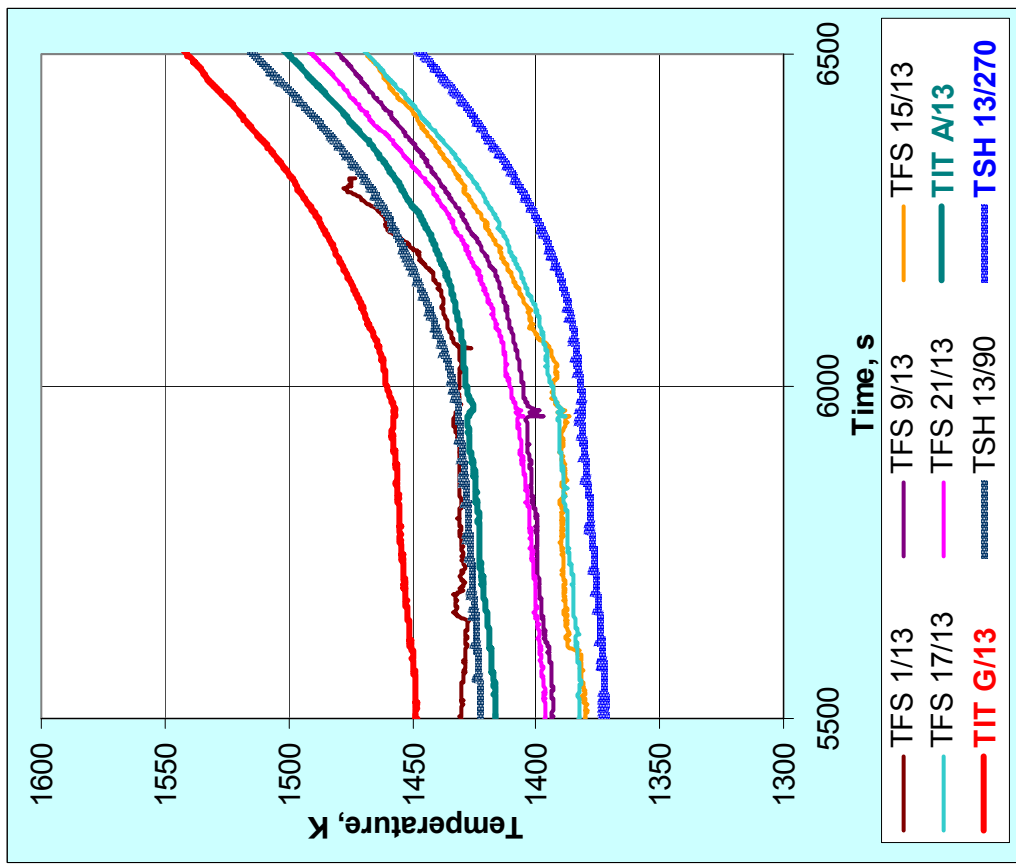
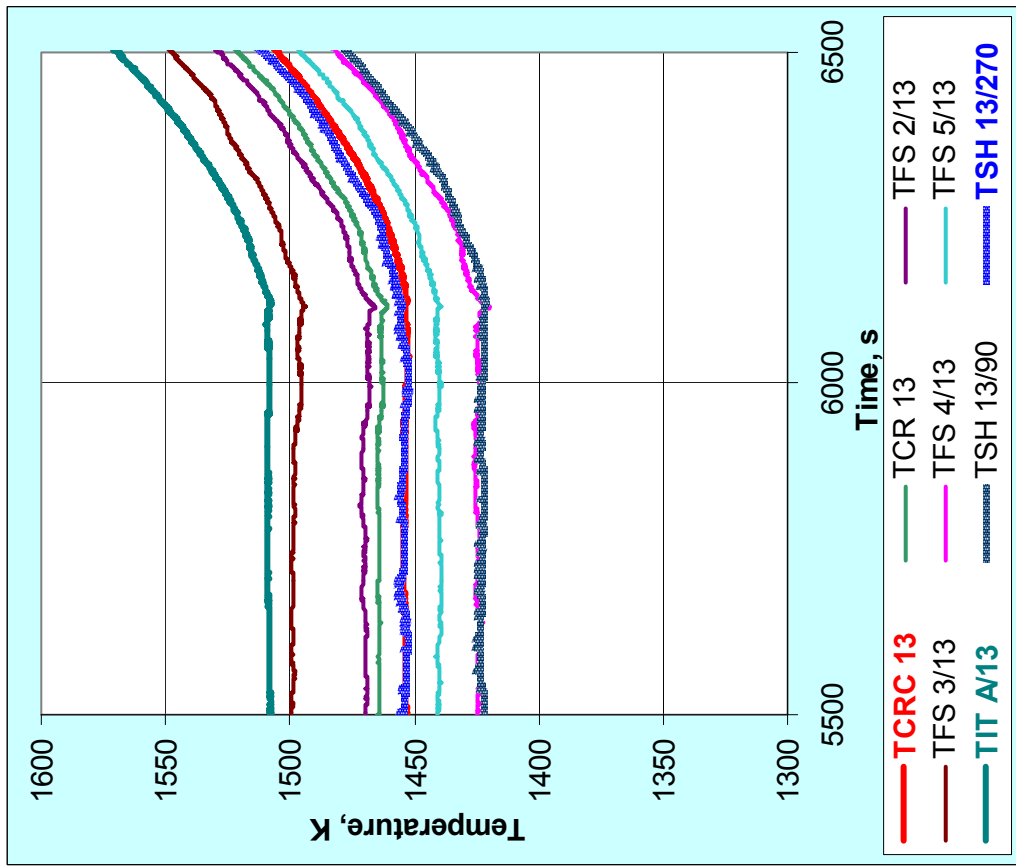
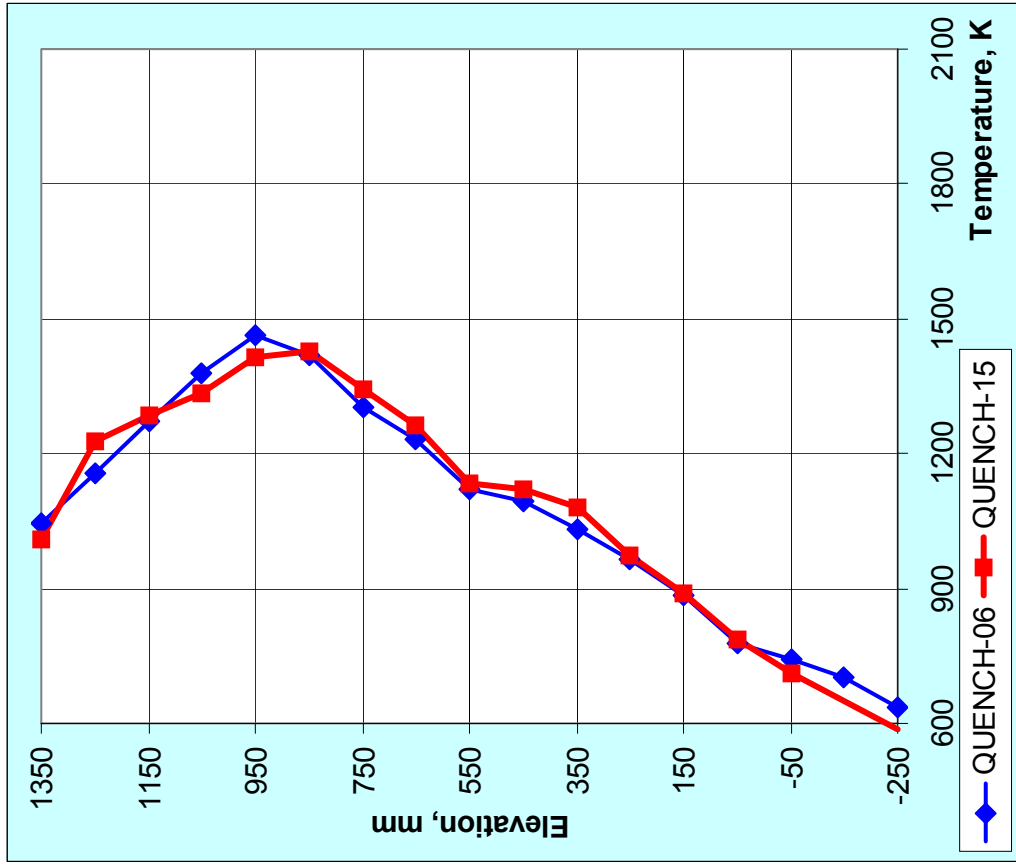
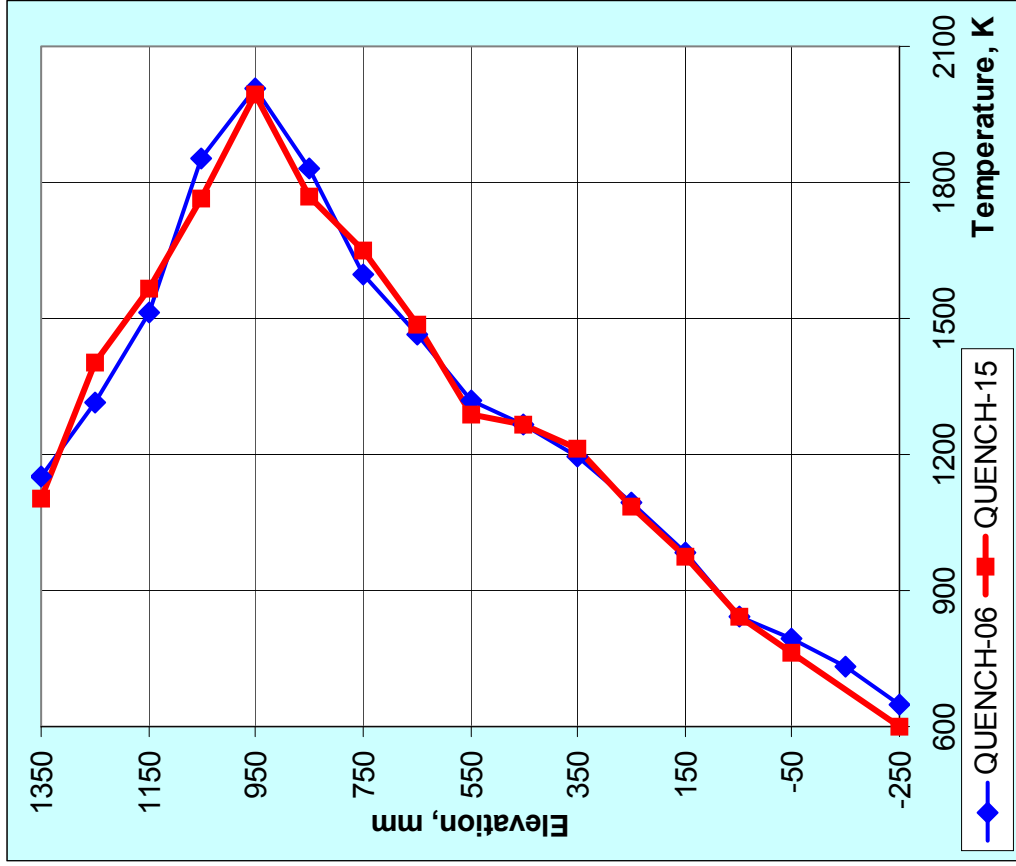


Fig. 26: Comparison of temperature radial scattering at hottest elevation of 950 mm for bundles QUENCH-06 (Zry-4) and QUENCH-15 (ZIRLO) on beginning of transient (~6000 s).



before transient



before reflood

Fig. 27: Comparison of axial bundle temperature profiles (averaged cladding surface TC readings) for QUENCH-06 (Ziy-4), -15 (ZIRLO).

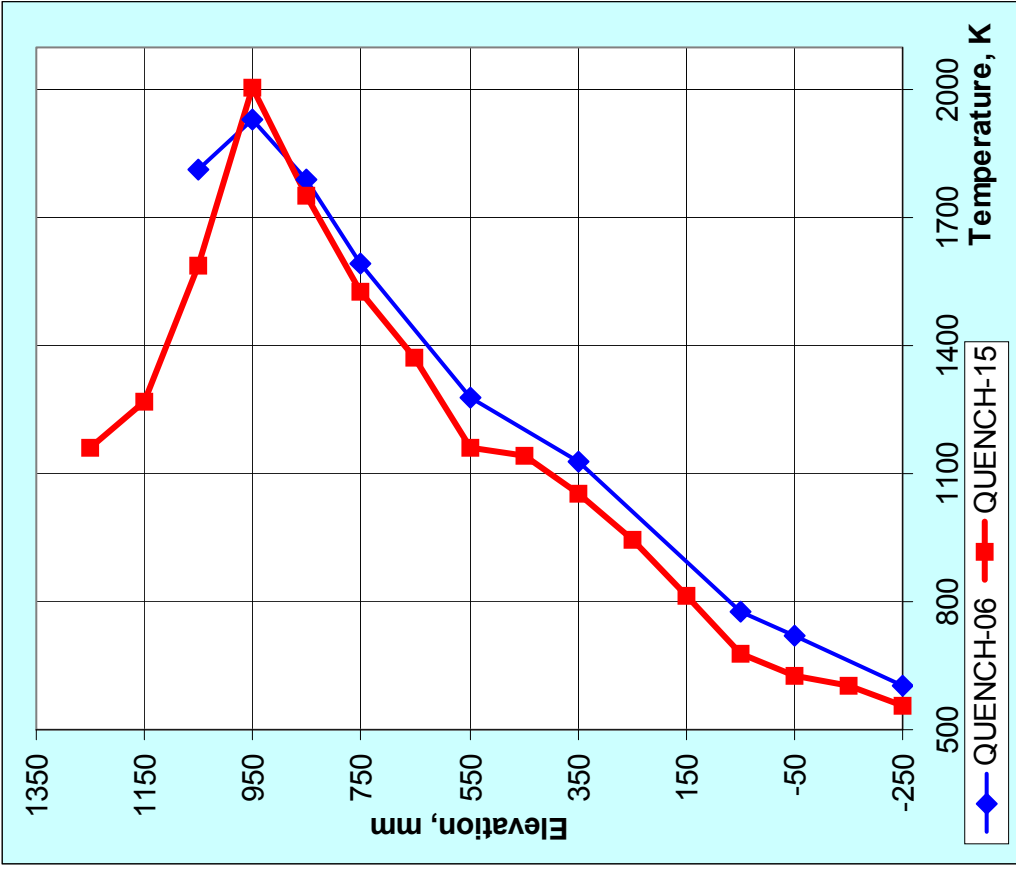
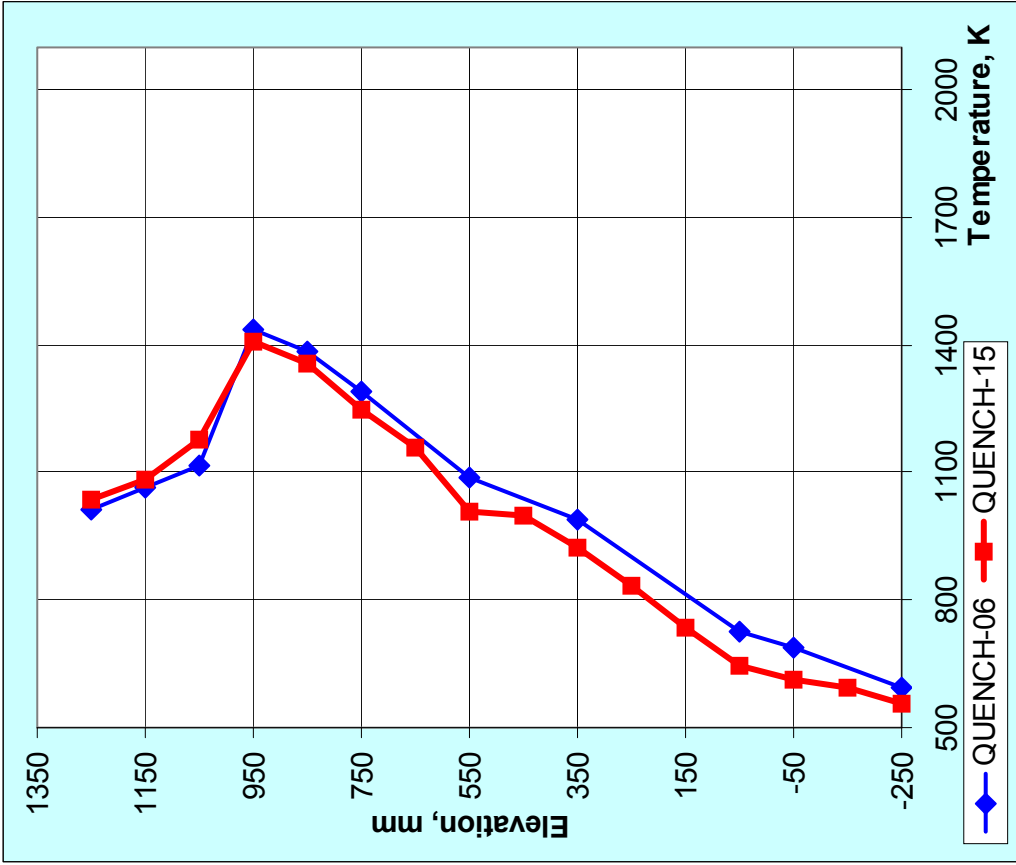


Fig. 28: Comparison of axial shroud temperature profiles (averaged shroud TC readings) for QUENCH-06 (Zry-4) and QUENCH-15 (ZIRLO).

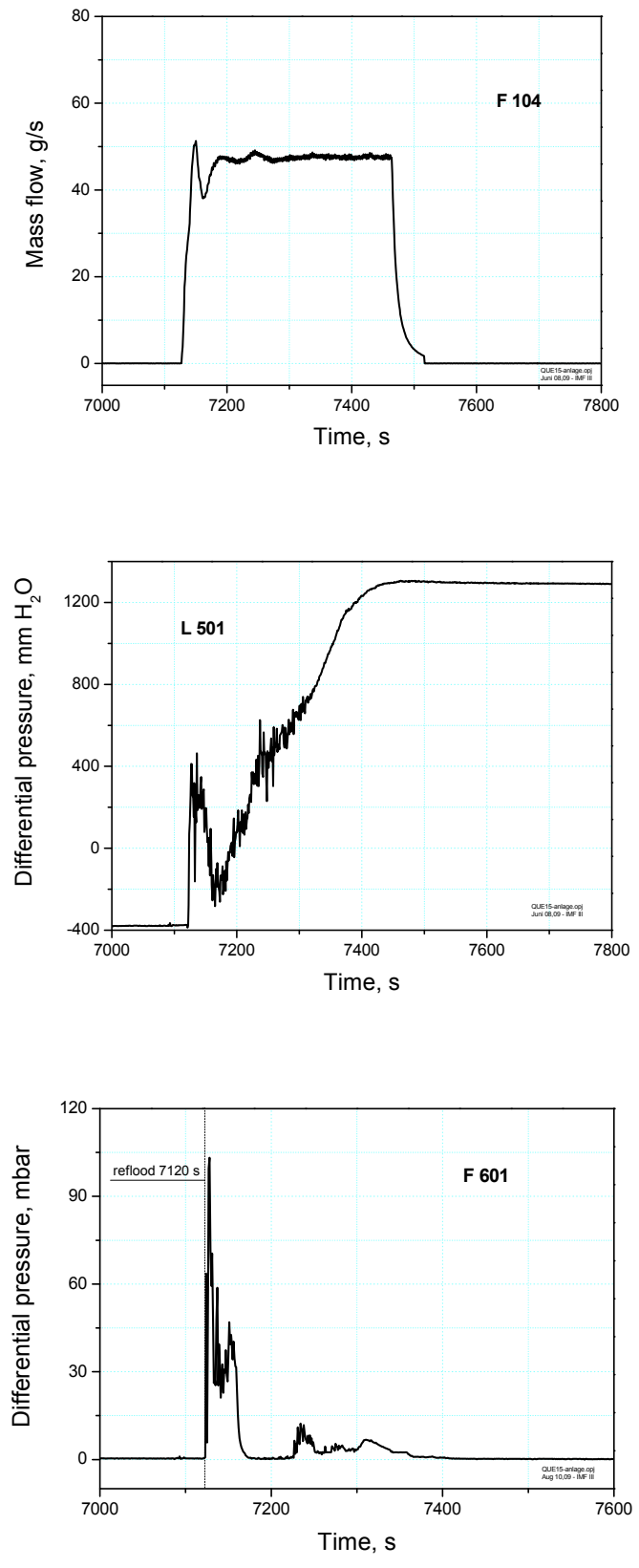


Fig. 29: QUENCH-15; Quench water mass flow rate (F 104), top, measurement of collapsed water level (L 501), center, off-gas flow rate (F 601), bottom.

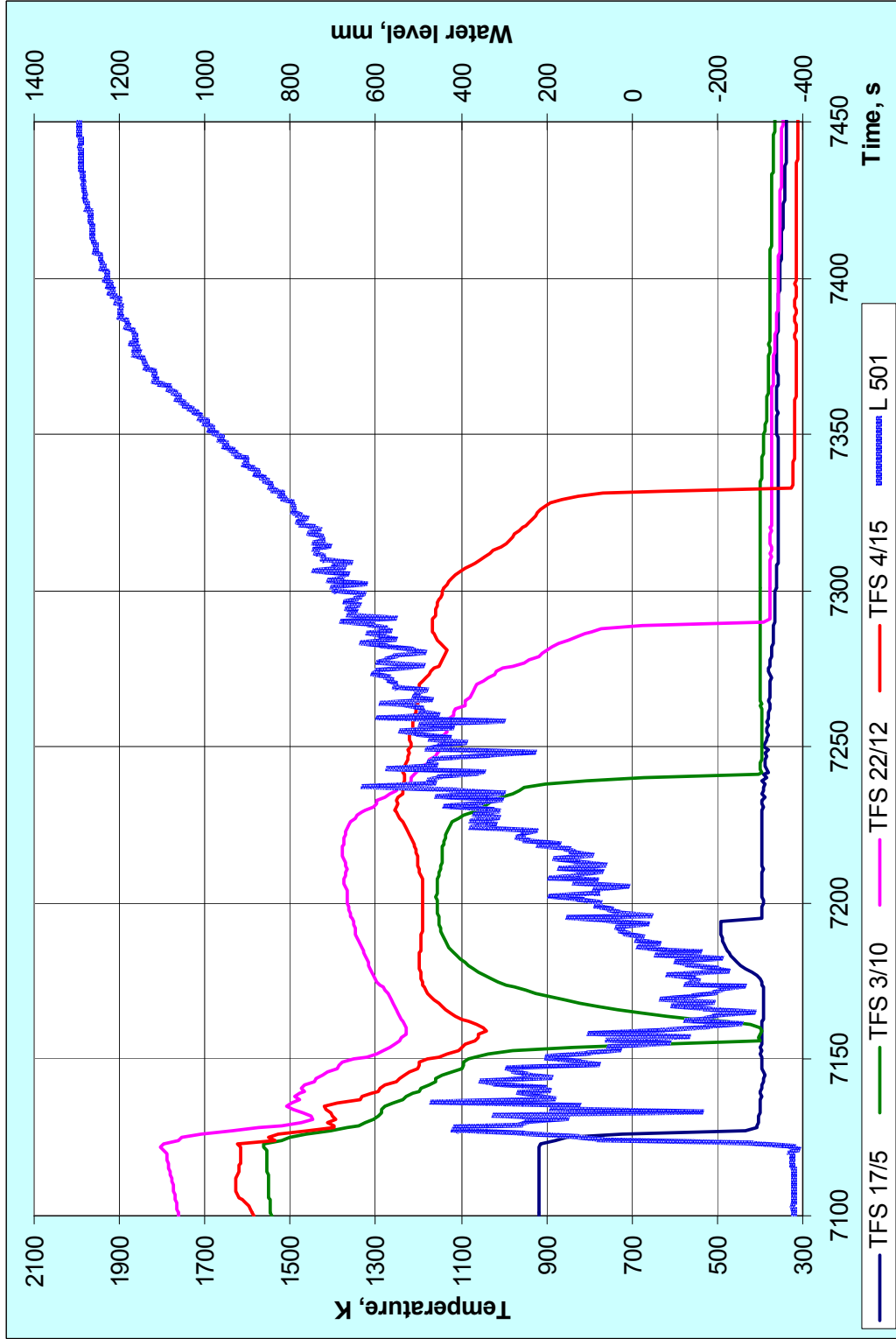


Fig. 30: QUENCH-15; cooling in 2-phase fluid above collapsed water surface during reflood phase.

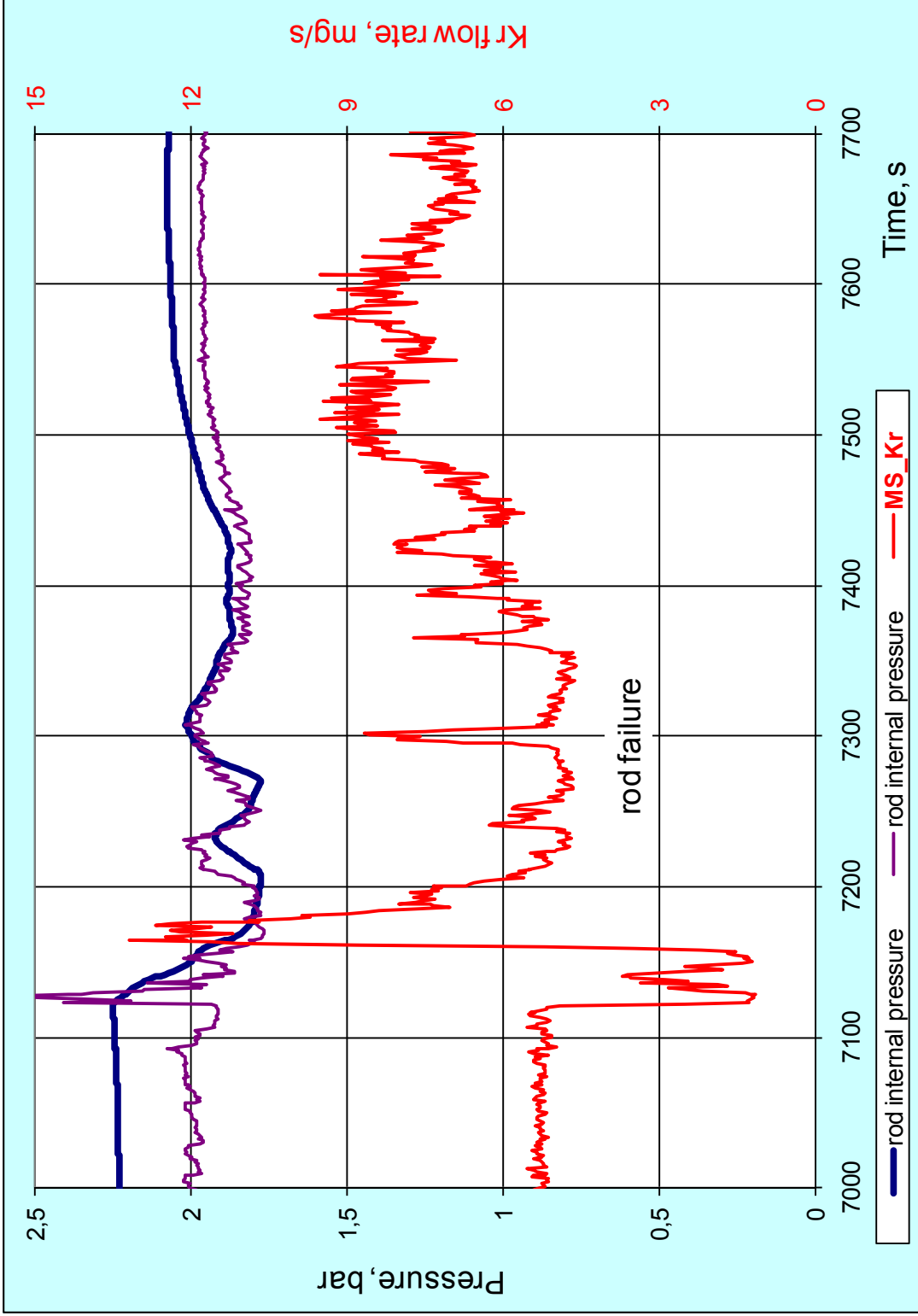
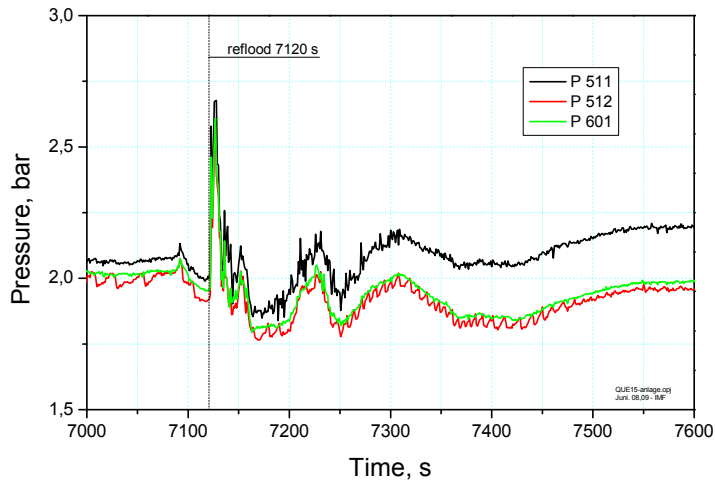
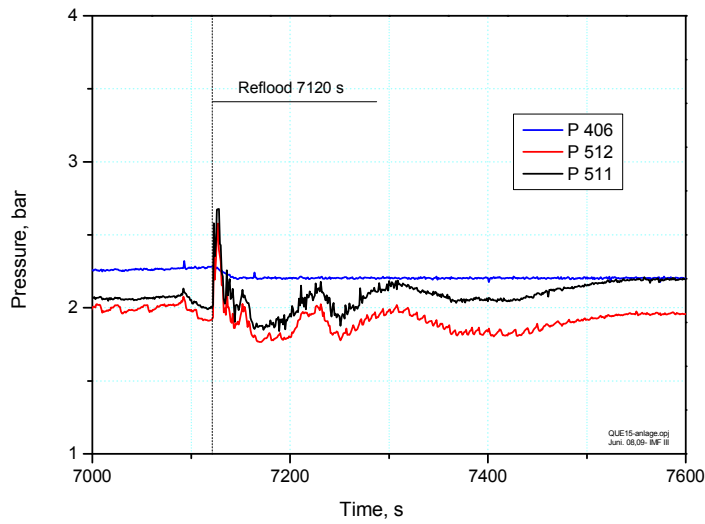


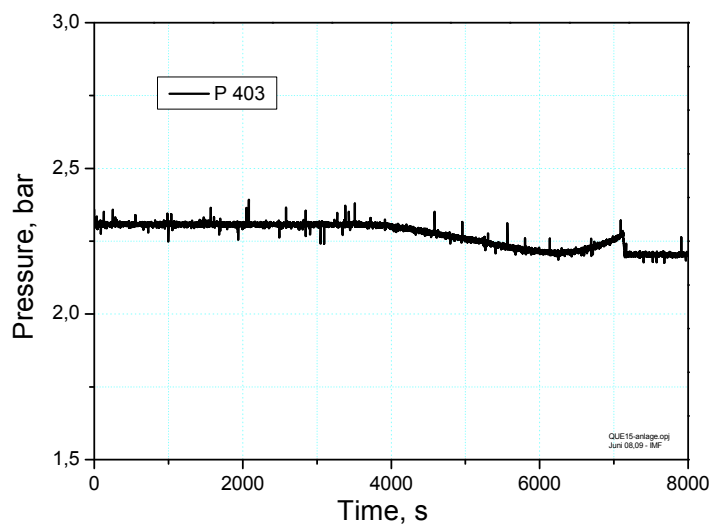
Fig. 31: QUENCH-15; indication of rod simulator failures on the basis of Kr release.



System pressure measured at test section inlet P 511, at outlet P 512, and in the off-gas pipe P 601.

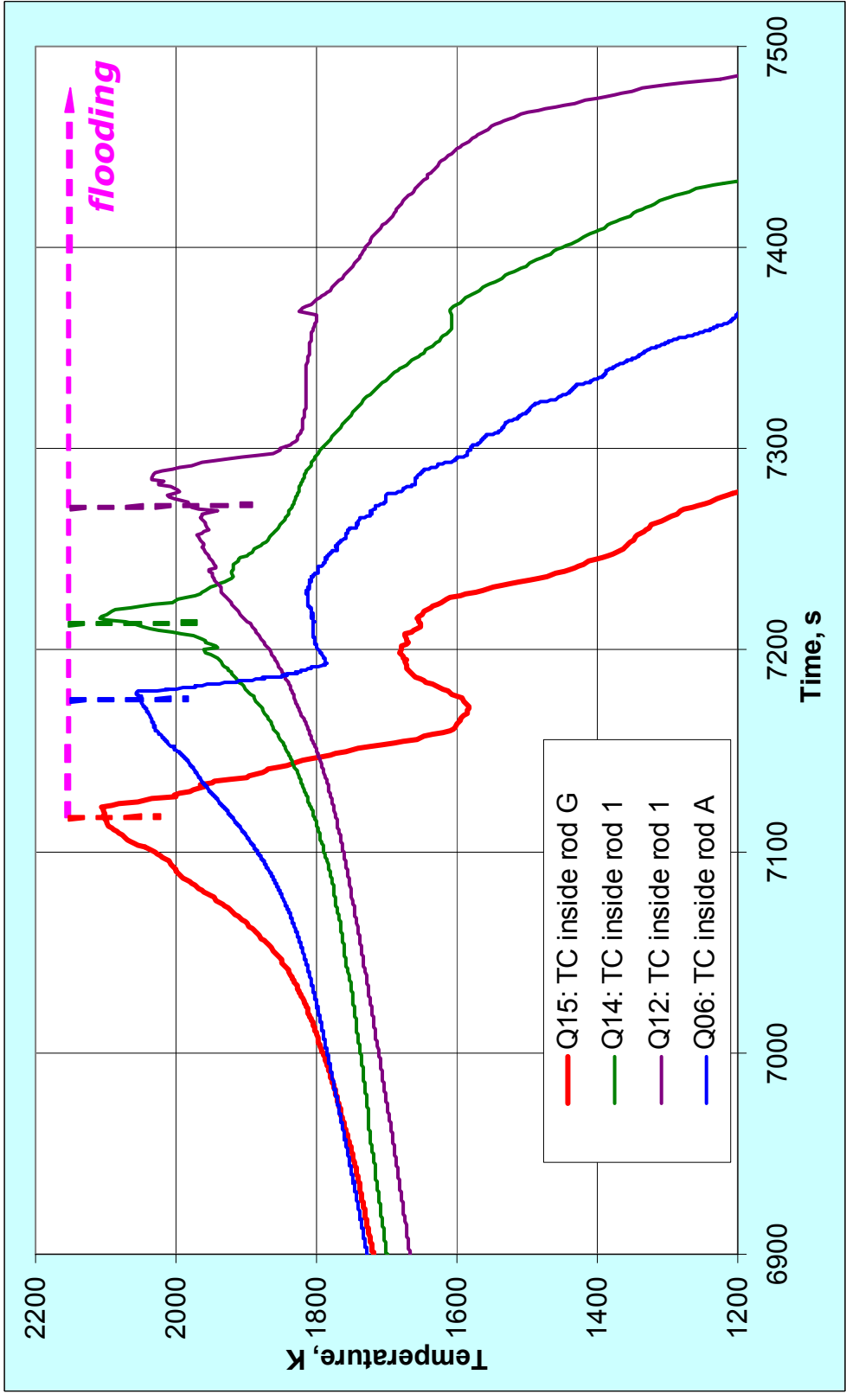


Argon pressure measured at shroud insulation P 406, together with system pressure at the test section inlet P 511 and outlet P 512 (the constant pressure P 406 indicates that there was no shroud failure).



Argon coolant pressure of the cooling jacket P 403 demonstrates tightness of the inner cooling jacket.

Fig. 32: QUENCH-15; Argon and system pressure.



common characteristics: similar temperature escalation at the end of transient
and similar cooling duration after reflood initiation

Fig. 33: Comparison of bundle peak temperature evolution for QUENCH-06 (Zry-4), QUENCH-12 (E110), QUENCH-14 (M5) and QUENCH-15 (ZIRLO).

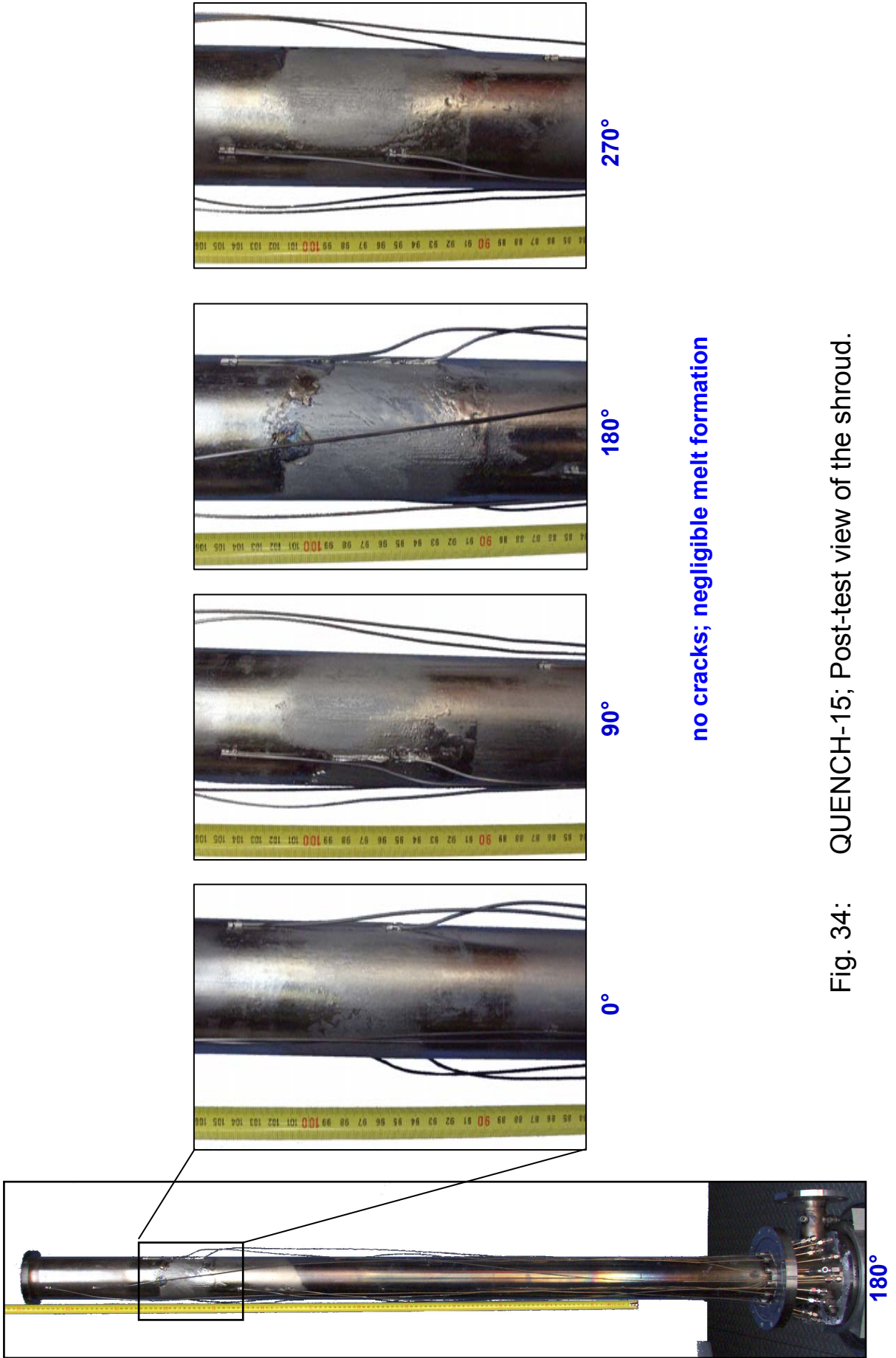


Fig. 34: QUENCH-15; Post-test view of the shroud.



Fig. 35: QUENCH-15; Appearance of withdrawn corner rods B, D, F, H – solid rods; A, C, E, G – tube at lower part (up to TIT position) and solid rod at upper part.

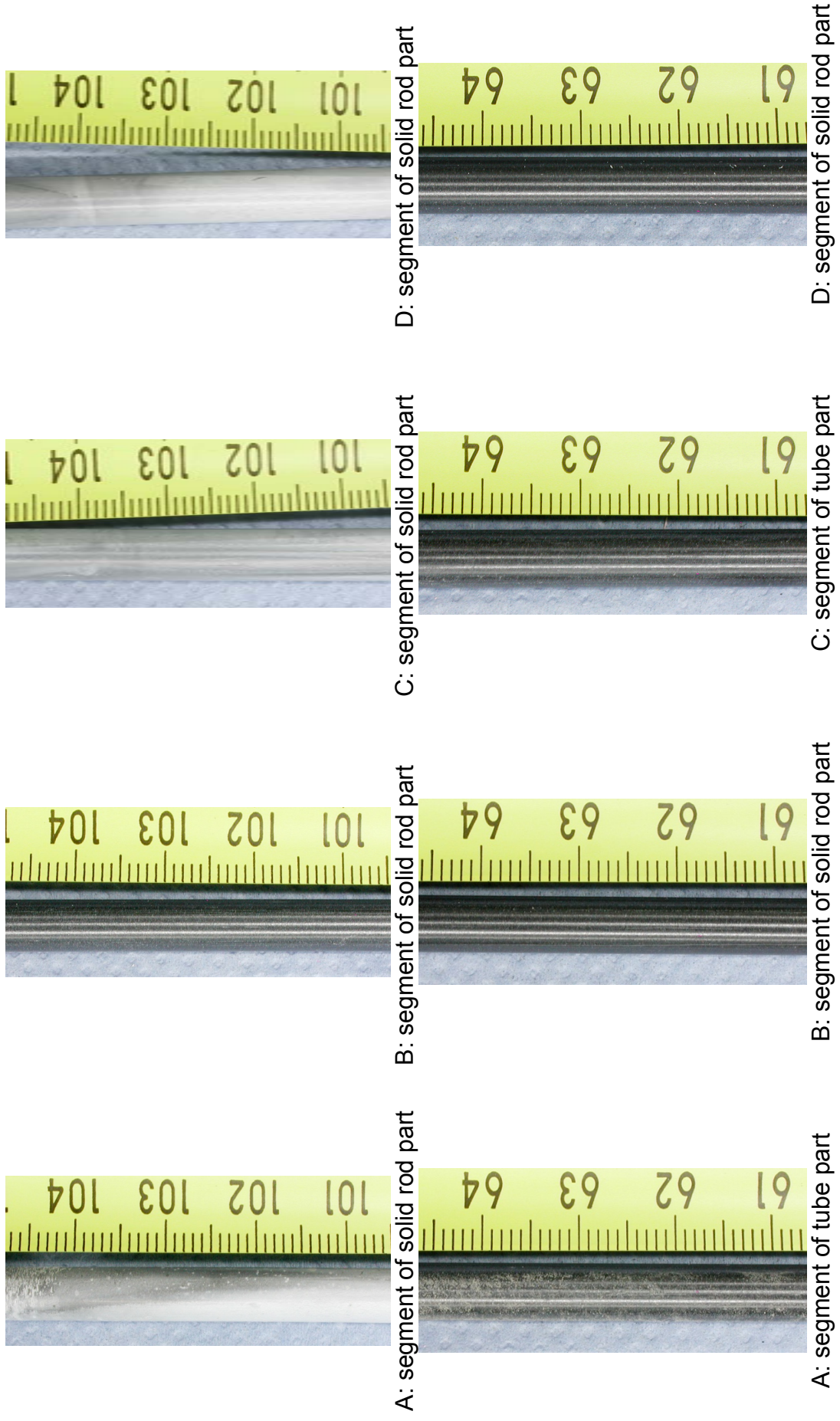


Fig. 36: QUENCH-15; Segments of Zircaloy-4 corner rods B (withdrawn before transient) and A, C, D (withdrawn after test).

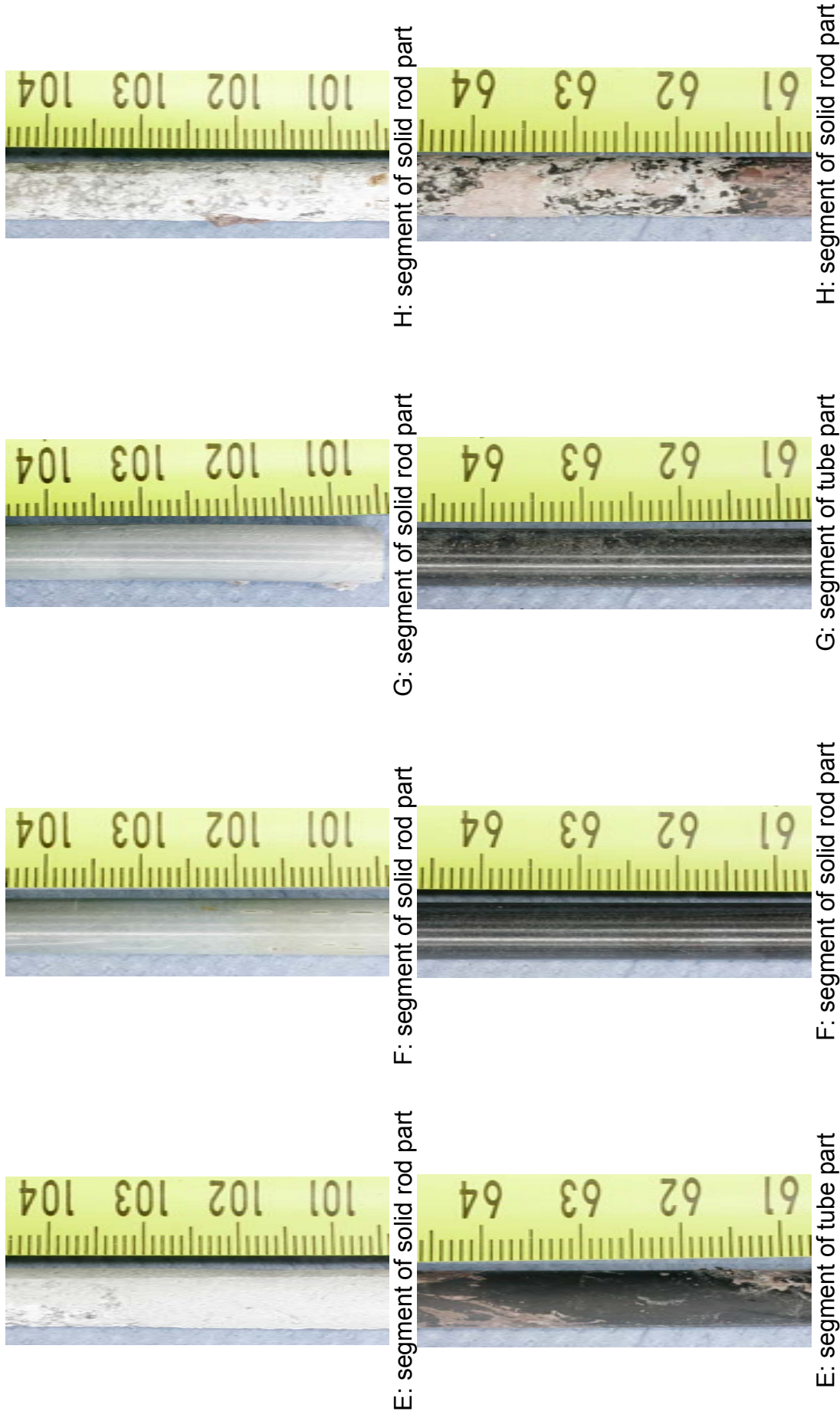


Fig. 37: QUENCH-15; Segments of corner rods F (Zry-4, withdrawn before transient), E and H (E110, withdrawn after test), G (Zry-4, withdrawn after test).

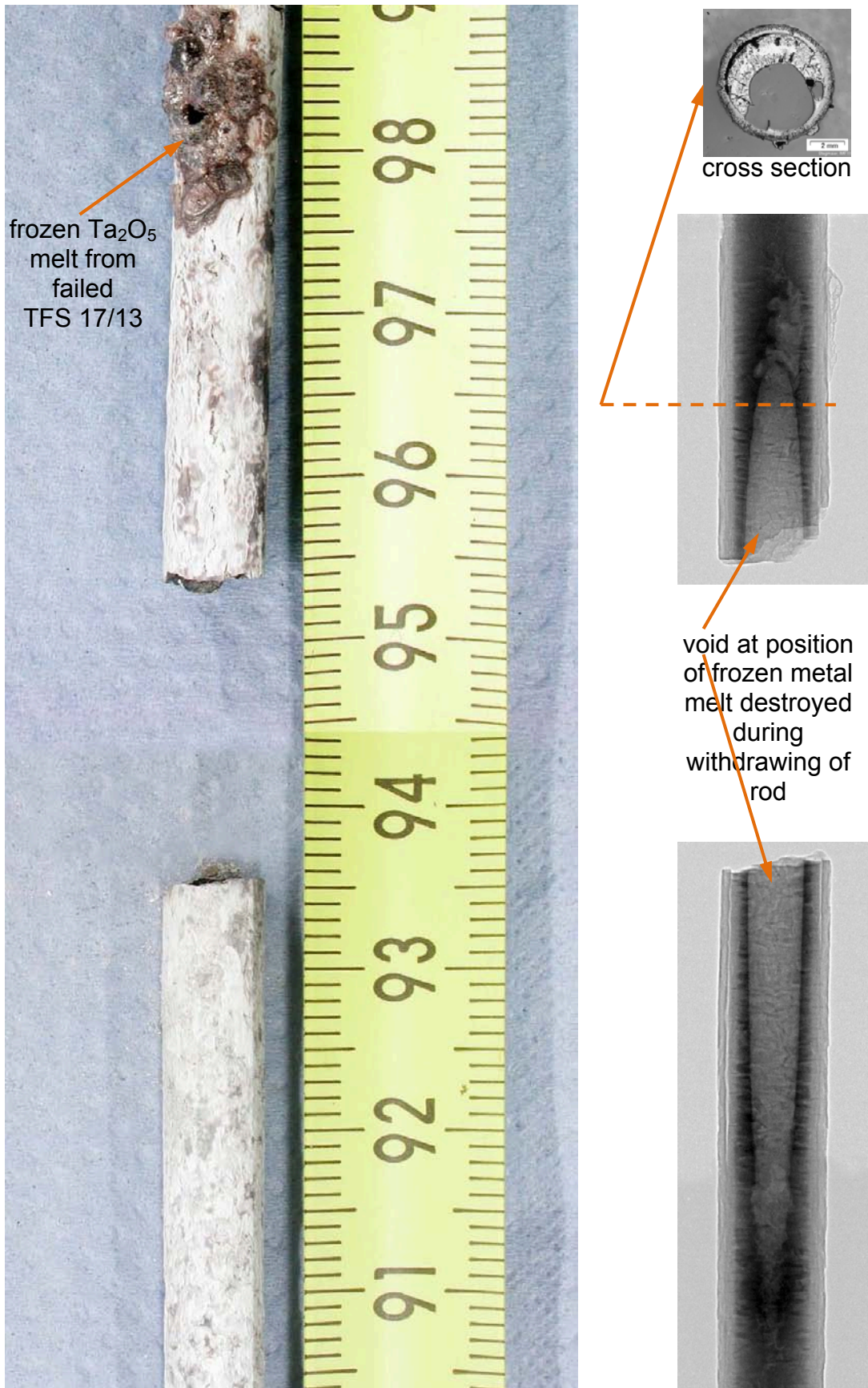


Fig. 38: QUENCH-15; position of molten metal segments of originally solid corner rod H: optical view (left), neutron radiography (right) and metallography (top right).

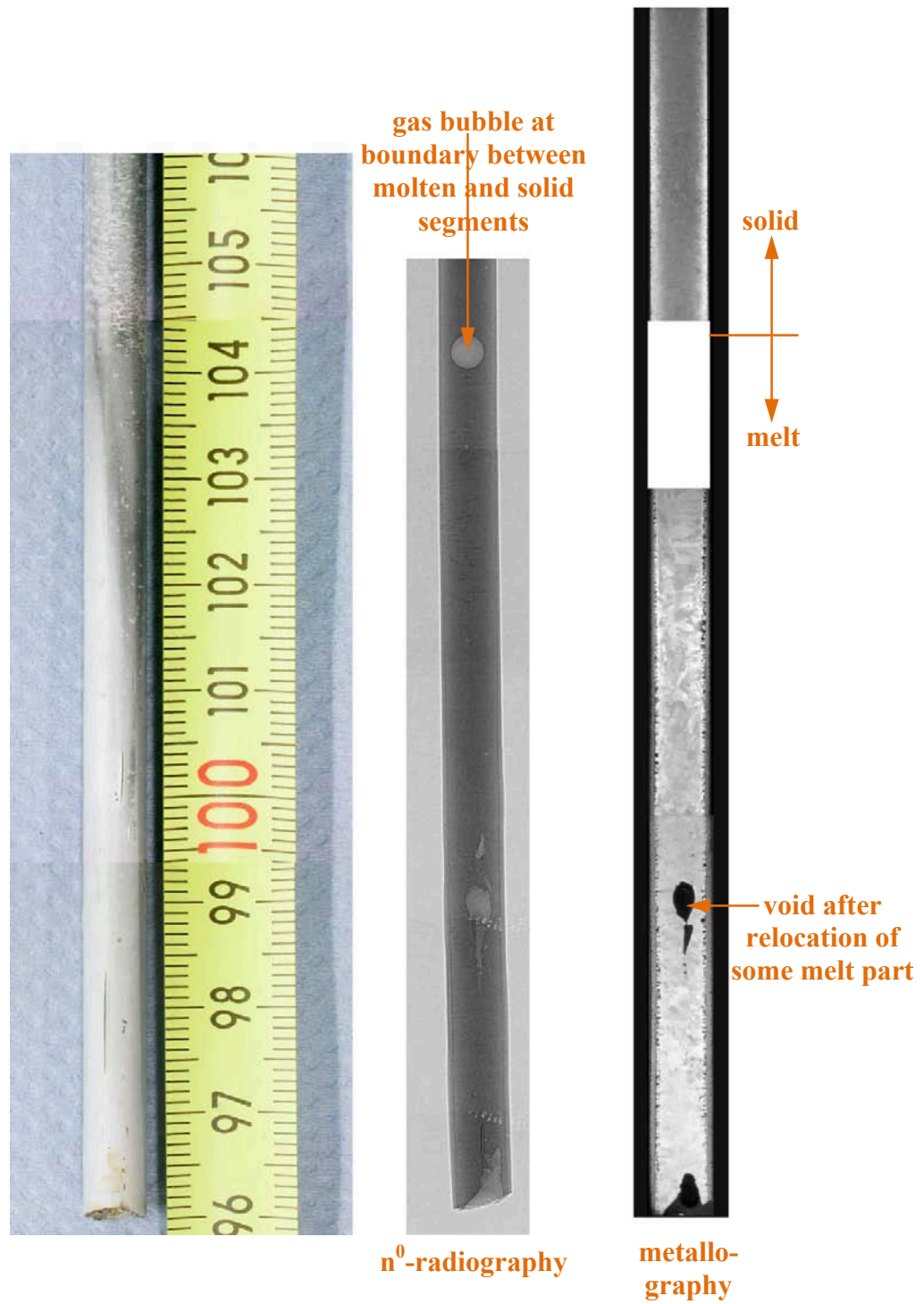


Fig. 39: QUENCH-15; Upper part of corner rod A: transition between molten and solid β -Zr.

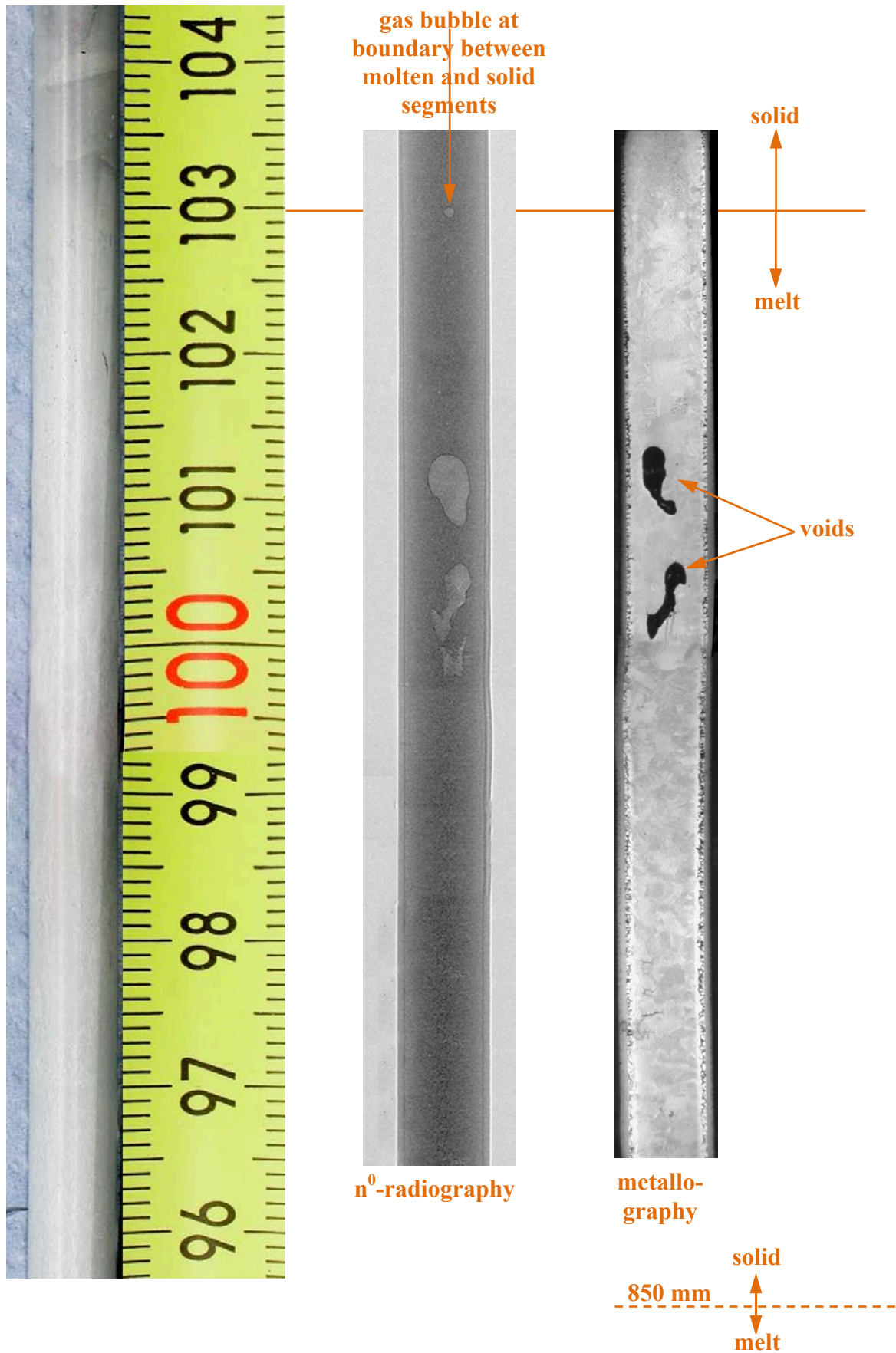


Fig. 40: QUENCH-15; Upper part of corner rod D.

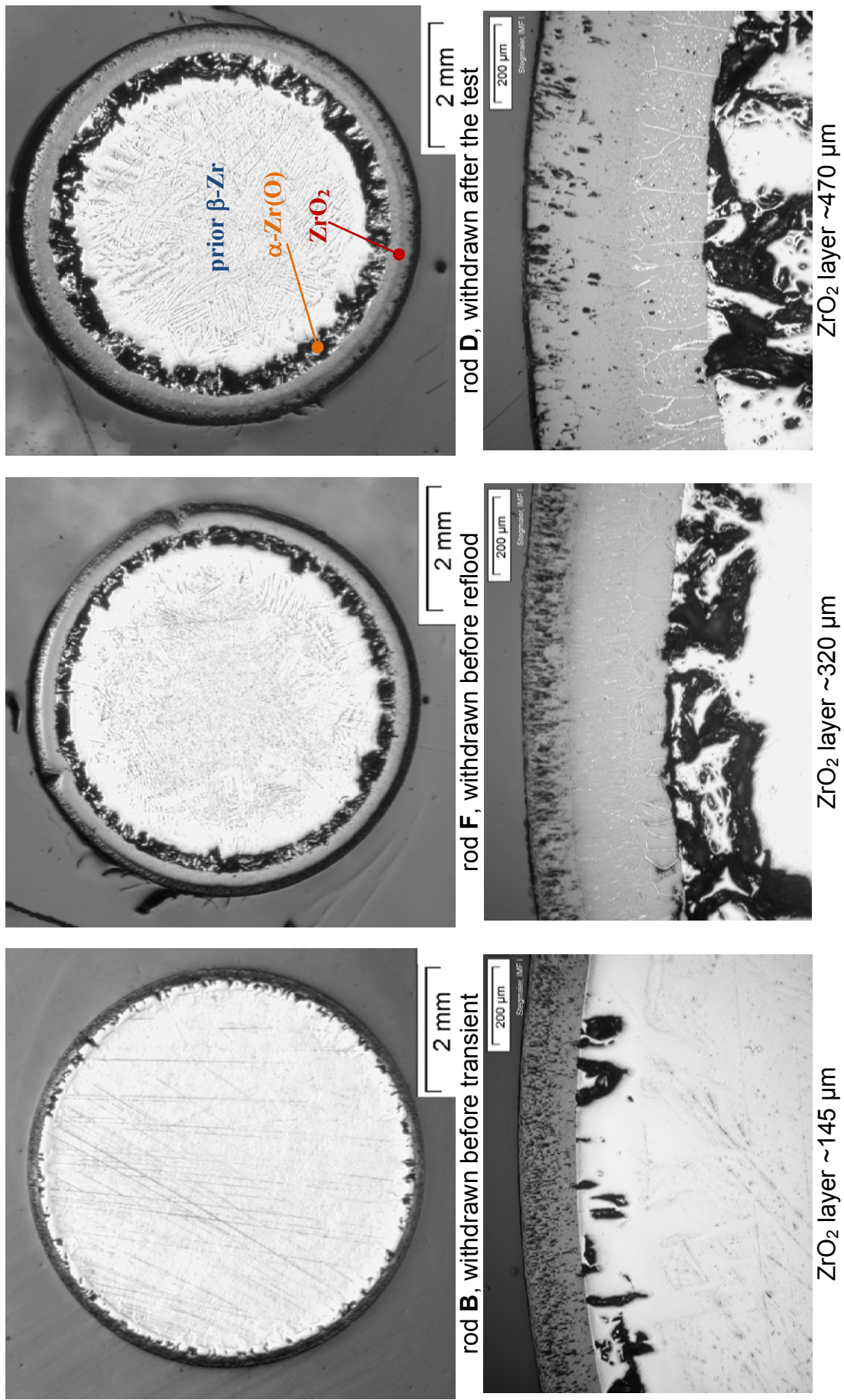


Fig. 41: QUENCH-15; Elevation 950 mm: cross-sections of the Zircaloy-4 solid corner rods B, F and D withdrawn at different test stages.

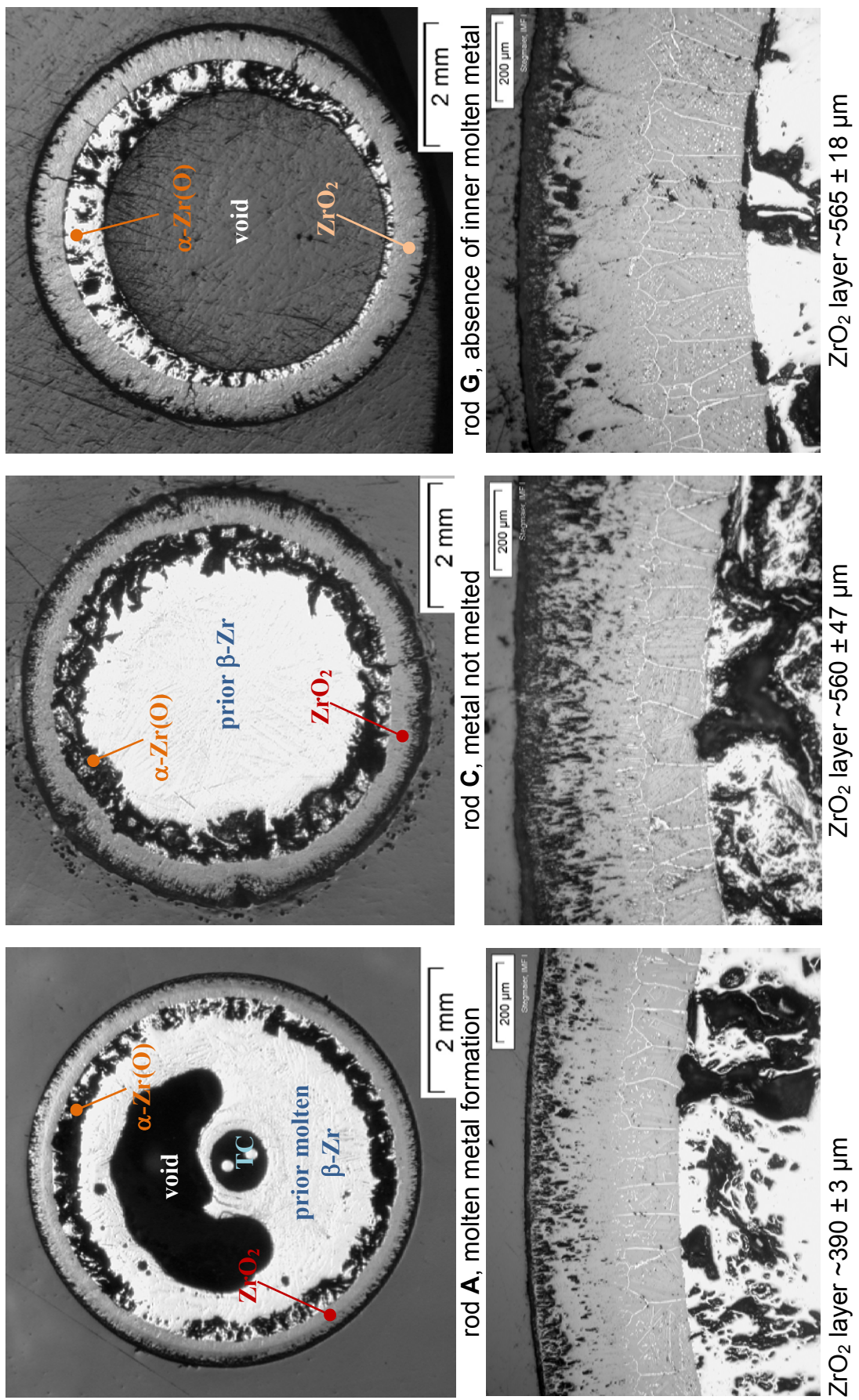


Fig. 42: QUENCH-15; Elevation 950 mm: cross-sections of the Zircaloy-4 instrumented corner rods A, C and G withdrawn after the test.

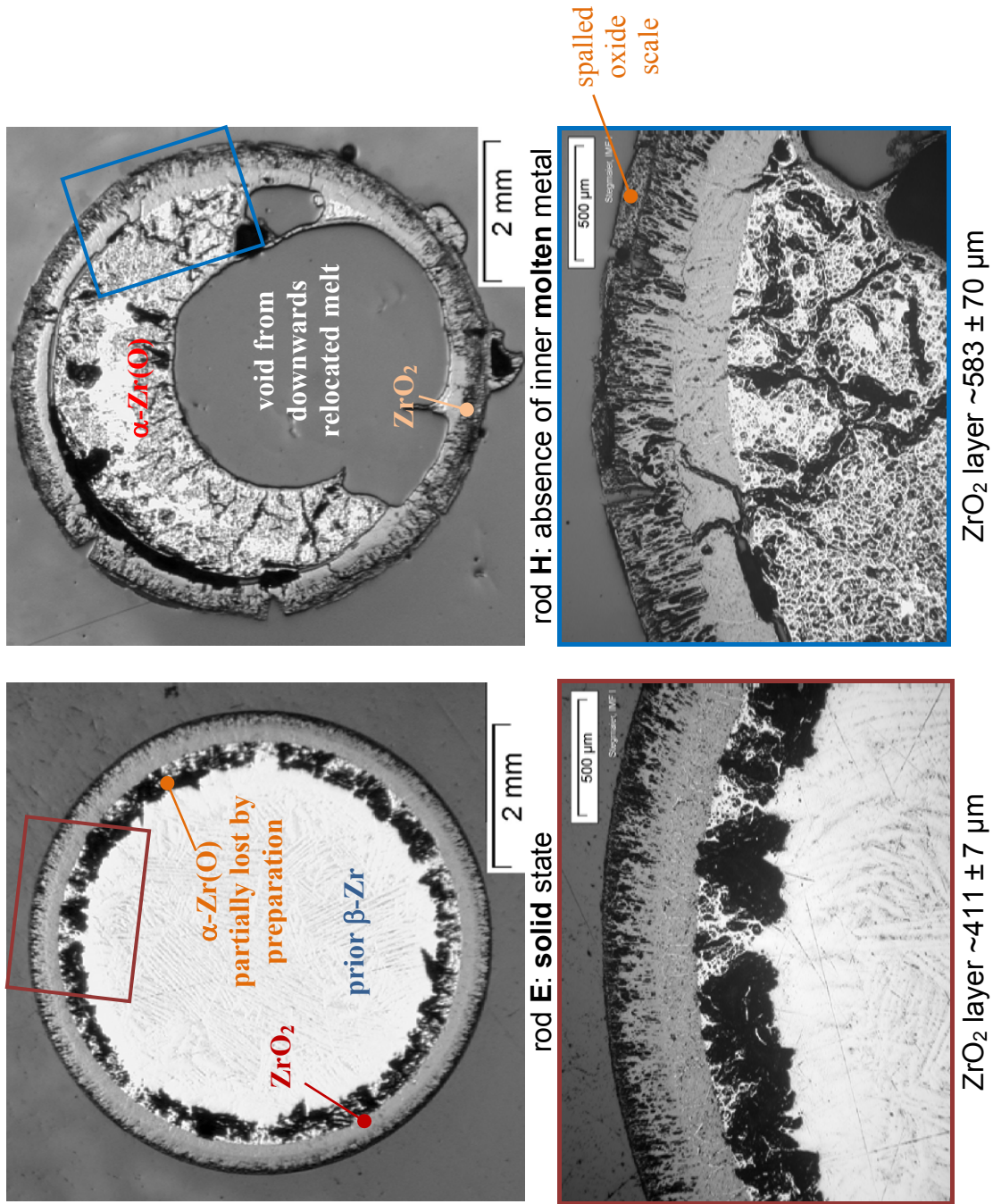


Fig. 43: QUENCH-15; Elevation 950 mm: cross-sections of the E110 corner rods E and H withdrawn after the test. Influence of bundle circumferential temperature difference.

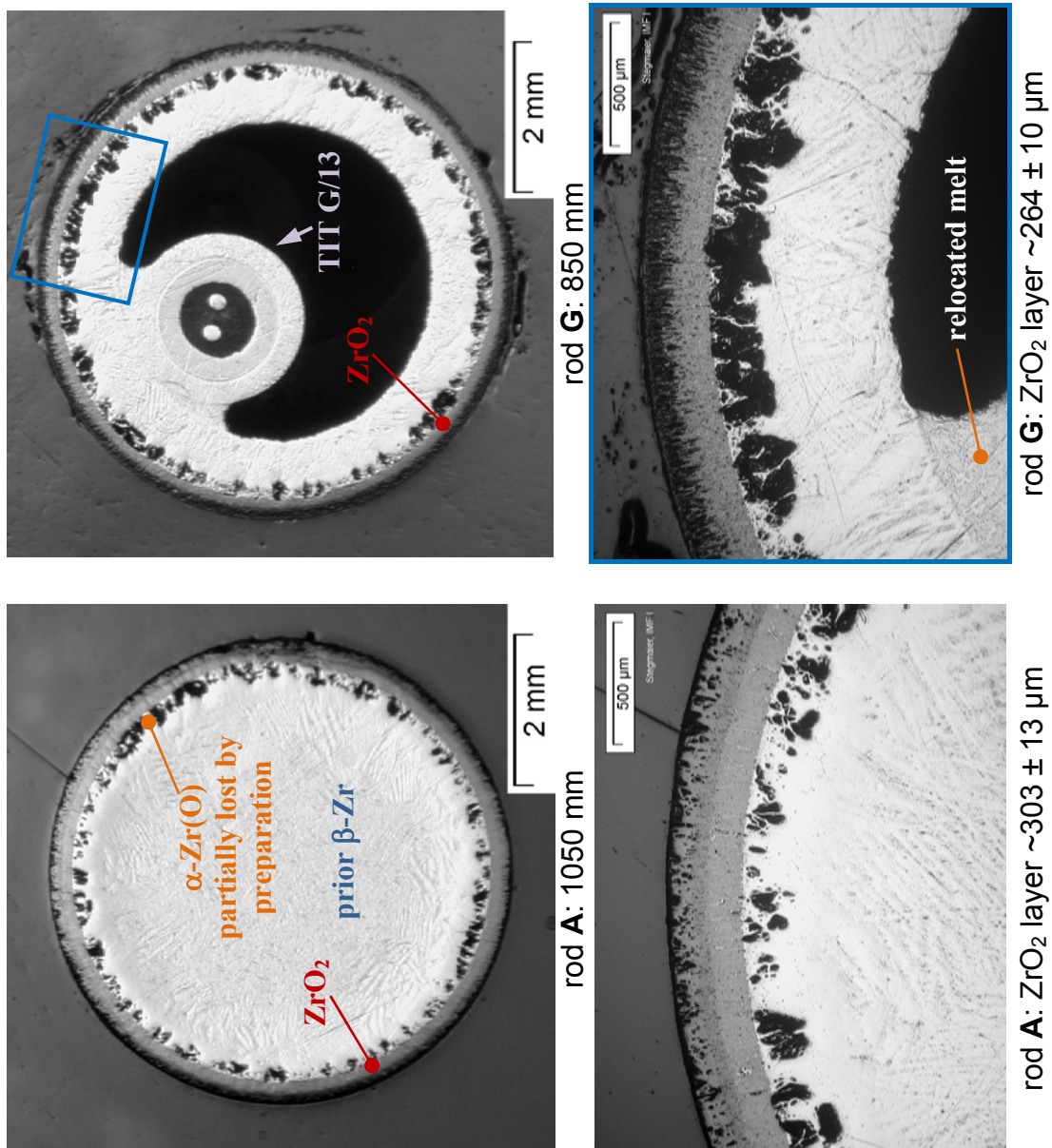
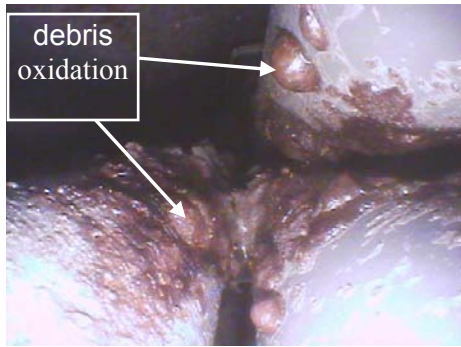


Fig. 44: QUENCH-15; Elevations lower (850 mm) and upper (1050 mm) of hottest elevation: cross-sections of the Zircaloy-4 corner rods A and G withdrawn after the test.



1000 mm, melt at location of destroyed grid spacer 4; deposits from destroyed TC



1030 mm, parts of destroyed grid spacer 4



930 mm, spalling of thin oxide scales



950 mm, circumferential cracks and negligible oxide spalling



700 mm, relocated part of grid spacer 4



900 mm, circumferential and longitudinal cracks of the fuel rod cladding



100 mm, top part of broken corner rod A, relocated and supported by grid spacer 2

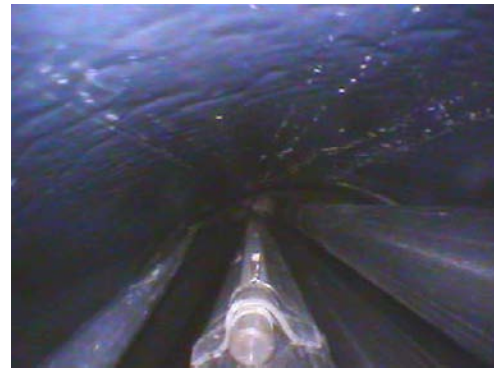


450 mm, top of corner rod A, relocated

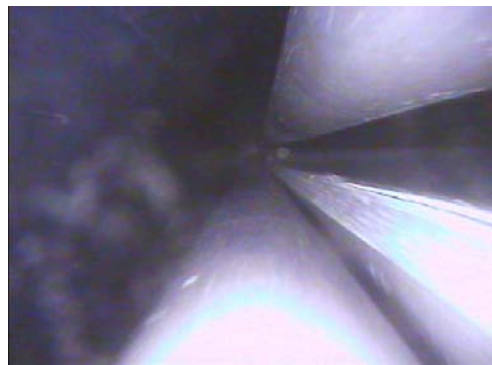
Fig. 45: QUENCH-15; Videoscope photos at the (partly empty) location of corner rod A, view from bottom, camera was moved along heated rod 6 and between rods 7 and 18.



1150 mm, oxidised cap of TFS 9/15



1150 mm, intact TFS 12/15



1050 mm, TFS 9/13 longitudinal crack



1070 mm, damaged TFS 14/14



950 mm, destroyed TFS 9/13



1000 mm, TFS 9/13 damaged sheathes



850 mm, intact TFS 22/12



900 mm, traces of Ta_2O_5 (with WO_3 traces) from destroyed TFS 9/13

Fig. 46: QUENCH-15; Videoscope photos taken at empty positions of the corner rods, exhibiting the status of different high-temperature W/Re thermocouples.

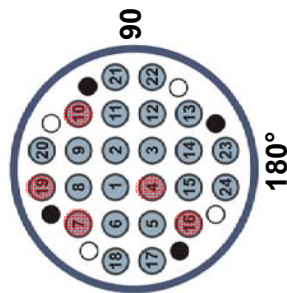
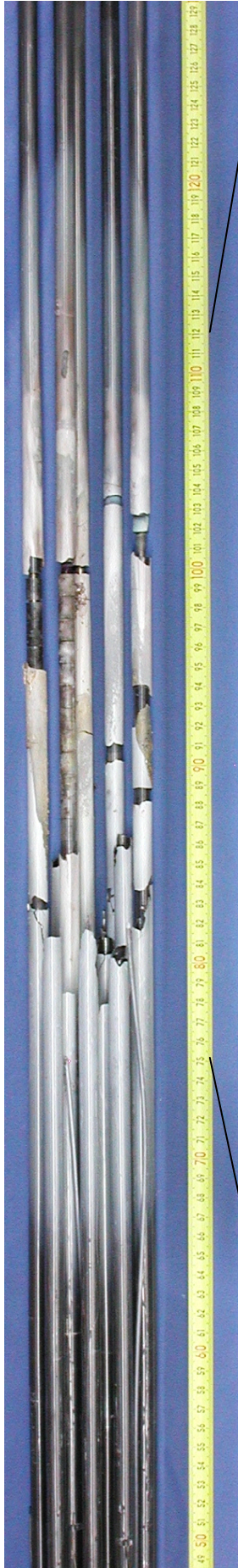


Fig. 47: QUENCH-15; bundle remnant after dismounting.

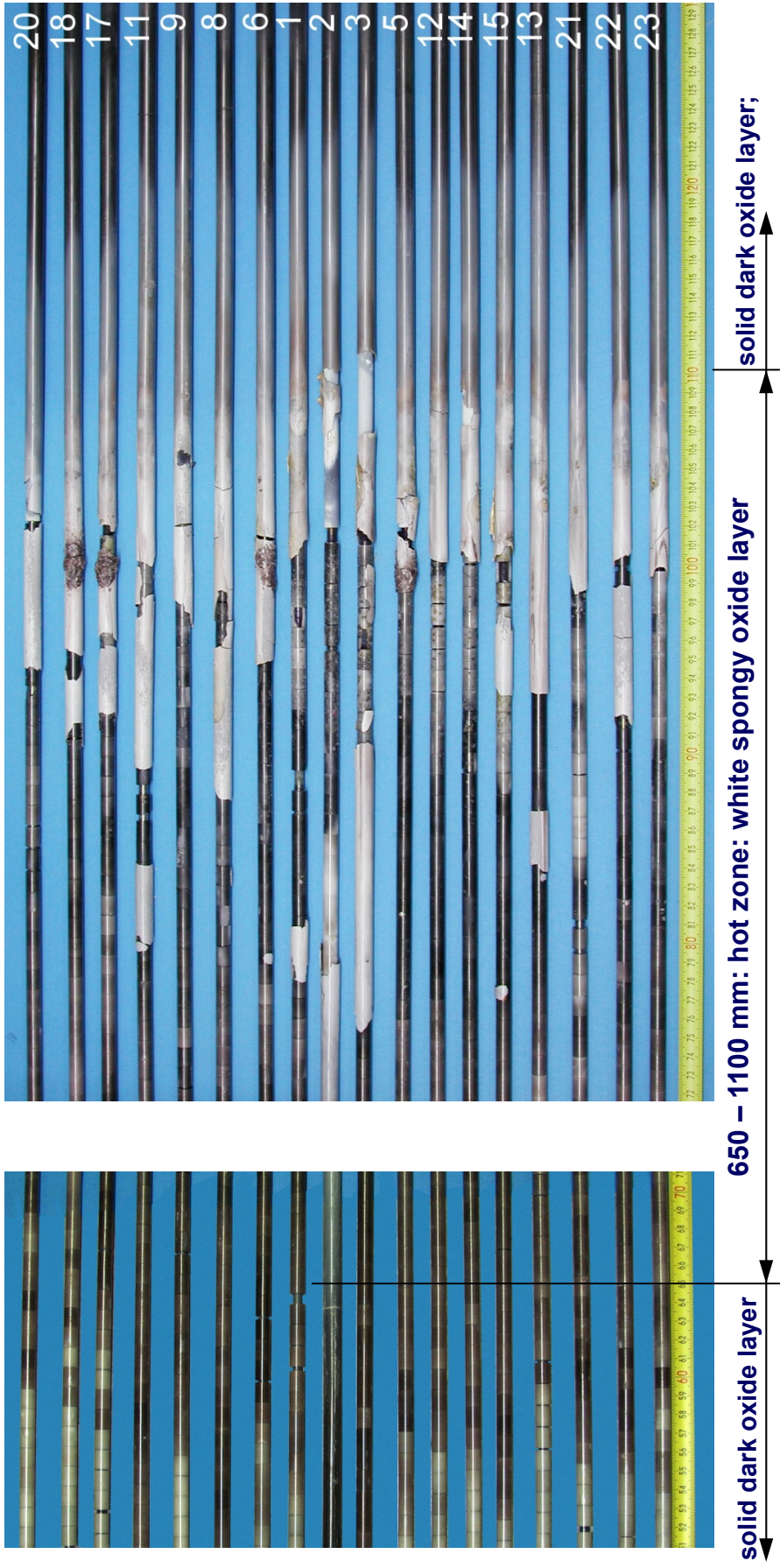


Fig. 48: QUENCH-15; Posttest view of 18 withdrawn fuel rod simulators at elevation 520-1300 mm.

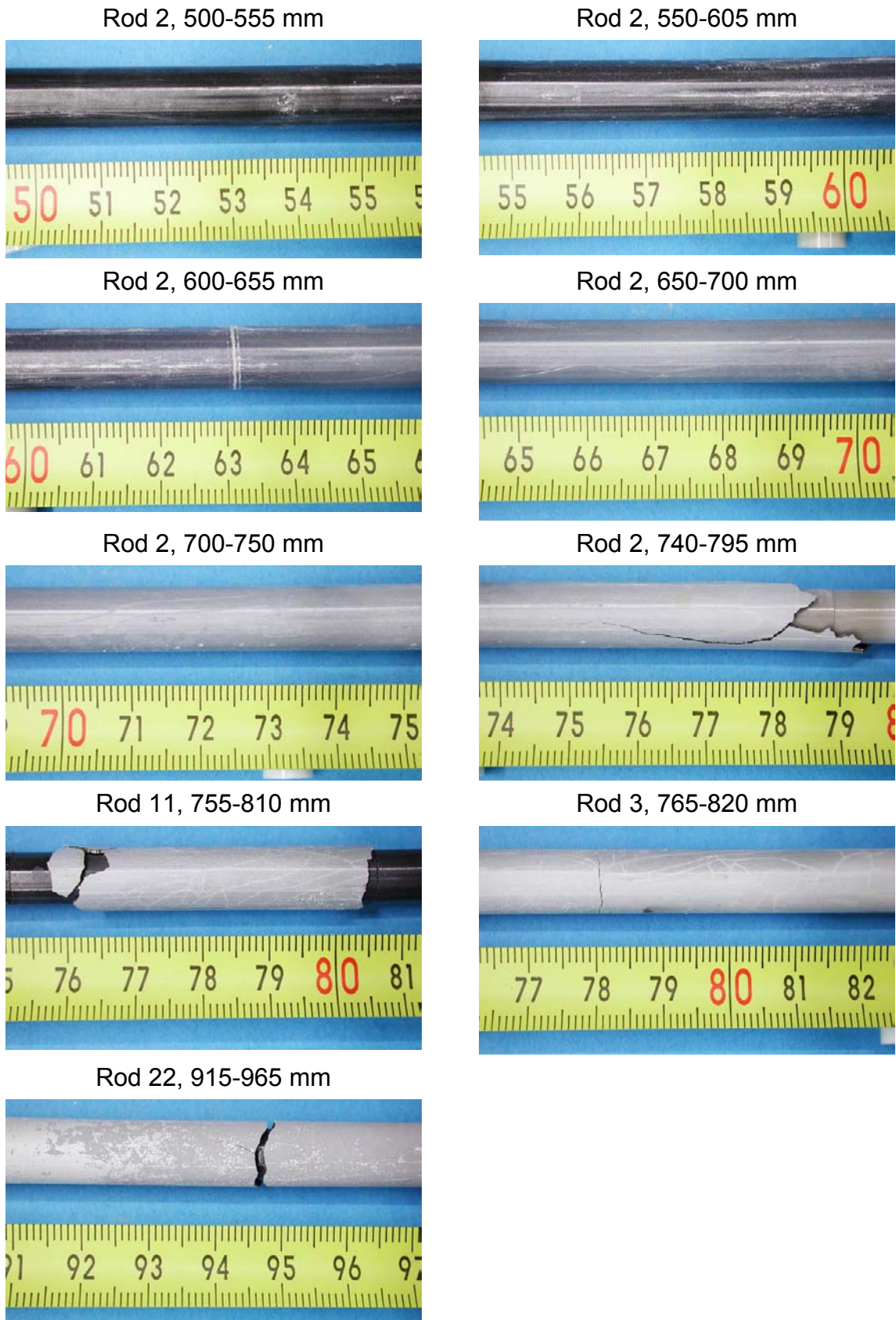


Fig. 49: QUENCH-15; Detailed photographs of the test rods 2, 3, 11, and 22.

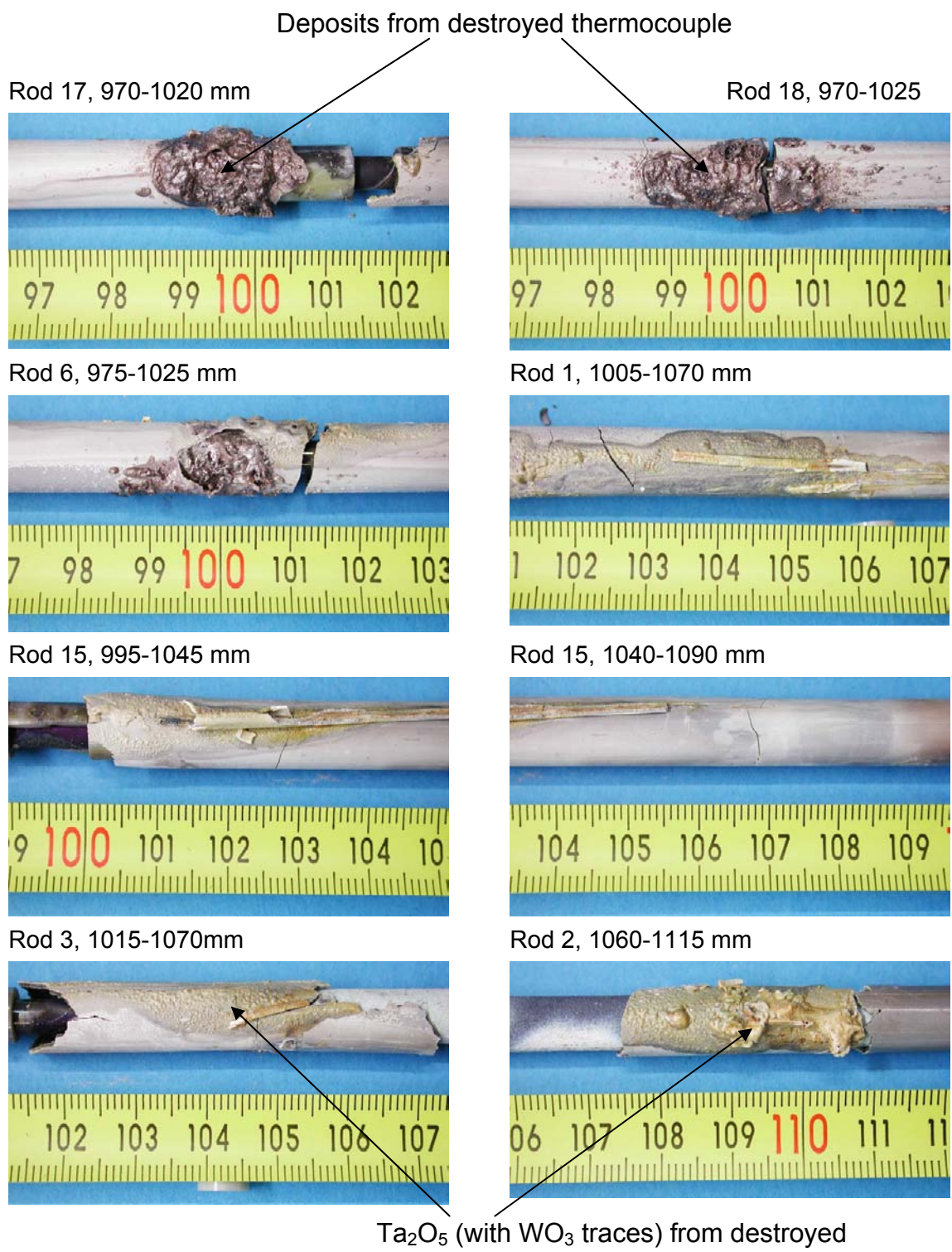
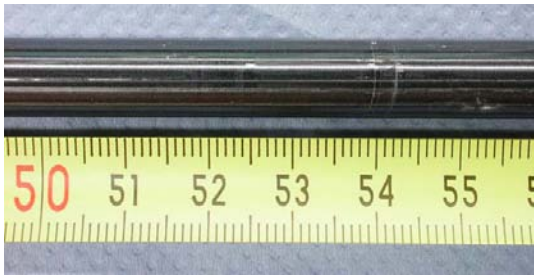
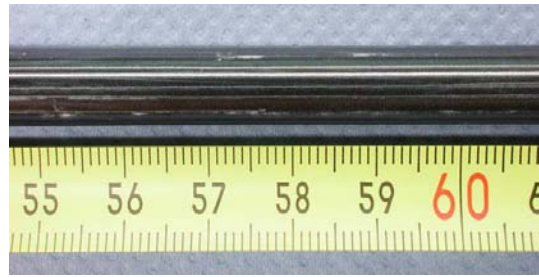


Fig. 50: QUENCH-15; Detailed photographs of the test rods 1, 2, 3, 6, 15, 17, and 18.

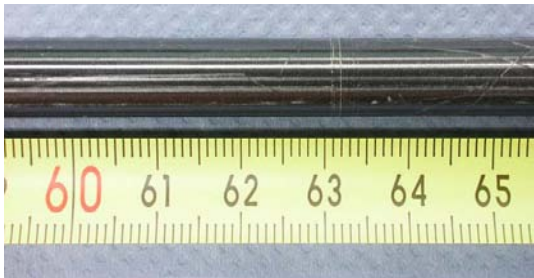
Rod 24, 500-555 mm



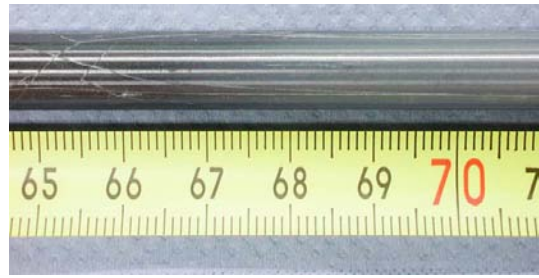
Rod 24, 550-605 mm



Rod 24, 600-650 mm



Rod 24, 650-700 mm



Rod 24, 700-755 mm



Rod 24, 745-805 mm



Rod 24, 785-825 mm



Fragment from above 820 mm



Fragment from above 820 mm



Fragment from above 820 mm



Fig. 51: QUENCH-15; Detailed photographs of the test rod No. 24.

Fragments from above 820 mm



Rod 24, 1050-1105 mm

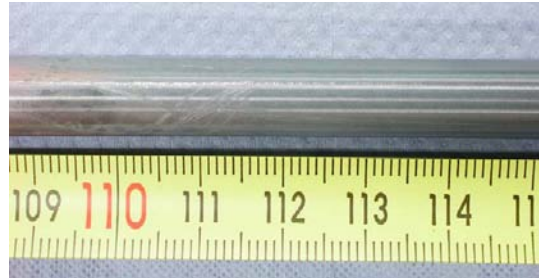
Fragment from above 820 mm



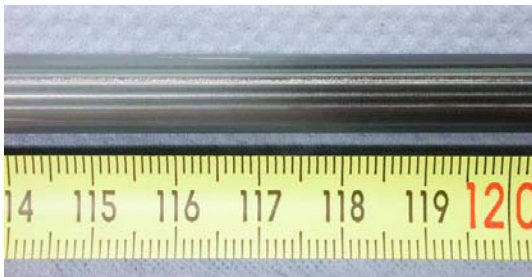
Rod 24, 1090-1145 mm



Rod 24, 1145-1200 mm



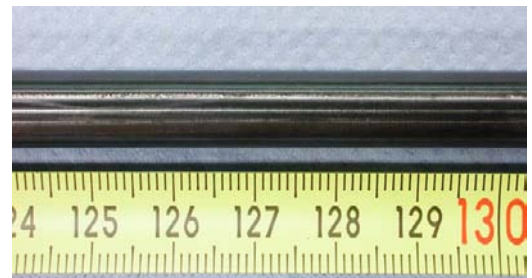
Rod 24, 1200-1250 mm



Rod 24, 1245-1300 mm



Rod 24, 1300-1350 mm



Rod 24, 1345-1400 mm



Fig. 52: QUENCH-15; Detailed photographs of the test rod No. 24.



QUE-15-1 (534 mm, bottom)



QUE-15-1 (550 mm, top)



QUE-15-2 (634 mm, bottom)



QUE-15-2 (650 mm, top)

Fig. 53: QUENCH-15; Bundle cross sections at 534 mm, 550 mm, 634 mm and 650 mm.



QUE-15-3 (734 mm, bottom)



QUE-15-3 (750 mm, top)



QUE-15-9 (734 mm, bottom)



QUE-15-9 (750 mm, top)

Fig. 54: QUENCH-15; Bundle cross sections at 734 mm and 750 mm.



QUE-15-4 (834 mm, bottom)



QUE-15-4 (850 mm, top)

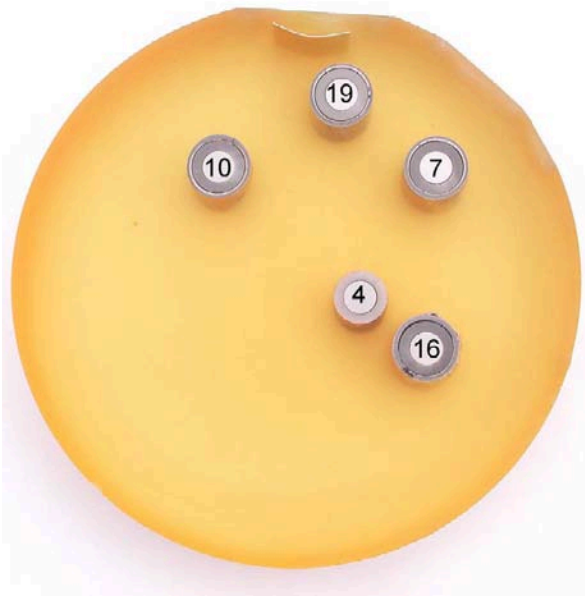


QUE-15-10 (834 mm, bottom)

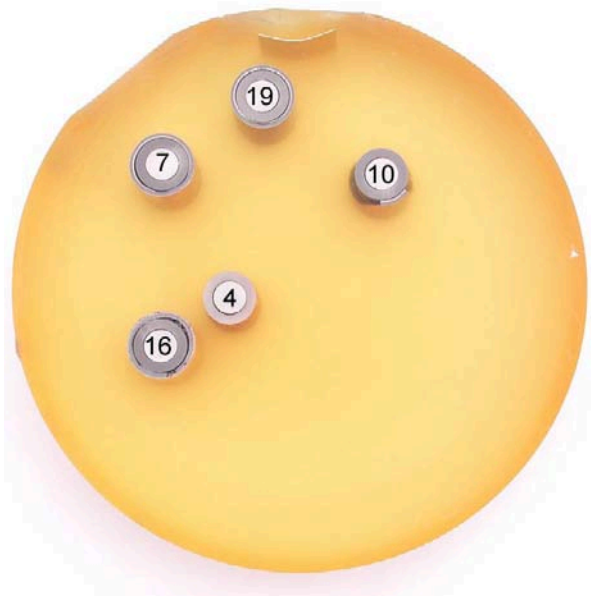


QUE-15-10 (850 mm, top)

Fig. 55: QUENCH-15; Bundle cross sections at 834 mm and 850 mm.



QUE-15-5 (934 mm, bottom)



QUE-15-5 (950 mm, top)

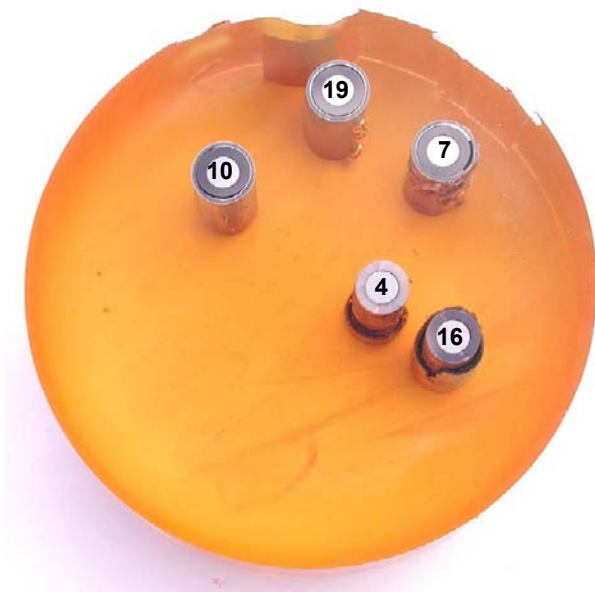


QUE-15-11 (934 mm, bottom)

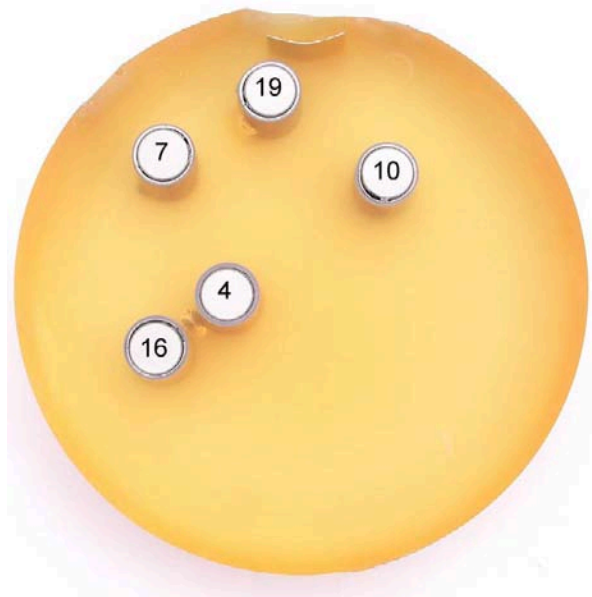


QUE-15-11 (950 mm, top)

Fig. 56: QUENCH-15; Bundle cross sections at 934 mm and 950 mm.



QUE-15-15 (1000 mm, bottom)



QUE-15-6 (1050 mm, top)

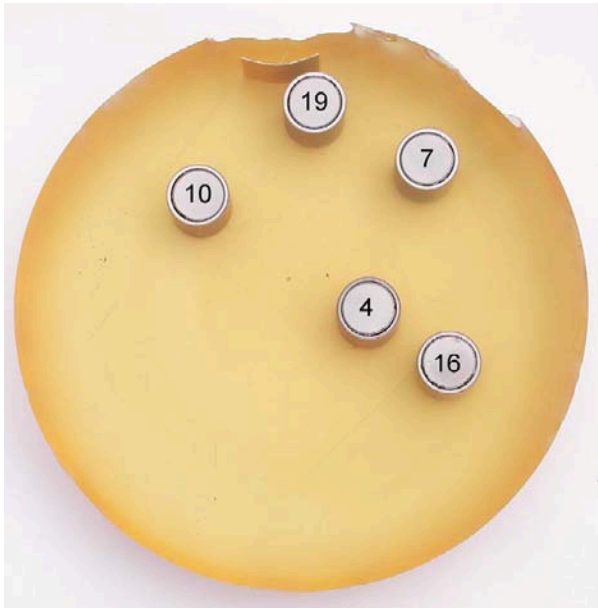


QUE-15-16 (1000 mm, bottom)



QUE-15-12 (1050 mm, top)

Fig. 57: QUENCH-15; Bundle cross sections at 1000 mm and 1050 mm.



QUE-15-7 (1134 mm, bottom)



QUE-15-7 (1150 mm, top)

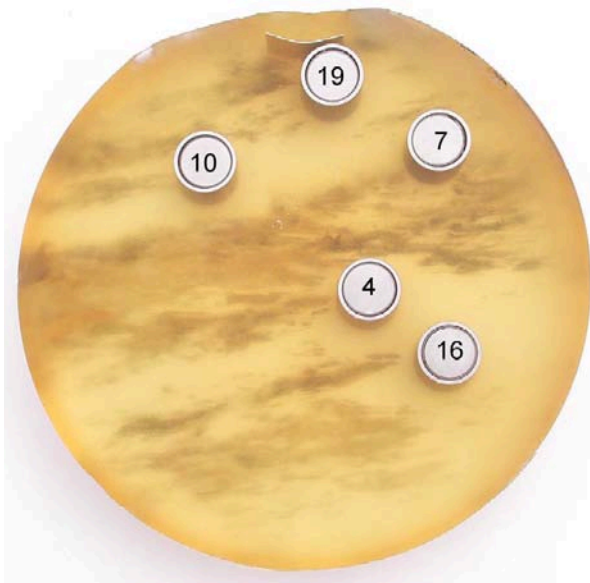


QUE-15-13 (1134 mm, bottom)

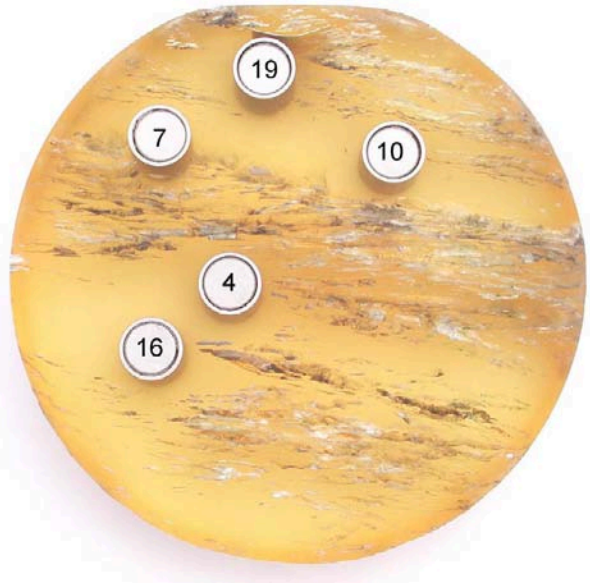


QUE-15-13 (1150 mm, top)

Fig. 58: QUENCH-15; Bundle cross sections at 1134 mm and 1150 mm.



QUE-15-8 (1234 mm, bottom)



QUE-15-8 (1250 mm, top)

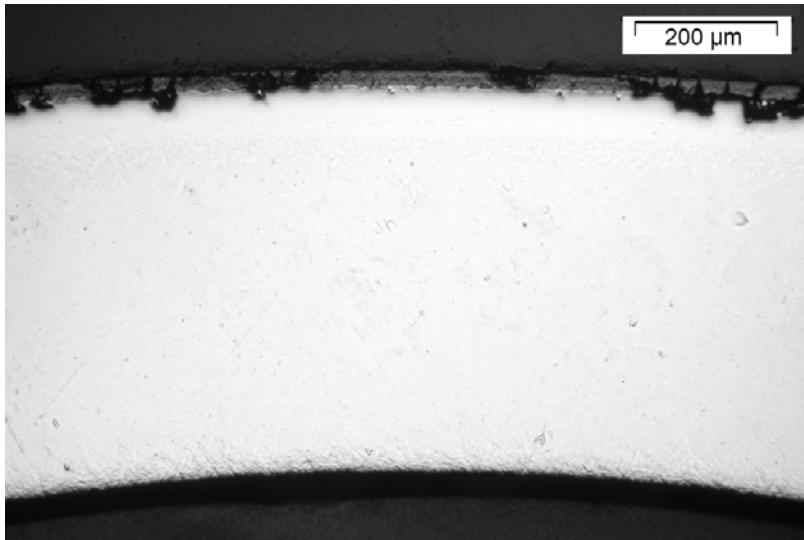


QUE-15-14 (1234 mm, bottom)

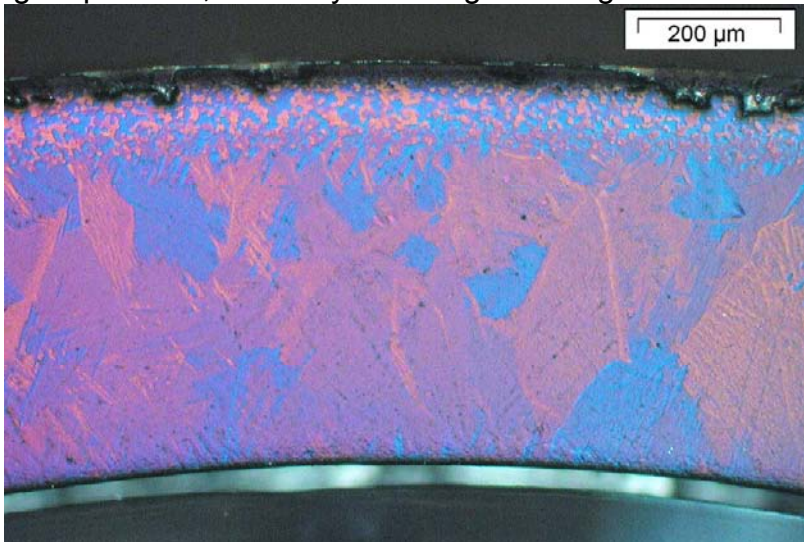


QUE-15-14 (1250 mm, top)

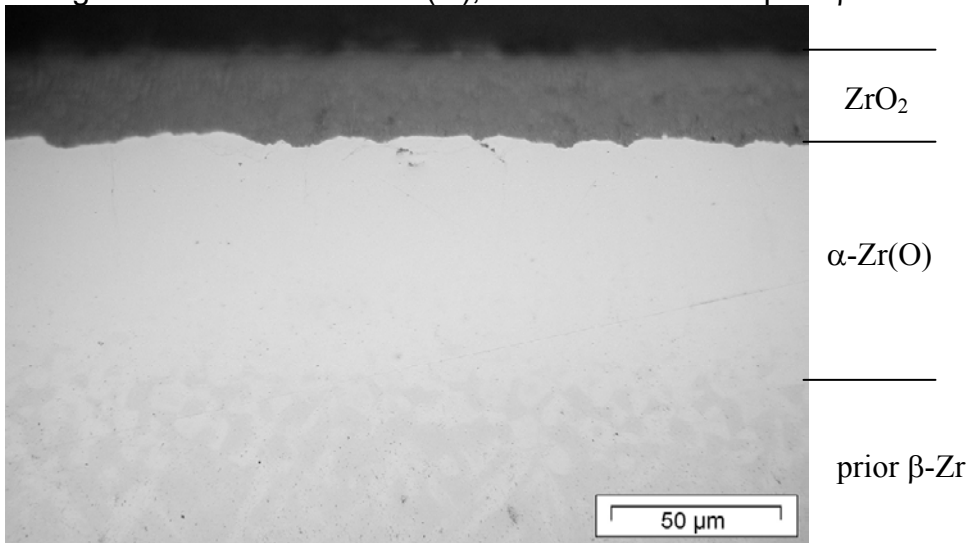
Fig. 59: QUENCH-15; Bundle cross sections at 1234 mm and 1250 mm.



cladding as polished; oxide layer damaged during bundle dismounting

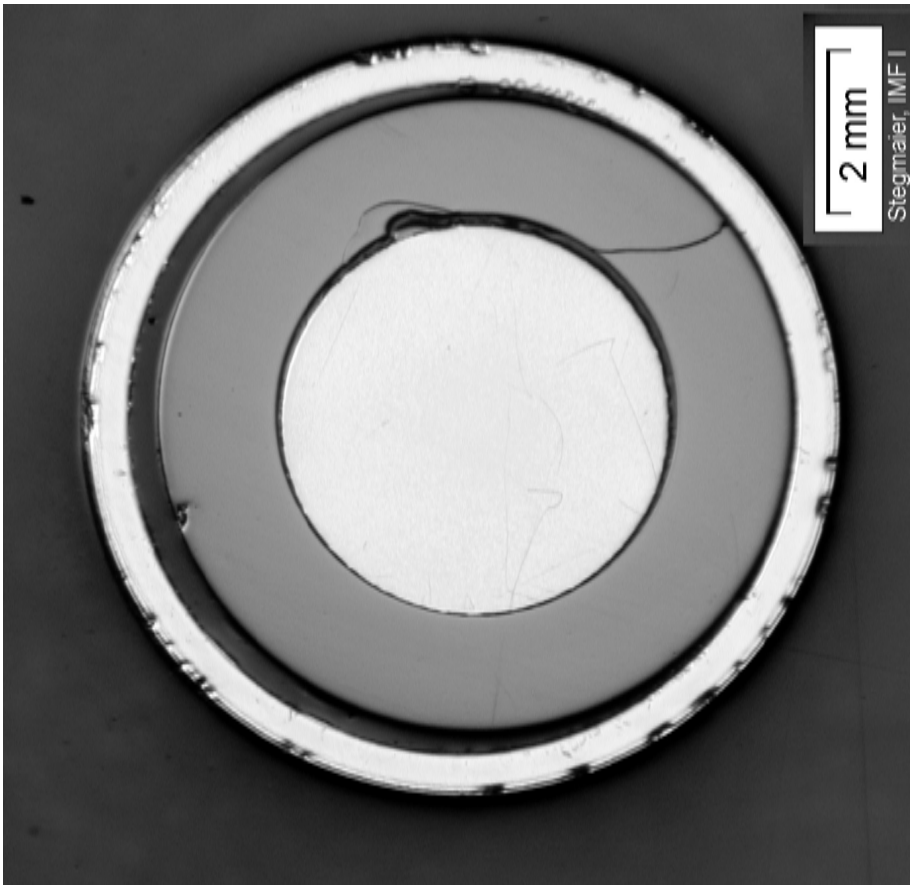


polarized light: fine structure of α -Zr(O); coarse structure of prior β -Zr

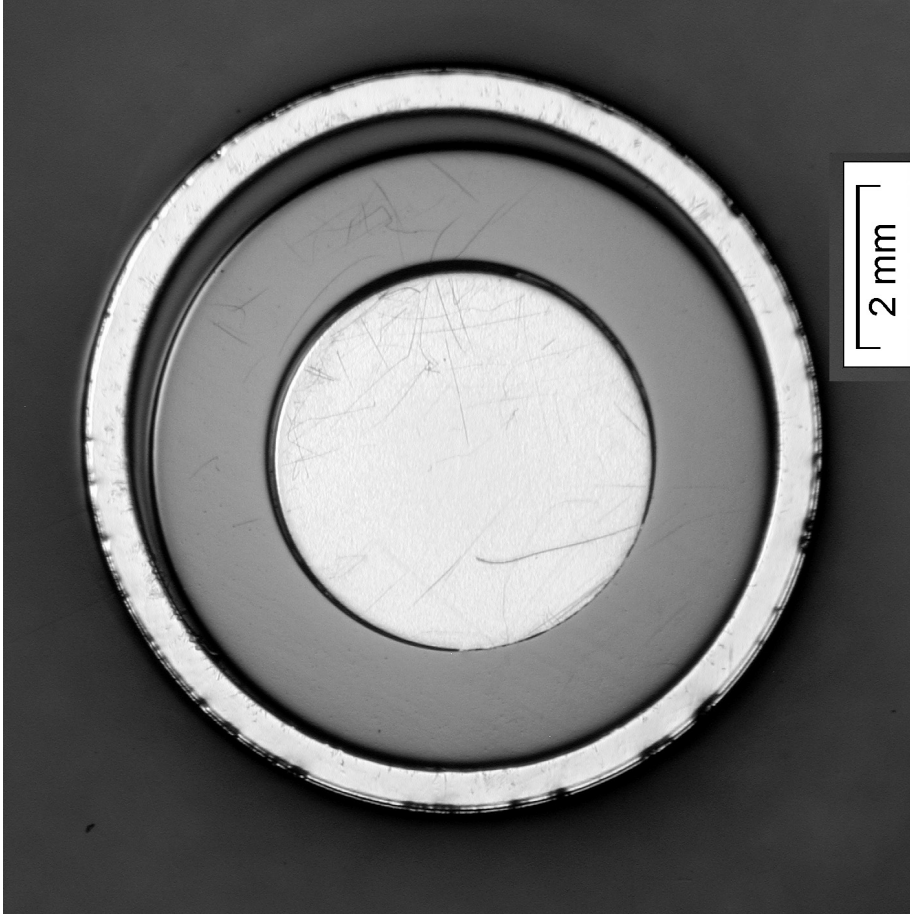


three typical layers at outer cladding surface

Fig. 60: QUENCH-15; Cladding structure of rod #12 at 550 mm, 0°.

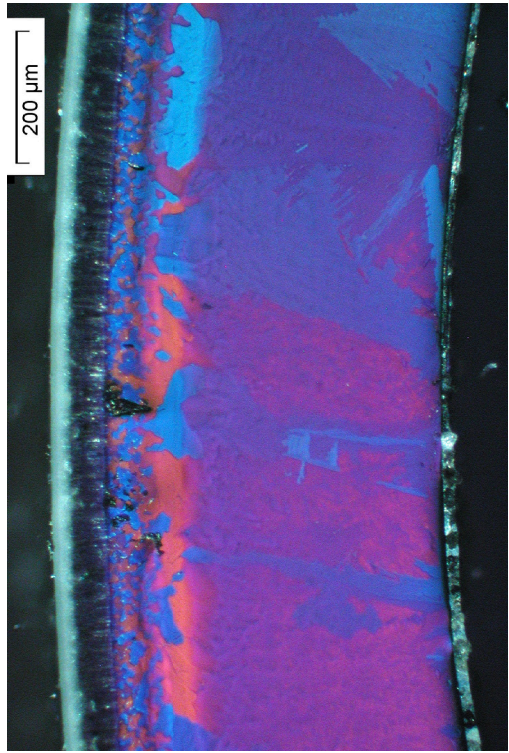


inner rod #4



outer rod #10

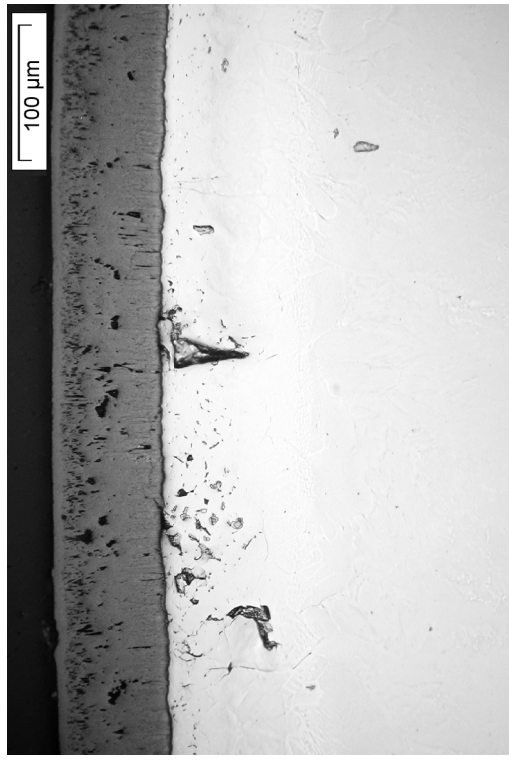
Fig. 61: QUENCH-15; Cross section at elevation 650 mm depicting individual test rods 4, 10.



cladding of rod #4 in polarized light

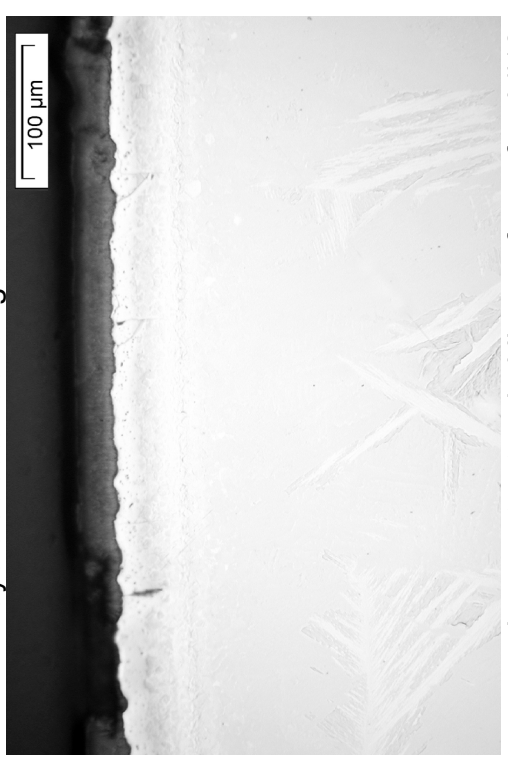


cladding of rod #10 in polarized light



layers at outer cladding surface of rod #4

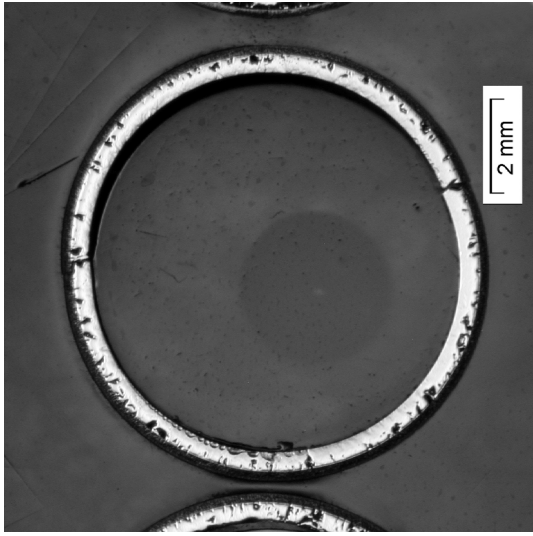
ZrO₂
 α-Zr(O)
 prior β-Zr



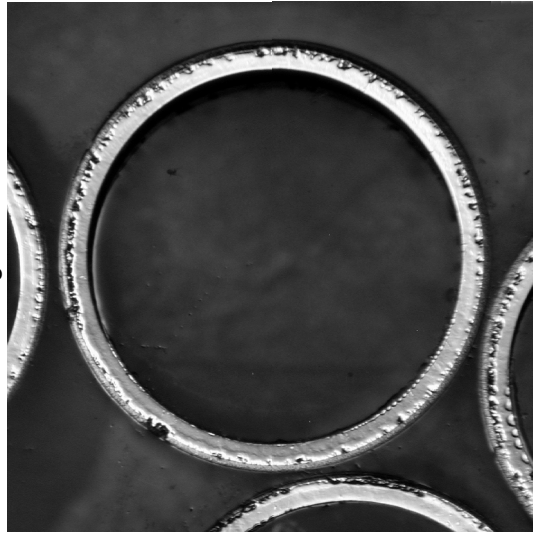
layers at outer cladding surface of rod #10

ZrO₂
 α-Zr(O)
 prior β-Zr

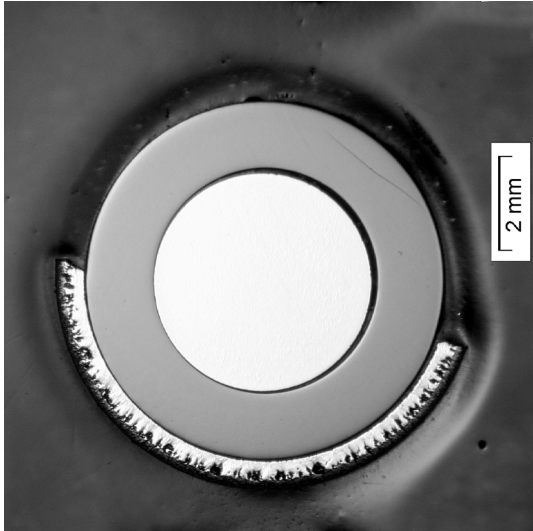
Fig. 62: QUENCH-15; Cladding structure of rods #4 and #10 at 650 mm, 0°: different oxidation degree for inner and outer rod groups.



cladding of rod 3



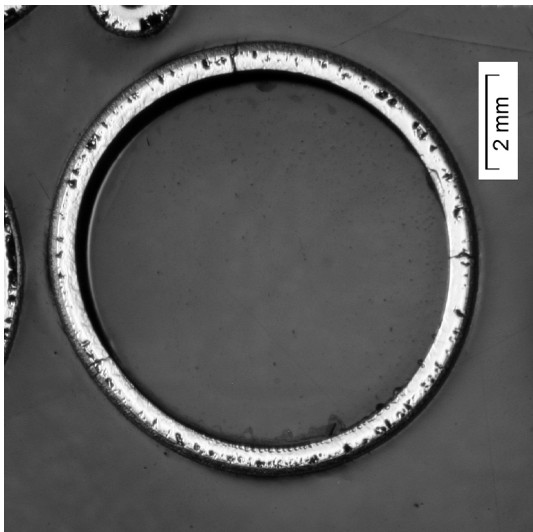
cladding of rod 6



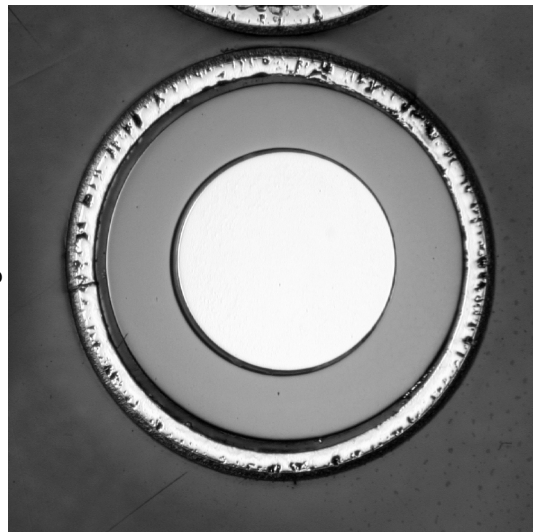
rod 2: loss of cladding segment by handling



cladding of rod 5



cladding of rod 1



rod 4

Fig. 63: QUENCH-15; Cross section at elevation 750 mm depicting individual test rods 1-6.

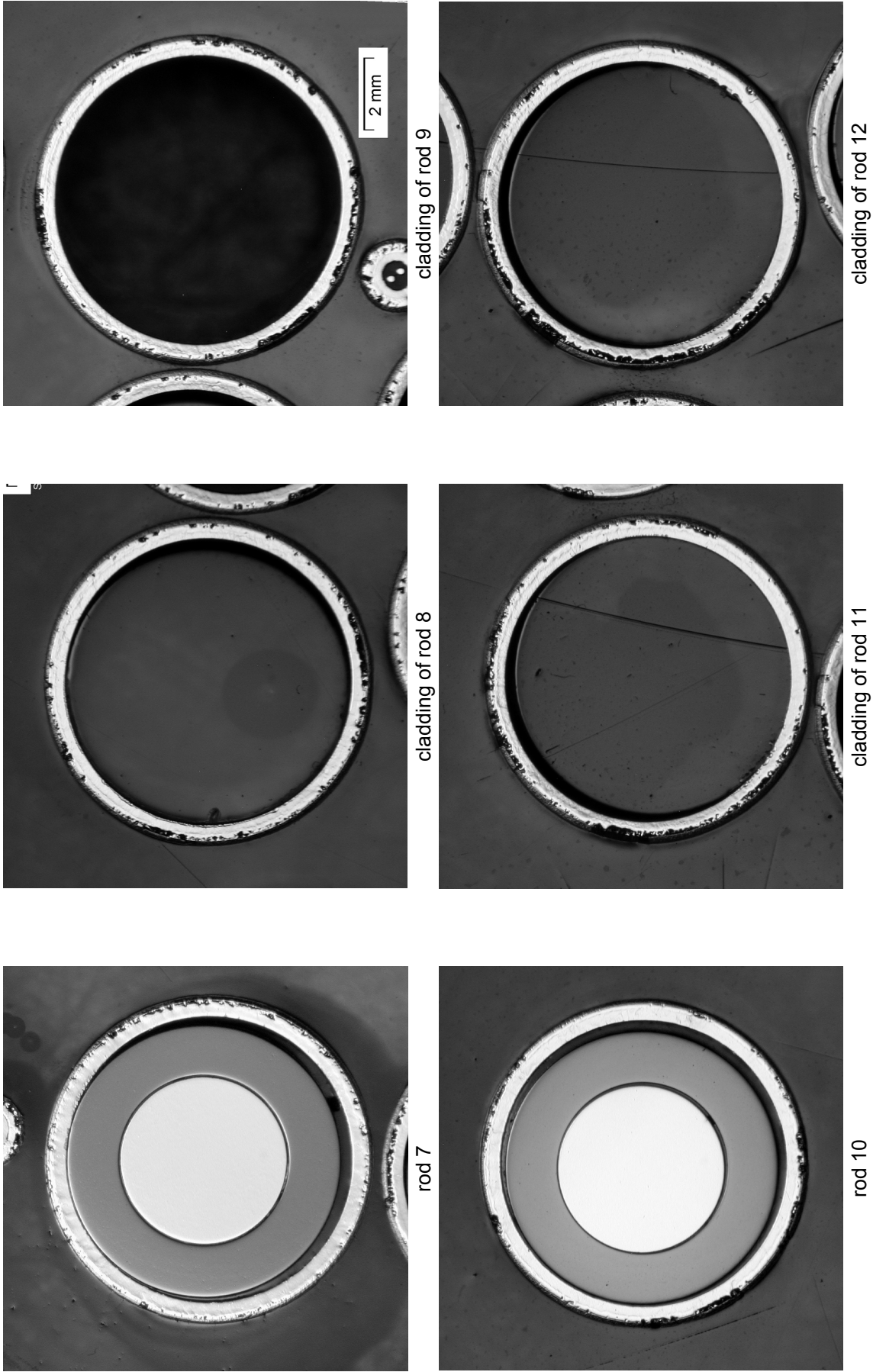
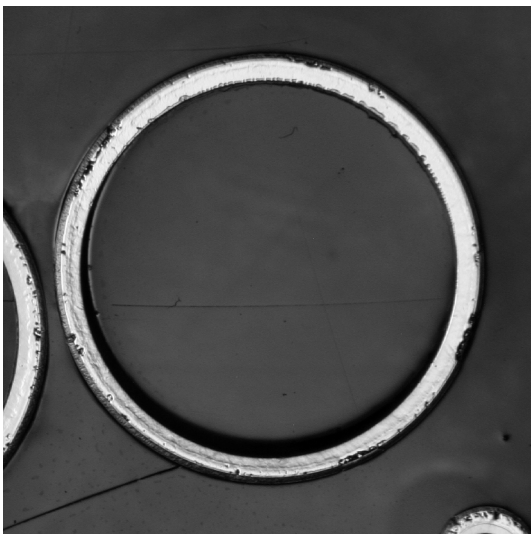
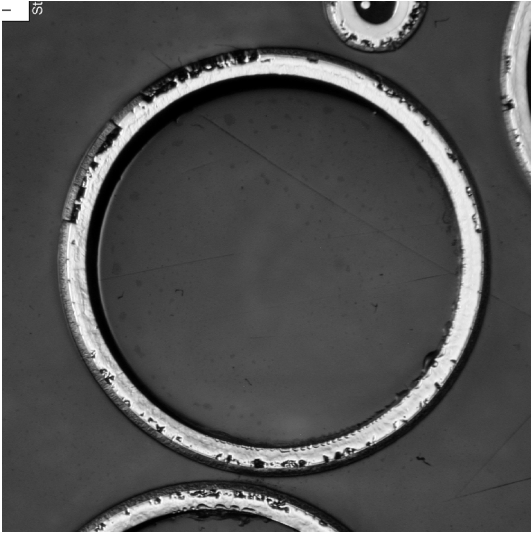


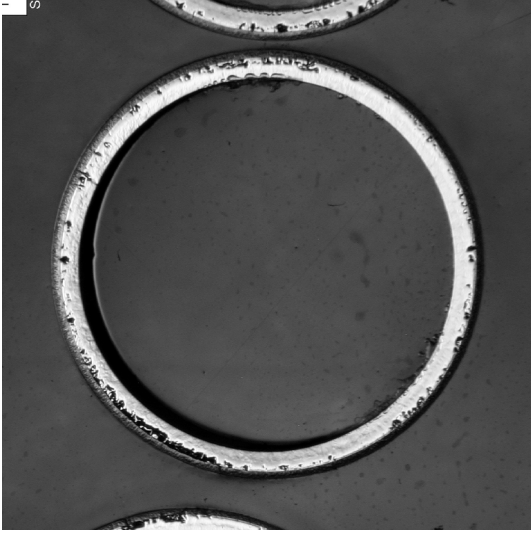
Fig. 64: QUENCH-15; Cross section at elevation 750 mm depicting individual test rods 7-12.



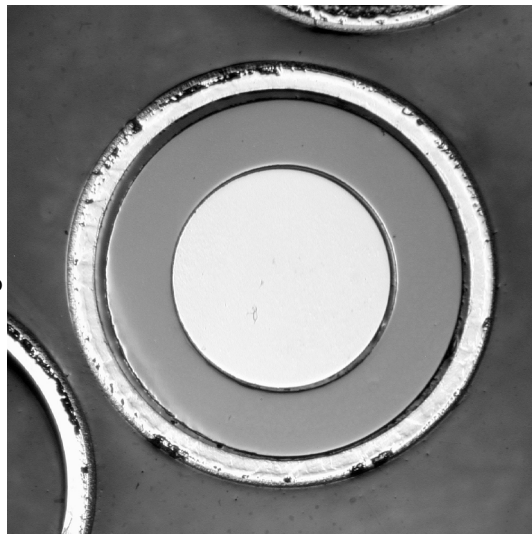
cladding of rod 13



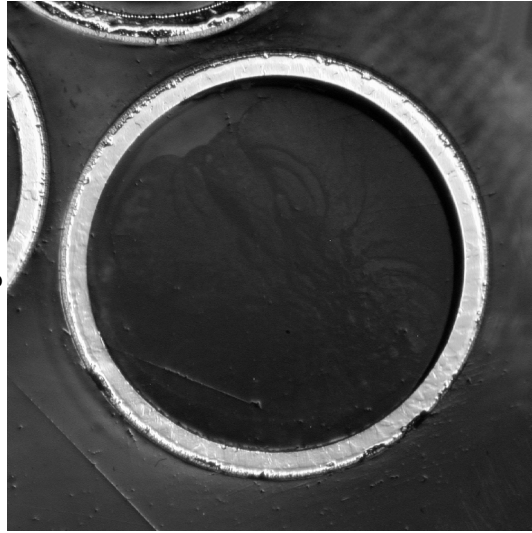
cladding of rod 14



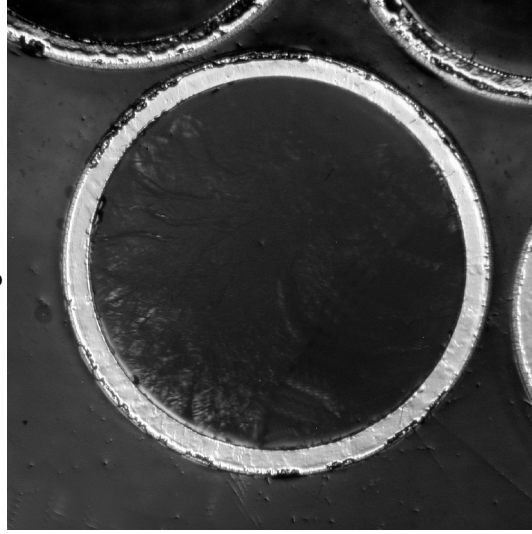
cladding of rod 15



rod 16

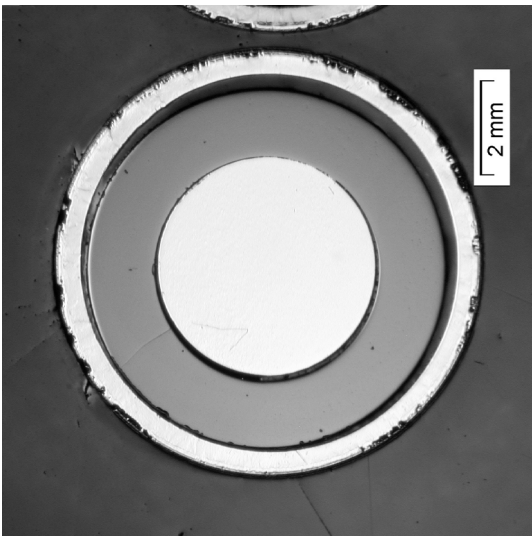


cladding of rod 17

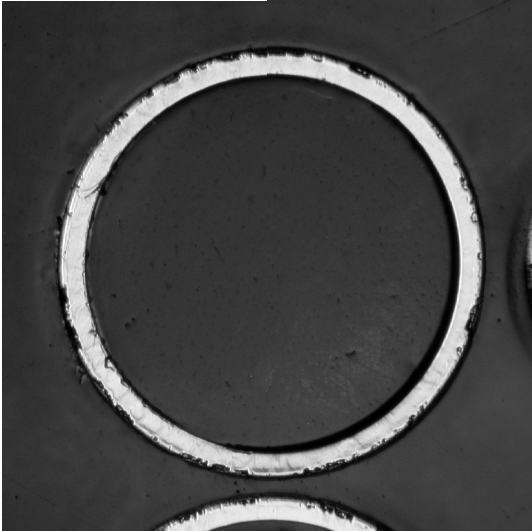


cladding of rod 18

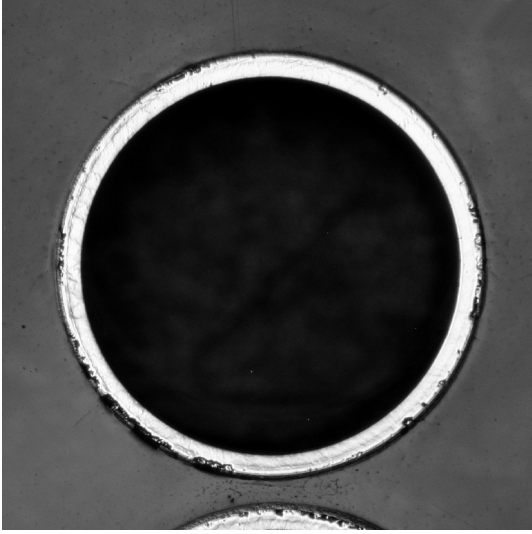
Fig. 65: QUENCH-15; Cross section at elevation 750 mm depicting individual test rods 13-18.



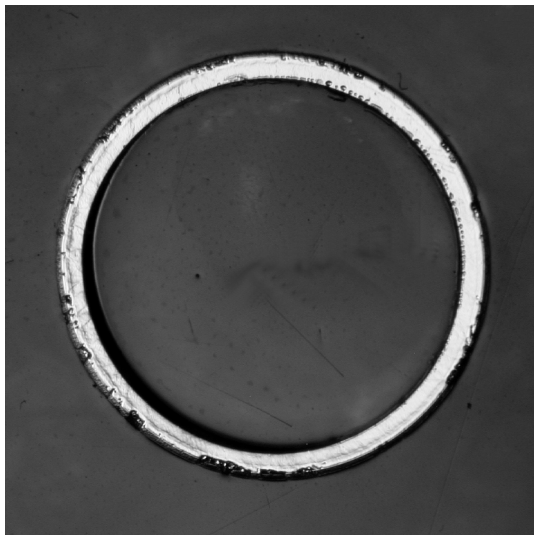
rod 19



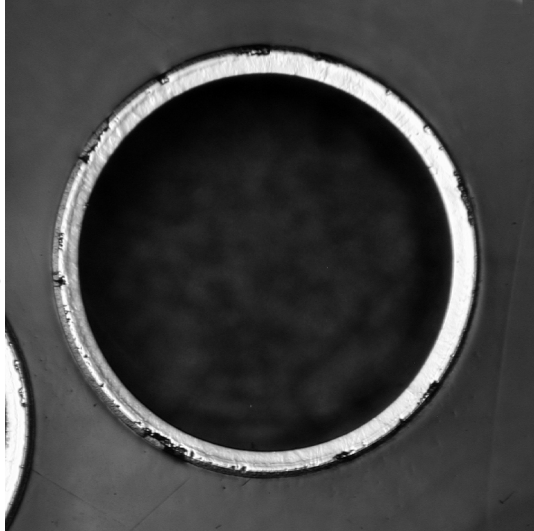
cladding of rod 20



cladding of rod 21



cladding of rod 22



cladding of rod 23

Fig. 66: QUENCH-15; Cross section at elevation 750 mm depicting individual test rods 19-23.

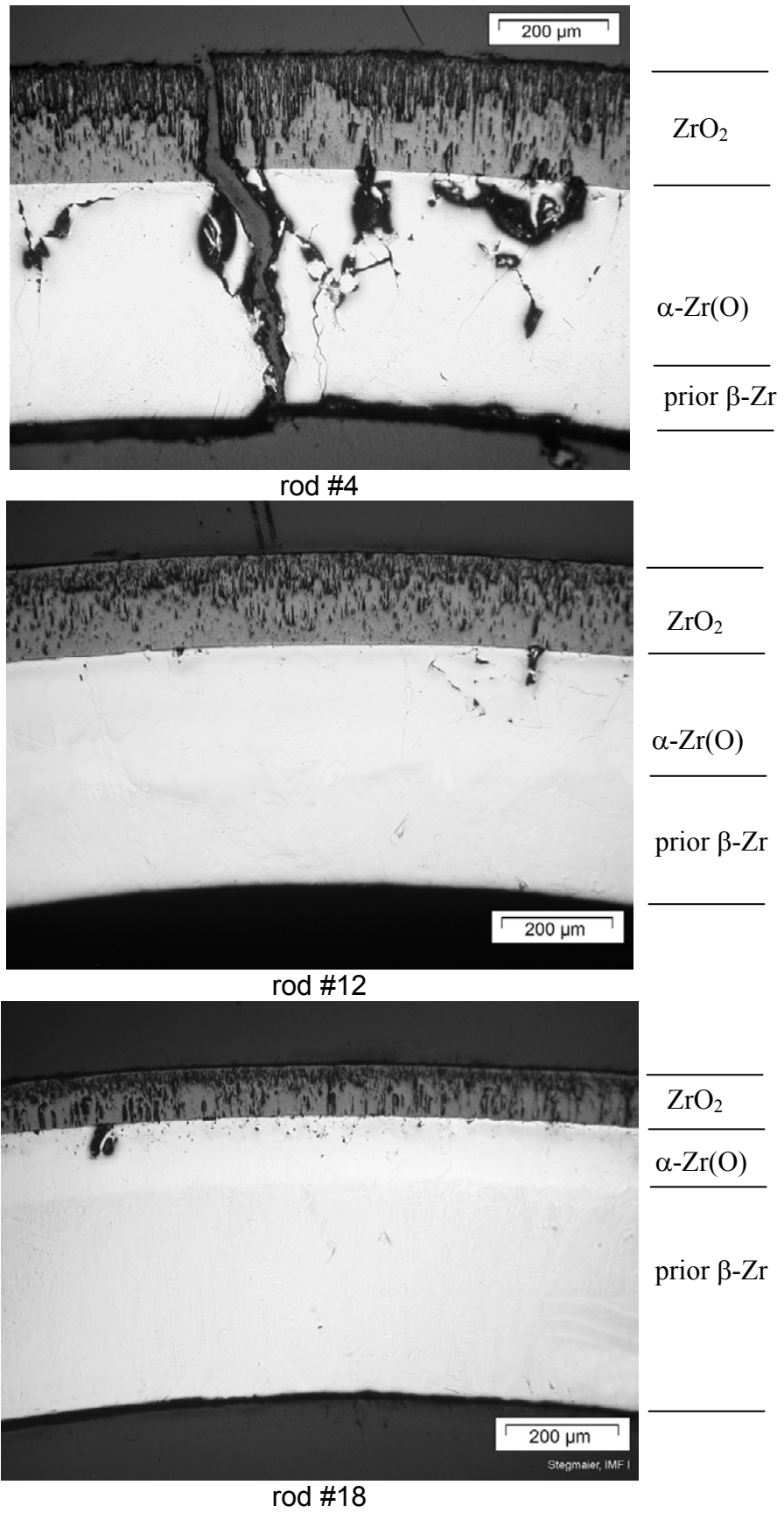
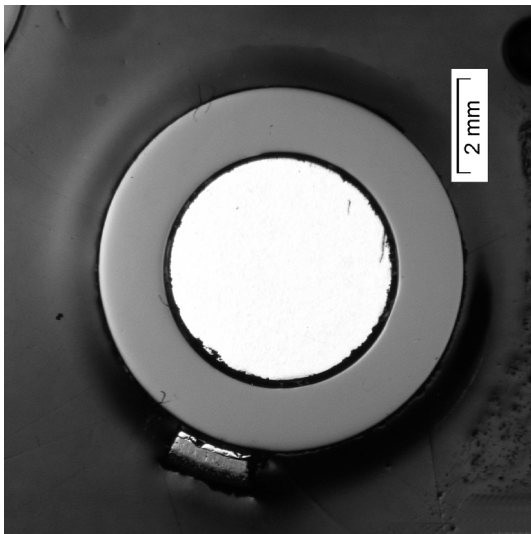
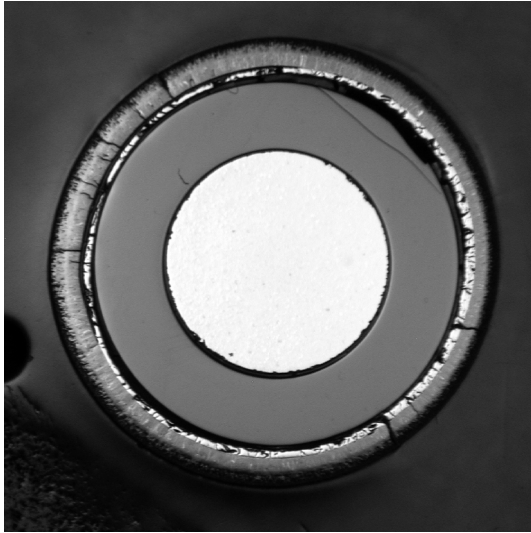


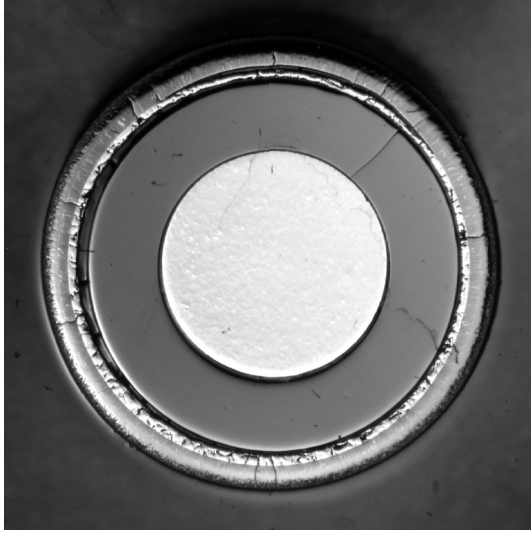
Fig. 67: QUENCH-15; Cladding structure of rods #4, #12 and #18 at 750 mm, 0°: different oxidation degree for inner and outer rod groups.



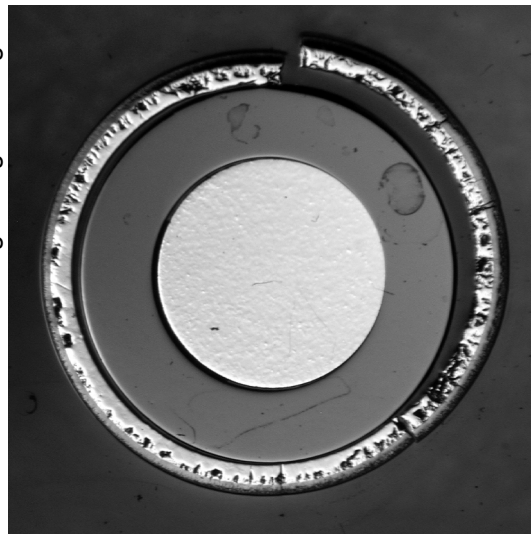
rod 1: loss of cladding during handling



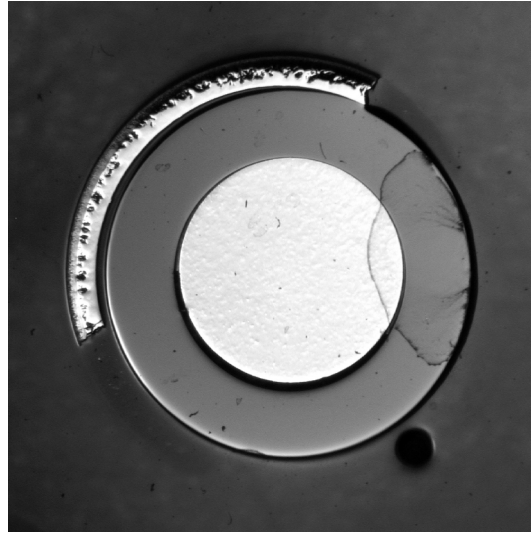
rod 3



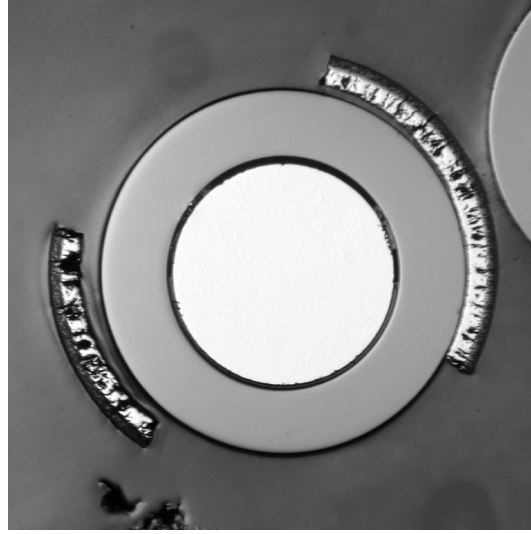
rod 4



rod 7

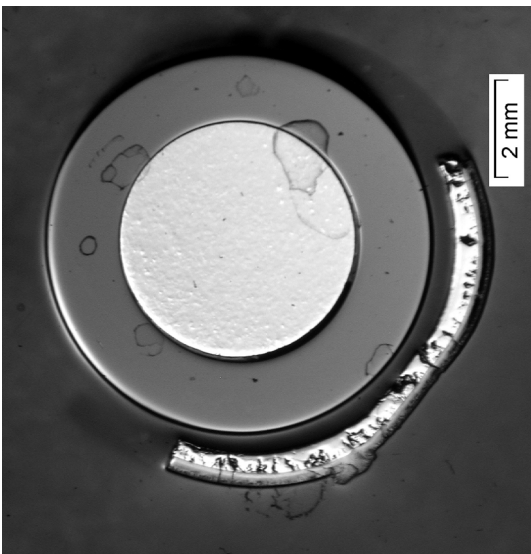


rod 10: loss of cladding segment during handling

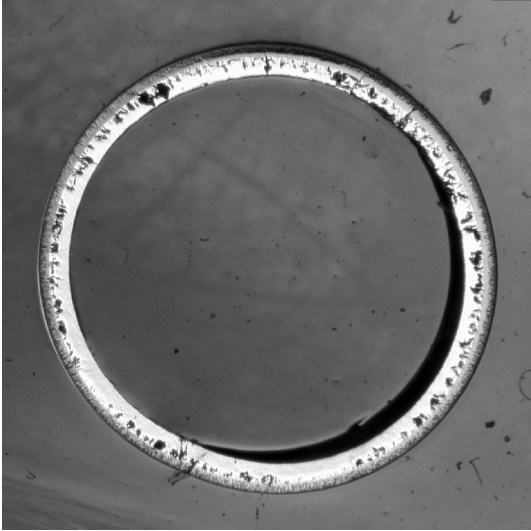


rod 11: loss of cladding segments during handling

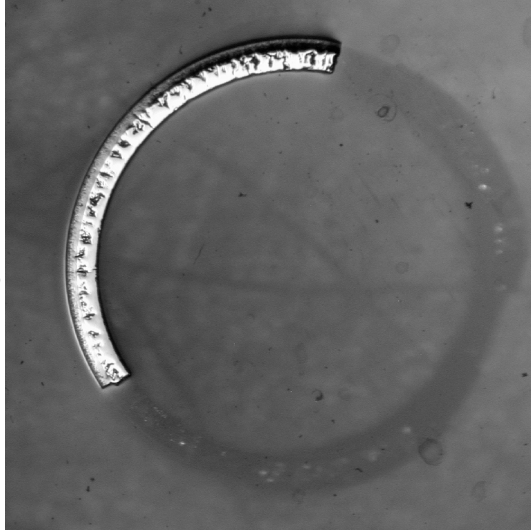
Fig. 68: QUENCH-15; Cross section at elevation 850 mm depicting individual test rods 1-11.



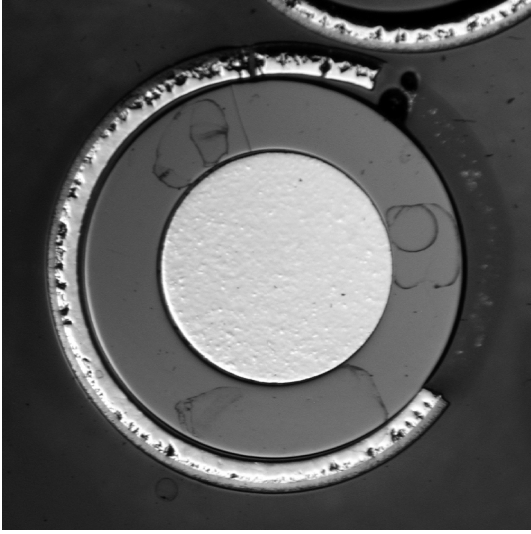
rod 16: loss of cladding segment during handling



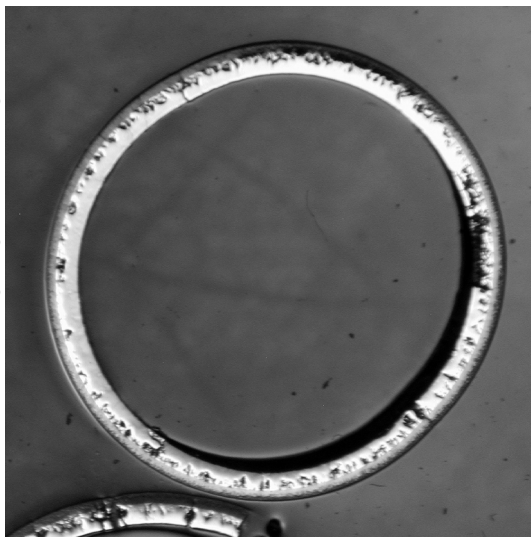
cladding of rod 18



cladding segment of rod 21



rod 19: loss of cladding segment during handling



cladding of rod 20

Fig. 69: QUENCH-15; Cross section at elevation 850 mm depicting individual test rods 16-21.

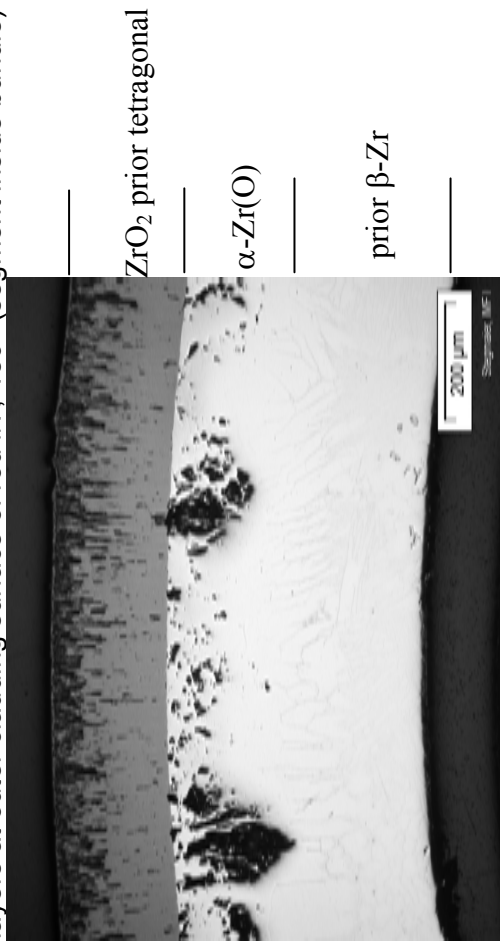
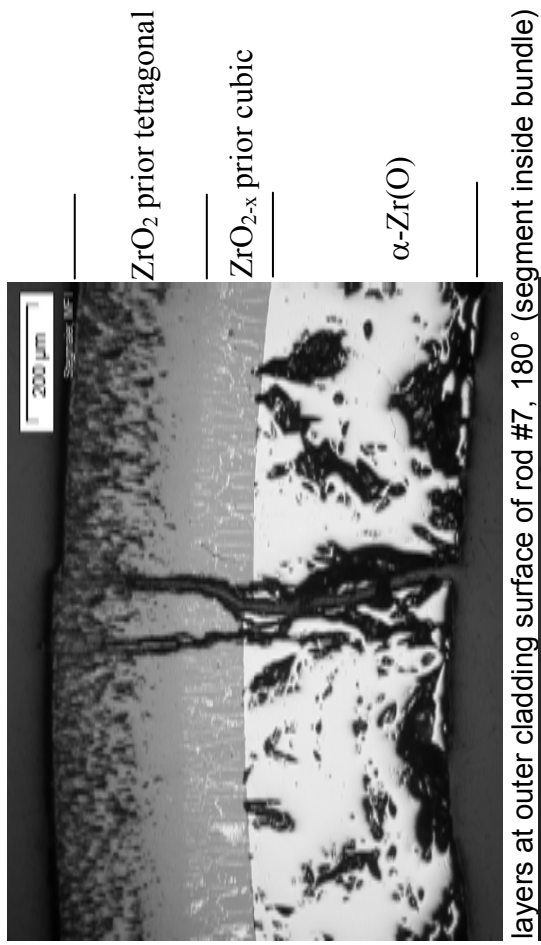
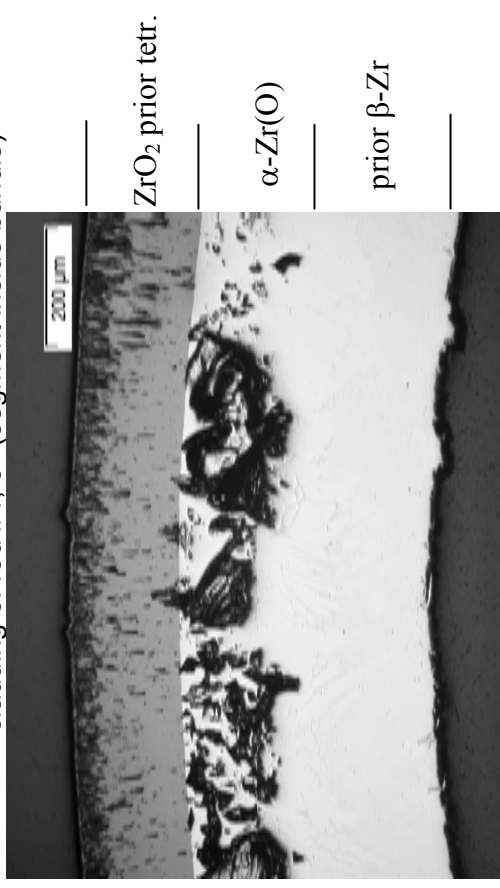
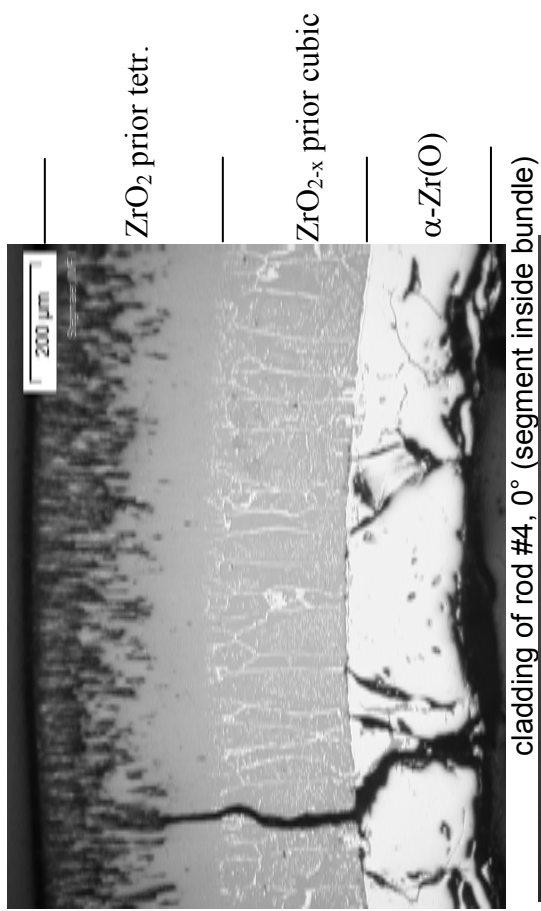


Fig. 70: QUENCH-15; Cladding structure of rods #4, #7 and #19 at 850 mm: different oxidation degree depending on radial position of cladding segment in bundle.

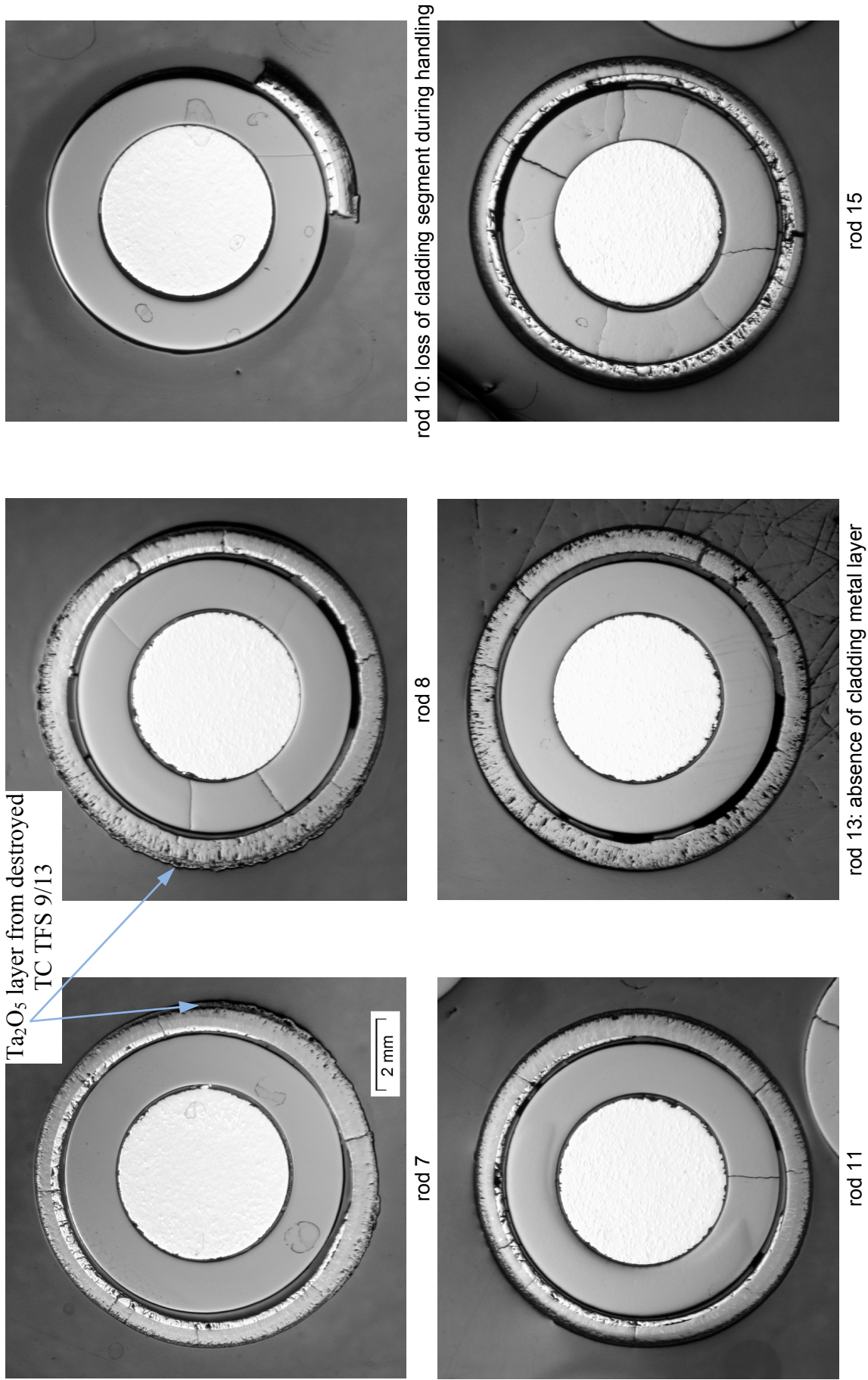


Fig. 71: QUENCH-15; Cross section at elevation 950 mm depicting individual test rods 7-15.

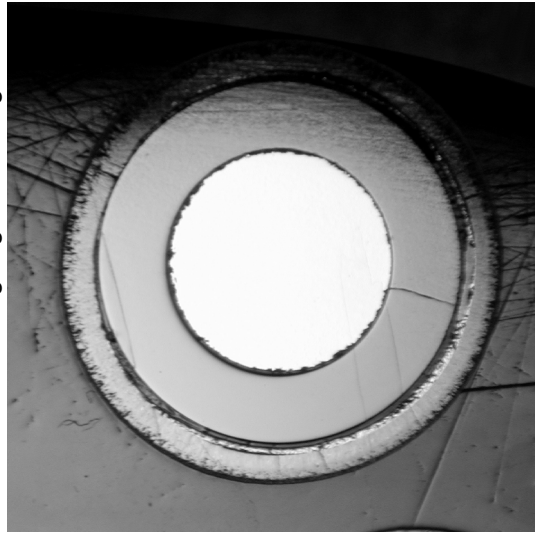
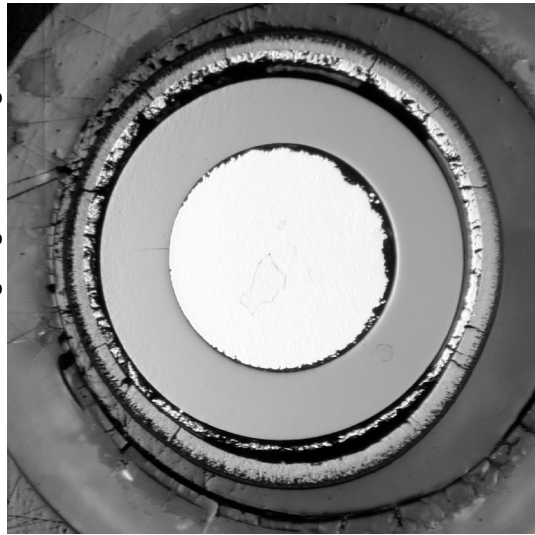
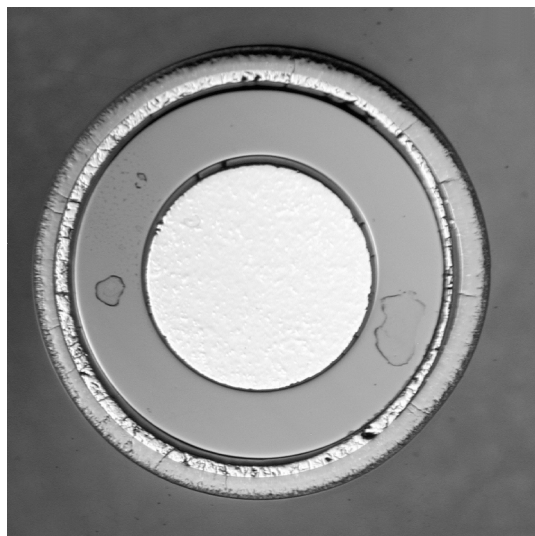
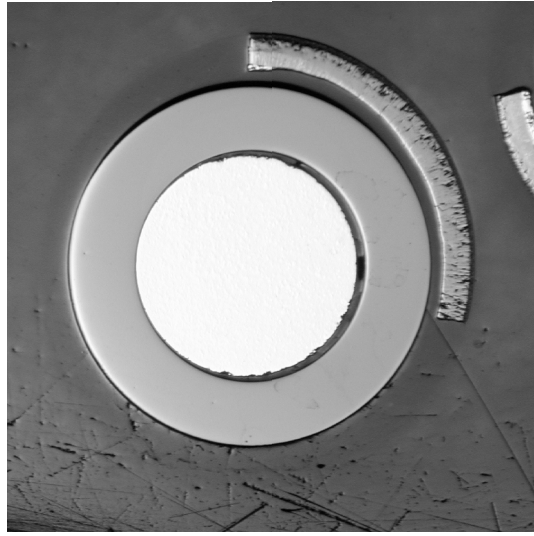
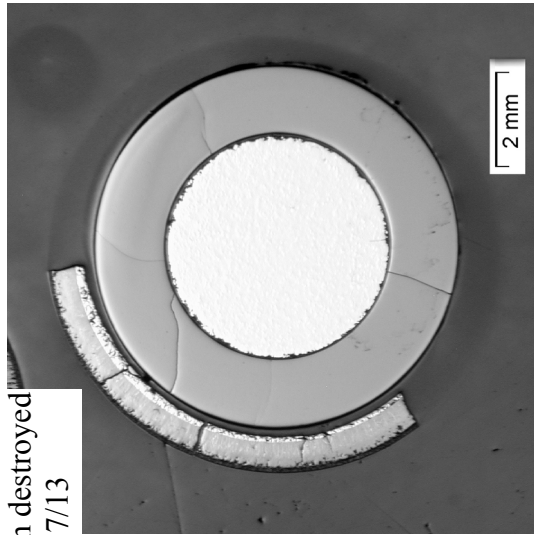
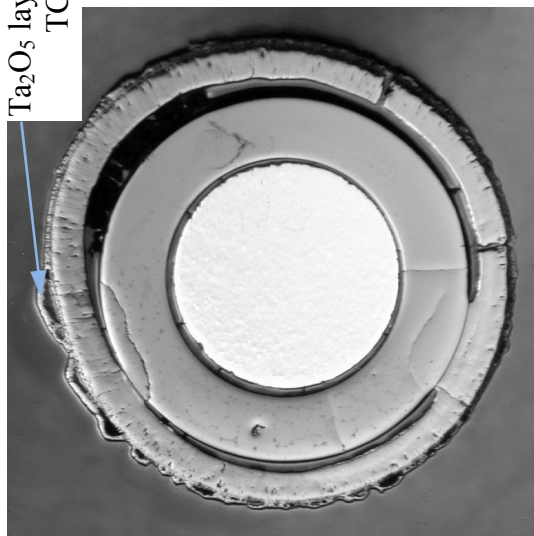
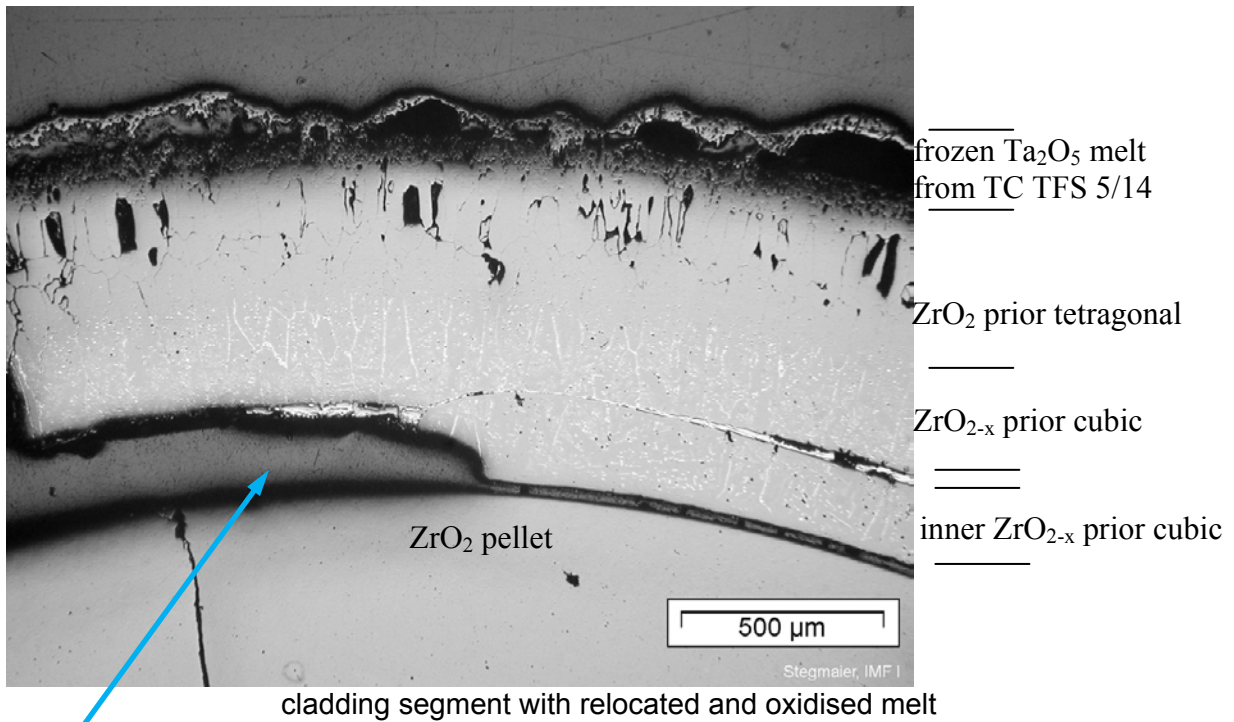
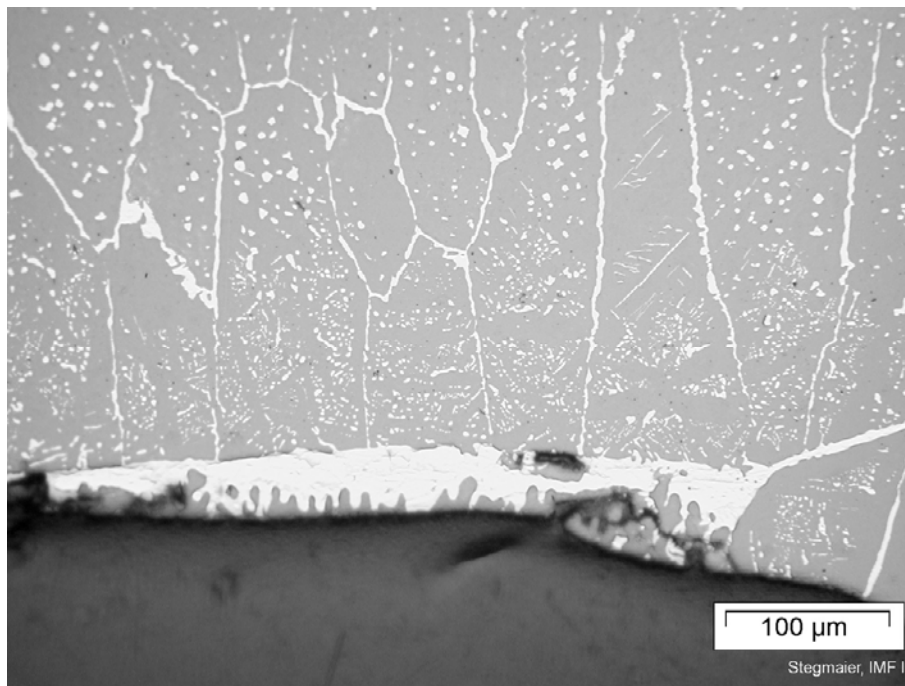


Fig. 72: QUENCH-15; Cross section at elevation 950 mm depicting individual test rods 16-22.

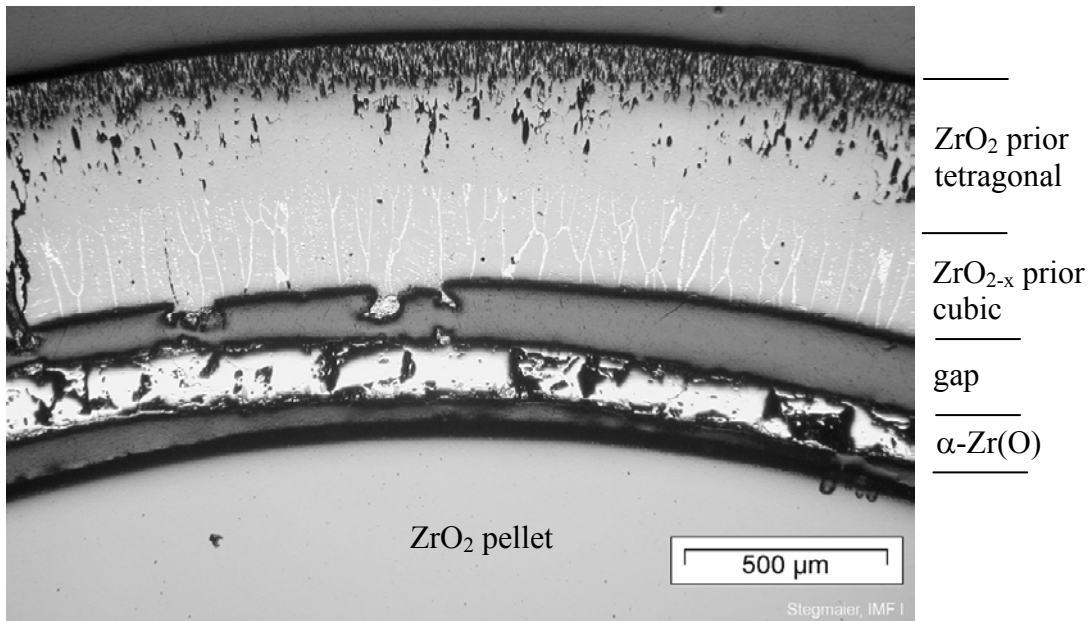


void

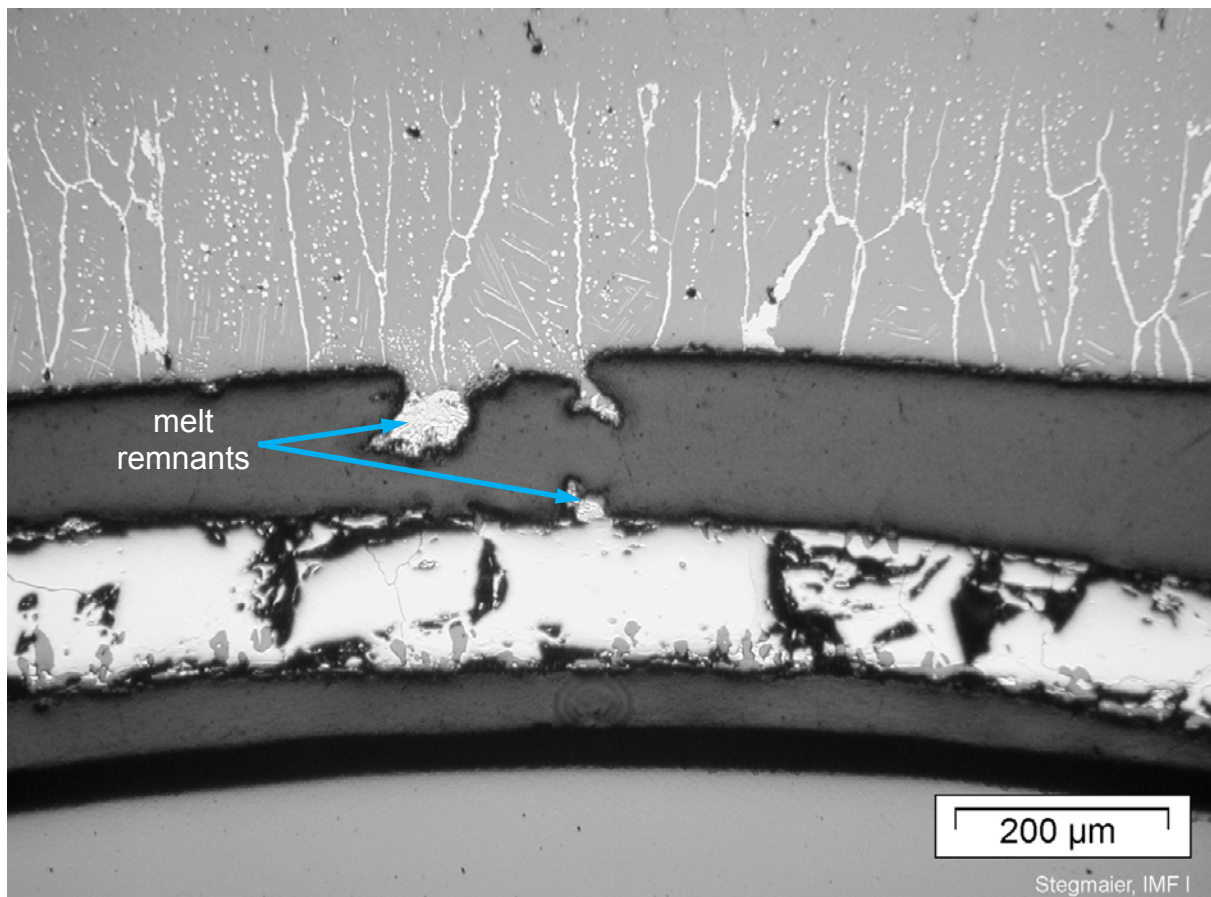


inner cladding surface formed during melt relocation and oxidation

Fig. 73: QUENCH-15; Cladding structure of rods #16 at 950 mm: absence of metallic layer due to melt relocation inside the pellet-cladding gap; inner oxide layer formation.

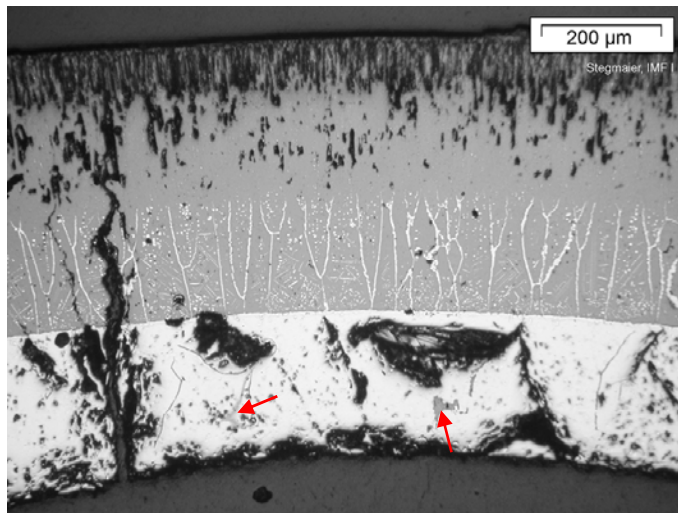


cladding segment with gap from relocated melt



melt remnants

Fig. 74: QUENCH-15; Cladding structure of rods #19 at 950 mm: melt relocation inside gap between oxide and α -Zr(O).

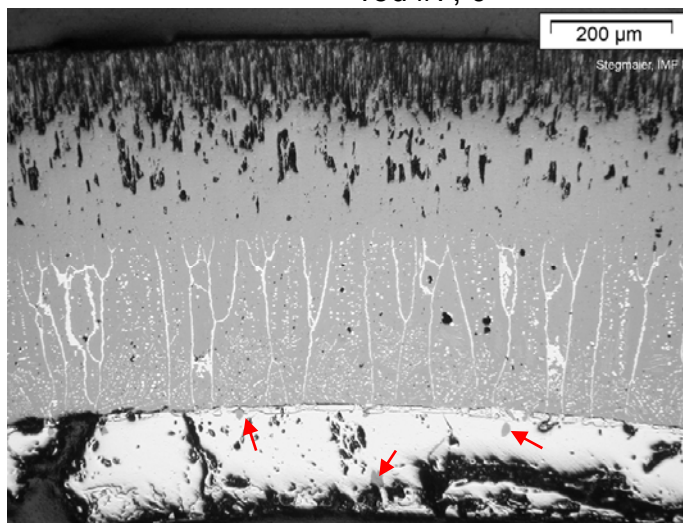


rod #7, 0°

ZrO₂ prior tetragonal

ZrO_{2-x} prior cubic

α-Zr(O)

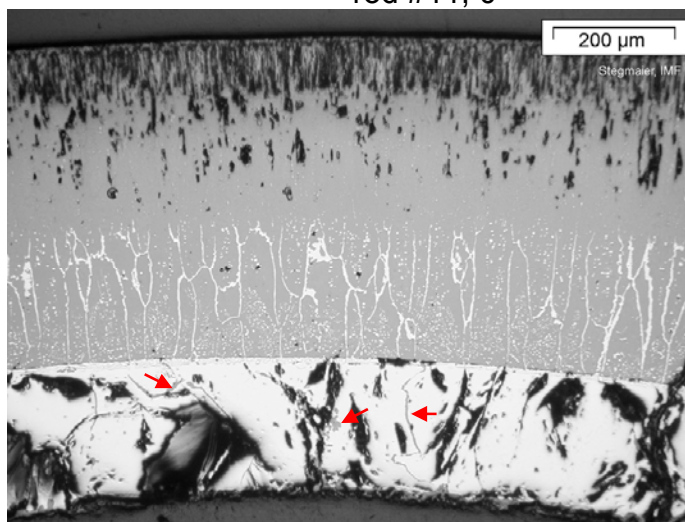


rod #11, 0°

ZrO₂ prior tetragonal

ZrO₂ prior cubic

α-Zr(O)



rod #19, 90°

ZrO₂ prior tetragonal

ZrO_{2-x} prior cubic

α-Zr(O)

Fig. 75: QUENCH-15; Cladding structure of rods #7, #11 and #19 at 950 mm: **oxide precipitates** inside α-Zr(O) layer.

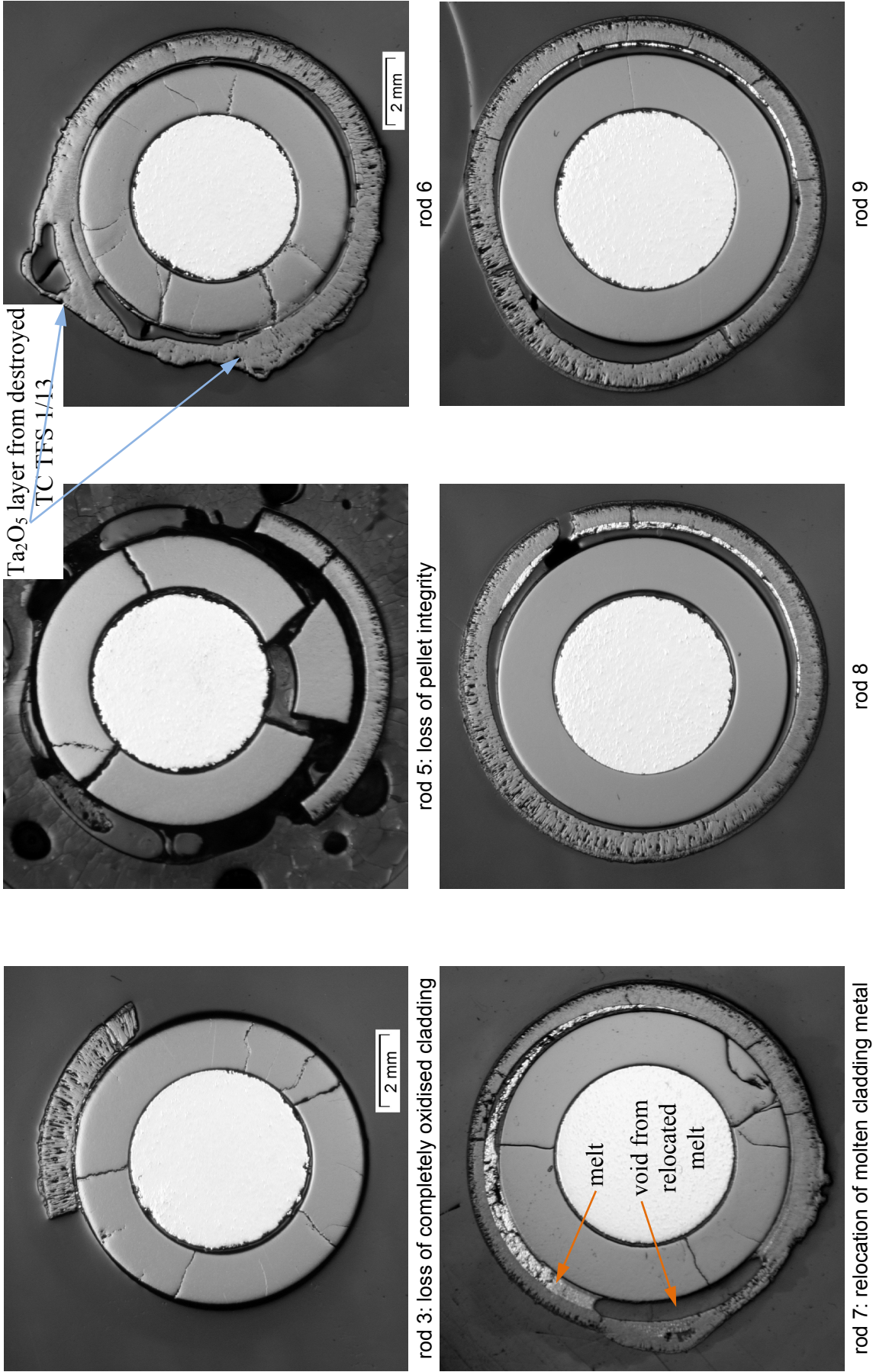
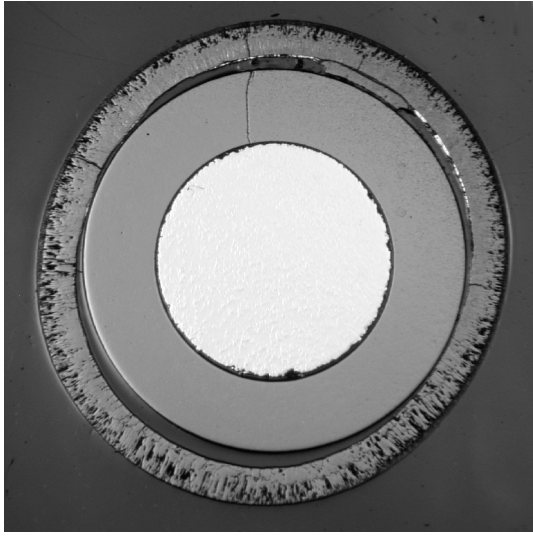
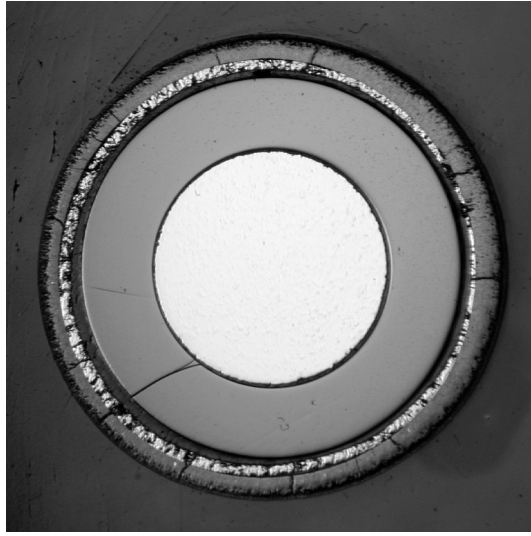


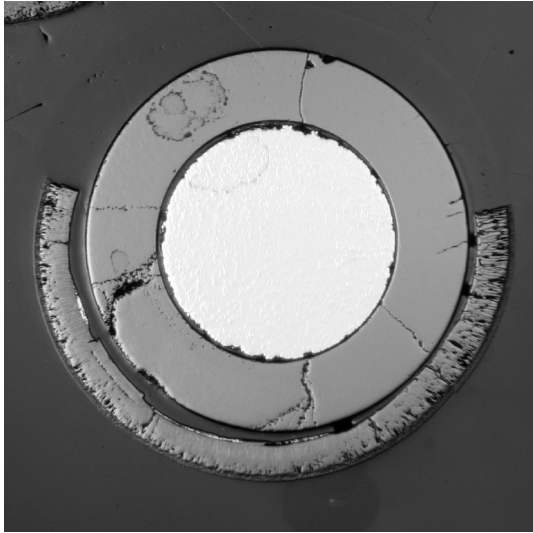
Fig. 76: QUENCH-15; Cross section at elevation 1000 mm depicting individual test rods 3-9.



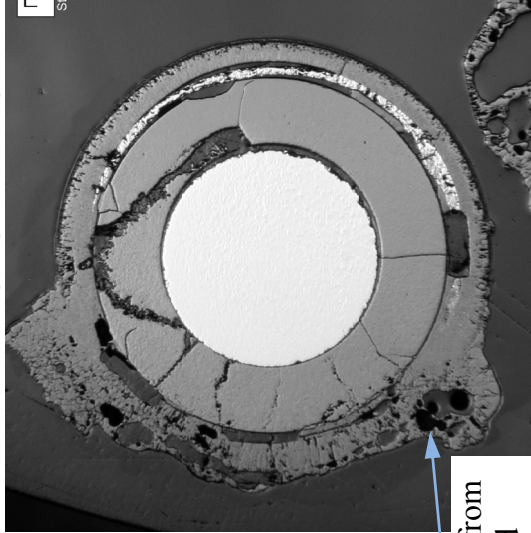
rod 13



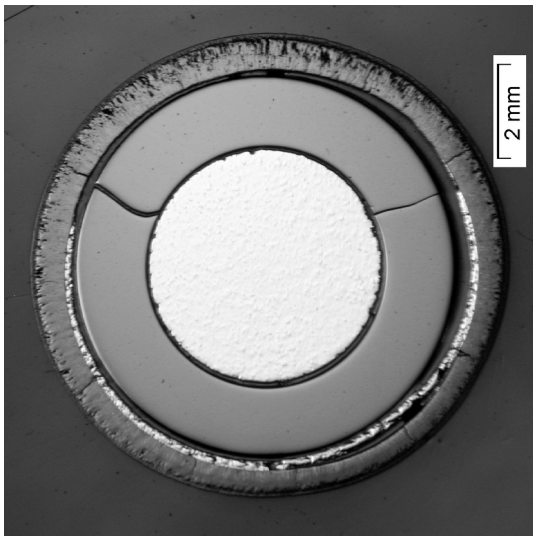
rod 19



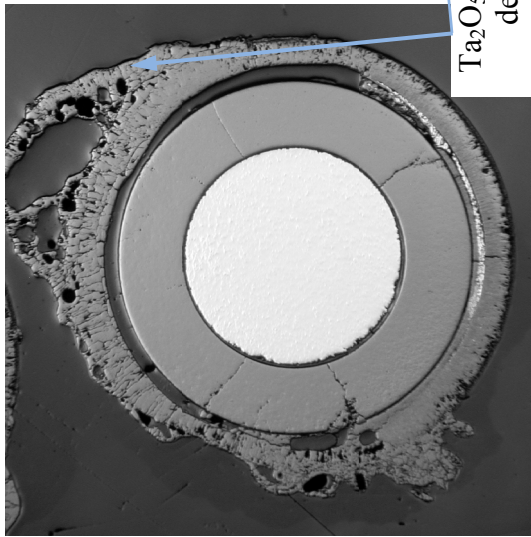
rod 11: loss of cladding segment during handling



rod 18



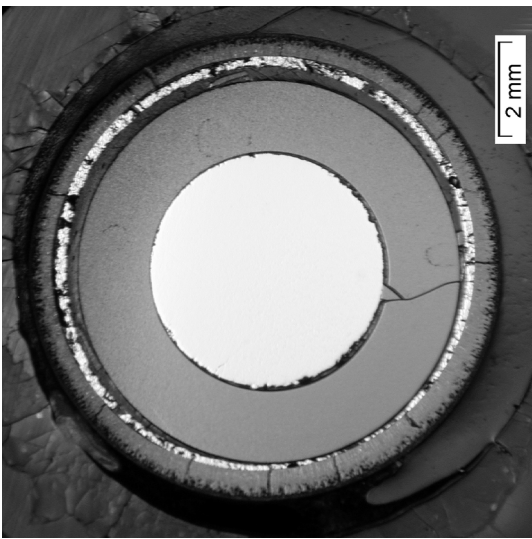
rod 10



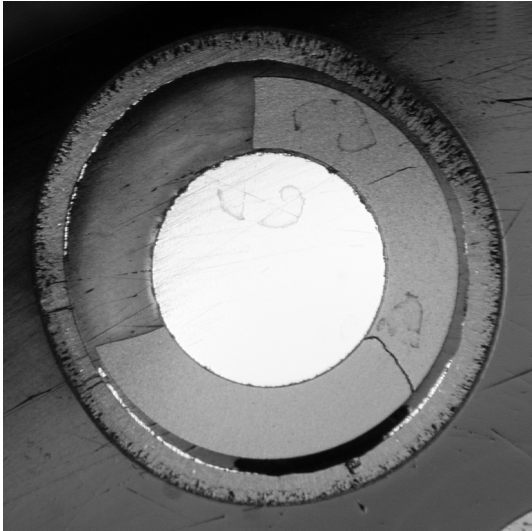
rod 17

Ta₂O₅ layer from destroyed TC TFS 17/13

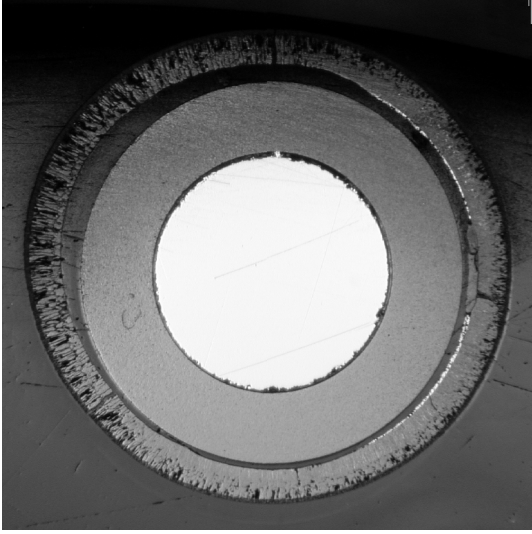
Fig. 77: QUENCH-15; Cross section at elevation 1000 mm depicting individual test rods 10-19.



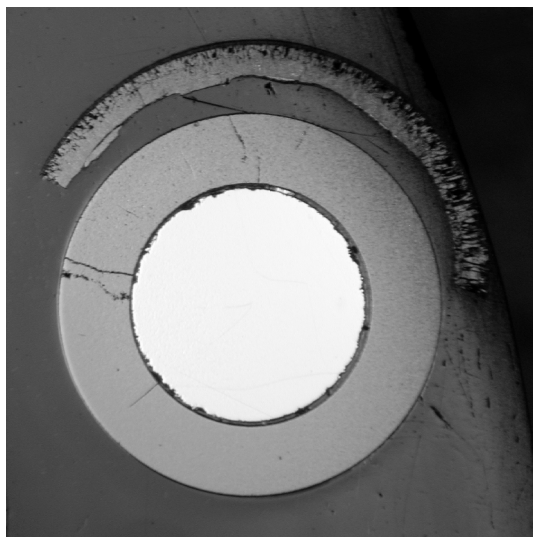
rod 20



rod 21

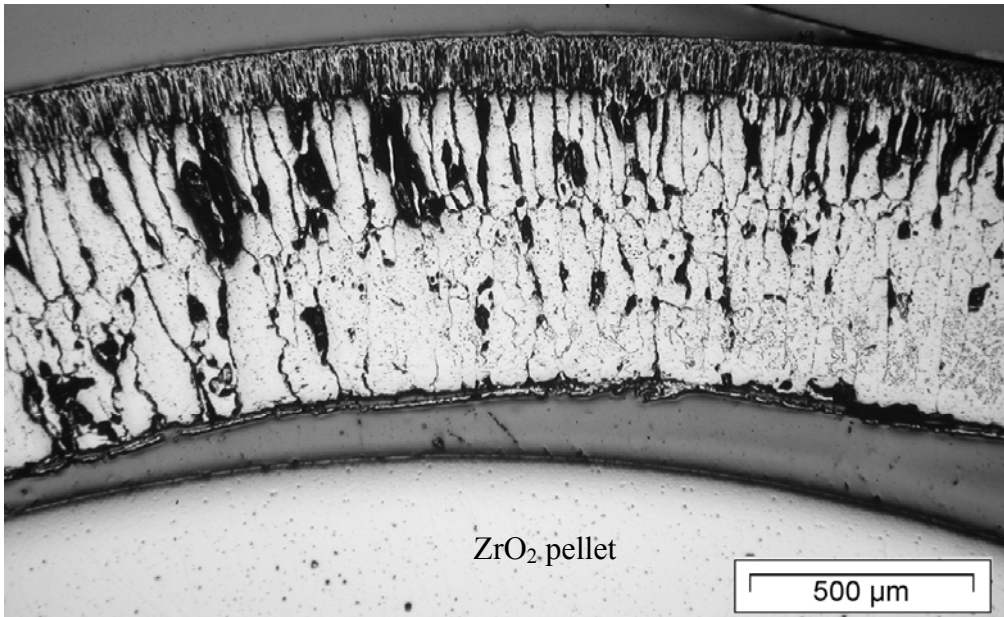


rod 22



rod 23: loss of cladding segment during handling

Fig. 78: QUENCH-15; Cross section at elevation 1000 mm depicting individual test rods 20-23.



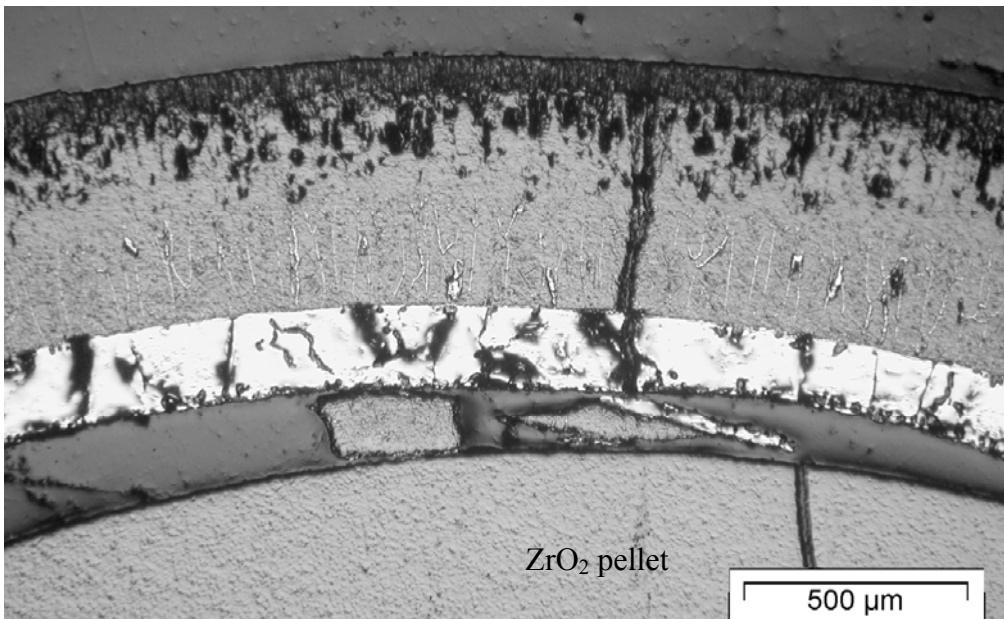
formed during
pre-oxidation
formed at
 $1450\text{K} < T < 1750\text{K}$

formed at
 $T > 1750\text{K}$

ZrO₂ pellet

500 μm

rod #9, 0°: prior tetragonal oxide



ZrO₂ prior
tetragonal

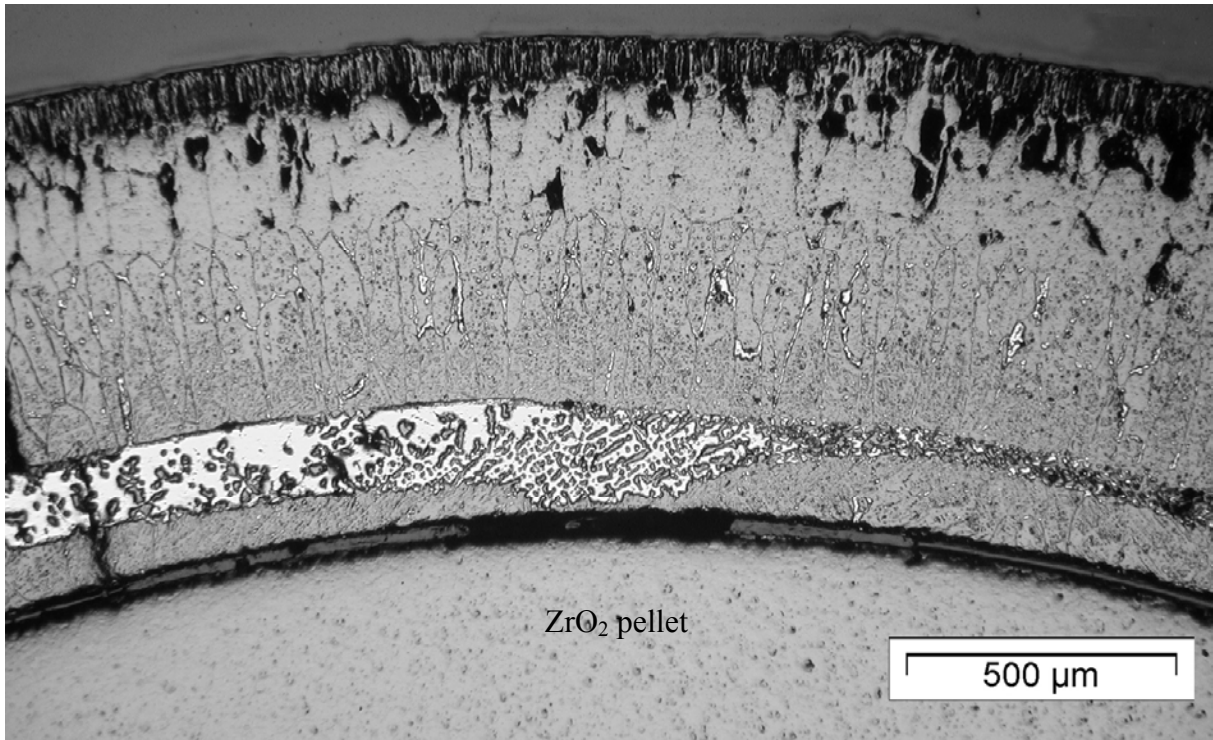
ZrO_{2-x} prior
cubic

ZrO₂ pellet

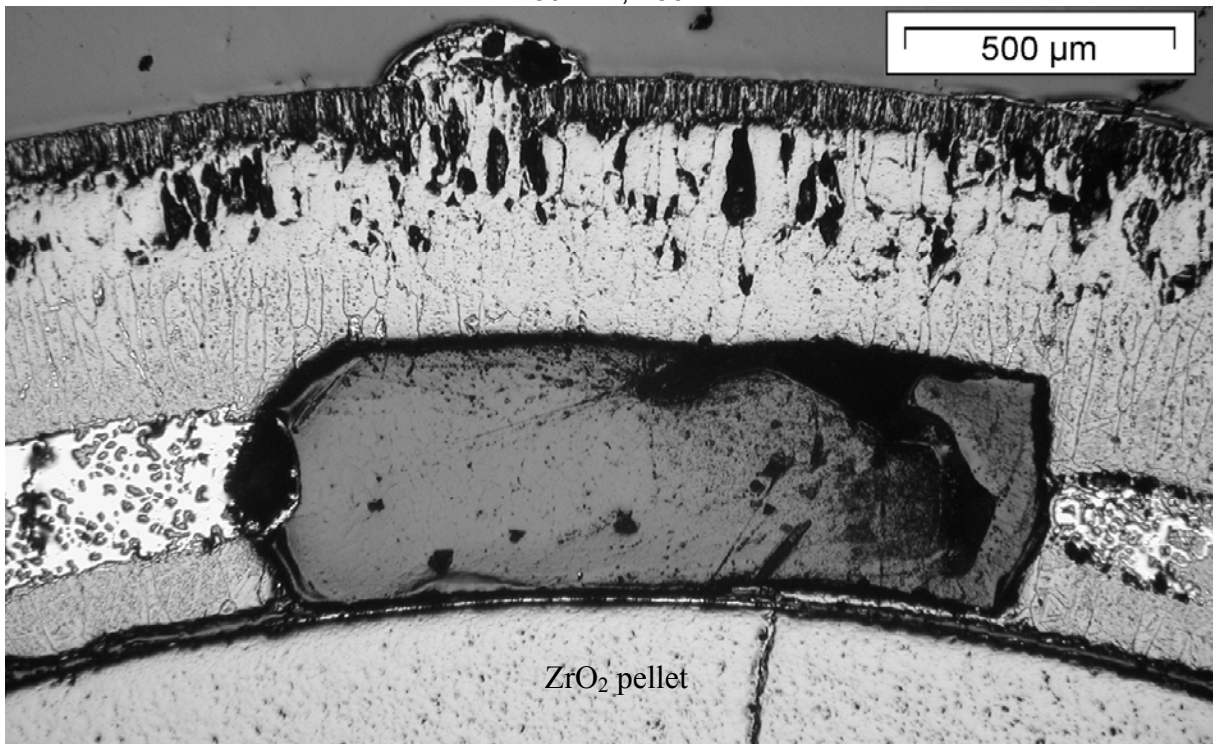
500 μm

rod #20, 180°: intensively oxidised cladding; pre-melted metal layer;
debris relocated inside gap

Fig. 79: QUENCH-15; Cladding structure of adjacent rods #9 and #20 at 1000 mm.



rod #17, 180°



rod #18, 180°:

Fig. 80: QUENCH-15; Cladding structure of adjacent rods #17 and #18 at 1000 mm: molten metallic layer; inner oxide layer; void formation due to melt relocated under outer oxide layer.

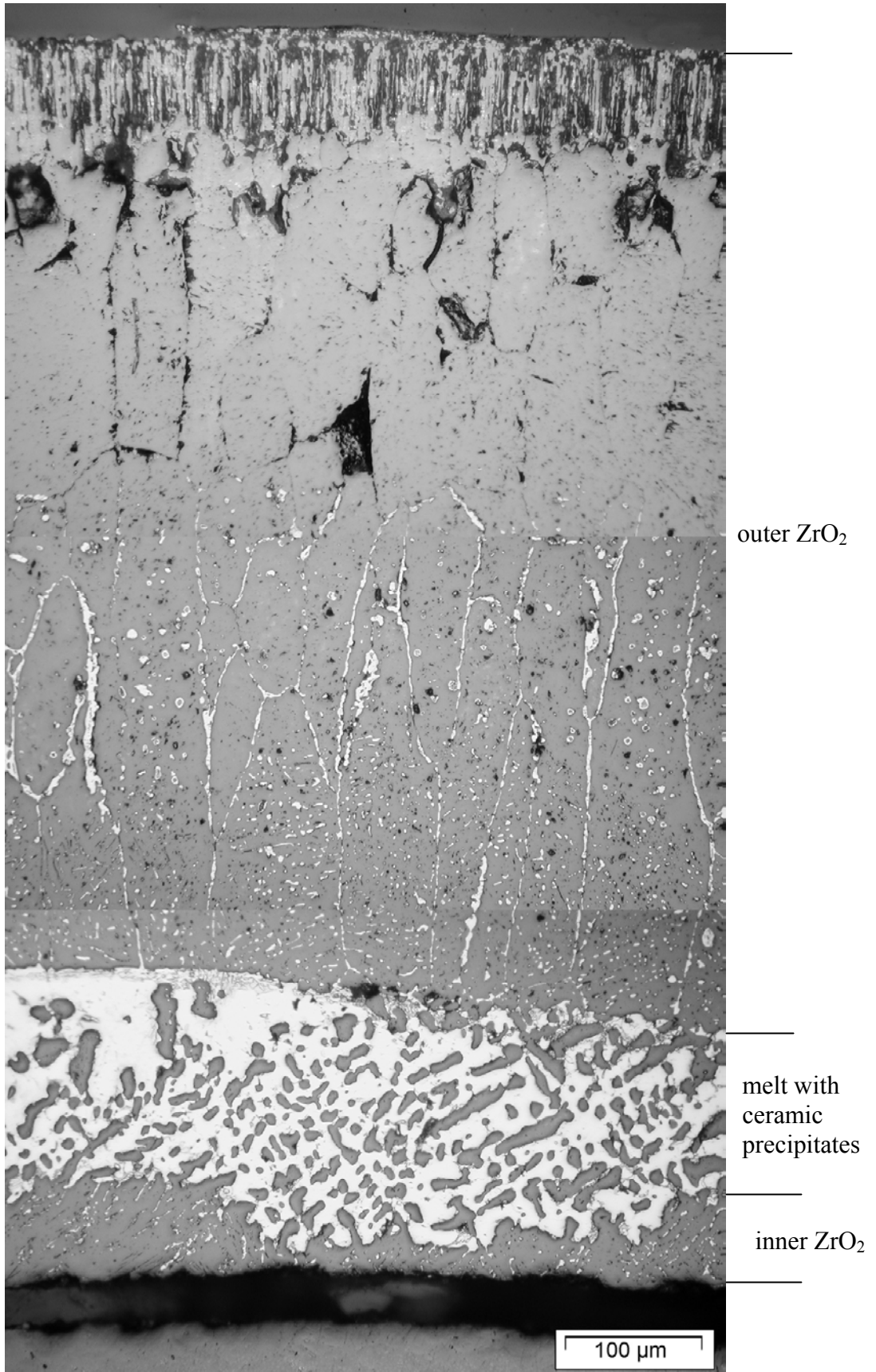
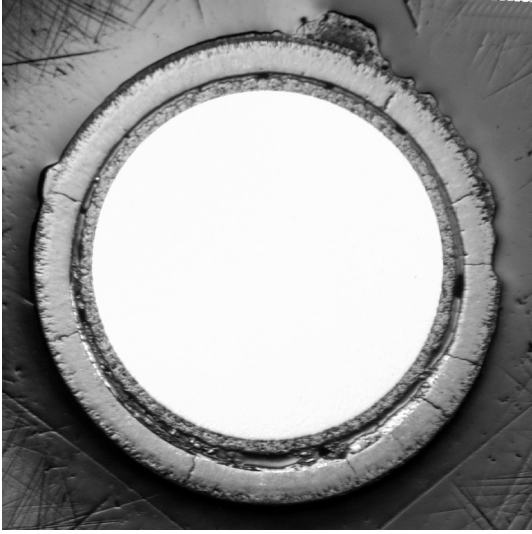
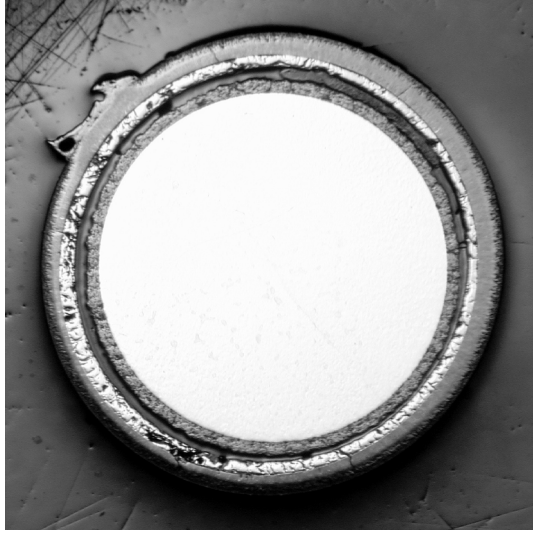


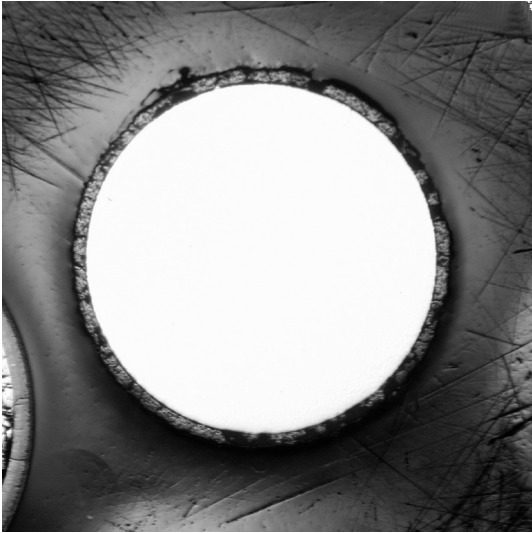
Fig. 81: QUENCH-15; Cladding structure of rod #17: oxidation of molten layer with ceramic precipitate formation at elevation of 1000 mm.



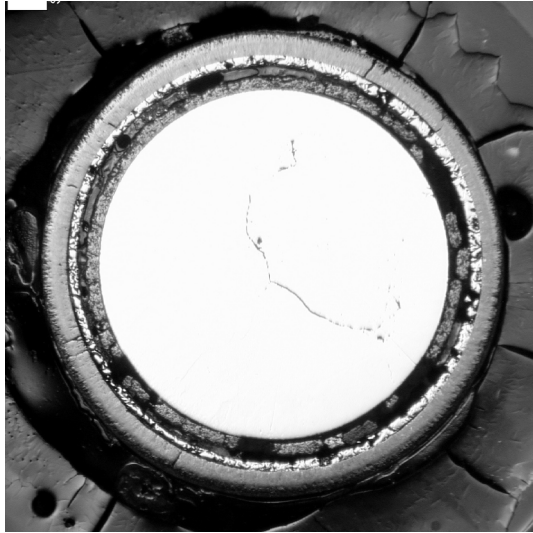
rod 3



rod 6



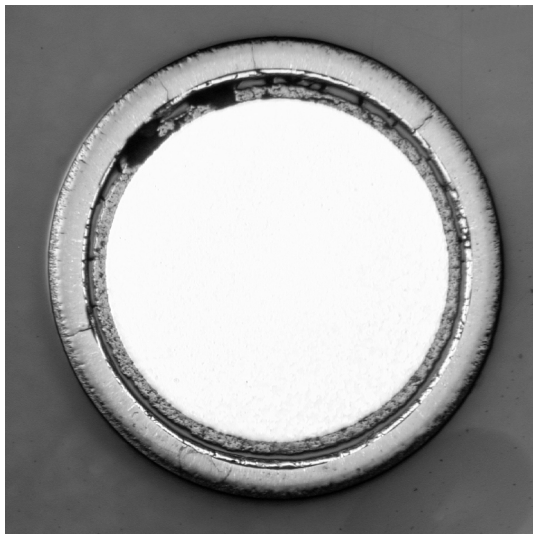
rod 2: loss of cladding during handling



rod 5



rod 1



rod 4

Fig. 82: QUENCH-15; Cross section at elevation 1050 mm depicting individual test rods 1-6.

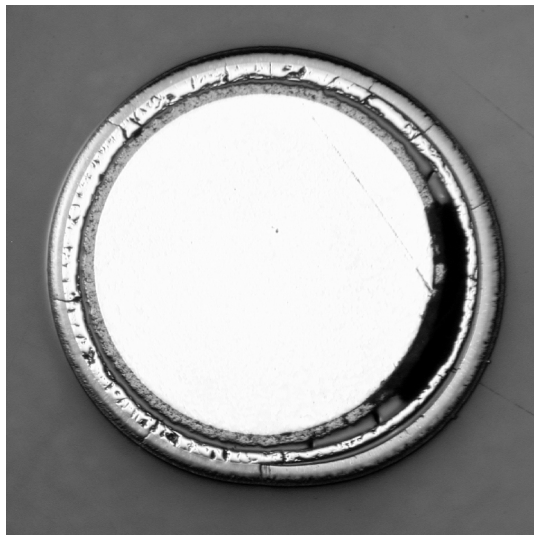
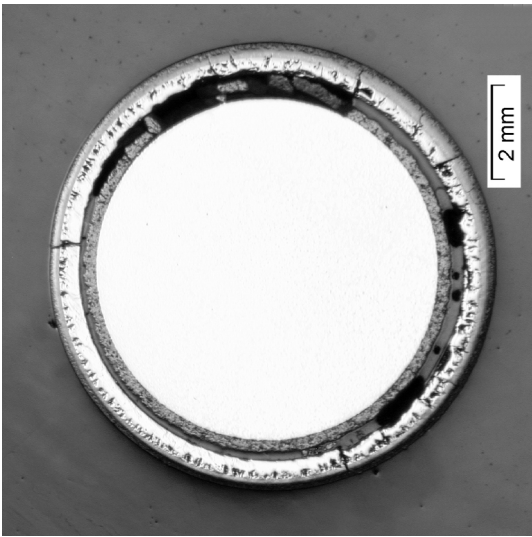
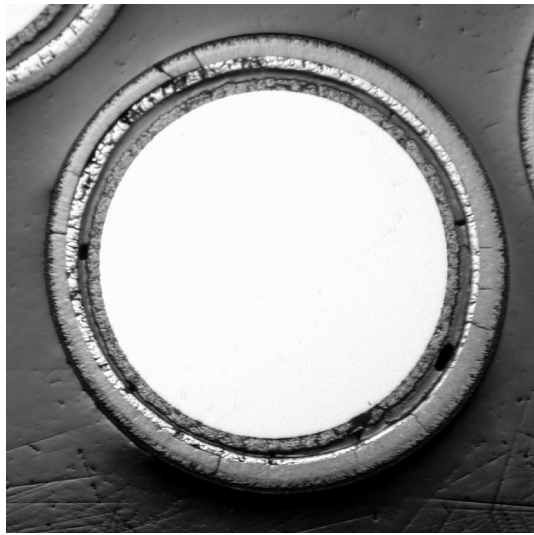
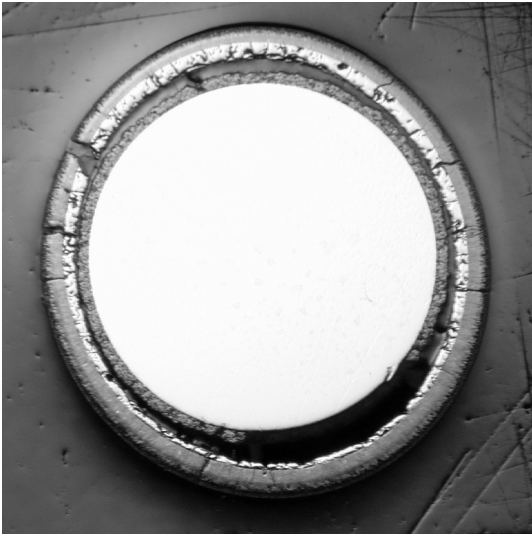
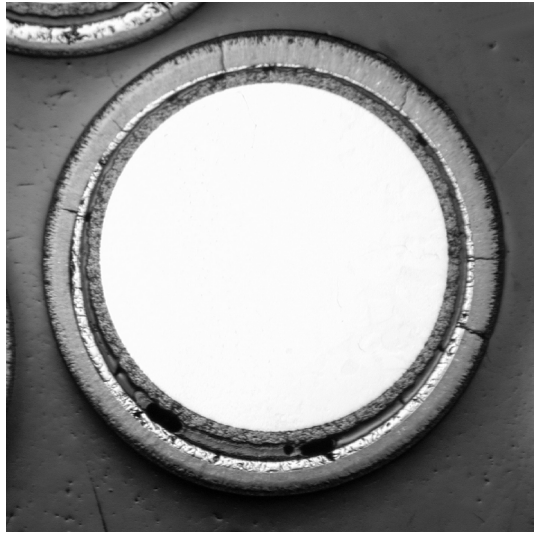
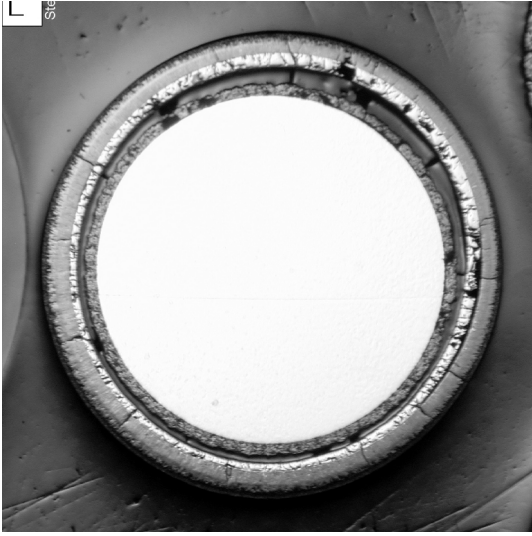
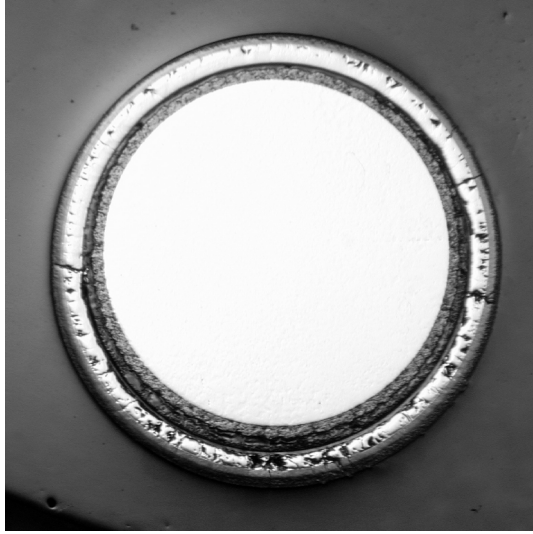


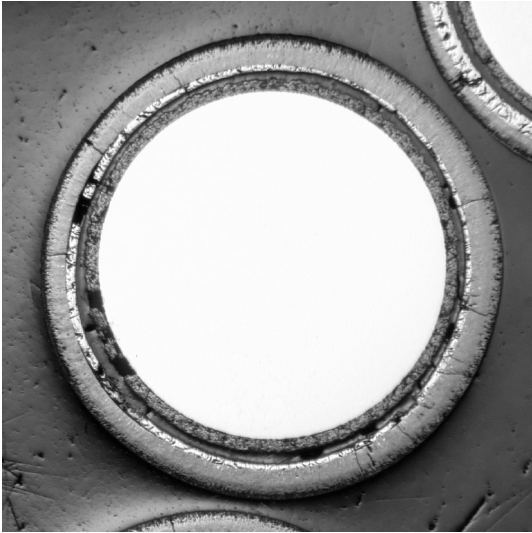
Fig. 83: QUENCH-15; Cross section at elevation 1050 mm depicting individual test rods 7-12.



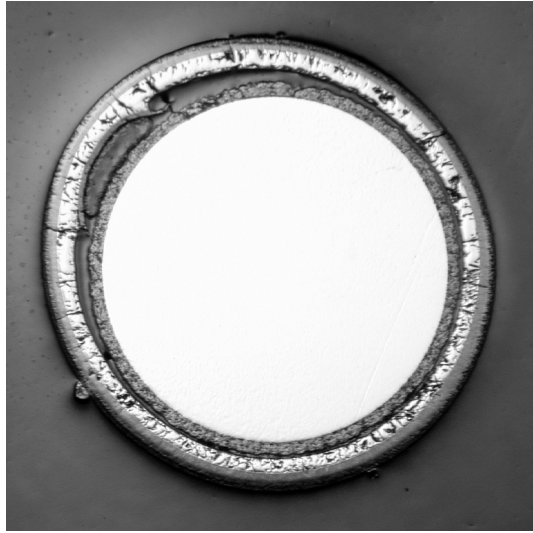
rod 15



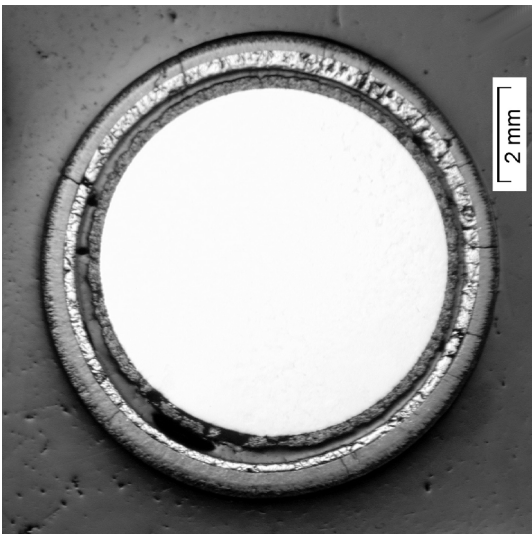
rod 18



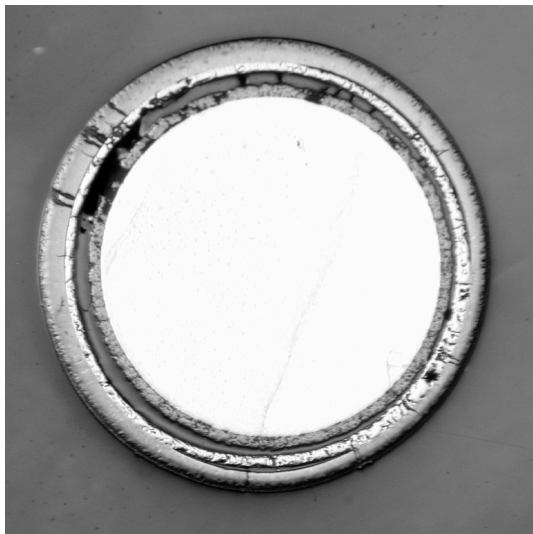
rod 14



rod 17

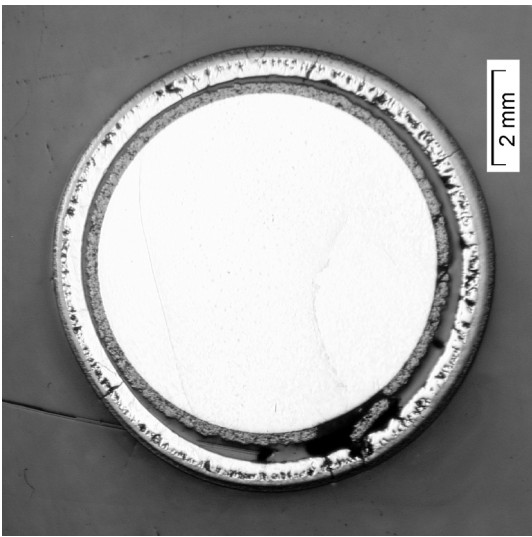


rod 13

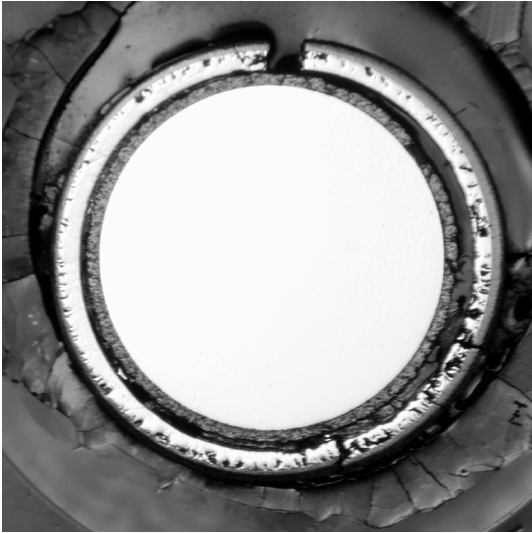


rod 16

Fig. 84: QUENCH-15; Cross section at elevation 1050 mm depicting individual test rods 13-18.



rod 19



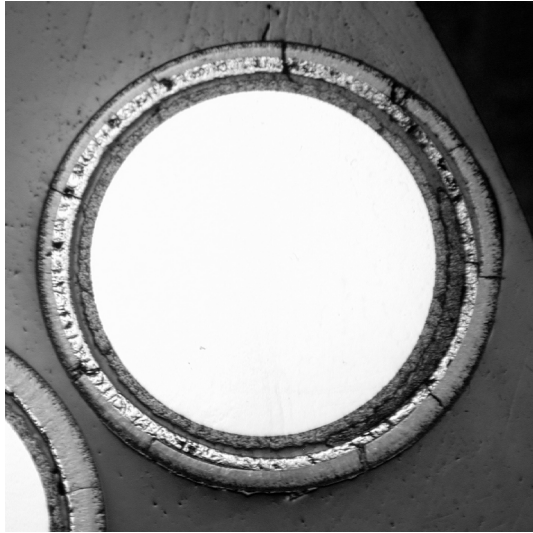
rod 20



rod 21

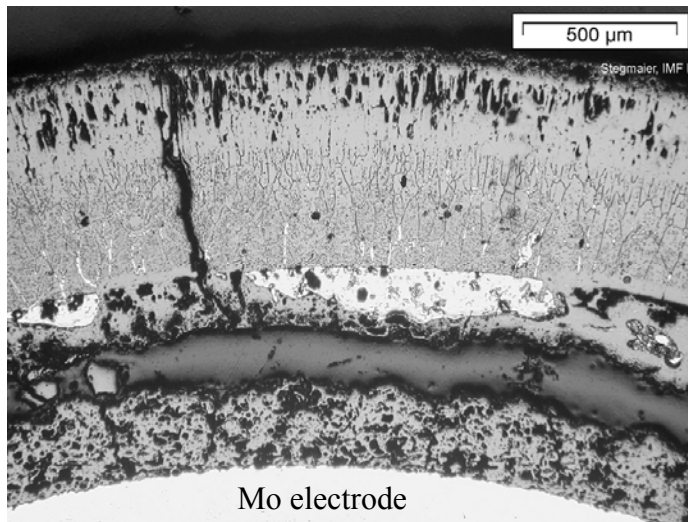


rod 22



rod 23

Fig. 85: QUENCH-15; Cross section at elevation 1050 mm depicting individual test rods 19-23.



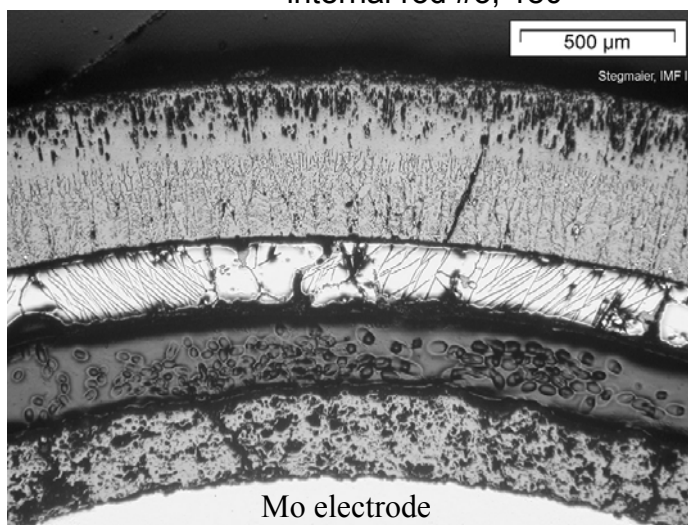
ZrO₂ prior tetragonal

ZrO_{2-x} prior cubic

prior molten α-Zr(O)
and inner oxide

epoxy

ZrO₂ coating



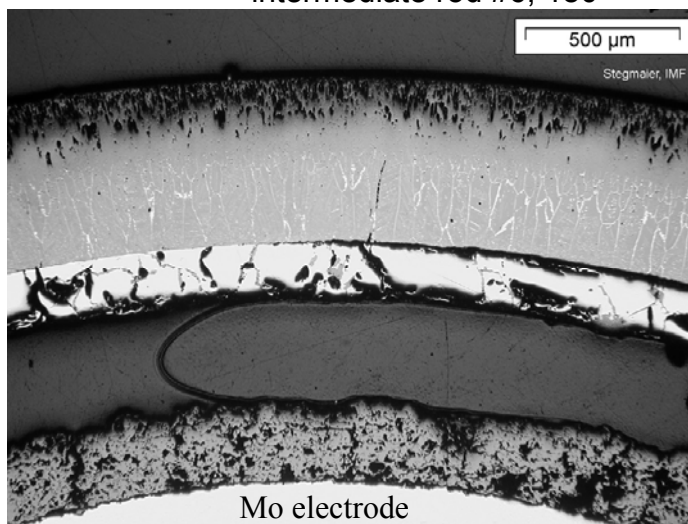
ZrO₂ prior tetragonal

ZrO₂ prior cubic

partially molten
α-Zr(O)

epoxy

ZrO₂ coating



ZrO₂ prior tetragonal

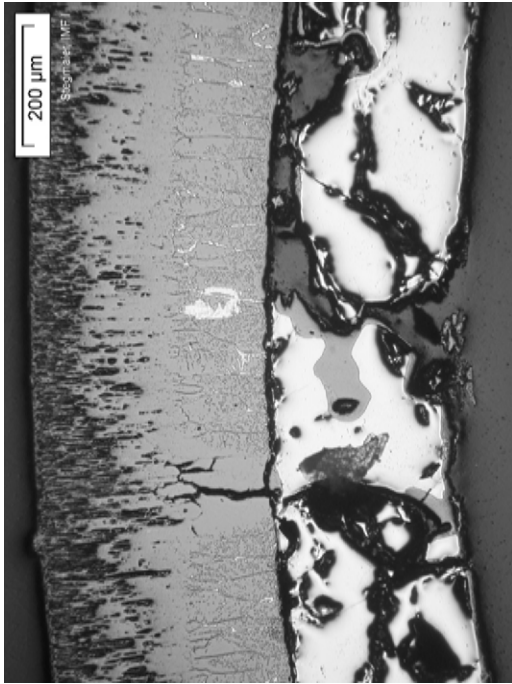
ZrO_{2-x} prior cubic

partially molten
α-Zr(O)

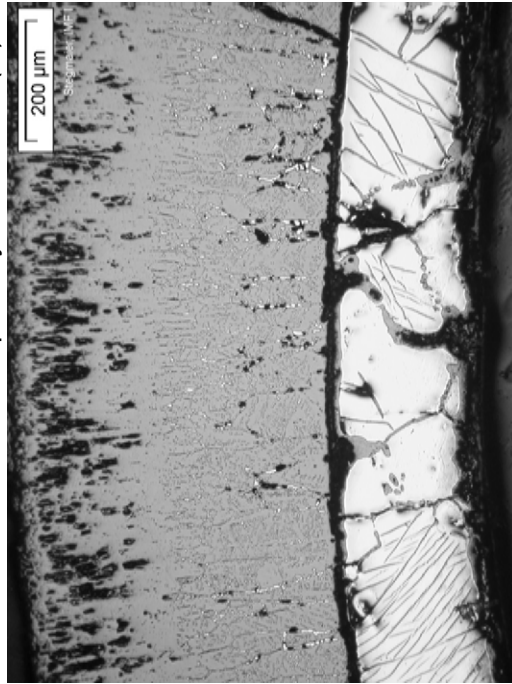
epoxy

ZrO₂ coating

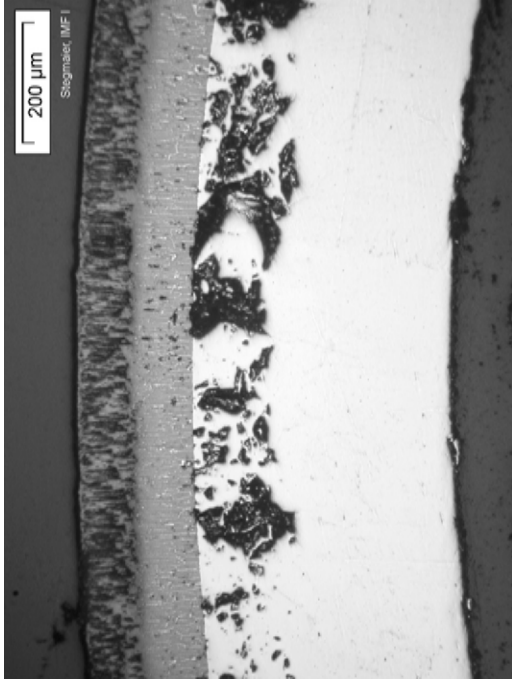
Fig. 86: QUENCH-15; Structure of rods #3, #6 and #16 at 1050 mm: partially molten α-Zr(O) layer.



rod 6, 90°: oxidation of partially molten α -Zr(O)



rod 6, 180°: oxidation of partially molten α -Zr(O)



rod 19, 0°: significant β -layer



rod 19, 180°: absence of β -layer

Fig. 87: QUENCH-15; Cross section at elevation 1050 mm depicting different oxidation degree for internal rod #6 and external rod #19.

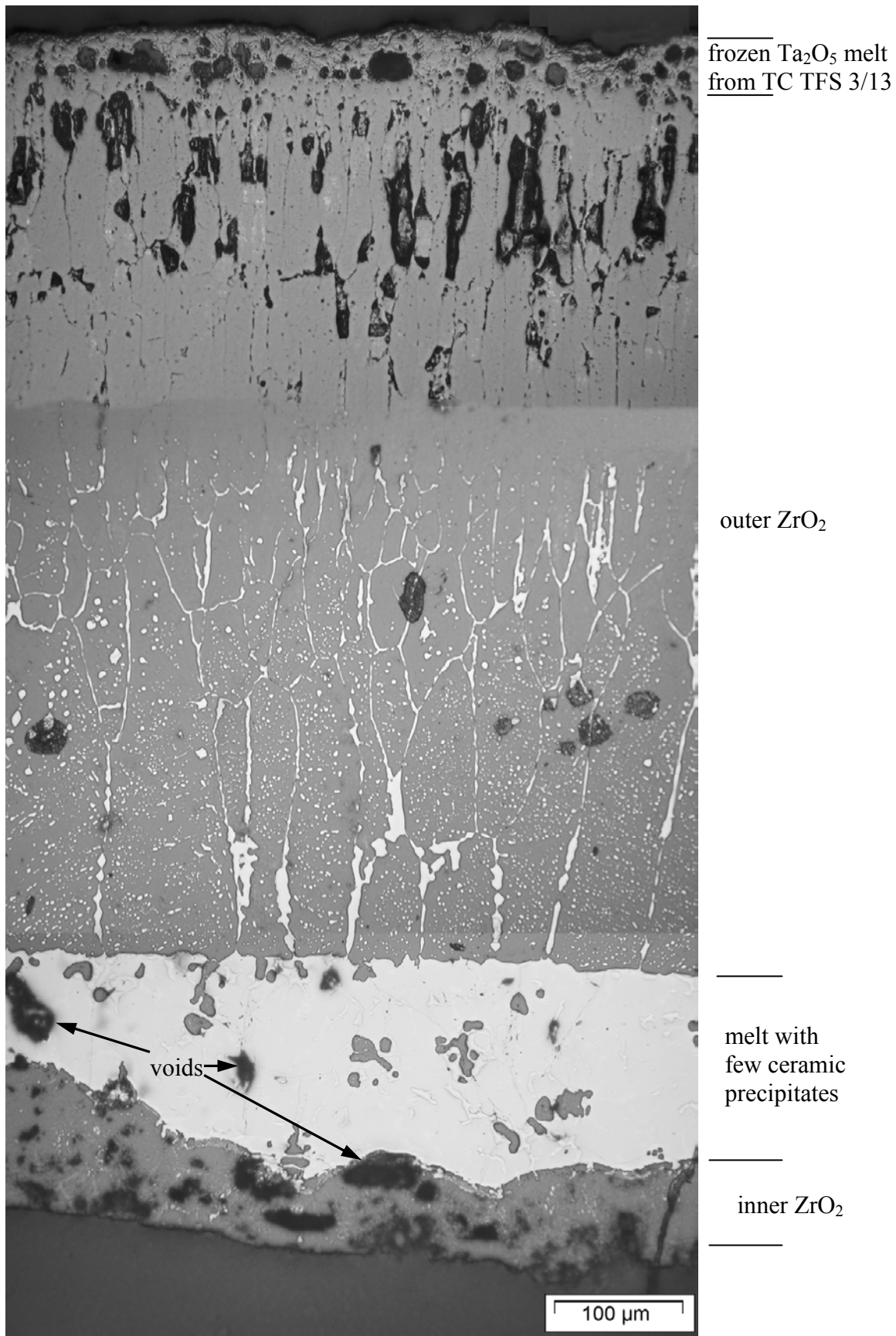


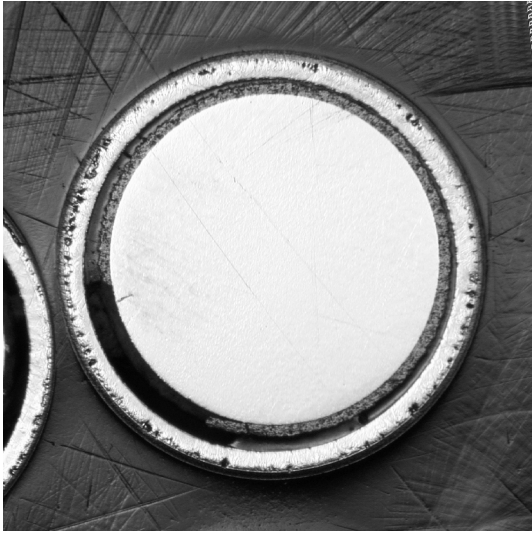
Fig. 88: QUENCH-15; Cladding structure of rod #3: oxidation of molten layer with inner oxide formation at elevation of 1050 mm.



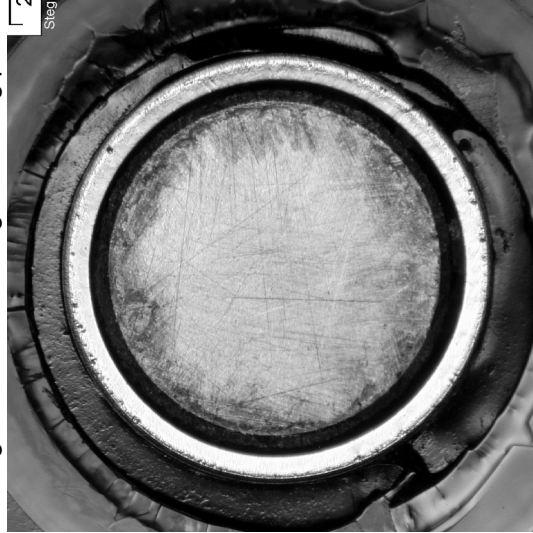
rod 3



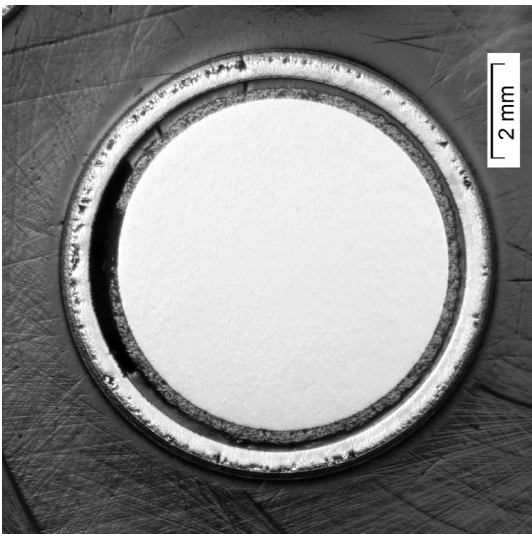
rod 6



rod 2: segment of Mo coating lost during polishing



rod 5

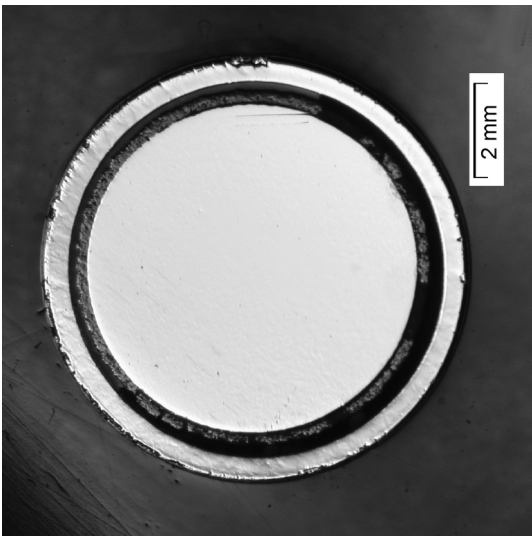


rod 1



rod 4

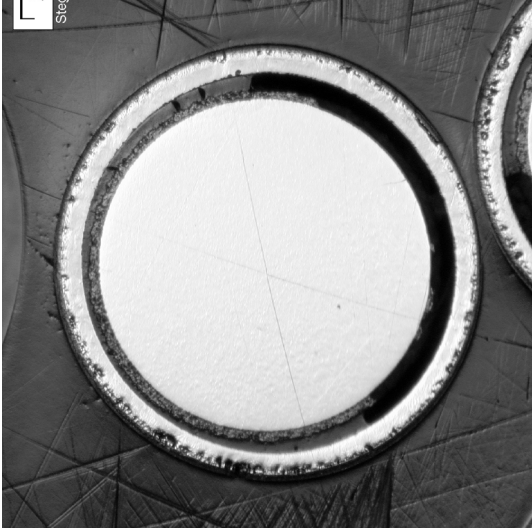
Fig. 89: QUENCH-15; Cross section at elevation 1150 mm depicting individual test rods 1-6.



rod 7



rod 8: Mo coating lost during polishing



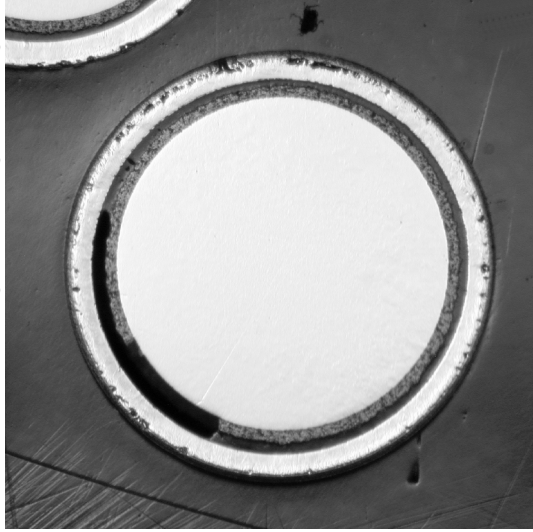
rod 9: Mo coating lost during polishing



rod 10: Mo coating lost during polishing

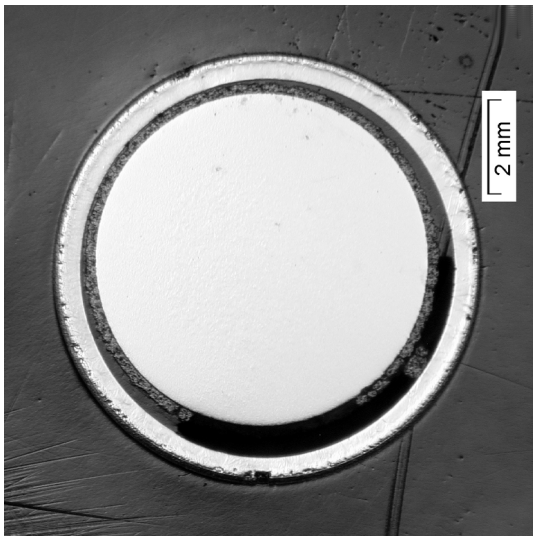


rod 11: Mo coating lost during polishing

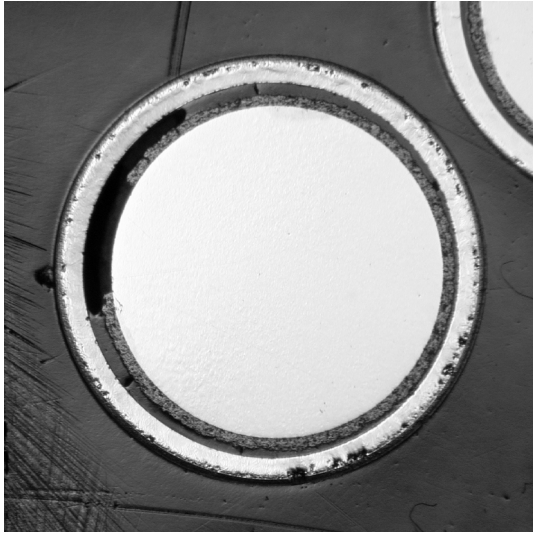


rod 12: Mo coating lost during polishing

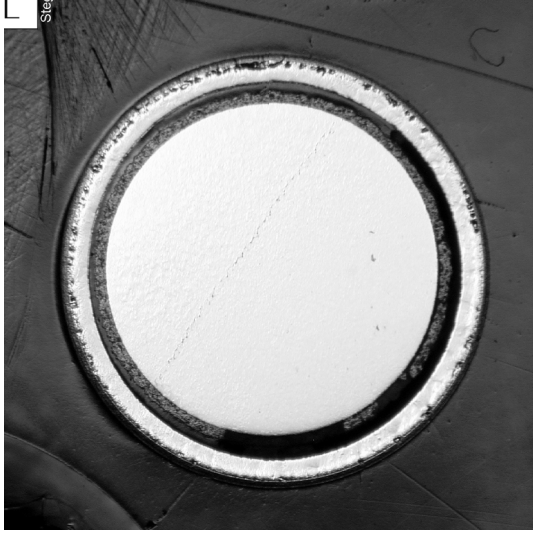
Fig. 90: QUENCH-15; Cross section at elevation 1150 mm depicting individual test rods 7-12.



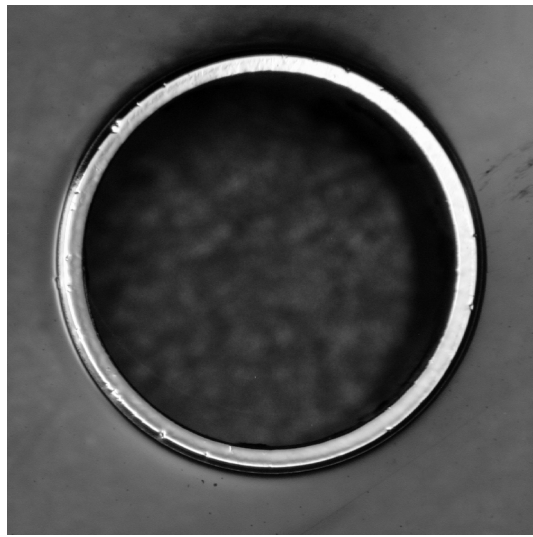
rod 13



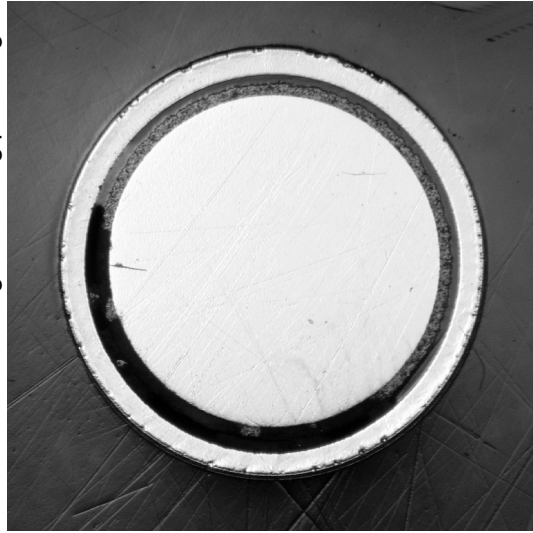
rod 14: Mo coating lost during polishing



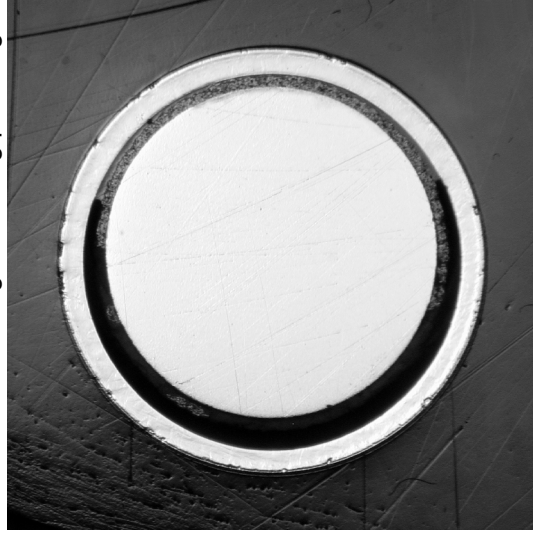
rod 15: Mo coating lost during polishing



cladding of rod 16

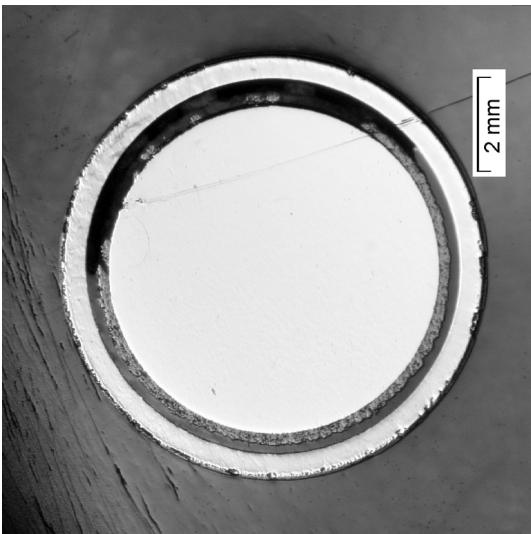


rod 17: Mo coating lost during polishing

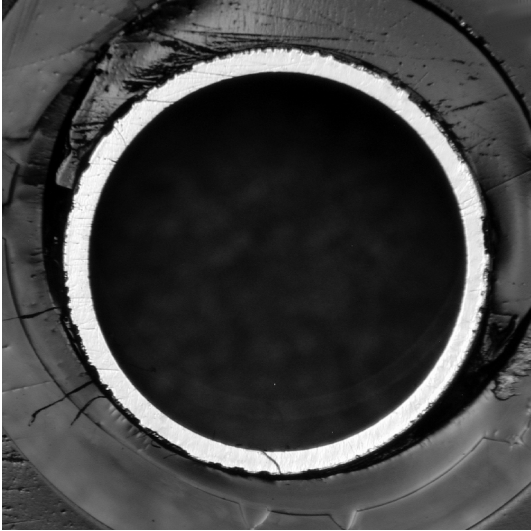


rod 18: Mo coating lost during polishing

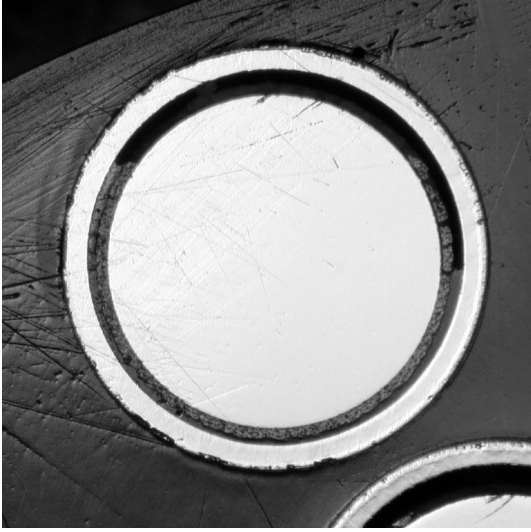
Fig. 91: QUENCH-15; Cross section at elevation 1150 mm depicting individual test rods 13-18.



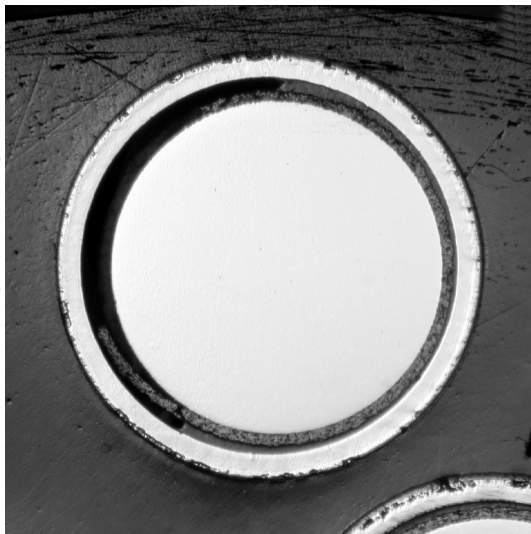
rod 19: Mo coating lost during polishing



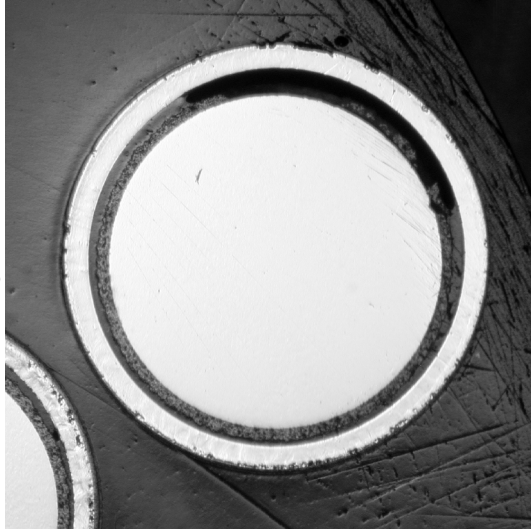
cladding of rod 20



rod 21: Mo coating lost during polishing



rod 22: Mo coating lost during polishing



rod 23: Mo coating lost during polishing

Fig. 92: QUENCH-15; Cross section at elevation 1150 mm depicting individual test rods 19-23.

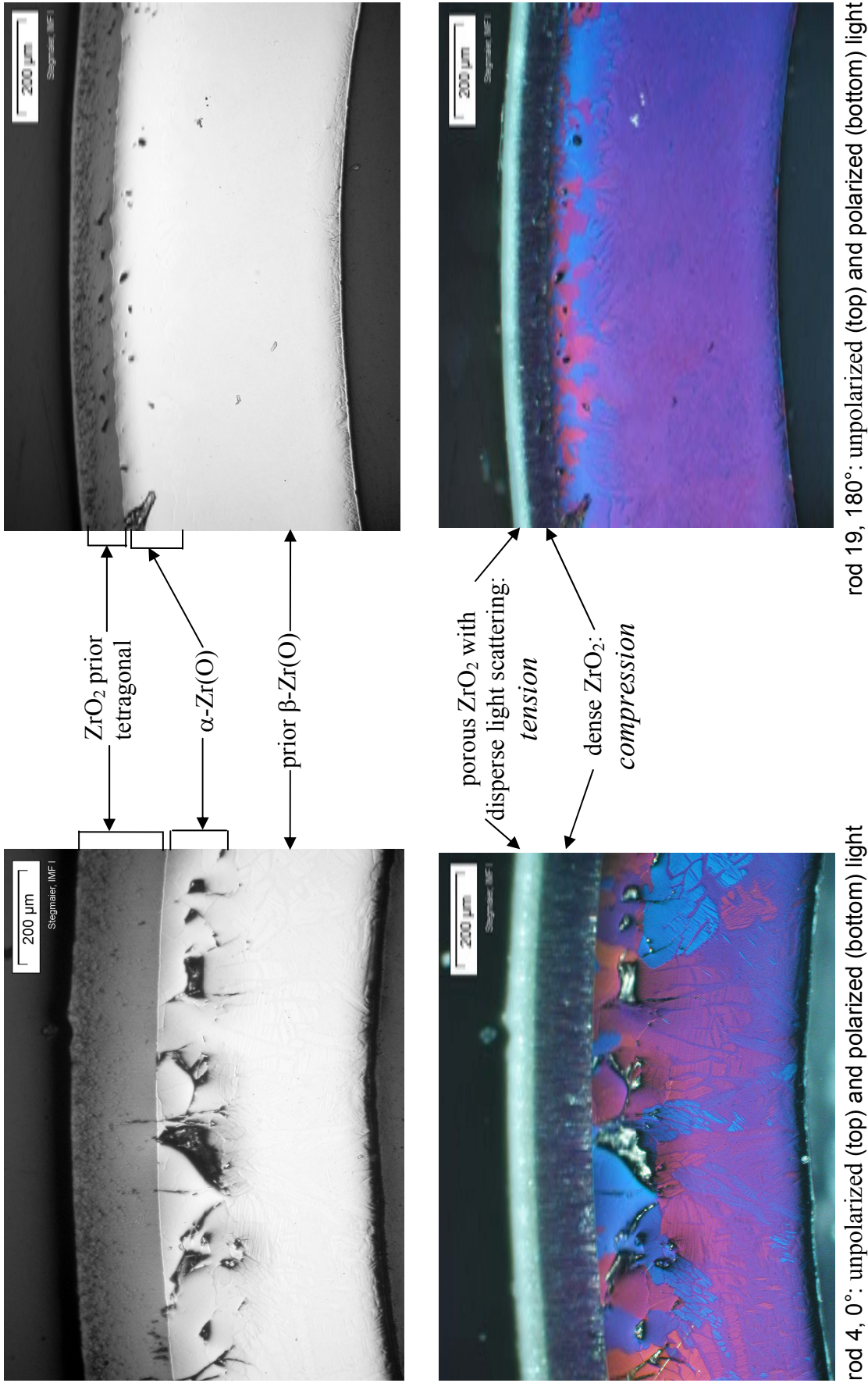
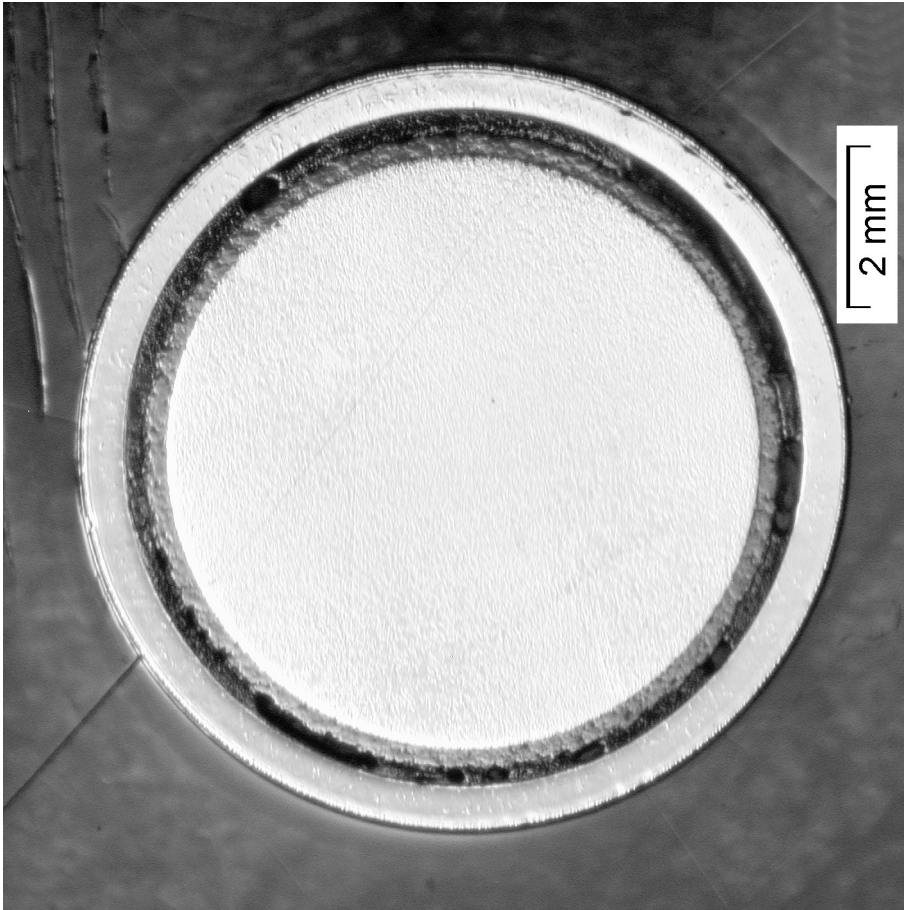


Fig. 93: QUENCH-15; Cross section at elevation 1150 mm depicting morphology of cladding layers for internal rod #4 and external rod #19. Two difference ZrO_2 sub-layers due to tensile and compressive stress.

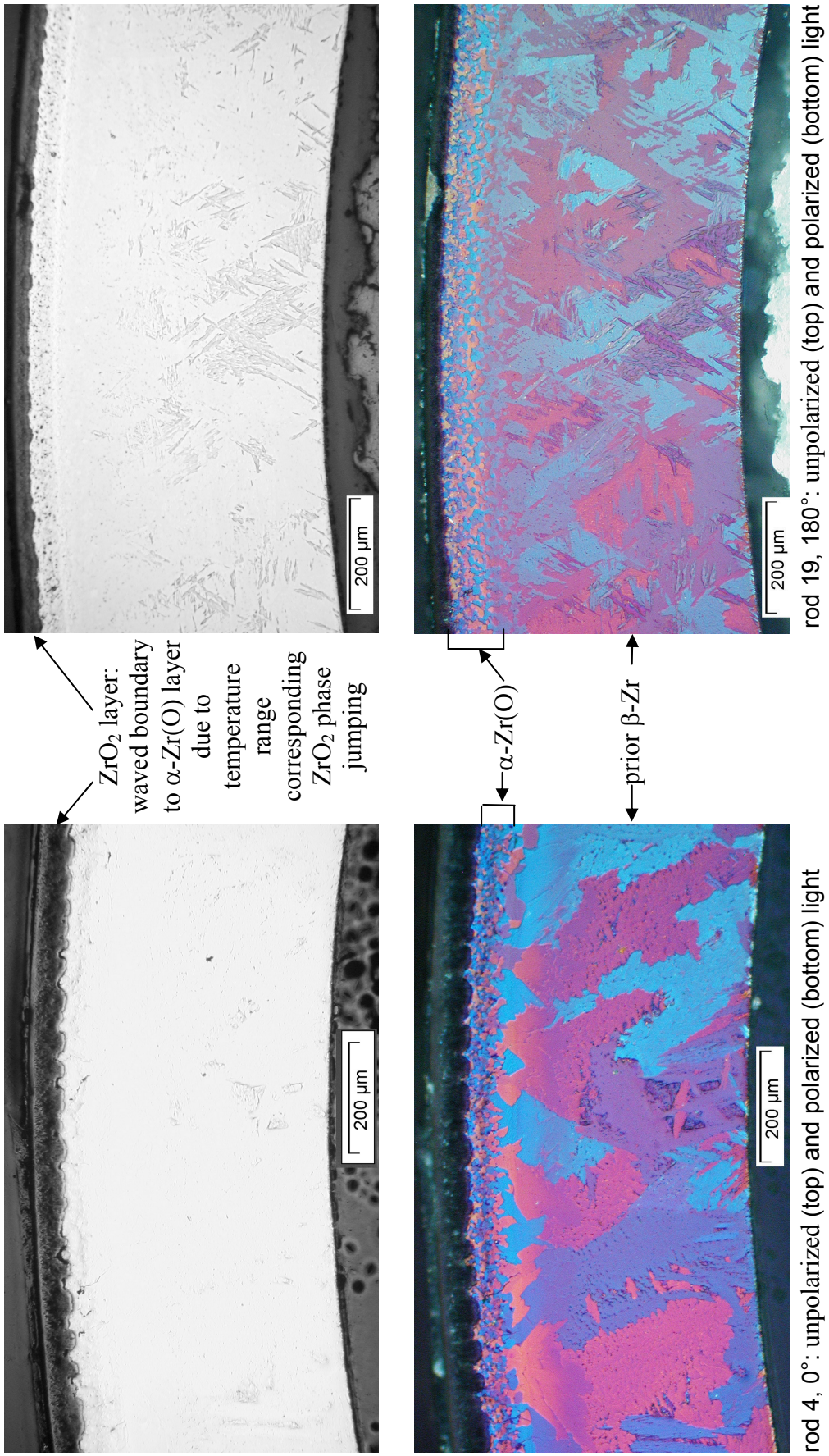


internal rod 4



external rod 19

Fig. 94: QUENCH-15; Cross section at elevation 1250 mm depicting individual test rods 4, 19.



rod 4, 0°: unpolarized (top) and polarized (bottom) light

rod 19, 180°: unpolarized (top) and polarized (bottom) light

Fig. 95: QUENCH-15; Cross section at elevation 1250 mm depicting morphology of cladding layers for internal rod #4 and external rod #19. Waved boundary between ZrO₂ and α-Zr(O) layers.

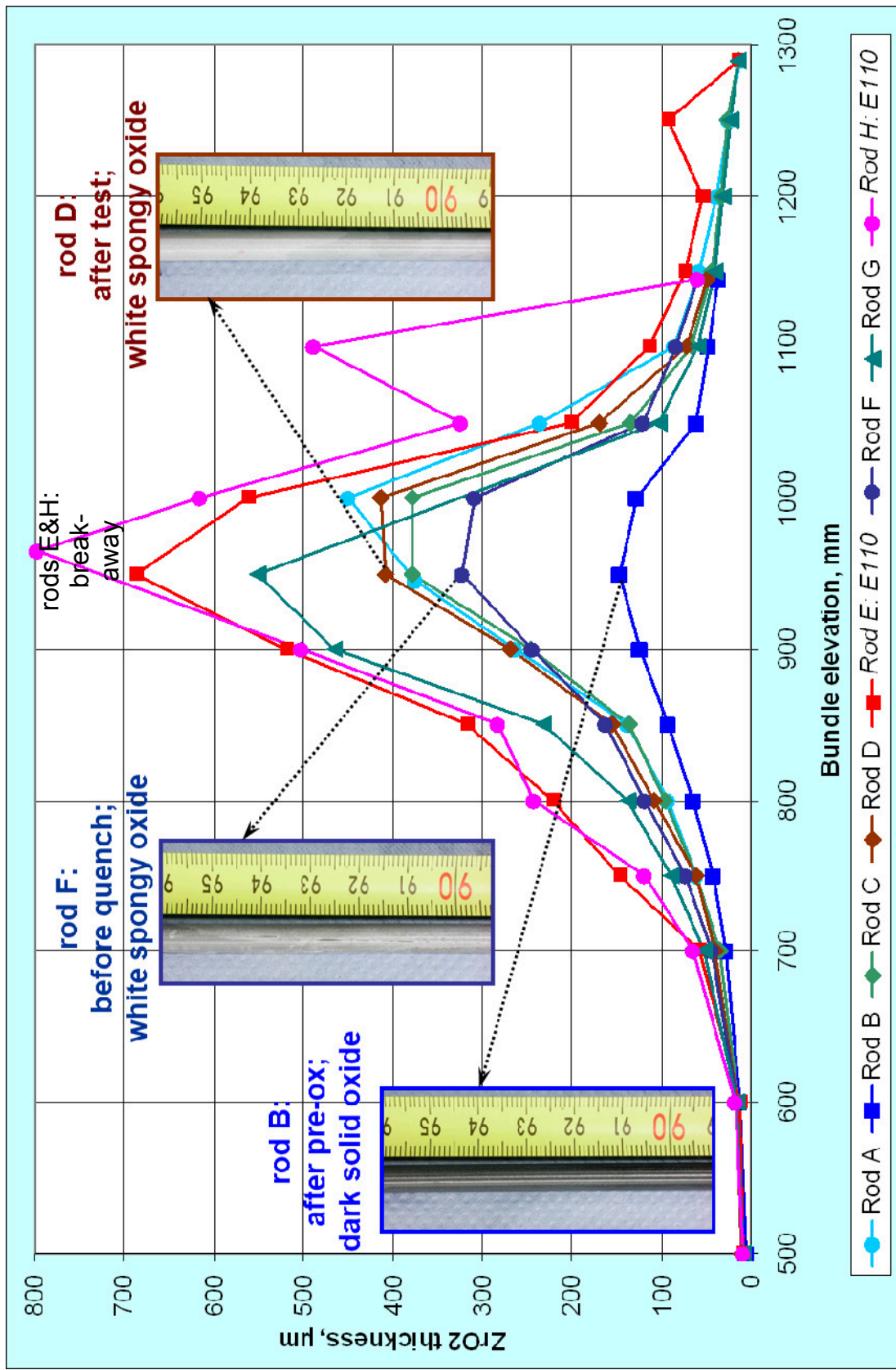


Fig. 96: QUENCH-15; axial distribution of ZrO₂ for corner rods. Eddy current measurement.

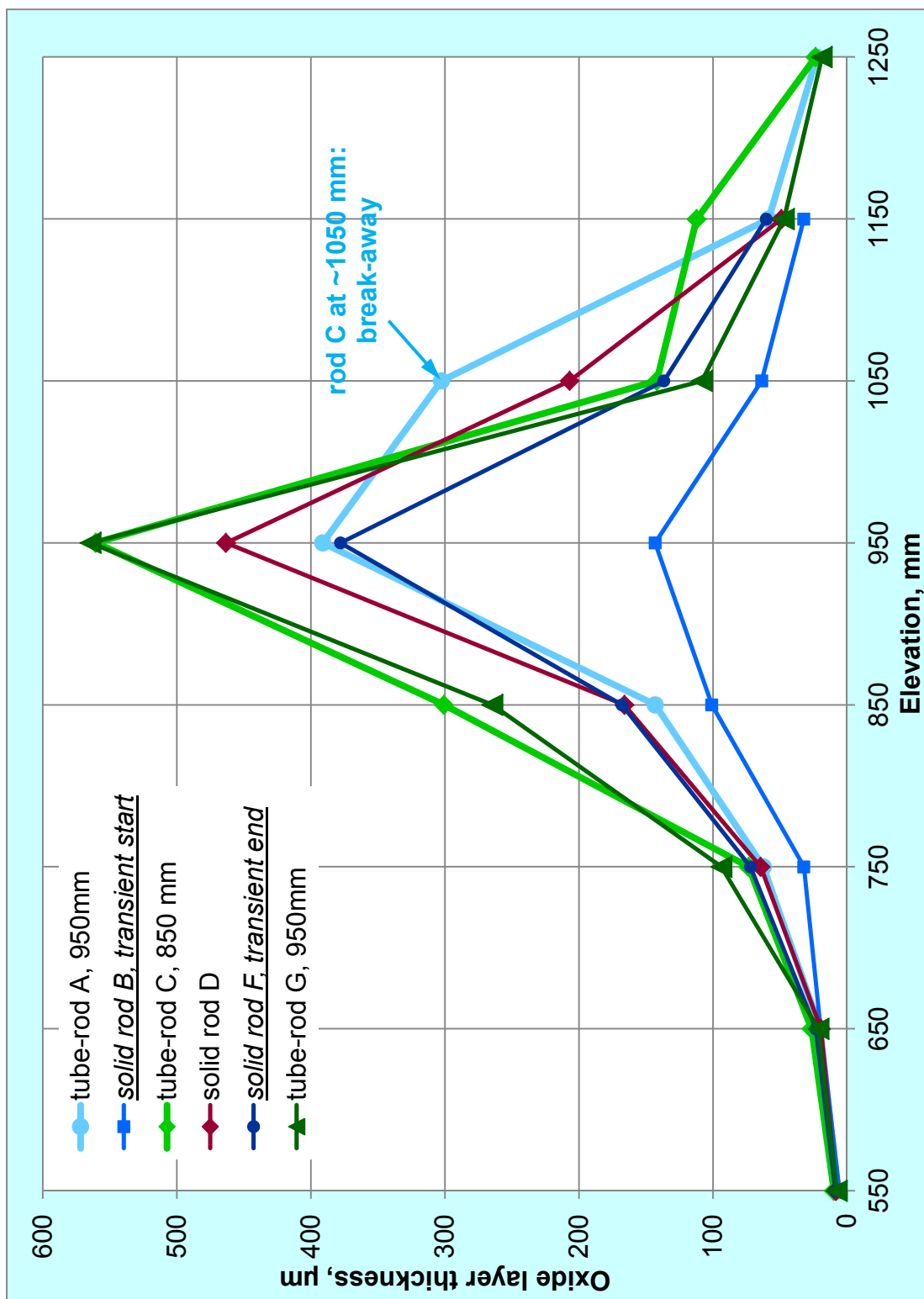


Fig. 97: QUENCH-15; axial distribution of ZrO₂ for Zry-4 corner rods. Metallographic results.

- oxide scale gone

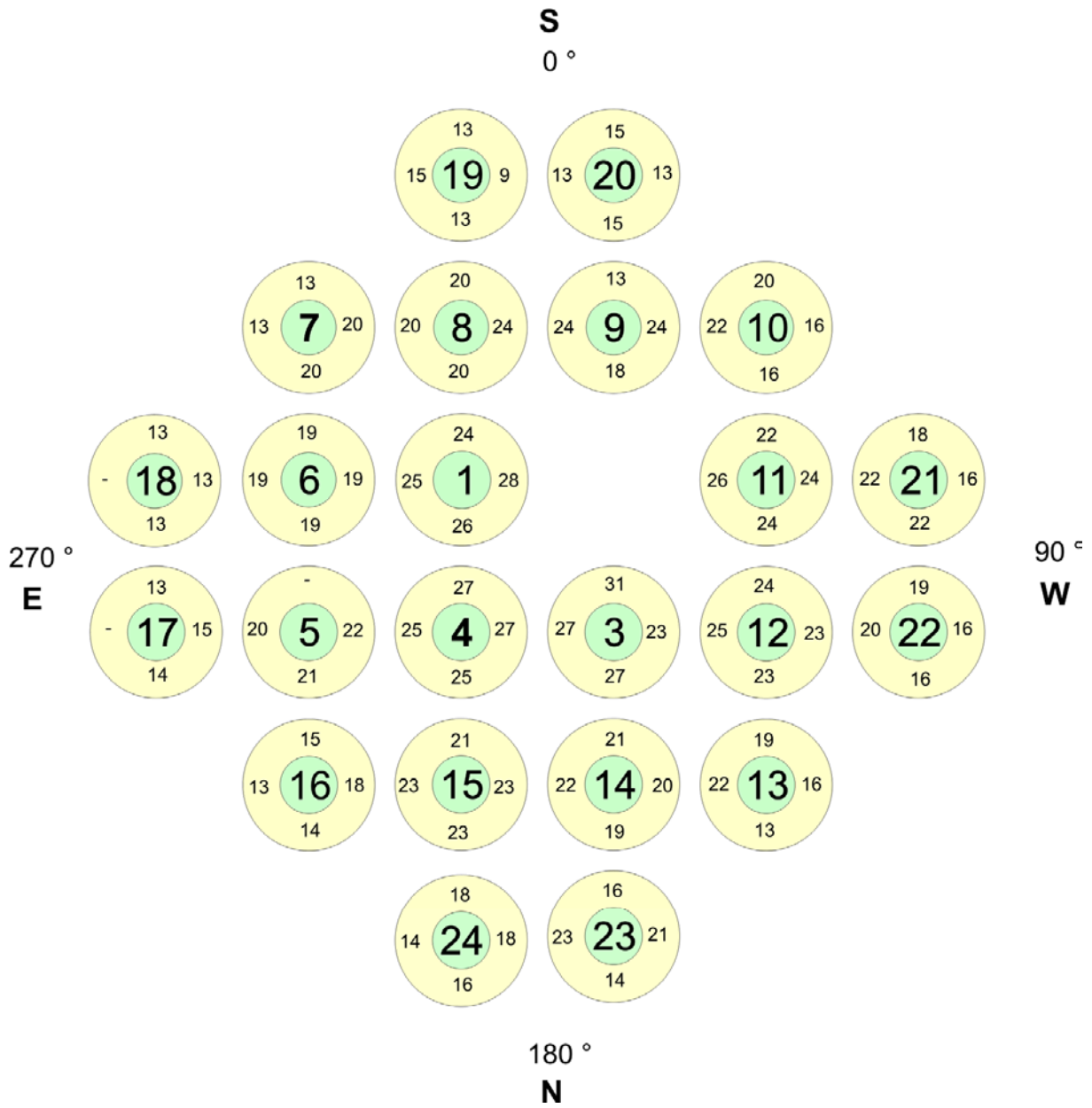


Fig. 98 -QUE15 cross section 15-550.doc
02.03.11 - IMF

Fig. 98: QUENCH-15; Oxide layer thickness at bundle elevation 550 mm (Cross section QUE-15-550).

- oxide scale gone

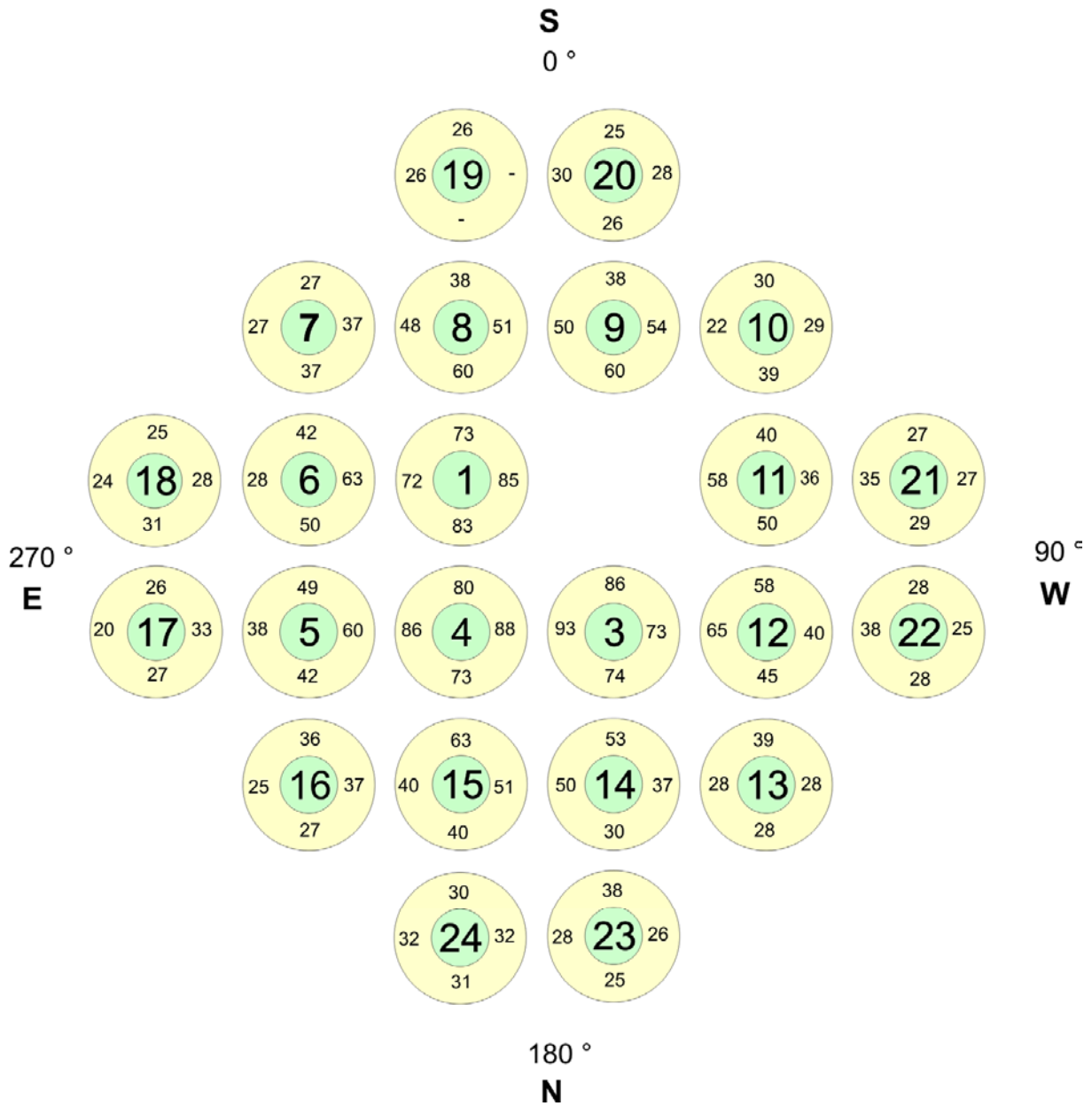


Fig. 99 -QUE15 cross section 15-650.doc
02..03.11 - IMF

Fig. 99: QUENCH-15; Oxide layer thickness at bundle elevation 650 mm (Cross section QUE-15-650).

- oxide scale gone

17 Rods that were at first removed from the bundle and later put back for embedding. Therefore the orientation is unsure.

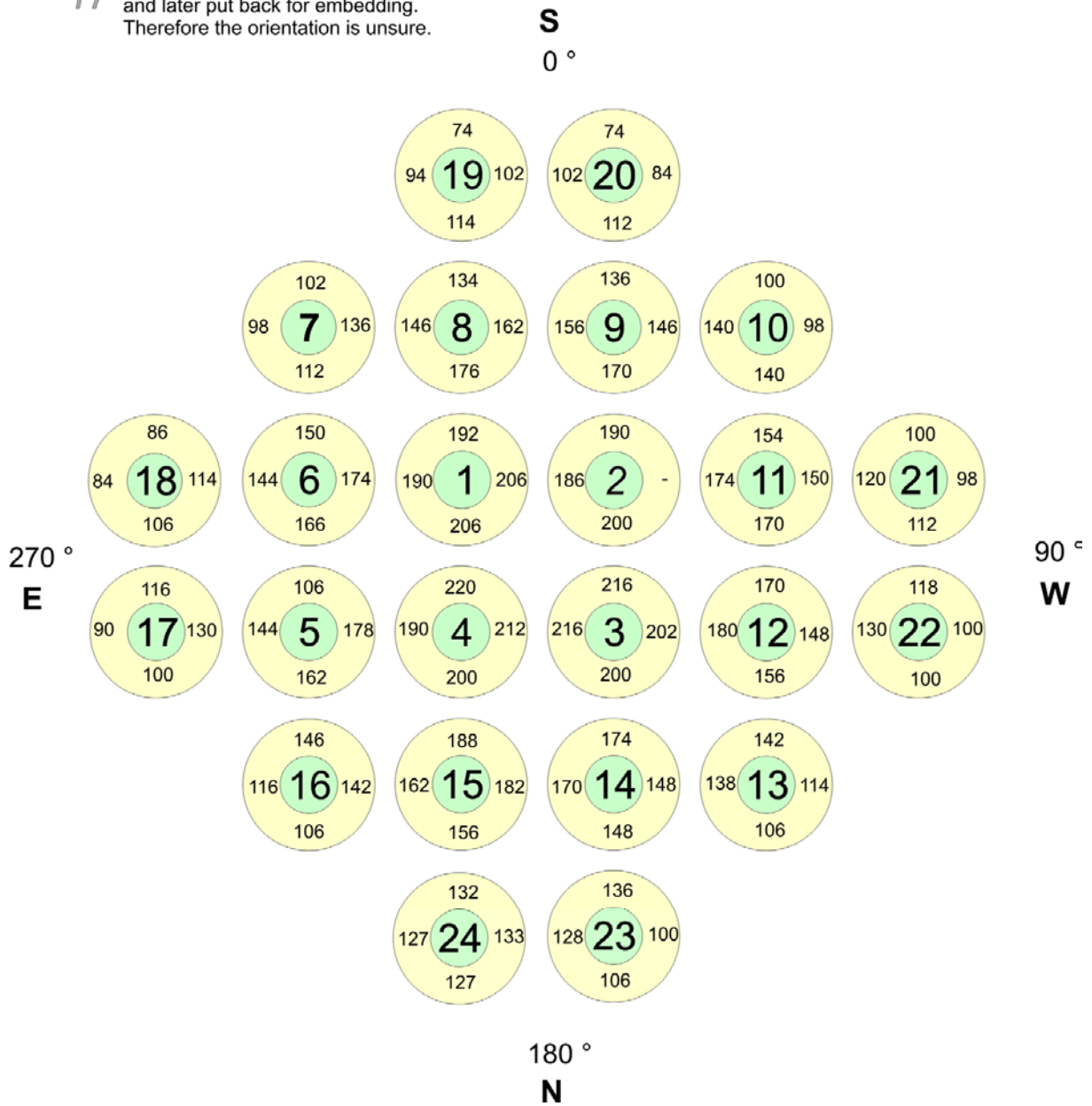


Fig. 100 -QUE15 cross section 15-750.doc
02.03.11 - IMF

Fig. 100: QUENCH-15; Oxide layer thickness at bundle elevation 750 mm (Cross section QUE-15-750).

xxx completely oxidised
 - oxide scale gone

17 Rods that were at first removed from the bundle and later put back for embedding. Therefore the orientation is unsure.

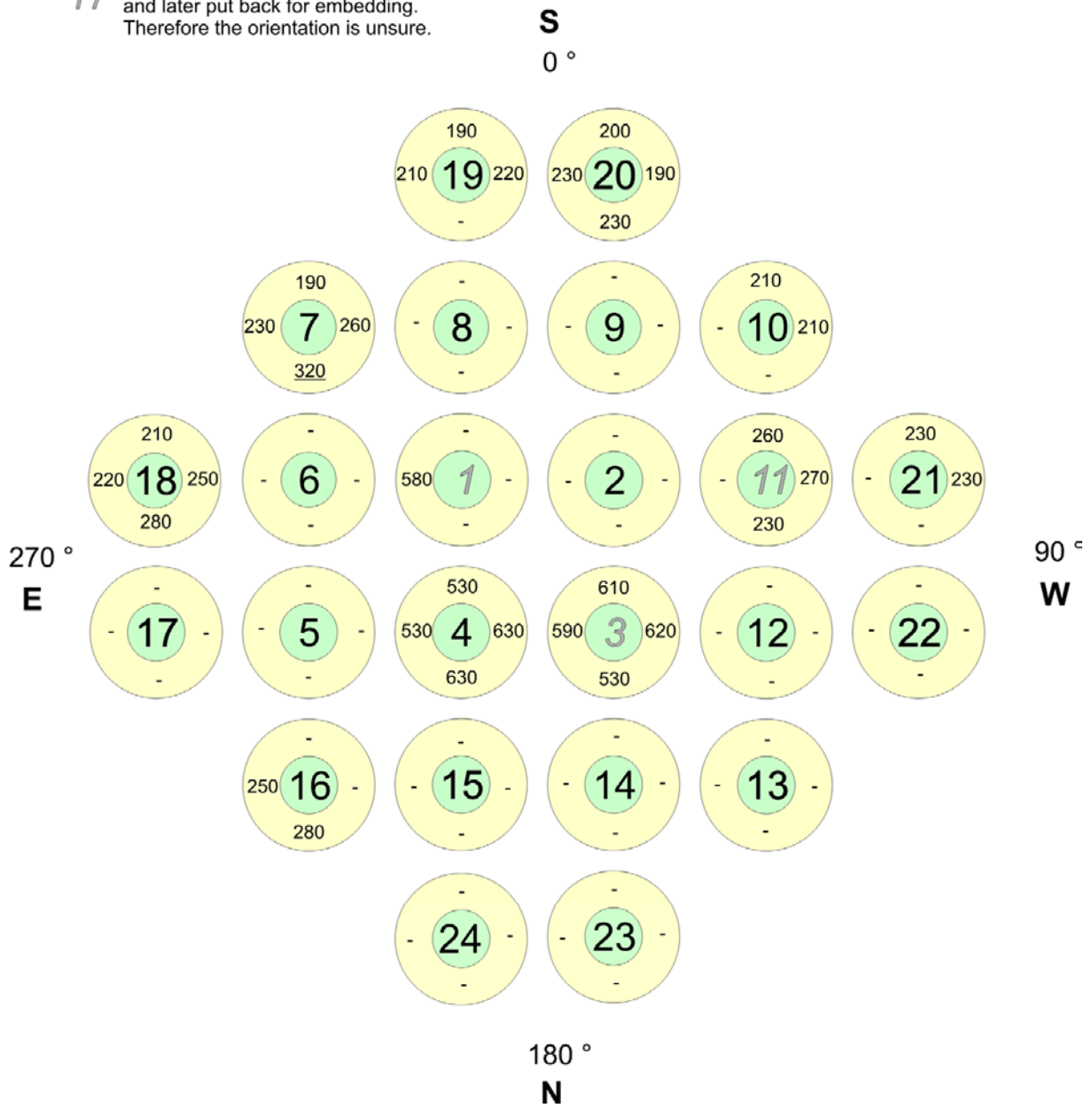


Fig. 101 -QUE15 cross section 15-850.doc
 02.03.11 - IMF

Fig. 101: QUENCH-15; Oxide layer thickness at bundle elevation 850 mm (Cross section QUE-15-850).

xxx completely oxidised
 - oxide scale gone

17 Rods that were at first removed from the bundle and later put back for embedding. Therefore the orientation is unsure.

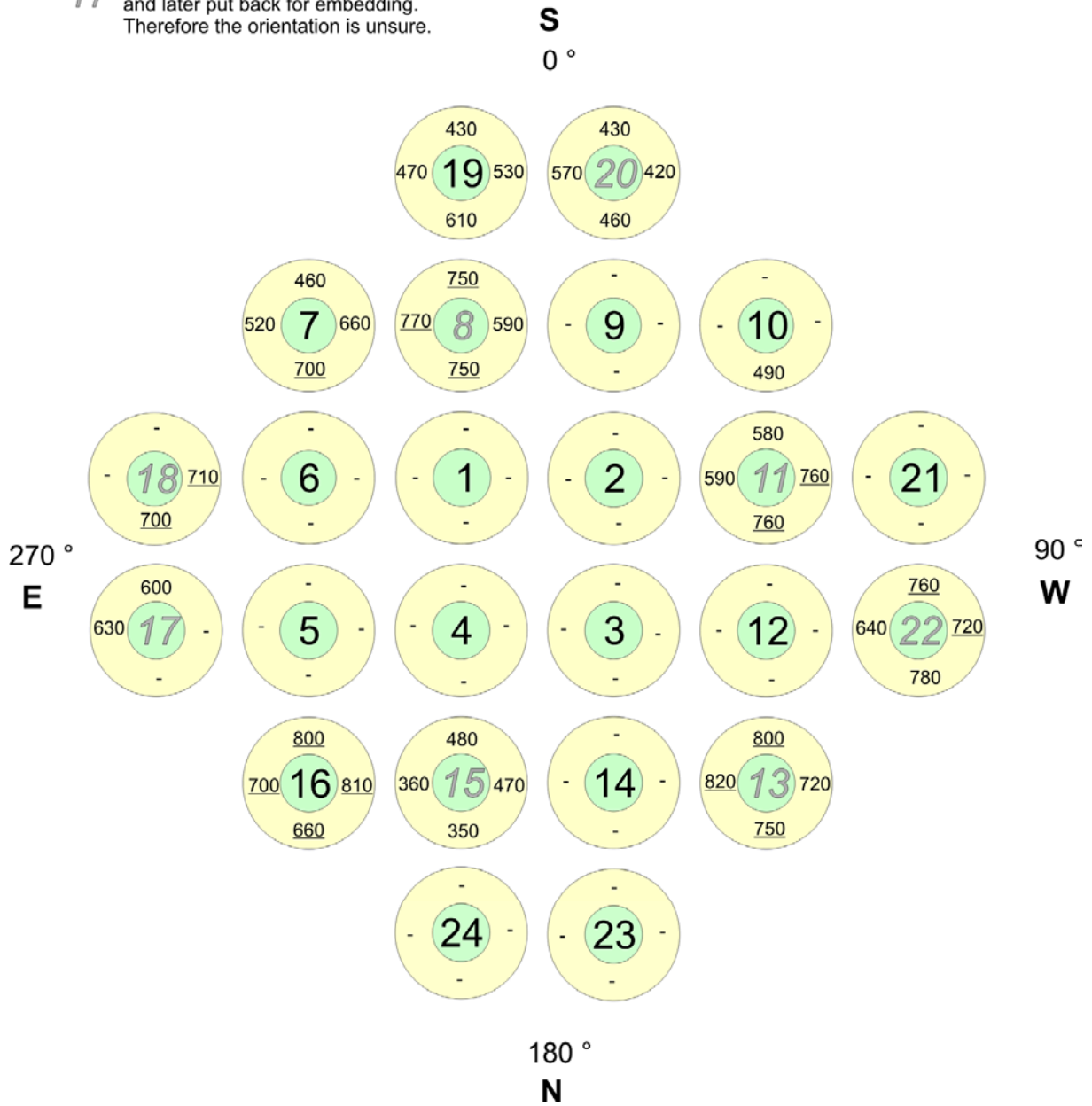


Fig. 102 -QUE15 cross section 15-950.doc
 02.03.11 - IMF

Fig. 102: QUENCH-15; Oxide layer thickness at bundle elevation 950 mm (Cross section QUE-15-950).

xxx completely oxidised
 - oxide scale gone

17 Rods that were at first removed from the bundle and later put back for embedding. Therefore the orientation is unsure.

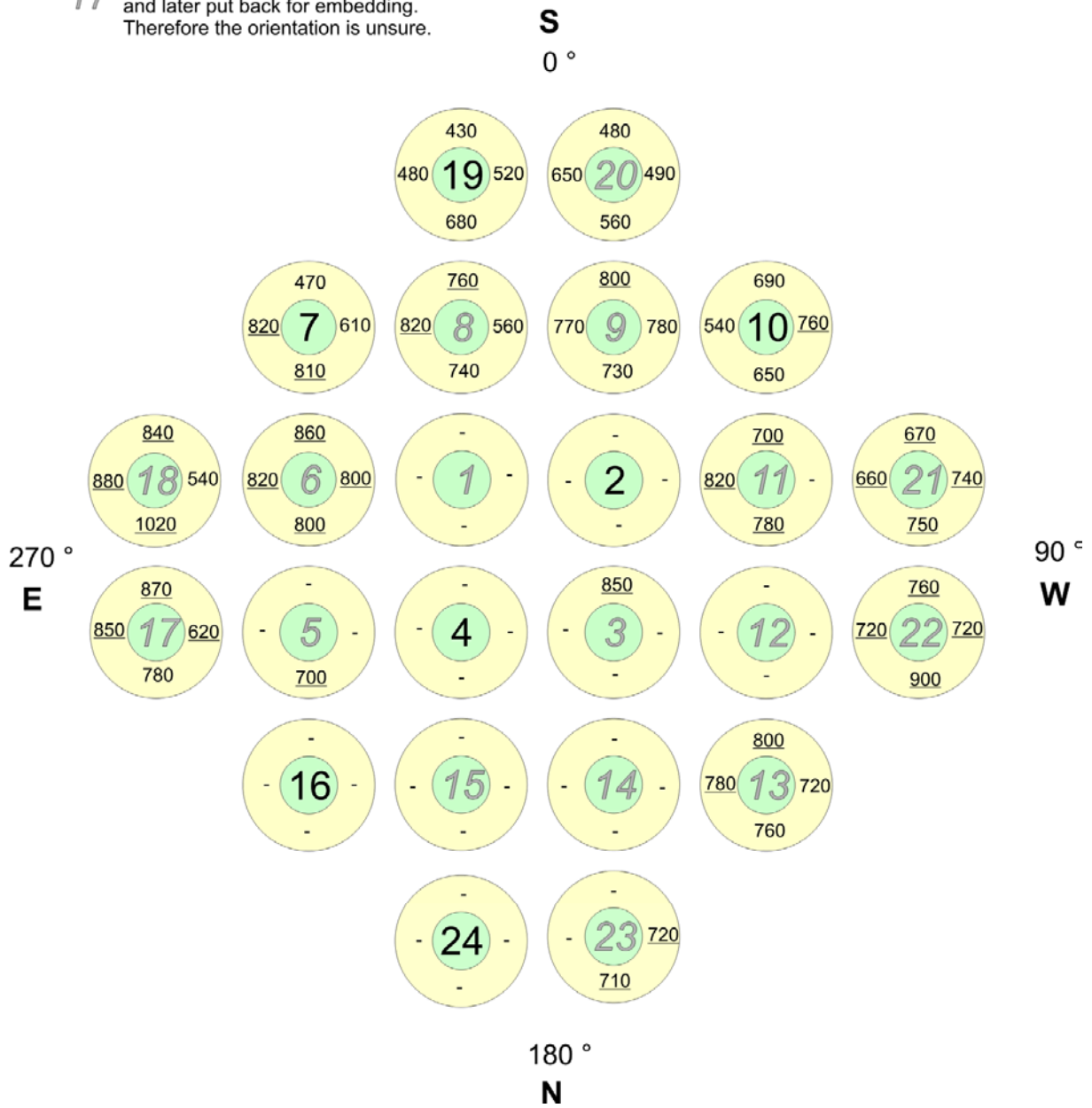


Fig. 103 -QUE15 cross section 15-1000.doc
 02.03.11 - IMF

Fig. 103: QUENCH-15; Oxide layer thickness at bundle elevation 1000 mm (Cross section QUE-15-1000).

xxx completely oxidised
 - oxide scale gone

17 Rods that were at first removed from the bundle and later put back for embedding. Therefore the orientation is unsure.

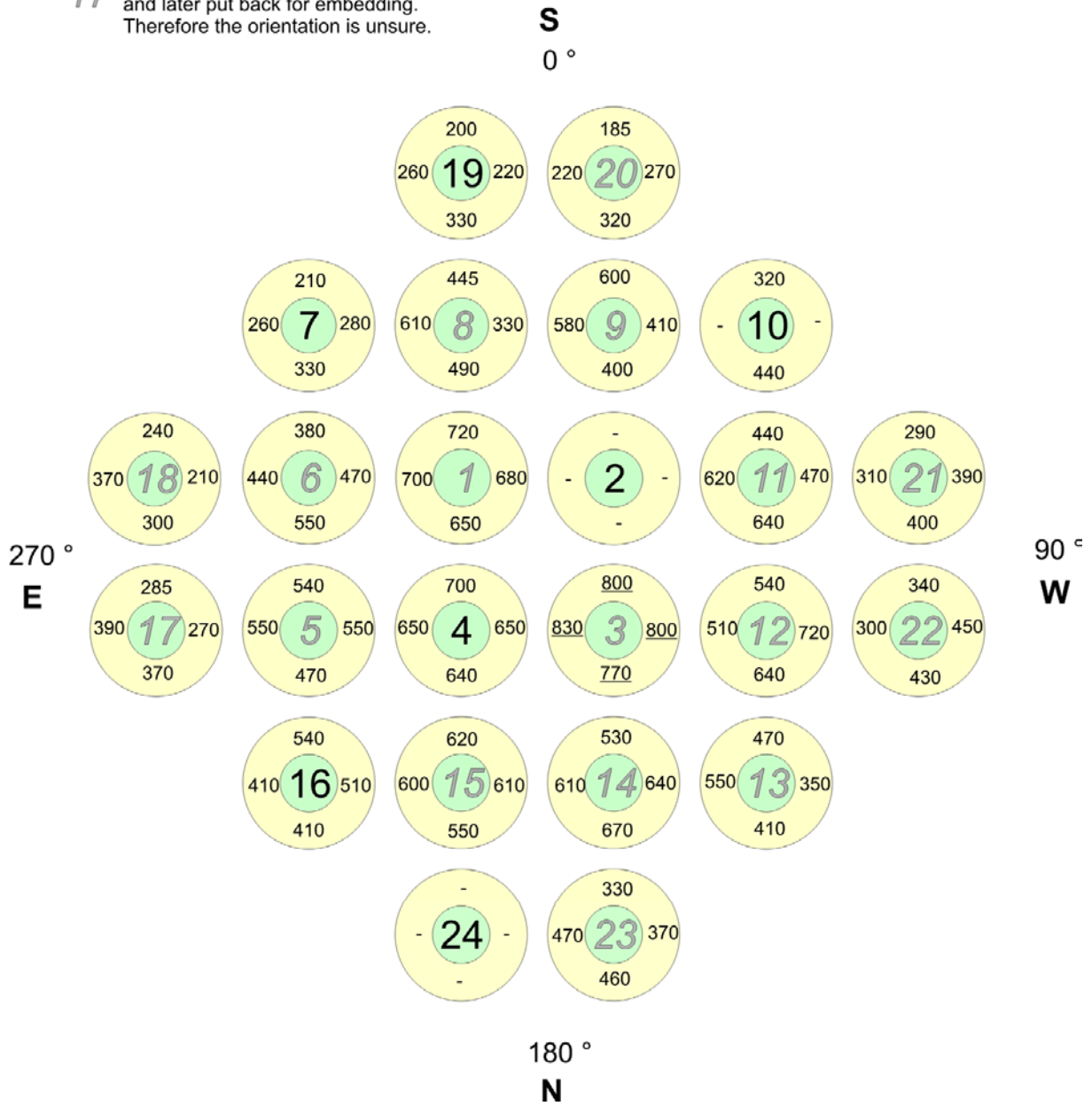


Fig. 104 -QUE15 cross section 15-1050.doc
 02.03.11 - IMF

Fig. 104: QUENCH-15; Oxide layer thickness at bundle elevation 1050 mm (Cross section QUE-15-1050).

xxx completely oxidised
 - oxide scale gone

17 Rods that were at first removed from the bundle and later put back for embedding. Therefore the orientation is unsure.

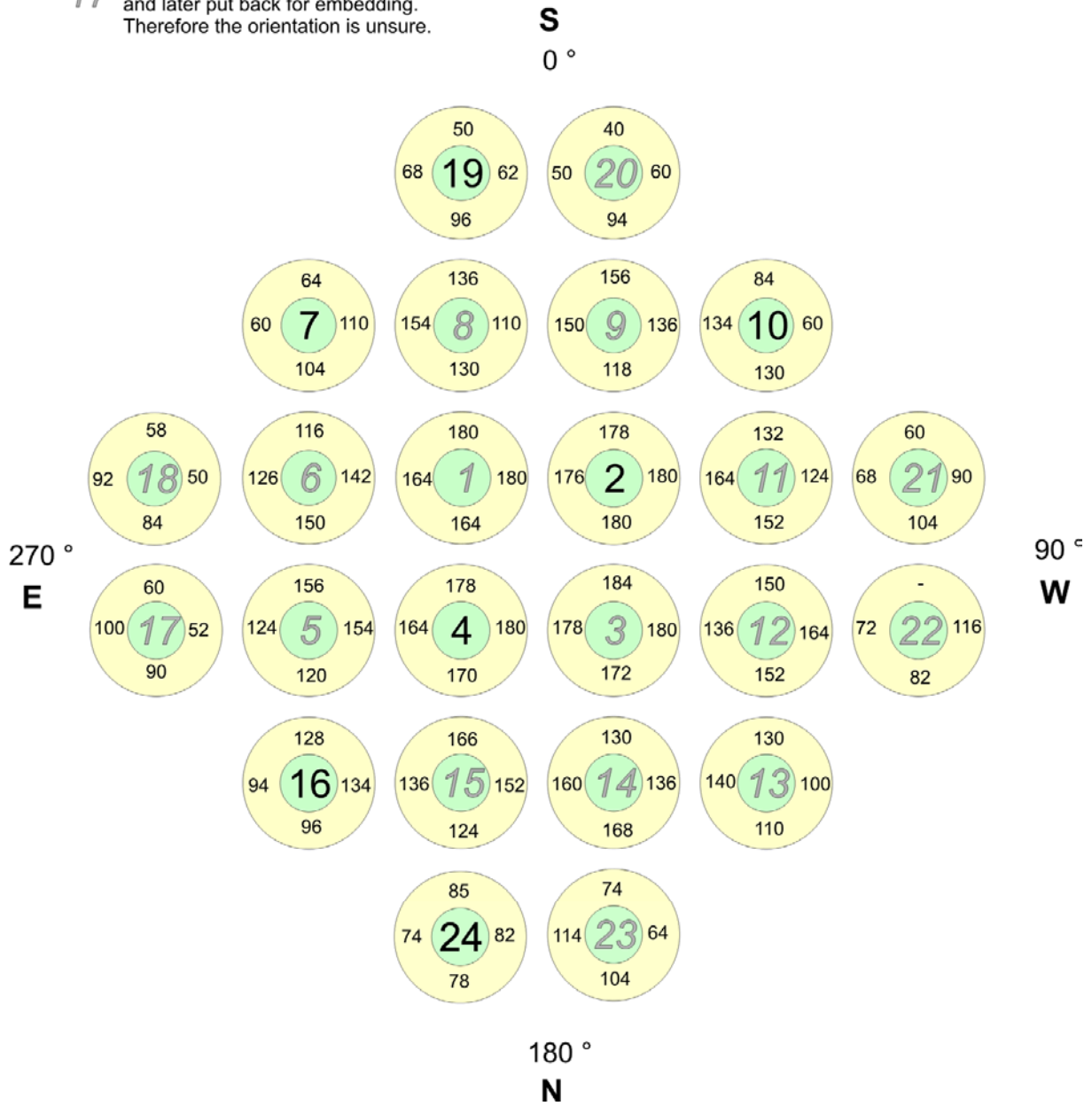


Fig. 105 -QUE15 cross section 15-1150.doc
 02.03.11 - IMF

Fig. 105: QUENCH-15; Oxide layer thickness at bundle elevation 1150 mm (Cross section QUE-15-1150).

xxx completely oxidised
 - oxide scale gone

17 Rods that were at first removed from the bundle and later put back for embedding. Therefore the orientation is unsure.

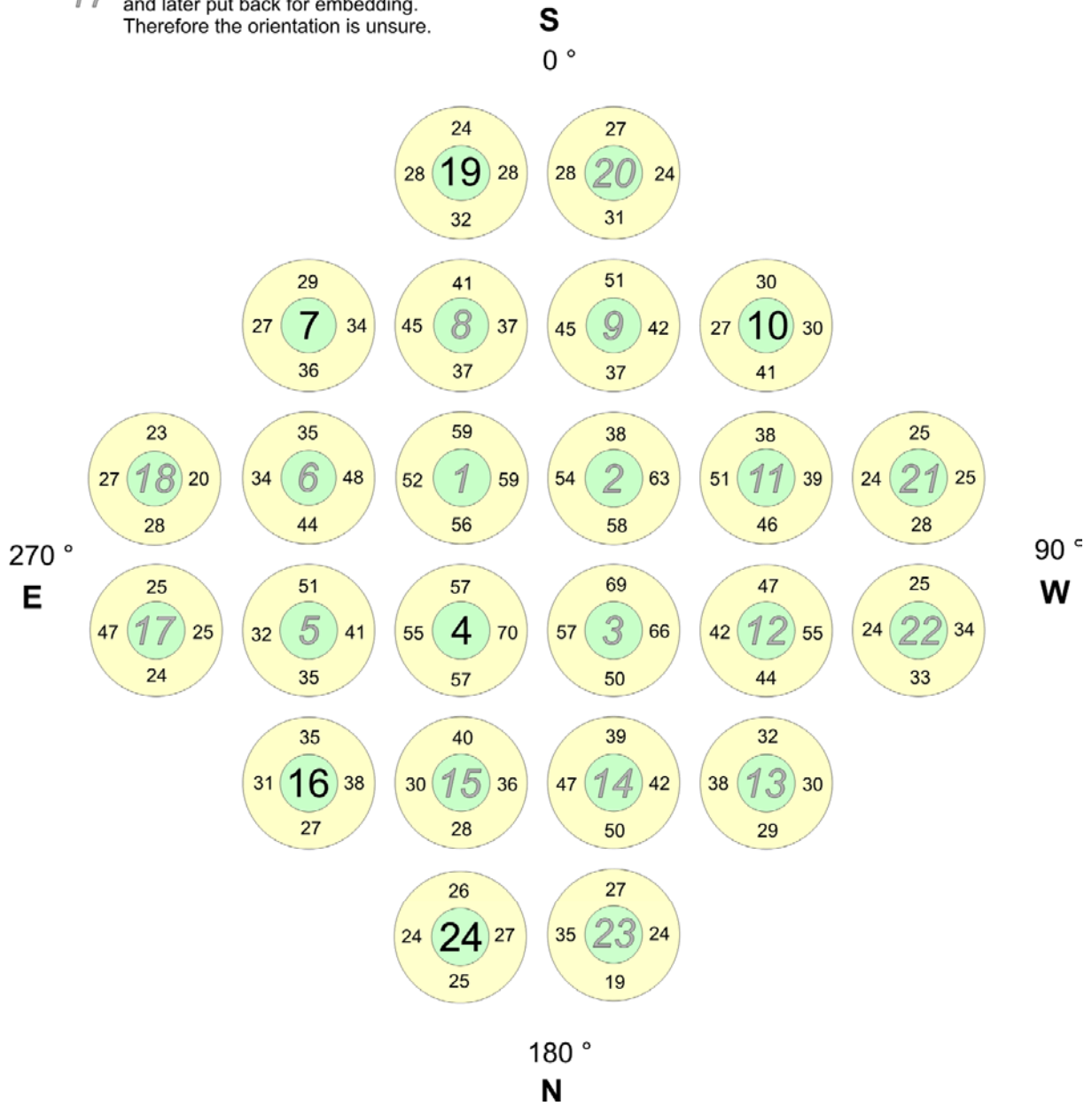


Fig. 106 -QUE15 cross section 15-1250.doc
 02.03.11 - IMF

Fig. 106: QUENCH-15; Oxide layer thickness at bundle elevation 1250 mm (Cross section QUE-15-1250).

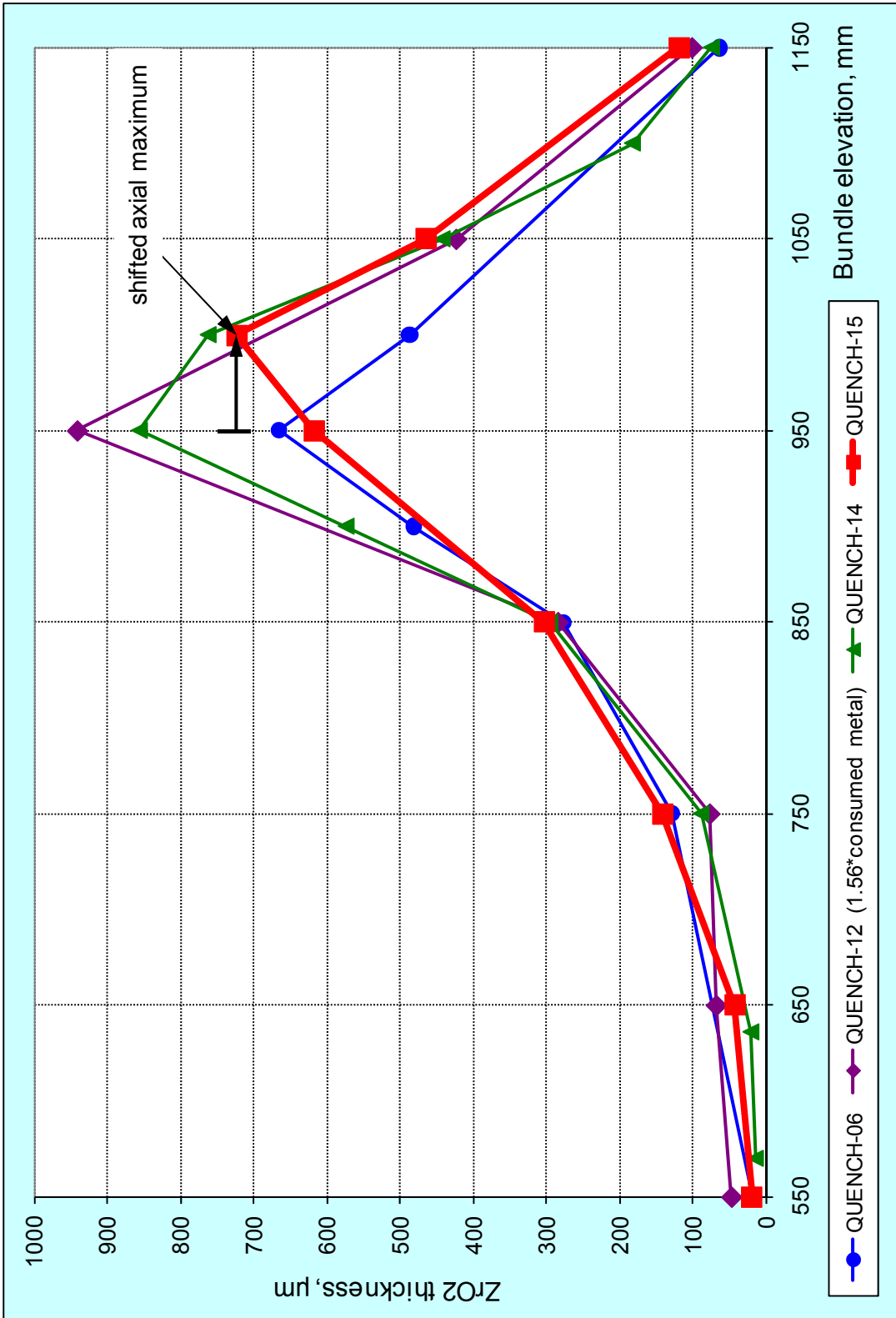


Fig. 107: Axial distribution of cladding outer oxide thicknesses for the bundles QUENCH-06 (Zry4), QUENCH-12 (E110), QUENCH-14 (M5) and QUENCH-15 (ZIRLO).

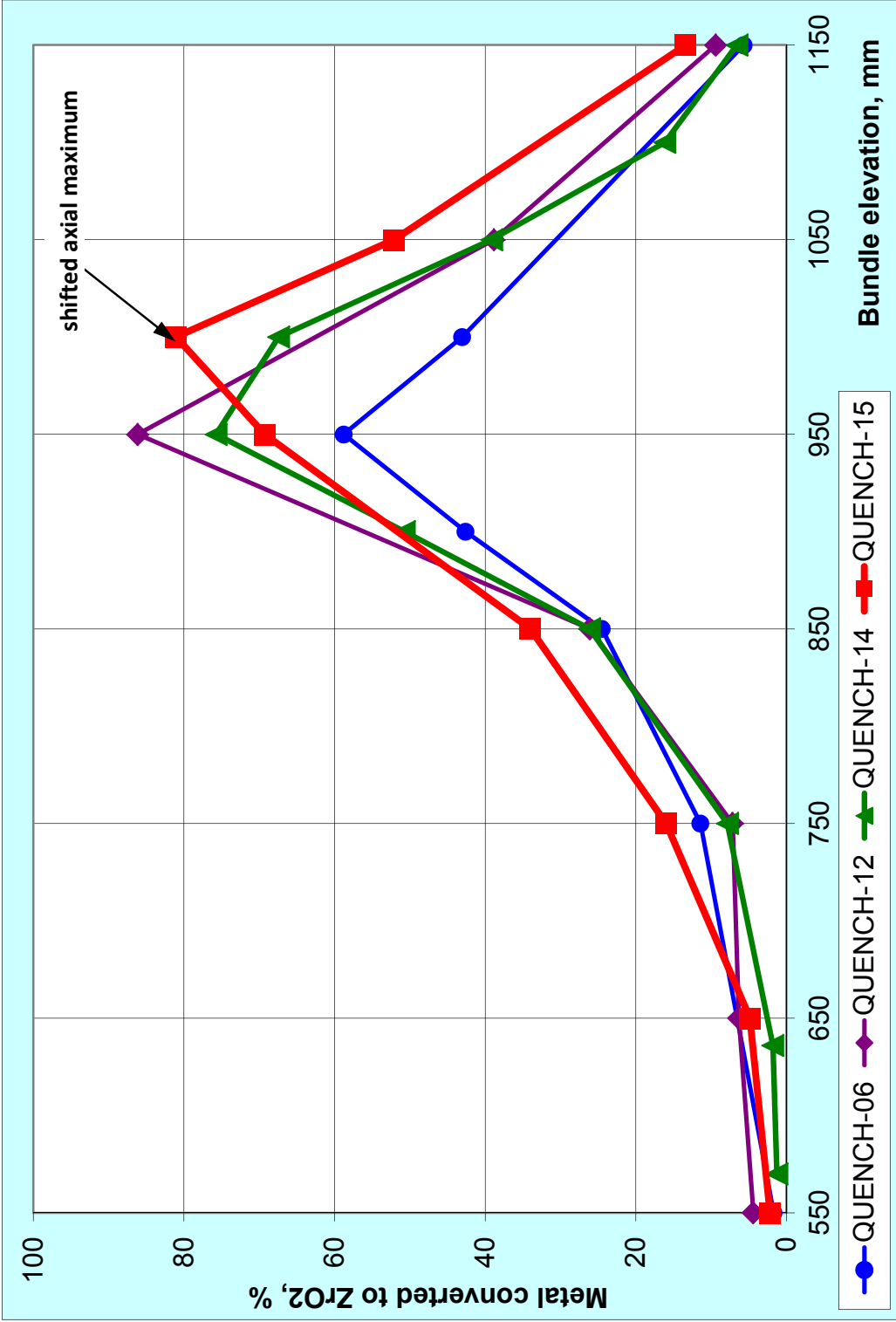


Fig. 108: Axial distribution of cladding metal converted to oxide for the bundles QUENCH-06 (Zry4), QUENCH-12 (E110), QUENCH-14 (M5) and QUENCH-15 (ZIRLO).

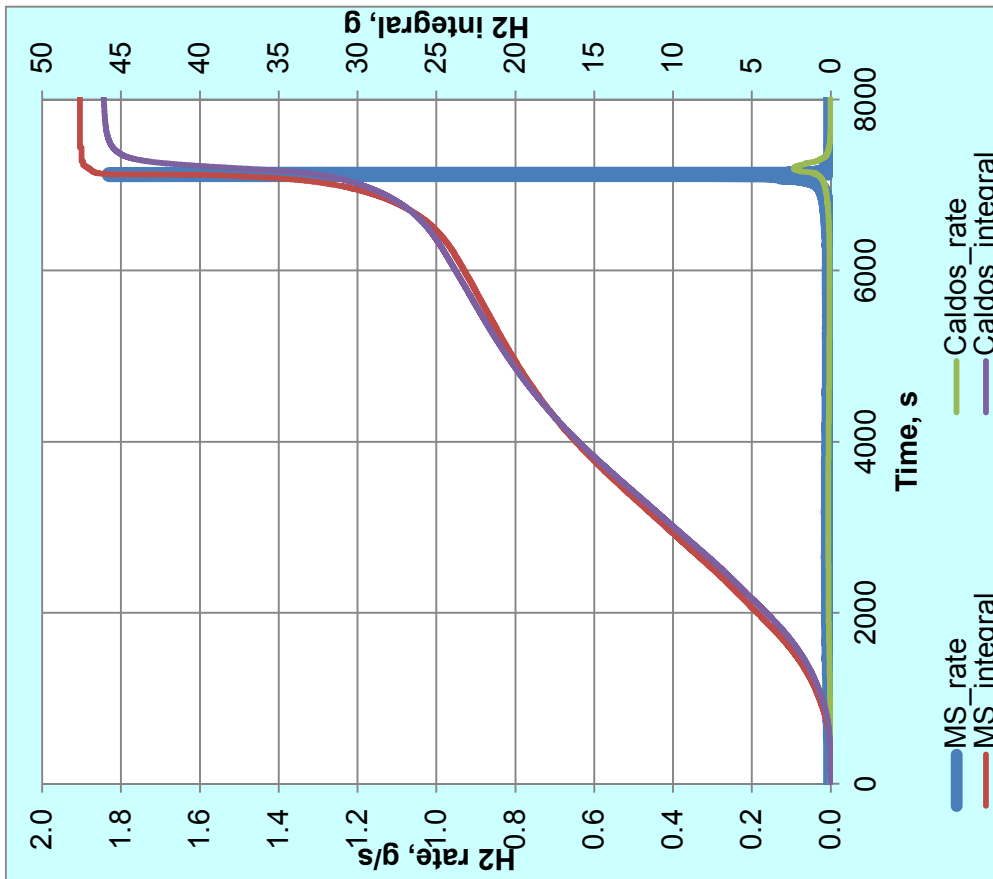
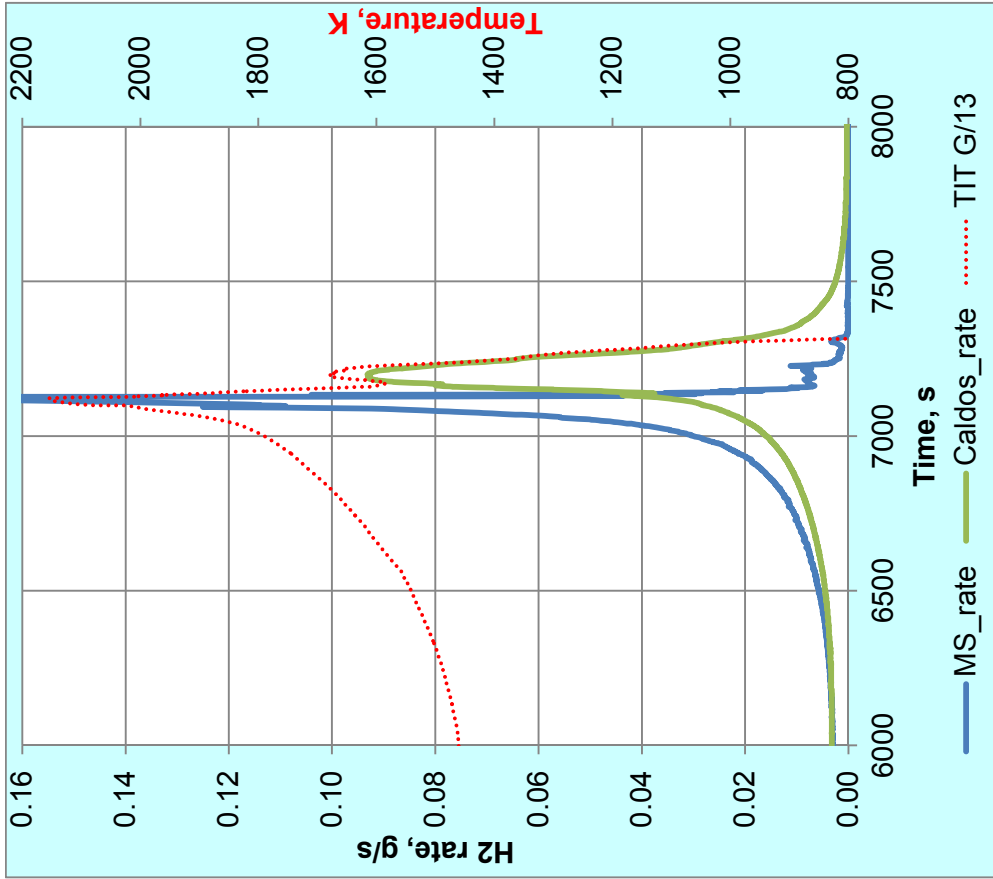


Fig. 109: QUENCH-15; Measurement of hydrogen production with mass spectrometer and CALDOS analyzer during whole test (left) and during transient and reflood phases (right).

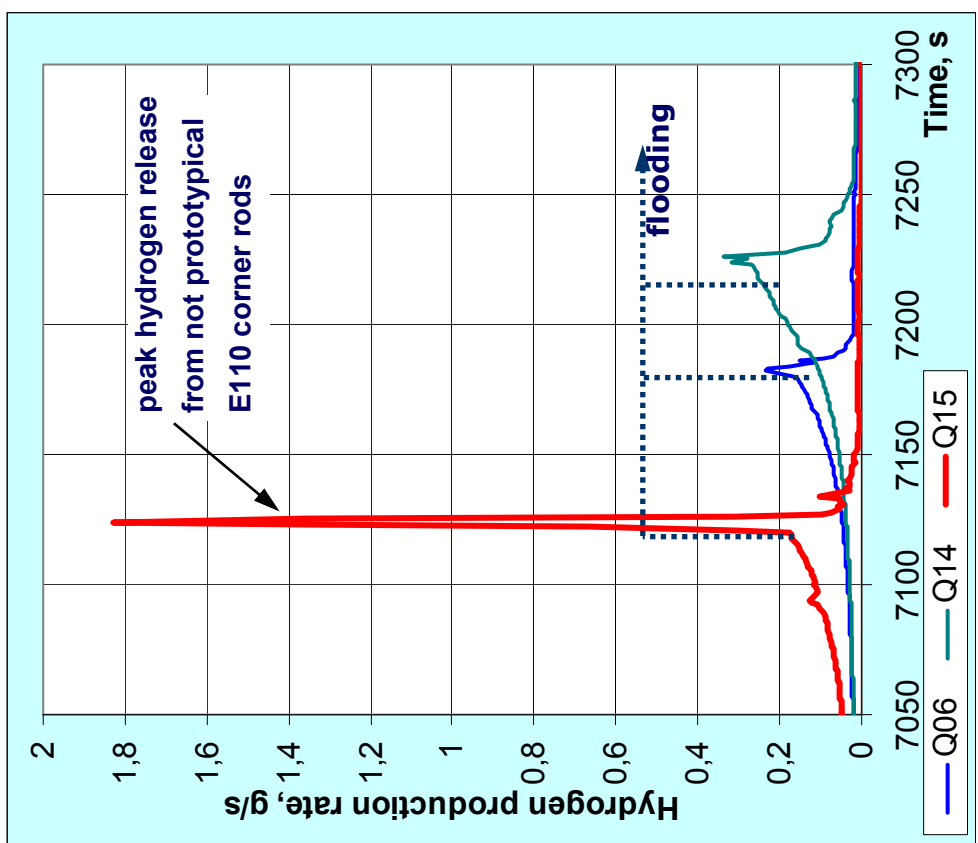
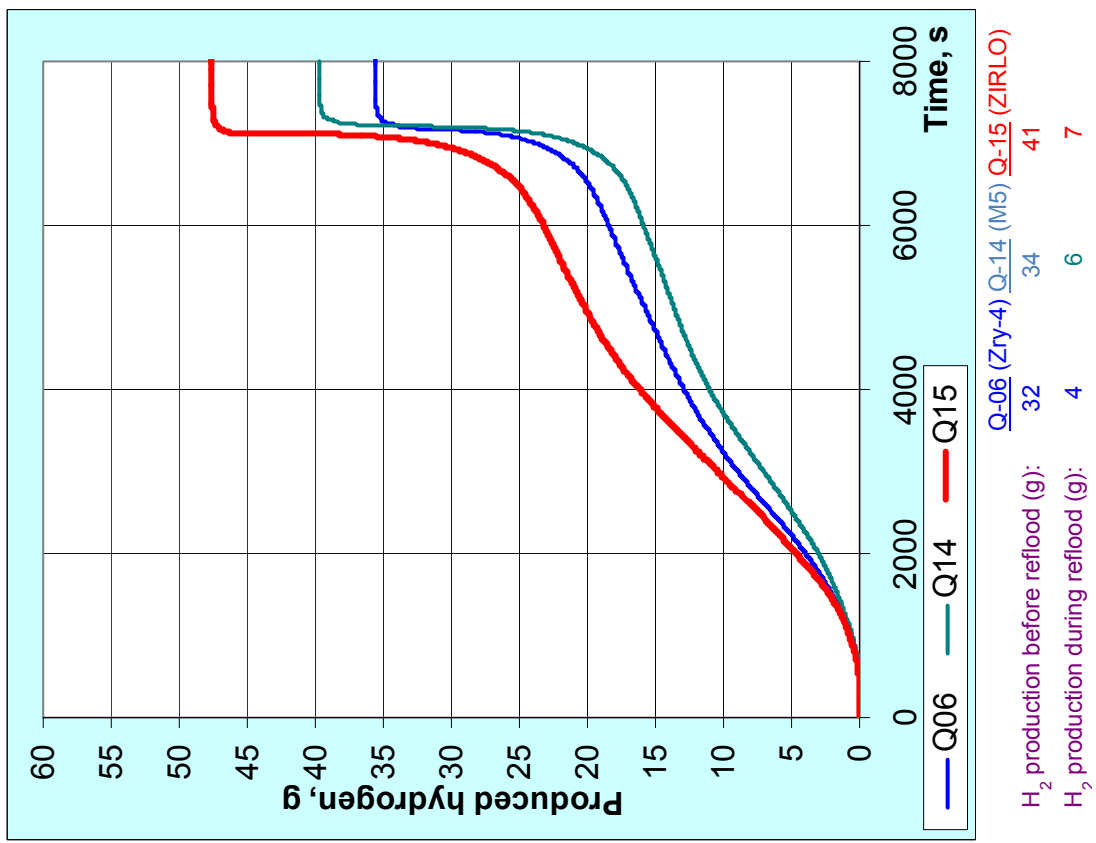


Fig. 110: Hydrogen production for three bundle tests according to mass-spectrometer measurements.

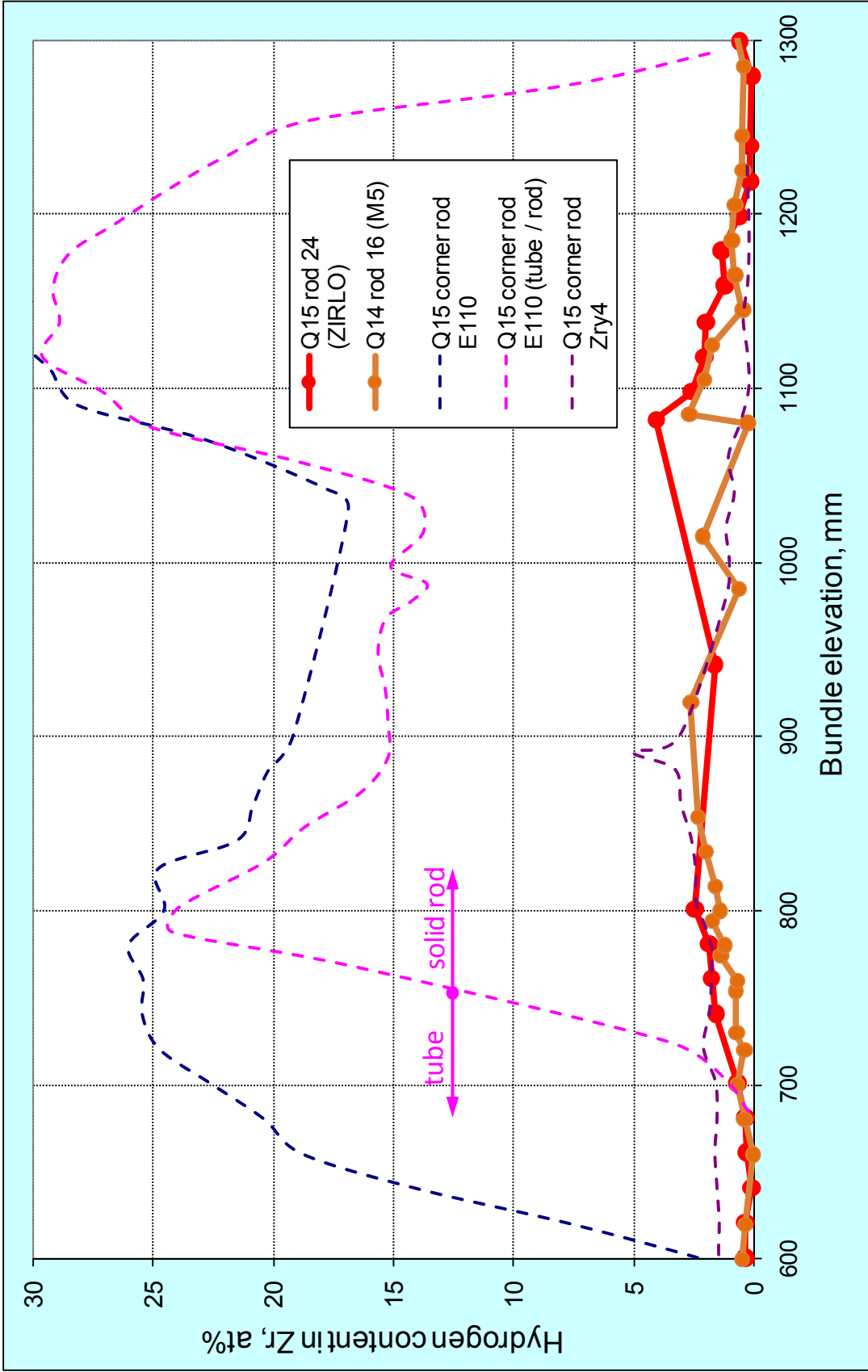
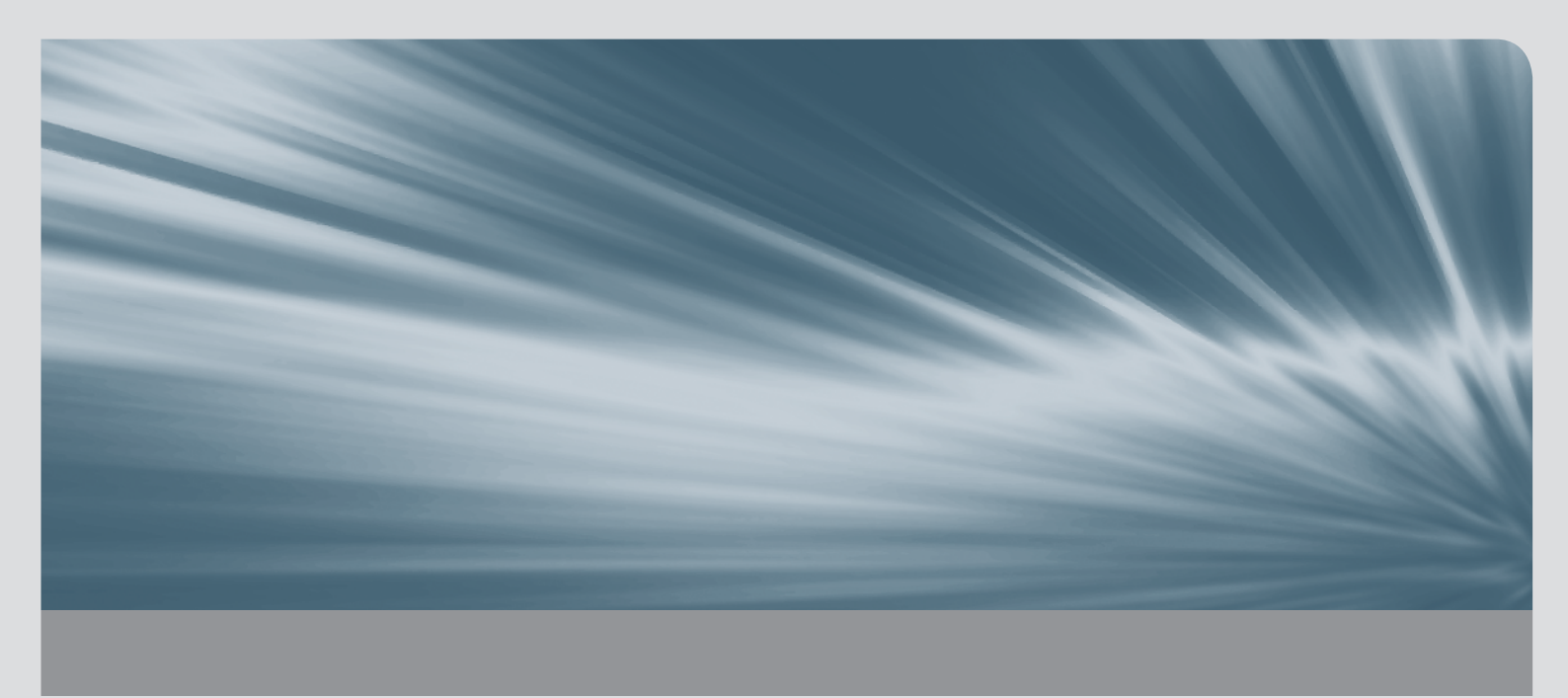


Fig. 111: Hydrogen uptake by ZIRLO cladding and different corner rods of QUENCH-15 bundle in comparison to M5 cladding of QUENCH-14.



The QUENCH experimental program at the Karlsruhe Institute of Technology is a) to investigate the hydrogen source term resulting from water injection into an uncovered core of a Light-Water Reactor, b) to examine the behavior of overheated fuel elements under different flooding conditions, and c) to create a data base for model development and improvement of Severe Fuel Damage code packages. The large-scale experiments are being performed in the QUENCH test facility with test bundles with a total length of approximately 2.5 m.

The QUENCH-15 experiment investigated the effect of ZIRLO™ cladding material on bundle oxidation and core reflood, in comparison with the tests QUENCH-06 (ISP-45, standard Zircaloy-4), QUENCH-12 (VVER, E110), and QUENCH-14 (M5®). The PWR type bundle QUENCH-15 consisted of 24 heated rods (ZIRLO™ claddings), eight corner rods made of Zircaloy-4 and E110, and a Zr-702 shroud. The test involved preoxidation in a flow of 3.45 g/s argon and 3.5 g/s superheated steam at ~1470 K and ~2800 s followed by the transient phase leading to maximum bundle temperatures of 2150 K. The quenching of the test bundle was done with 48 g/s of water and reduction of electrical power. The total hydrogen production amounts to 48 g, compared to QUENCH-06, -12, -14 with 36, 58 and 40 g, respectively. Of 48 g of the total H₂, 41 g were produced during the preoxidation and transient phases and 7 g during quenching in test QUENCH-15. The post-test metallography of the bundle showed neither noticeable breakaway oxidation of the cladding nor melt release into space between rods. The molten cladding metal at the hottest elevation was localized between outer and inner oxide layers. In summary, the analyses of the QUENCH-15 test data indicate a similar global bundle behavior as of experiments QUENCH-14 (M5® cladding) and QUENCH-06 (Zircaloy-4 cladding).

ISSN 1869-9669

ISBN 978-3-86644-670-0

